Fission fragment angular distribution and fission cross section validation

Lou Sai Leong

Université Paris Sud

ECOLE DOCTORALE 534 : MIPEGE

Laboratoire : Institut de Physique Nucléaire

discipline: physique nucleaire

THESE DE DOCTORAT

soutenue le 27/09/2013

par

Lou Sai Leong

Fission fragment angular distributions and fission cross section validation

Composition du jury

Président	*Yorick Blumenfeld*
Rapporteur	*Nicola Colonna*
Rapporteur	*Jean-luc Sida*
Examinateur	*Katsuhisa Nishio*
Examinateur	*Emmeric Dupont*
Directeur de thèse	*Laurent Tassan-Got*

Remerciements

Je remercie tout d'abord l'ensemble de l'IPN d'Orsay pour l'accueil durant ces années de thèse. Mes remerciements vont également à Nicola Colonna et Jean-luc Sida, qui ont accepté d'être les rapporteurs de ce travail malgré le peu de temps qui leur était imparti, et avec qui j'ai pu avoir des discussions approfondies. Et puis merci à Yorick Blumenfeld qui a bien voulu présider le jury au beau milieu de ses déplacements en conférences. Je remercie Katsuhisa Nishio qui a accepté de faire ce long déplacement depuis le Japon pour participer au jury. Je remercie profondément Emmeric Dupont, qui a également accepté d'être membre de ce même jury, et qui a lu très attentivement le manuscrit et apporté de nombreuses corrections pour l'améliorer.

Je remercie très profondément, mon directeur de thèse Laurent Tassan-Got qui est le plus sympatique, intelligent, sportif et parfait que j'aie jamais rencontré, avec plein de connaissances pas seulement en physique, mais aussi pour la vie quotidienne.

Mes trois années de thèse se sont déroulées dans le groupe PACS dans une excellente ambiance, très sympatique tous les jours. Merci à Laurent Audouin qui m'a aidé pour ma participation à l'expérience en Allemagne et qui s'est beaucoup impliqué dans la correction du manuscrit dans la dernière ligne droite. Merci à Mathieu Lebois qui était toujours disponible pour m'expliquer le fabuleux ROOT, à Jonathon Wilson mon directeur de stage qui m'a attiré dans le domaine de physique nucléaire, à Charles-Olivier Bacri avec ses délicieux chocolats, à Sylvain David le vrai physicien curieux qui ose tenter toutes les activités de 9 ans à 90 ans. Les cris et chants de Baptiste Leniau m'ont marquée pour toujours. Merci pour les dépannages de MCNP avec Baptiste et Marc Ernoult, et pour les café-breaks et breaks après breaks. Merci également à Pierre Halipré, Chloé Gerin (merci pour le thé), Xavier Doligez (le français que je connais au langage le plus rapide tout en étant raffiné) et Hervé Lefort.

J'ai énormément apprécié l'ambiance de travail de la collaboration n_TOF, ainsi que tous les membres de cette collaboration, plus particulièrement Frank Gunsing, Eric Berthoumieux, Carlos Paradela, Diego Tarrío, Francesca Belloni, Esther Leal, Mark Vermeulen et Carlos Guerrero (merci pour tes superbes organisations des réunions, discussions, et du travail pour nTOF).

Merci aussi à mes voisins pour les nombreuses soirées que nous avons passées ensemble et pour m'avoir encouragé à rédiger la thèse, Cedric G (poutoux), Cedric M, Marie, Vincent, Michel, Lapo, Arun, Shadi, Frederica, François. Merci à Lucie qui m'a donné la force et m'a accompagnée pendant la période difficile juste avant la soutenance.

Je remercie également Michael pour ses précieuses corrections d'anglais et pour m'avoir accordé 2 heures de cours d'anglais à cette occasion.

Je tiens à remercier la famille Allain et Jouffe. C'est une superbe famille si gentille, sympathique et solidaire que je considèrerai toujours comme ma proche famille. Merci à tous mes proches, Shuoshuo, Caili, Amyeric, Lixun, Annie.

Au final, merci à ma mère et mon frère. Vous êtes loin mais vous m'avez toujours soutenue en arrière-plan malgré toutes mes bêtises...

A mon père...

Contents

List of Figures

List of Tables

Chapter 1

Introduction

1.1 Nuclear power

1.1.1 A brief outlook about energy

Although energy is a subject of passionate debates, there is a wide consensus to foresee a large increase of the global energy demand over the next decades. The very possibility to fulfill this demand is much more disputed; more and more voices call for active policies aiming at reducing the energy demand.

An undisputed point, though, is that the energy production will not keep its present structure. Today, around 80% of the world energy is based on fossil fuels. As fossil reserves are by definition limited, their production will necessarily decline at some point, leading to ever-increasing prices and thus to critical problems for the global economy. In addition, the use of fossil fuels results in an increase of the greenhouse effect, which is becoming a major threat for the sustainability of the world development. Carbon-free energy sources must therefore be developed.

The potential of hydro-electricity has largely been put in use. Solar and wind energies offer nearly unlimited resources, and their prices are dropping steadily, but they are still relatively expensive, especially when one has to account for their intermittent character. The use of biomass for energy production competes with human food supply. Thus, while the nuclear power accounts for only 6% of the global energy consumption, it may have to play an increased role in the future.

1.1.2 Nuclear reactors, past and present

The time lapse between the first clue of the fission phenomena and the first nuclear reactor was remarkably short: the discovery of the neutron took place in 1932, fission was described in 1938, and the world's first "nuclear plant" was built at the site of EBR-I, Iadho and produced 0.8 kW during a test on December 20th, 1951. Several types of reactors have been operated commercially since this date, and various prototypes have been built to test a wider range of concepts.

Basically, all nuclear power plants are steam engines. The nuclear reactor produces heat; this heat is used to vaporize water; and the resulting steam pressure drives a turbine, which in turns drives an alternator, thus creating electricity. The singularity of nuclear power plants lays in the method used for the heat production. It is caused by the chain reaction that takes places in the core, where neutrons induce fission which are accompanied by the emission of neutrons, which in turn trigger new fission, and so on. Most of the fission energy is carried away as kinetic energy by the two fission fragments. These fragments quickly dissipate their kinetic energy in the surrounding material, leading to an increase of its temperature.

Most presently-operated reactors are called thermal, by reference to the thermalization of the neutrons (i.e. their slowing down to thermal kinetic energy, a process called "moderation"). Thermal reactors are particularly suitable to take advantage of the very large fission cross section of ^{235}U with thermal neutrons. Pressurized water reactor (PWR) are an example of thermal reactors. The core is filled with water, with a high-enough pressure to keep it liquid. This water is force-circulated and acts as both a very efficient neutron moderator and as a primary heat transporter. This primary circuit vaporizes the water from a secondary water circuit through a heat exchanger. By contrast, boiling water reactors (BWR) have a simpler design: the steam generation takes place directly in the core. Both types of reactors require an enrichment of the uranium in order to increase its ^{235}U content from 0,7% up to 3,5%. CANDU reactors are similar to PWR in their principle, except that they can be operated with natural uranium thanks to the use of heavy water (D_2O) moderator, which absorbs less neutrons. However, they require a much more frequent fuel replacement.

Another approach is to use unmoderated neutrons, called fast neutrons. A high interest of fast breeder neutrons reactors (FBR) is their capability to convert fertile nucleus ^{238}U to the fissile nucleus ^{239}Pu. The typical example is the conversion of

^{238}U to ^{239}Pu:

$$^{238}\mathrm{U} + n \rightarrow ^{239}\mathrm{U}\ (23\,min) \xrightarrow{\beta^-} ^{239}\mathrm{Np}\ (2.3\,d)(\beta^-) \xrightarrow{\beta^-} ^{239}\mathrm{Pu}\ (24000\,yr) \qquad (1.1)$$

A similar cycle is possible using thorium:

$$^{232}\mathrm{Th} + n \rightarrow ^{233}\mathrm{Th}\ (22\,min) \xrightarrow{\beta^-} ^{233}\mathrm{Pa}\ (27\,d) \xrightarrow{\beta^-} ^{233}\mathrm{U}\ (160000\,yr) \qquad (1.2)$$

The conversion rate can balance or even exceed the consumption rate of the fissile material, leading to a breeding reactor. In both cases, the reactor needs to be refilled only to replace the fraction of ^{238}U (or ^{232}Th) which has been converted and underwent fission. Therefore the net consumption of resources is strongly reduced in comparison to a thermal reactors burning ^{235}U. A major difficulty, though , is to avoid the neutron moderation in the core. This can be achieved by using either a liquid metal or a gas as a primary coolant. Due to this technical challenge, only a few prototypes of such fast neutrons reactors (FNR) have been built for civil use up to now.

1.1.3 Toward a fourth generation of reactors and fuel cycles

The pressurized water reactors (PWR) operated in France were built in the 1970s and 1980s, the major decades of the nuclear power development. Boiling water reactors (BWR) have been commonly used in the United States. These two reactor types are the backbone of the so-called "Generation II" of nuclear reactors. The first "Generation III" reactors are being built by now, in France, Finland and China. These reactors can be seen as an upgrade of the presently-operated reactors, and are expected to provide significant gains in terms of safety, electricity production and waste generation.

All commercial nuclear reactors use uranium as fuel, and a large majority of them are thermal reactors, in which the major part of the fission is due to the sole isotope 235. This isotope accounts only for 0,7% of the natural Uranium : hence, the consumption of uranium is much larger than in a system where all nuclei could undergo fission. If the nuclear power across the world remains at the present level, our reserves shall last for centuries. But if the use of nuclear power is to increase,

these reserves may quickly become hampered. In this case, a better use of the uranium nuclei, or even the use of another nuclei would be mandatory.

In order to address this question, but also to progress further in terms of safety, waste reduction, and proliferation resistance, a strong effort of research has been undertaken around the world on several very innovative reactor designs regrouped under the "Generation IV" label. Most of these "Gen. IV" concepts are based on fast neutrons, with different primary coolant:

- Lead-Alloy Cooled Fast Reactor (LFR)
- Sodium-Cooled Fast Reactor (SFR)
- Gas-Cooled Fast Reactor (GFR)
- Supercritical-Water-Cooled Reactor (SCWR)

But innovative concepts based on thermal spectrum are also studied :

- Very-High-Temperature Reactor (VHTR)
- Molten Salt Reactor System (MSR)

All these studies make extensive use of numerical simulations, which require precise data on all nuclear reactions taking place in the reactor.

1.1.4 The question of the nuclear wastes and their incineration

As any industry, nuclear power generation produces wastes, many of them dangerous. In this work, we will not discuss industrial processes and we will focus on

the heart of the subject, the spent fuel, that we will simply call waste. Basically, this waste can be classified in two groups: fission products, which are short- or medium-lived (meaning that their activity is practically extinct after a few centuries) and are β^- emitters, and actinides, which are responsible for most of the long-term radio-toxicity and are α emitters. During the reactor operation, the fission reactions create hundreds of different fission products, and a variety of actinides (such as Np, Pu, Am...) are formed by successive capture of neutrons on the actinides initially present in the fuel.

The toxicity of nuclear waste, due to their radioactivity, is a major issue of the nuclear energy generation. A reduction of the nuclear wastes, especially the very long-lived ones, has become an important topic among the prospects aiming at developing nuclear energy. A reduction of the wastes can be achieved by using new fuel cycle and/or by actively trying to destroy some of them.

Unfortunately, radioactivity is a spontaneous phenomenon over which science offers no direct control - at least yet. A nuclear reaction is the sole way to alter the course of the evolution of a nucleus by transforming it in one or several other nuclei more stable or short-lived. Only three human devices can generate such reactions: particle accelerators, nuclear reactor cores, and nuclear bombs. The later are obviously not to be considered, the particle accelerators consume too much energy to be used directly to destroy nuclear waste at an industrial scale (although they might be used as part of a waste incineration system - see below). Hence, only reactors may be helpful to reduce the nuisance of nuclear wastes.

The comparatively short half-life of the fission products and their isotopic mixing between radioactive and stable product make them poor candidates for nuclear transmutation. On the other hand, actinides are responsible for most of the long-term radio-toxicity, and can fission (although most of the time only with the action of fast neutrons), which in most cases will result in a drastic reduction of their radio-toxicity. Two main approaches are considered: the insertion of some actinides in the fuel of energy-producing reactors, either thermal or fast, or the use of dedicated actinides burners.

Accelerator-driven system (ADS) have been considered since the mid-90's as a promising concept of radio-nuclei incinerators. They are fast reactors associating a sub-critical assembly and a complementary neutron source consisting of a proton beam impinging on a Pb/Bi target. Neutrons produced by the spallation reactions

sustain the reaction rate in the assembly, while offering neutronics characteristics compatible with a safe use of a fuel heavily loaded in minor actinides. The very hard neutron spectrum from such a reactor would be most efficient to trigger fission from non-fissile actinides; however, such a machine represents an unmatched technical challenge. More conservative options, like the insertion of some actinides in PWR or FBR, are therefore also studied.

1.2 Nuclear Data

Whether one talks about new reactor concepts, new fuel cycles, or the possibility to incinerate a part of the nuclear wastes, a common constraint is the availability of precise information about the nuclear reactions that would be involved. Such information, usually called "nuclear data", are required for a much wider range of nuclei and in a much larger energy range than what was necessary to design and build the first generations of reactors. Furthermore, the required level of precision has been dramatically increased. Hence, in the last two decades, the effort toward providing nuclear data has been strongly increased.

Nuclear data encompass measured and evaluated data of various physical nuclear interactions. They are used as input for numerical calculations in practically all fields related to nuclear science, from nuclear reactor to nuclear modeling and astrophysics. A large number of physical quantities are included, especially reaction and scattering cross sections (including differential cross sections with respect to energy and/or angle) and nuclear structure and decay parameters. Nuclear data are usually limited to particle- or light-nuclei-induced reactions (neutrons, photons, protons, α, etc) on materials that can be handled in a laboratory: they do not include reactions between heavy ions or reactions with exotic nuclei.

1.2.1 Data libraries

Data libraries provide direct access to sets of measured data. They are supposed to contain systematic and statistical errors. The most commonly used library is the one maintained by the International Atomic Energy Agency, EXFOR (http://www-nds.iaea.org/exfor/exfor.htm). It contains the results of more than

20000 experiments. Neutron-induced reactions are extensively covered. Charged-particles and photon reactions are also largely surveyed.

1.2.2 Evaluated data

Multiple data set can co-exist for the same reaction while other reactions have never been measured. In order to feed simulations without having to manage the over-abundance as well as the holes in the data sets, a demand for standardized data emerged early in the nuclear science history. Evaluated data are a response to this requirement of the physics community. They are produced through calculations based on a mix of experimental data (when they exist) and theoretical and empirical modeling.

Nuclear reaction databases contain evaluated cross sections, spectra, angular distributions, fission product yields, thermal neutron scattering, photo-atomic data, etc. Like data libraries, they put an emphasis on neutron-induced reactions, and also cover photon and charged particles reactions. Databases are considered as a strategic resource, so all major global powers have developed their own libraries: JEFF in Europe, ENDF/B in the US, JENDL in Japan, CENDL in China, BROND in Russia.

A large part of the evaluation activity consists of selecting and/or weighting the experimental data sets which will be used, based on the quality of the experimental work. During this process, some data may be re-analyzed in light of new experimental evidences, error bars may be corrected, or data sets may be re-normalized. Different types of data can also be usefully confronted: for example, differential cross sections can be convoluted to a known neutron flux (most likely the flux from a reactor), and compared to the fission yield actually measured in this flux.

A variant of these so-called integral measurements are criticality experiments. They consist of determining the critical point of an assembly. Results can be compared to a benchmark of the same assembly: if the nuclear data used for the calculation are correct, the benchmark should result in the same criticality level as the experiment. Such a comparison is part of this work, as we wanted to test the ^{237}Np fission cross section obtained at n_TOF, which is about 6% higher than the previous measurements above 1 MeV. This particular study is the subject of chapter 7.

1.3 Motivations for the measurement of fission fragments angular distributions

While it is overall correct to describe the fission as an isotropic phenomena, there are cases in which some directions are strongly favored. As it will be explained in chapter 2, this is especially the case around the thresholds of the first, second and third chance fission. The measurement of these anisotropies has a direct interest in terms of basic science, as it provides unique information about the physical properties of the fissioning system. But fission anisotropies also have an impact on the measurement of a key nuclear data: the fission cross sections.

In many cases, the required accuracy for fission cross sections falls down to a few percents - even 2% for fission and capture cross sections on some key isotopes like ^{239}Pu or ^{235}U. Reaching such accuracy in nuclear physics experiment is a formidable challenge. And indeed, in most cases, the presently available data are closer to 5 or 10%, and sometimes much more for nuclei difficult to produce and/or measure.

In the case of fission cross sections, a potential source of experimental bias is the variation of the detection efficiency. Fission fragment have a very short path in solids, barely more than a few micrometers; so even the thinnest targets actually have a non-negligible thickness compared to the fragments path. For a fission taking place at a given depth in the target, the larger the angle of emission of the fragments with respect to the normal to the target surface, the longer the distance to travel in the target to get out of it and be detected. Therefore, at some point, a growing part of the fragments will remain stuck in the target, resulting in a decline of the actual detection efficiency of the system. As the anisotropies are very different from one nucleus to another, and as they strongly depend on the neutron energy, they must be known in order to correct the measurement for the detection efficiency; otherwise, the obtained fission cross section will be flawed.

Figure 1.1 shows the available data on the anisotropy of ^{237}Np. The anisotropy is quantified as the ratio of the number of fission fragments emissions aligned on the incident neutron direction, $W(0°)$, over the number of fission fragments emissions taking place orthogonal to the neutrons direction, $W(90°)$. While this is not the complete angular distribution, this quantity still gives a significant information on the distribution behavior. The second figure represents the ^{232}Th

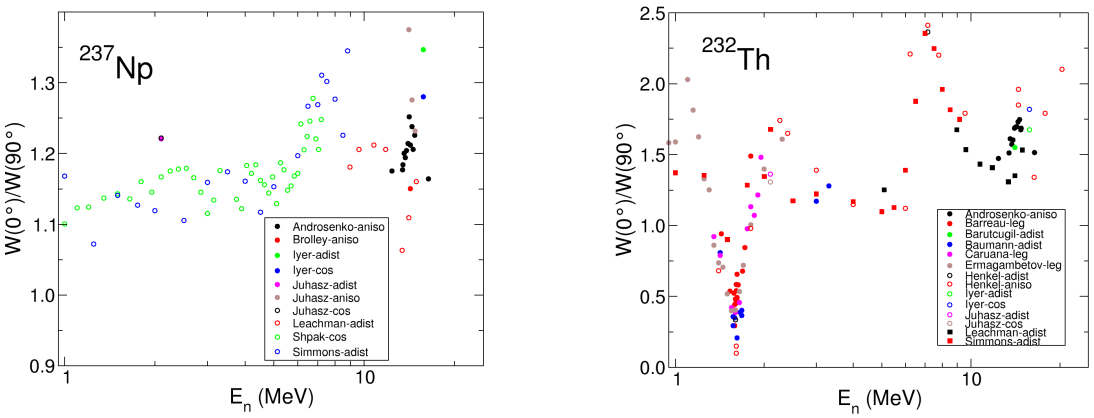

FIGURE 1.1: Existing measurements of the anisotropy of fission fragments for ^{237}Np (left) and ^{232}Th (right). For sake of clarity the uncertainty is not reported, the dispersion of the points is an indication of the actual uncertainty.

data. ^{232}Th (even-even nucleus) anisotropy is higher than in ^{237}Np (odd nuclei) in the energy range between 1 MeV and 20 MeV. The existing measurements are in good agreement with one another up to 10 MeV, but large discrepancies are visible at 14 MeV, even around 14 MeV which has been measured many times with neutrons from $D-T$ reactions.

These figures also illustrate the fact that data are extremely scarce beyond 20 MeV, except for ^{232}Th and ^{238}U which were measured by Ryzhov and the Uppsala group (see fig. 1.2). Fission cross section in this energy region (beyond 20 MeV) is generally regarded as less important for reactors, because even FNR spectrum extend only to a few MeV. However, in ADS, the energy spectrum may reach to hundreds of MeV - as already mentioned, this is a net advantage as it significantly increases the fission yield of many actinides.

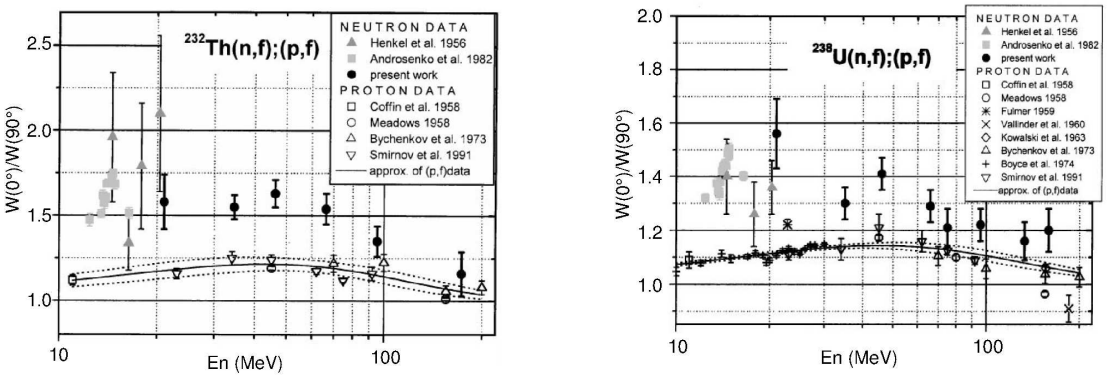

FIGURE 1.2: Comparison of anisotropy for neutron- and proton-induced fission for ^{232}Th (left) and ^{238}U (right) [1].

Tutin[1] proposed a comparison of the ^{232}Th and ^{238}U data obtained with protons and with neutrons (figure. 1.2). At intermediate energies if the incoming nucleon is captured the fissioning system is different for the two systems ^{232}Th+p and ^{232}Th+n and a difference in the angular distributions is expected, and actually observed. In the spallation regime though, the incident particle is not stopped inside the target, so that the same fissioning pre-fragments are produced. Both systems should therefore present a very similar behavior. However, data show the persistence of significant discrepancies. If these discrepancies are confirmed by new measurement, they may shed new lights on the reaction mechanisms. Beyond the application level, this is an additional motivation to study the anisotropy of the ^{232}Th fission.

1.4 Overview of this document

In chaapter. 2, we will discuss the fission theory, especially the relation between the angular distribution and the nuclear spin. In chapter 3 we will present the n_TOF facility and the experimental set-up we used for fission cross section and angular distribution measurements. In chapter 4 we will describe the analysis method leading to the reconstruction of the fission directions. Chapter 5 addresses the second part of the analysis: the extraction of the angular distribution from the fission directions, taking int account the detector efficiency. The final result and the interpretation of the data will be presented in chapter 6. In addition, we will present a validation of fission cross section measured with our set-up with a criticality experiment in chapter 7.

Chapter 2

Theory

2.1 Fission

Fission is the process by which a nucleus of an atom splits into two smaller fragments either after a nuclear collision or even spontaneously. A fission process produces two main fission fragments, free neutrons and releases a large amount of energy, about 200 MeV. Although it is widely known to apply to the actinides, from actinium (Z=89) to nobelium (Z=102) among which there are thorium, uranium, neptunium, plutonium, it is a more general process acting on all heavy nuclei.

Fission is normally binary and sometimes ternary. In the latter case the third nucleus is at 90% α, and sometimes a triton or a carbon. For the actinides, fission is always exoenergetic. Its total released energy is around 200 MeV, which 165 MeV (around 75%) is for fission fragments kinetic energy, about 10% for prompt neutrons, 4% for prompt γ and 8% for delayed neutrons.

In 1938, Fermi received a Nobel prize in physics for his demonstration of the existence of new radioactive elements produced by neutron irradiation, and for his related discovery of nuclear reactions brought about by slow neutrons.
After that, Meitner and Frisch gave a first explanation in the framework of the charged liquid drop model (LDM). They supposed that a uranium nucleus vibrates when collided by a neutron and then breaks up into two smaller fragments, hence coining the name of "fission". Those fragments stop in the surrounding materials and release an energy of about 200 MeV. Afterwards, in 1939, Bohr and Wheeler

described a more detailed theory of fission based on the liquid drop model [11]. Subsequently, the theory has been proven in the same year by Frederic Joliot.

2.1.1 The liquid drop model

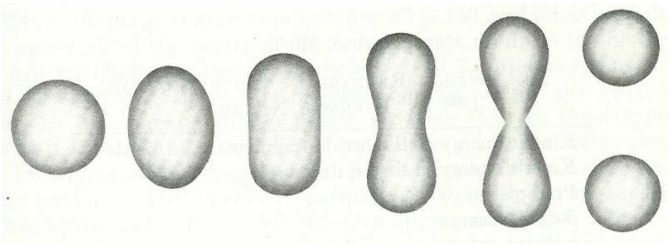

FIGURE 2.1: Sequence of shapes from a spherical nucleus to 2 well separated fragments, similar to the break up of liquid drop. The penultimate drawing corresponds to the scission point.

From the properties of the nuclear interaction and the systematics of binding energies a semi-empirical formula for the binding energy of nuclei, called Bethe-Weizsäcker's formula, has been inferred and fitted. This equation has five terms describing the attractive strong nuclear force: a volumetric term, a surface energy term, an asymmetry term and a pairing term, and a fifth term for the electrostatic mutual repulsion of the protons.

The volumetric term is proportional to the nucleus mass A. It reflects the incompressibility of nuclear matter in normal conditions and the saturation of the nuclear force: each nucleon interacts with a constant number of nucleons due to its short range.

The surface term is justified to correct the volume term since those nucleons on the surface of the nucleus have fewer nearest neighbors thereby reducing their binding energy.

The asymmetry term goes as the square of the proton or neutron excess and takes into account the fermionic property of nucleons preventing them to go to lower occupied states. It takes also into account the difference of the interaction of a proton and a neutron in an asymmetric medium.

The pairing energy reflects the fact that pairs of nucleons have a lower energy when they couple with opposite spins. An even number of particles is more stable than an odd number.

As described so far Bethe-Weizsäcker's formula always predicts a lower energy for spherical shapes due to the minimization of the surface energy. In fact true nuclei have often a static deformation due to quantum effects. However we first examine the case of a spherical nucleus and the form taken by the LDM formula of the binding energy in this case.

Static spherical drop

The radius is denoted R_0. The incompressibility of nuclear matter implies: $R_0 = r_0 A^{1/3}$ where r_0 is a constant.

- Volume energy $E_v = C_v A$
- Surface term $E_s = C_s A^{2/3}$ because the surface area goes as $A^{2/3}$

The Coulomb repulsion between each pair of protons inside the nucleus is a long-range force, contributing toward decreasing its binding energy.

- Coulomb term: $E_c = C_c \frac{Z^2}{A^{1/3}}$.

This results from the Coulomb energy of a uniformly charged drop proportional to Z^2/R_0.

- Asymmetry term: $E_{asym} = C_a \frac{(Z-\frac{A}{2})^2}{A}$.

Eventually, an energy which is a correction term that arises from the tendency of proton and neutron pairs to form. This is the principle of pairing.

- Pairing term: $E_p = \pm\delta(Z) \pm \delta(N)$ that depends on the even-odd character of proton and neutron numbers.

Thus the liquid drop energy for a spherical shape is:

$$E_{LDM} = C_v A - C_s A^{2/3} - C_c \frac{Z^2}{A^{1/3}} - C_a \frac{(Z-\frac{A}{2})^2}{A} \pm \delta(Z) \pm \delta(N) \tag{2.1}$$

2.1.2 Nucleus deformation

To describe the fission process, Bohr considered a quadrupole deformation of a liquid drop, the radius elongation is described as a function of polynomial:

$$R(\theta) = R_0 \left[a_0 + a_2 \, P_2(\cos\theta)\right]. \tag{2.2}$$

where a_2 is a parameter quantifying the deformation ($a_2 = 0$ for a sphere) and P_2 is a Legendre second order polynomial P_2. θ is the angle between symmetry axis and $O\vec{M}$. a_0 is adjusted to conserve the volume. The advantage of this expansion is that only a few terms are needed and the orthogonality of these polynomials lightens the calculations. See Appendix A for their properties.

Then the deformation leads to two halves of the not-exactly-spheroidal drop found at a larger distance apart, see in fig. 2.1.

Bohr looked at the variation of the LDM energy brought by this deformation.

$$E_{def} = E_{LDM}(a_2) - E_{LDM}(0) \tag{2.3}$$

where $E_{LMD}(0)$ is the LDM energy of the undistorted sphere. The volume energy remains invariant with the deformation due to the low compressibility of nuclear matter. Thus the deformation energy depends on surface and Coulomb terms: the former increases with the deformation while the latter decreases, so that they compete.

$$E_{def}(a_2) = E_s(0) + E_c(0) - E_s(a_2) + E_c(a_2) \tag{2.4}$$

$E_s(0)$ and $E_c(0)$ are the surface and Coulomb energies of the undistorted sphere.

The surface and Coulomb energies for small distortions are given by Bohr and Wheeler [11]:

$$E_s(a_2) = E_s(0)(1 + 2/5a_2^2); \quad E_c(a_2) = E_c(0)(1 - 1/5a_2^2) \tag{2.5}$$

Consequently, the stability of a spherical nucleus is given by the fact that $E_c(0) < 2E_s(0)$. This leads to the definition of the **fissility parameter**.

$$x = \frac{E_c^0}{2E_s^0} \quad \propto \frac{Z^2}{A} \tag{2.6}$$

The higher the fissility parameter, the more easily the nucleus will be deformed.

In general the quadrupole deformation is not accurate enough to describe the shapes along the fission process, as depicted in figure 2.1. Other terms in the Legendre polynomial expansion should be added. In case of axially symmetric shapes:

$$R(\theta) = R_0 \left[a_0 + \sum_{l=0}^{\infty} a_l P_l(\cos\theta) \right] \tag{2.7}$$

with $R_0 = r_0 A^{1/3}$.
In this sum the dipole term ($l = 1$) is omitted because it corresponds to a shift of the shape. Beyond the quadrupolar term ($l = 2$) the odd terms define the mass asymmetry, in particular the octupole term ($l = 3$). The $l = 4$ term is the hexadecapolar contribution. Again the monopole term a_0 is tuned so as to conserve the volume.

Fission barrier

When the nucleus starts to deform its surface energy increases faster than the reduction of the electrostatic energy as illustrated in the upper left diagram of figure 2.2. Therefore the nucleus is stable against this deformation at low amplitude. But if the deformation increases the electrostatic energy drops quickly so that the deformation energy starts to decrease. Therefore the deformation energy reaches a maximum which is called the barrier (figure 2.2 upper left: curve labeled "Net"). If the deformation corresponding to the barrier is reached the nucleus evolves inexorably toward fission.

When the deformation is defined by an ensemble of parameters (the a_l for example), the barrier is the minimal energy among all the possible paths in the space of the parameters, leading to a splitting into 2 fragments. Generally it corresponds to a maximum along one direction and a minimum in the other degrees of freedom, that's why it is called "saddle point". This is illustrated in the upper right diagram of figure 2.2 where the deformation is described with quadrupolar (β_2) and hexadecapolar (β_4) terms and gets the shapes shown in the lower part of the figure. The barrier corresponds to a maximal energy along the diagonal indicated by the dashed line, whereas it's a minimum in the other direction.

In order that fission takes place the excitation energy of the nucleus should be higher or at least close to the barrier. In this case as a coupling exists between the intrinsic states populated by thermal excitation and the vibrational states

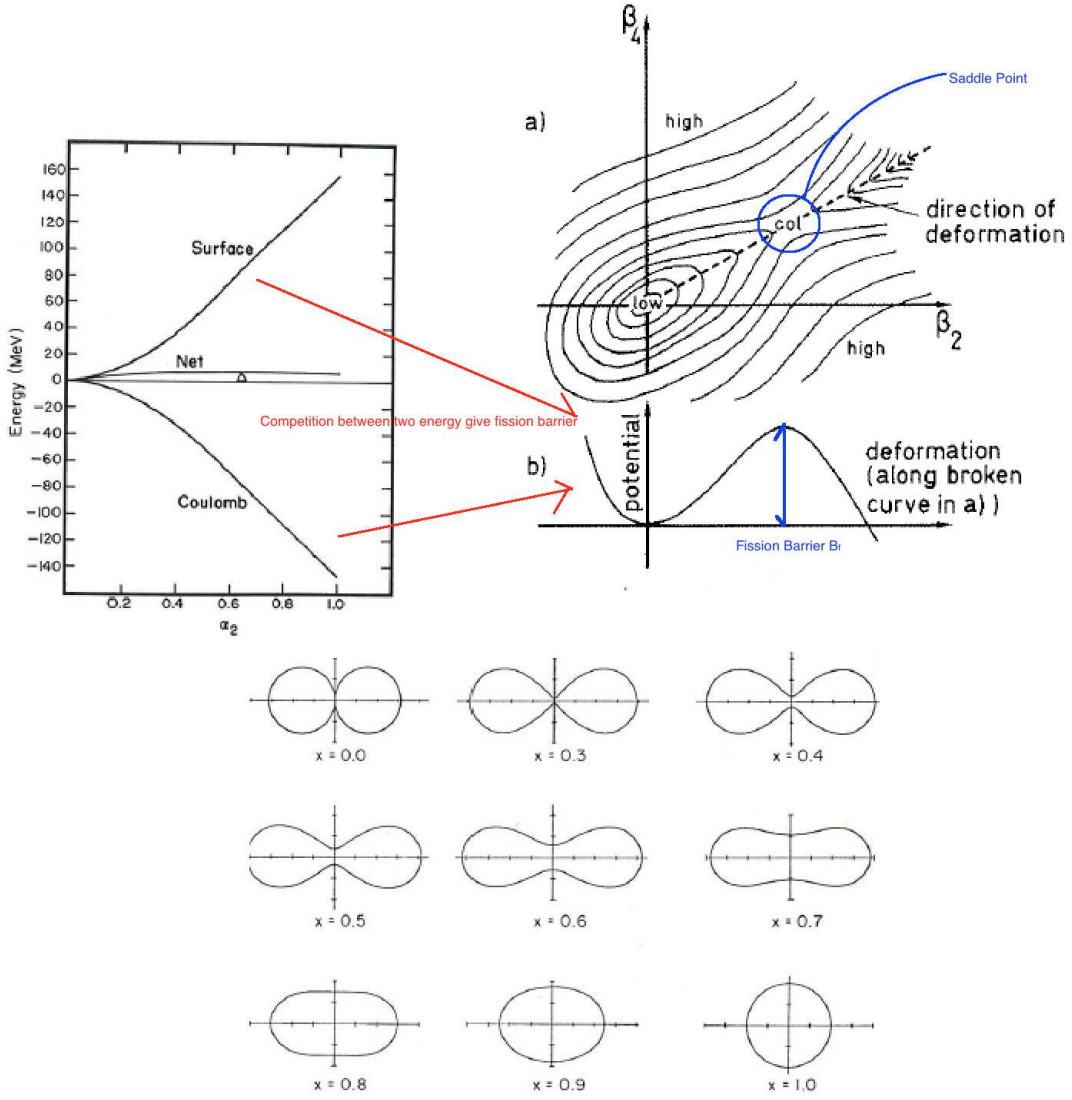

FIGURE 2.2: The fission barrier is a deformation energy of nucleus resulting from the competition between surface energy and Coulomb energy. Illustration with deformation described with quadrupolar and hexadecapolar terms [2].

which act on the deformation coordinates, part of the thermal excitation energy is converted into deformation energy, and the elongation can reach the saddle point and eventually the nucleus may fission. In case of spontaneous fission the excitation energy is lower than the barrier, but the crossing of the barrier is possible by tunneling, with a life time much longer than usual fission.

Although the liquid drop model offers a general framework which explains several features of fission it fails to explain some of them. For example it always predicts a symmetric splitting of the nucleus. This symmetric fission is indeed observed for ^{209}Bi when it is heated at high excitation beyond its high barrier. But for most

of the actinides at low excitation energy the splitting is asymmetric. It cannot explain also the elongated shapes which are evidenced for some isomeric states of the actinides.

Those features can receive an explanation only by taking into account the quantum nature of the nucleus.

2.1.3 Nuclear shell Model

The basic quantum description of the nucleus started from the finding that the interaction of one nucleon with the others is almost continuous due to the short range of the force and to the Pauli principle which prevents many collisions between nucleons. Therefore a mean field is a good representation of the interaction with the other nucleons. This is the basis of the shell model where a nucleon moves in an effective potential well created by the forces of all the other nucleons. This leads to an energy quantization in a manner similar to the quantum harmonic oscillator potentials.

For a spherical potential and including the strong spin-orbit coupling one obtains the single particle states which exhibit, as experimentally observed, the magic nucleon numbers 2, 8, 20, 28, 50, 82, 126 where the nucleus is more stable due to shell closure with a large energy gap above the Fermi sea. As shown in figure 2.3 the nucleon states are quantized in a way similar to electrons in atoms, but in the nucleus the j-j coupling is imposed by the strong spin-orbit term, and as a result the magic numbers are different.

As a result of the representation with single particle states, the mean field depends on the populated states, so that the nucleus may take a permanent deformation which has to be accounted back to define the single particle states.

Nilsson and collaborators have conducted calculations to account for the not-exactly-spheroidal shape. The mean field approach is again used but the potential takes an ellipsoid form. The states having different projection values of the same j are no longer degenerated and split according to this projection. This development helped understand the spin and parity of many nuclei which appeared to have a static deformation.

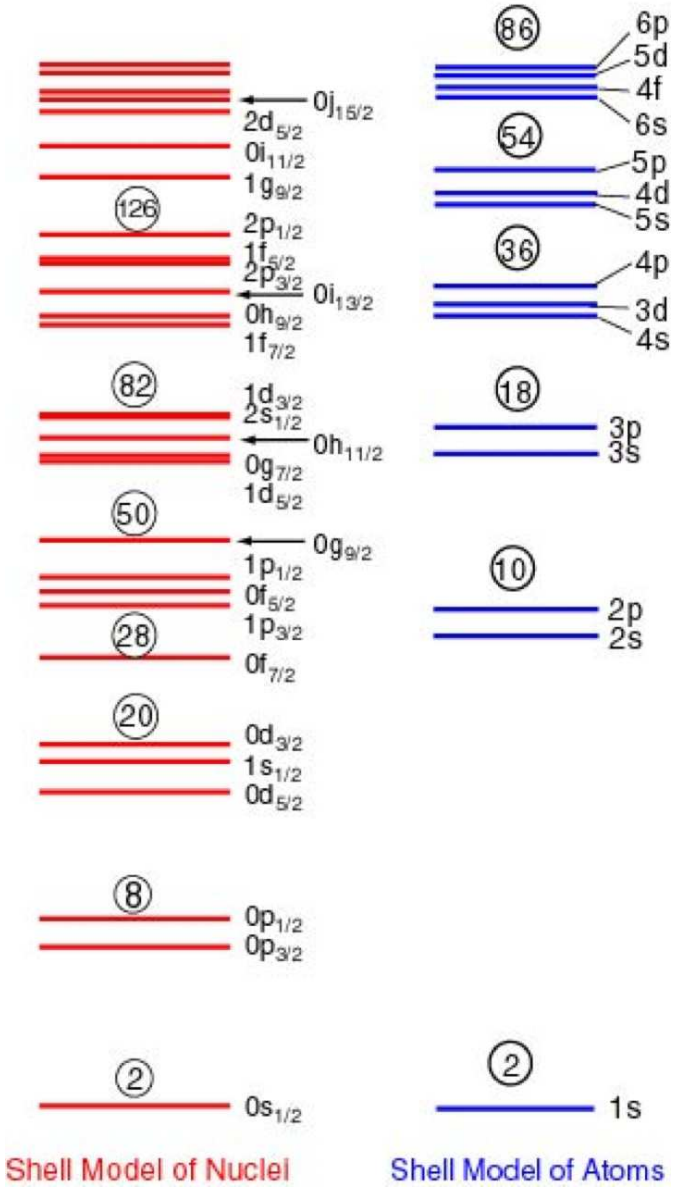

FIGURE 2.3: Single particle states of a spherical field for a nucleus (left) and an atom (right).

2.1.4 Strutinsky's method

The single particle model, spherical or deformed, is well suited for describing the properties of the nucleons close to the Fermi level, because the potential has been fitted to describe the energy, spin and parity of the ground states and the first excited states. However it is not able to reproduce some important quantities as the total binding energy which involves nucleons deep inside the Fermi sea. On the

contrary the LDM has this capability although it fails to predict the fluctuations of this energy in a given area of the (N,Z) map.

In 1967 Strutinsky got the idea [12] to associate both approaches: the general trend of the energy is given by the LDM, and a shell correction is added, which is computed with the deformed shell model.

For a given nucleus with a given deformation, the total energy is taken as:

$$E = \bar{E} + \widetilde{E} \tag{2.8}$$

$\bar{E}$ is a smooth energy calculated by the LDM and $\widetilde{E}$ is a correction based on the energies of the single particle states in the vicinity of the Fermi level μ:

$$\widetilde{E} = \int_{-\infty}^{\mu} \epsilon g(\epsilon) d\epsilon - \int_{\infty}^{\bar{\mu}} \epsilon \bar{g}(\epsilon) d\epsilon \tag{2.9}$$

$g(\epsilon)$ is the level density of single particle states as calculated with the given potential $\bar{g}(\epsilon)$ is a smooth level density as averaged over many nuclei around.

Strutinsky calculated a smooth level density by convolution of g with a normalized Gaussian. This method which combines the liquid drop model and the single particle method is called the macroscopic-microscopic approach.

2.1.5 The double-humped fission barrier

This method has been applied to compute the deformation energy when a nucleus deforms in its way to fission. Figure 2.4 represents such a deformation energy for a typical actinide, as a function of the elongation in the case of shapes generated by quadrupole and hexadecapole deformations. The LDM curve is shown as a dashed line and the difference between the calculated solid line and the dashed line is the shell correction as computed by the Strutinsky method. The shell correction split the potential hill into 2 barriers separated by a well.

The first minimum is at the lowest energy and represents the actinide in its ground state. The second minimum in the deformation potential of most actinide nuclei, is due to the strong negative shell correction, and occurs at a deformation where the LDM fission barrier is located. It offers a natural explanation for the fissioning

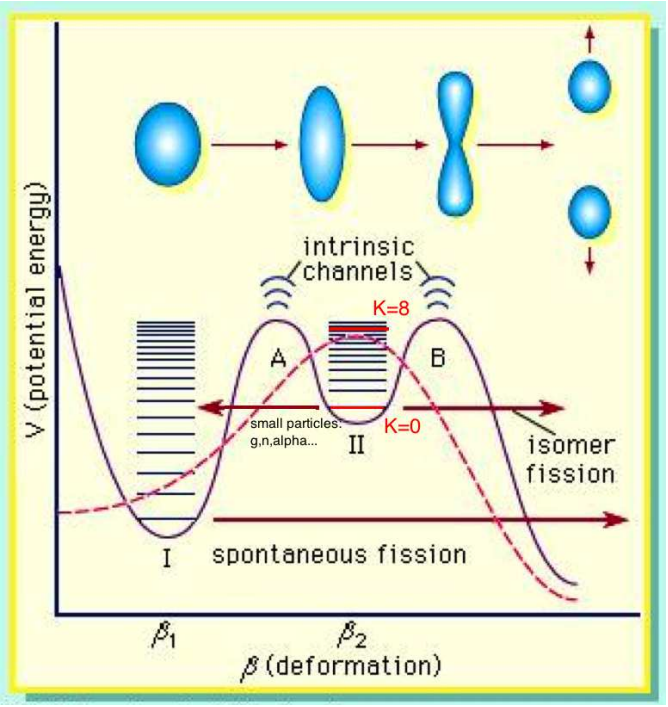

FIGURE 2.4: The double-humped fission barrier.

isomers, which has been known as shape isomers and for structures in neutron-induced fission cross section.

2.2 Nuclear reaction

When a neutron collides with a nucleus, different mechanisms can happen. E. Weisskopf presented a simple conceptual picture [13] represented in figure 2.5. As fission is a slow process, because it needs conversion of the intrinsinsic excitation energy into collective vibrational degrees of freedom which are slow, it takes place after all fast channels (direct and pre-equilibrium) and it is one of the decay modes of the *compound nucleus*. The lifetime of the compound nucleus is large enough so that it forgot how it has been formed. Therefore its decay depends only on its conservative quantities as excitation energy E^*, spin J and parity Π. The probability to decay by channel χ is written $G_\chi^{CN}(E^*, J, \Pi)$. The channel χ we are interested here is fission but it often competes with neutron and γ by emission as sketched in figure 2.6.

Around 10 MeV the pre-equilibrium emission is low so that the whole energy and angular momentum brought by the incoming neutron are deposited in the

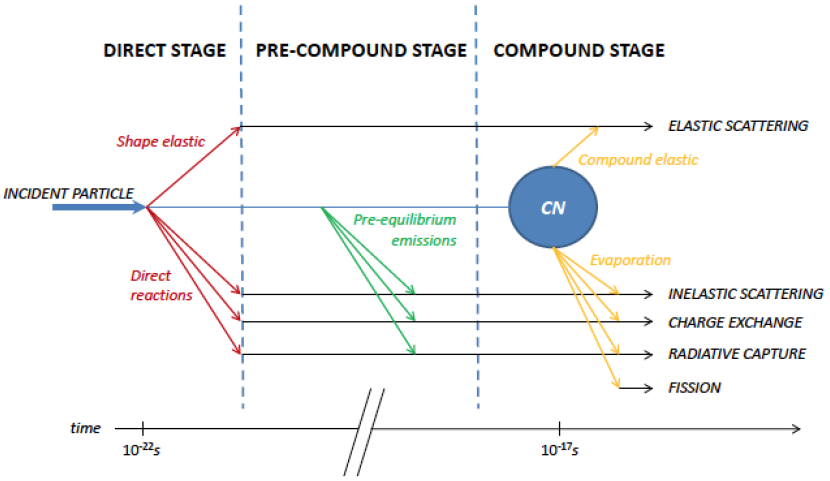

FIGURE 2.5: Conceptual view of a nuclear reaction

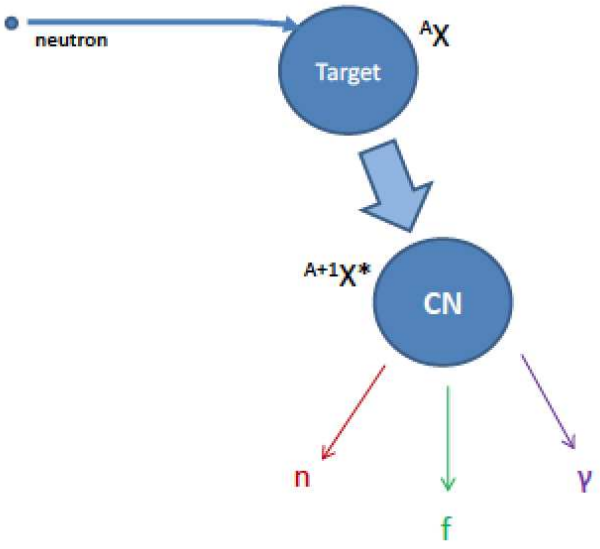

FIGURE 2.6: Neutron-induced reaction leading to compound-nucleus $^{A+1}X^*$ [3]

excitation of the compound nucleus because the neutron is captured into the target and forms the compound nucleus.

$$n(\epsilon) +^{A} X \Rightarrow^{A+1} X^*$$

where A is the mass of the target nucleus.

In this case the excitation energy E^* is the sum of the separation energy and the neutron kinetic energy, and its spin J and parity Π result from the composition of projectile and target spins and parity with those of the orbital motion.

The cross section for going to the channel χ (in particular fission) is the product of the cross section for forming the compound nucleus and its probability to decay through χ. In the Hauser-Feschbach formalism accounting for spin and parity, it reads:

$$\sigma_{n,\chi}(E_n) = \sum_{J\Pi} \sigma^{CN}(E^*, J, \Pi) G_\chi^{CN}(E^*, J, \Pi) \tag{2.10}$$

where :
$\sigma_{n,\chi}(E_n)$ is the neutron-induced reaction cross section for the reaction $X_N^A(n,\chi)$.
$J\Pi$ is the spin and parity of the compound-nucleus.
σ^{CN} is the compound-nucleus $^{A+1}X^*$ formation cross section in the E^*, J, Π state.
E^* is the excitation energy of the compound-nucleus.
$G_\chi^{CN}(E^*, J, \Pi)$ is the decay branching ratio of the compound state.

At high energy (beyond 100 MeV), i.e. the spallation domain, pre-equilibrium emission becomes important. In this case the incoming light projectile (neutron or proton) may escape with lower energy and knock out a few energetic nucleons. Therefore the excitation energy has lower values than in the case of capture and it spreads over a distribution. Nevertheless a compound nucleus is still formed and fission is still one of the decay channels of this compound nucleus and its probability is computed in the same way as before.

2.3 Fission fragment angular distribution (FFAD)

2.3.1 Rotating deformed nucleus

When a nucleus is deformed with an axial symmetry it can be demonstrated that its total spin $\vec{J}$ has a good quantum number J for its modulus, its projection M along an arbitrary fixed axis, but also its projection K along the moving symmetry axis Oz', so that the spin is defined by the triplet (J,M,K).

The projection $\vec{K}$ is due to the projection of the angular momentum of the nucleons in the frame of the rotating deformed nucleus and the overal rotation of the deformed nucleus is like a rigid body rotation with an angular momentum $\vec{R}$

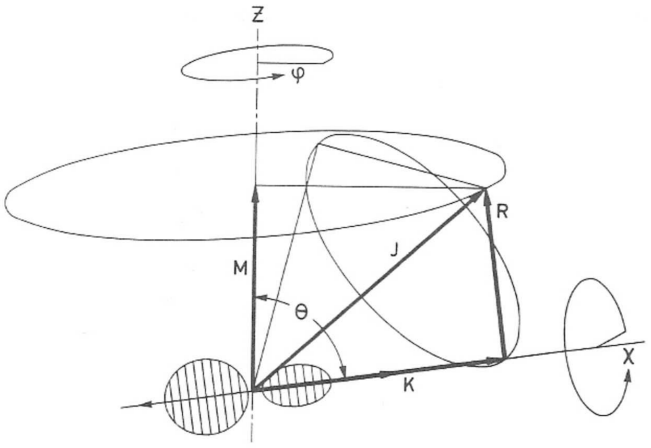

FIGURE 2.7: Angular momentum components for a rotating deformed nucleus [2].

orthogonal to the symmetry axis as illustrated in figure 2.7 Therefore:

$$\vec{J} = \vec{R} + \vec{K} \tag{2.11}$$

with $\vec{R}$ orthogonal to $\vec{K}$ and $J_{z'} = K$.

Now according to the rigid body rotation the deformed nucleus rotates around $\vec{R}$. But if there is a $\vec{K}$ component, as $\vec{J}$ must be constant in time (conservation of the total angular momentum) $\vec{R}$ and $\vec{K}$ rotate around $\vec{J}$. Therefore the deformed nucleus rotates around a rotating axis.

In this picture when expressed with θ the angle between the nuclear symmetry axis and the space-fixed axis, ϕ the azimuthal angle around it and χ the angle around the symmetry axis, the angular wave function Ψ of the rotating deformed nucleus obeys the equation as shown by Reiche and Rademacher, and by Kronig and Rabi [14]:

$$\frac{\hbar}{2J_\perp}\left[\frac{1}{\sin\theta}\cdot\frac{\partial}{\partial\theta}(\sin\theta\cdot\frac{\partial\Psi}{\partial\theta}) + \frac{(\cos\theta\frac{\partial}{\partial\chi} - \frac{\partial}{\partial\phi})^2\Psi}{\sin^2\theta}\right] + \frac{\hbar^2}{2J_{||}}\cdot\frac{\partial^2\psi}{\partial\chi^2} + E\cdot\Psi = 0 \tag{2.12}$$

where $J_{||}$ is the moment of inertia for the rotation around the symmetry axis, and $J_\perp$ the moment of inertia around a direction perpendicular to it. The solution of the equation is:

$$\Psi = \sqrt{\frac{2J+1}{8\pi^2}}\cdot e^{iM\phi}\cdot e^{iK\chi}\cdot d^J_{M,K}(\theta) \tag{2.13}$$

where $d^J_{M,K}(\theta)$ is the rotation matrix, independent of ϕ and χ and introduced by Wigner [15],

$$d^J_{M,K}(\theta) = \sqrt{(J+M)!(J-M)!(J+K)!(J-K)!}\times \sum_n (-1)^n \frac{[\sin(\theta/2)]^{M-K+2n}\,[\cos(\theta/2)]^{2J+K-M-2n}}{(J-M-n)!(J+K-n)!(M-K+n)!n!} \tag{2.14}$$

Therefore the distribution of orientations of the axis of the deformed nucleus is given by:

$$W^J_{M,K}(\theta) = \frac{2J+1}{2}|d^J_{M,K}(\theta)|^2; \tag{2.15}$$

and the energies of the levels are deduced from the wave function:

$$E_{rot} = \frac{\hbar^2}{2J_\perp}[J(J+1) - K^2] + \frac{\hbar^2}{2J_{||}}K^2 \tag{2.16}$$

which is a rotational energy of the fissioning system.

2.3.2 Application to fission

During the fission process the deformation of the nucleus increases and the formalism described above is applicable. The direction of fission is the symmetry axis, so that the probability of emission in a given direction is given by (2.15).

In this statement a hypothesis has been assumed: the K component which is the projection $\vec{J}$ on the symmetry axis remains constant along the fission trajectory from the saddle-point, where fission is decided, to the scission point where the fragments separate. This is a condition which is true if the nucleons stay on their individual orbits along deformation.

Several angular momenta are involved in the reaction. The quantities $\vec{I_0}$, $\vec{s}$ and $\vec{S}$ are the target spin, projectile spin (=1/2 for a neutron or a proton) and channel spin (total spin of compound nucleus) respectively. The channel spin $\vec{S}$ is defined by the relation:

$$\vec{S} = \vec{I_0} + \vec{s} \tag{2.17}$$

The total angular momentum $\vec{J}$ is given by the sum of the channel spin $\vec{S}$ and nucleus orbital angular momentum $\vec{l}$

$$\vec{J} = \vec{S} + \vec{l} \tag{2.18}$$

Usually the fixed projection axis defining $M$is the direction of the incident neutron. This is a simplification because the incoming orbital momentum has a 0-projection along this axis.

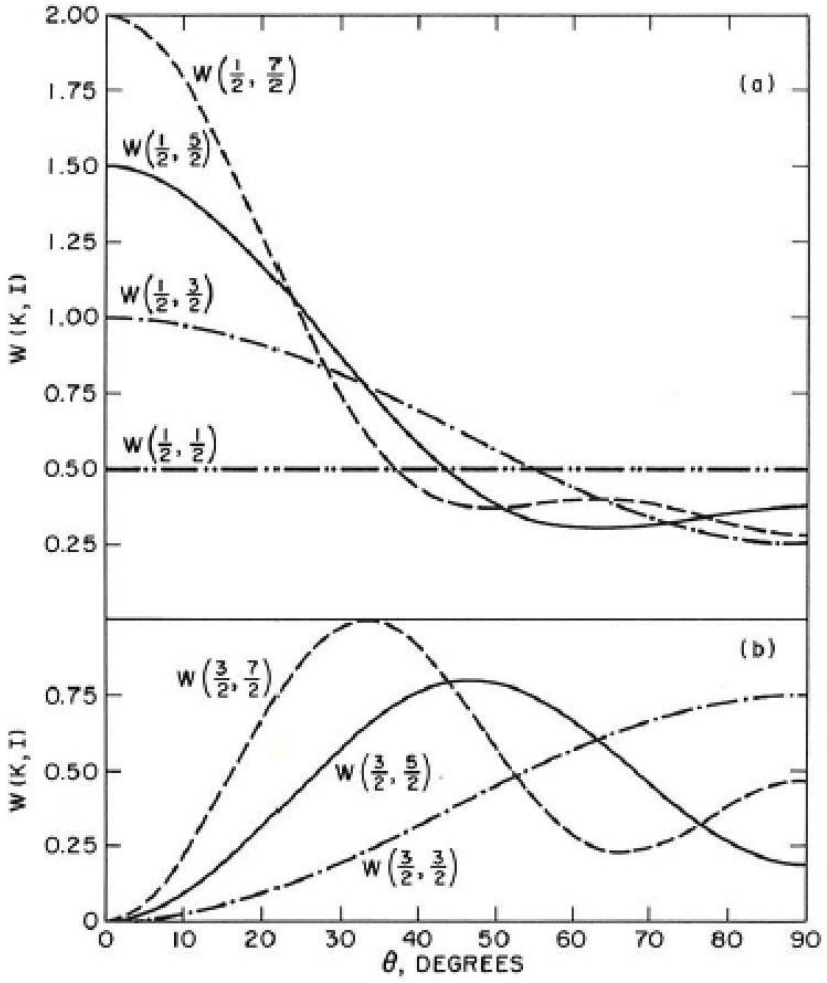

FIGURE 2.8: Theoretical FFAD $W(K, J)$ calculation of even-even target ($I_0 = 0$. When $K \ll J$ the fission is forward-backward peaked, when $K \approx J$ FFAD is sideward peaked [2].

2.3.3 Case of even-even targets

A specific simple situation is the case of even-even targets as ^{232}Th, ^{234}U,^{238}U. In this case $I_0 = 0$, $S = s = 1/2$ and $J = l \pm 1/2$, and also $M = \pm 1/2$ with the same probability for the 2 opposite values. The angular distribution for a given J and K is:

$$W_{K,J}(\theta) = \frac{2J+1}{4} \left(|d^J_{-1/2,K}(\theta)|^2 + |d^J_{1/2,K}(\theta)|^2 \right); \tag{2.19}$$

Figure 2.8 shows the angular distributions for different values of the couple (K,J).

The quantum trends can be derived from classical arguments.

- If only s-waves ($l = 0$) are involved: $J = K = 1/2$ and the FFAD is flat. This is a general property which holds also for $I_0 \neq 0$ because $\vec{J}$ is fully de-oriented. This is the reason why at low incident energy ($E_n < 10$ keV) the emission is only isotropic because s-waves dominate the cross section.
- By looking at figure 2.7 one sees that when $K \ll J$ the emission is orthogonal to $\vec{J}$. Now the direction of J is very close to l (otherwise the above inequality is impossible) which is orthogonal to the beam axis. For all reaction events $\vec{J}$ takes all directions in the plane orthogonal to the beam. When the fragments are emitted orthogonally to $\vec{J}$ there is only one direction where all the contributions from all directions of $\vec{J}$'s add up: the beam axis. Therefore the FFAD is forward-backward peaked. The quantum computation is in accordance with this conclusion: see the curves $W(1/2, 7/2)$ and $W(1/2, 5/2)$ in figure 2.8.
- When $J \approx K$ the fission axis is along $\vec{J}$. As $\vec{J}$ is orthogonal to the beam axis, so is the fission direction and the FFAD is sideward peaked. This is verified for example for the case $W(3/2, 3/2)$ in figure 2.8.

2.3.4 Case of odd nuclei

Typical examples are ^{235}U and ^{237}Np. In this case the target spin is not 0: $I_0^\pi = 7/2^-$ for ^{235}U, $I_0^\pi = 5/2^+$ for ^{237}Np. The channel spin is $S = 3$ or $S = 4$ in the former case, $S = 2$ or $S = 3$ for the latter. As this channel spin is unpolarized it contributes significantly to the de-orientation of $\vec{J}$ (the only oriented contribution comes from $\vec{l}$). Therefore the FFAD is flatter than in the case of even-even nuclei, and higher incoming partial waves have to be involved for the onset of anisotropy.

2.3.5 Low excitation energy fission

At low excitation energy, close to the fission barrier, fission occurs through transitional states (states defined with the collective degree of freedom corresponding to elongation) lying in the second well (class II states) of definite J and K. The

FFAD is directly obtained from equation (2.15) with a sum over M corresponding to the equally probable projections of the spin channel, and a possible summation of a few J and K in case of mixing.

This is typically the situation which is found for the vibrational resonance existing at 1.6 MeV in neutron-induced fission of ^{232}Th.

2.3.6 Statistical description at higher excitation energy

J is the quantity related to the entrance of the reaction, whereas K is an internal quantity of the fissioning nucleus. Therefore the J population is defined by the probability that a given J contribute to the formation of the compound nucleus and this has been already expressed in equation (2.10).

At high excitation energy the distribution of K becomes statistical and the probability is proportional to the number of instrinsic single particle states contributing to this K at the saddle-point. The thermal excitation energy at the saddle-point is:

$$E^* = E_0^* - B_f - E_{rot} \tag{2.20}$$

where E_0^* is the total excitation energy, B_f is the fission barrier and E_{rot} is the rotational energy defined by (2.16). The density of states goes as $\exp(E^*/T)$ where T is the temperature defined as:

$$E^* = a_f T^2 \tag{2.21}$$

where a_f is the level density parameter at the saddle-point deformation. This leads to the following expression of K probability ($K < J$):

$$P(K) \approx \exp -K^2/2K_0^2 \tag{2.22}$$

which is a gaussian distribution of width:

$$K_0^2 = \frac{J_{eff}\, T}{\hbar^2} \tag{2.23}$$

with for the effective momentum of inertia:

$$J_{eff} = J_\perp J_{||}/(J_\perp - J_{||}) \tag{2.24}$$

One notices that the K distribution extends to higher values when the temperature increases, or when the mass increases because the moments of inertia increase accordingly.

At high incident energy l increases more rapidly than K_0 so that K is generally lower than J, therefore, following the arguments developed above, the FFAD are often forward-backward peaked.

When a new fission chance opens (fission occurring after a neutron has been evaporated) the total angular momentum J is only slightly affected whereas K_0 drops due the brutal decrease of the temperature after emission of the neutron. Therefore the forward-backward peaking is enhanced.

The exact theoretical expression for angular distribution is:

$$W(\theta) \propto \sum_{J=0}^{\infty} \sum_{M=-(I_0+s)}^{+I_0+s} \{ \sum_{l=0}^{\infty} \sum_{S=|I_0-s|}^{+I_0+s} \sum_{\mu=-I_0}^{+I_0} \frac{(2l+1)T_l |C^{S,l,J}_{M,0,M}|^2 |C^{I_0,s,S}_{\mu,M-\mu,M}|^2}{\sum_{l=0}^{\infty}(2l+1)T_l} \} \times \frac{\sum_{K=-J}^{J} (2J+1)|d^J_{M,K}(\theta)|^2 \exp(-K^2/2K_0^2)}{\sum_{K=-J}^{J} \exp(-K^2/2K_0^2)} \tag{2.25}$$

The T_l's represent the probability that a partial wave l leads to the compound nucleus formation. This is an indispensable ingredient for computing the J population of the compound nucleus and it is one of the ingredients in the computation of $\sigma^{CN}(E^*, J, \Pi)$ in equation (2.10). The C's are Clebsch-Gordan coefficients coupling the spins. The second one couples the spins of target and projectile to form the channel spin S, and the first one couples this channel spin with the orbital angular momentum l to form J.

Chapter 3

Description of the experiment

The experiment was performed at the CERN neutron beam n_TOF, but before going into the details of the facility we will make a quick survey of the different methods used to produce practical neutron beams.

3.1 Production of neutron beams

As free neutrons are not available due to their limited life time, neutrons have to be produced by nuclear reactions: reactions with isotopes of hydrogen, charge exchange reactions, photo-excitation of fissile nuclei, spallation of heavy nuclei, neutrons created by fission in a reactor and eventually moderated.

3.1.1 Low energy reactions

The reaction involves deuterons and tritons. For example:

$$d + d \longrightarrow {}^3\mathrm{He} + n$$

$$d + t \longrightarrow {}^4\mathrm{He} + n$$

The projectile energy is low, a few tens or hundreds of keV, and the outgoing neutrons are almost mono-energetic, 2.7 MeV in the first case and 14 MeV in the second. This production mode has abundantly been used in the past but it is

limited in the energy range. However this limitation can be overcome by increasing the projectile kinetic energy by using a Van de Graaff, as at the CENBG (Bordeaux France) for example, or a Tandem accelerator.

3.1.2 Charge exchange reactions

In this case a proton is first accelerated to an energy between 1 and 200 MeV and directed to a light target of ^{7}Li or ^{9}Be. The knock out reactions are almost binary and eject neutrons of a given energy depending on the outgoing angle. Usually the forward direction is preferred, because the cross section is higher, and a quasi mono-energetic beam is obtained after the primary proton beam has been swept out with a magnetic field.

This method is used for example at TSL (Uppsala Sweden) for producing neutron beams up to 196 MeV. Usually a rough time of flight is needed to reject the low energy tails coming from other type of mechanisms, such as pre-equilibrium reactions.

3.1.3 Inverse kinematic reaction

Recently, a new project (LICORNE) based on inverse kinematic reaction $^{7}\mathrm{Li}(p,n)$ is being developed with Tandem at Orsay. The reaction is the same as above (charge exchange) but instead of accelerating protons the ^{7}Li is accelerated to above 10 MeV and thrown onto a proton target. This method permits to generate an intense quasi-mono-energetic beam into a conical solid angle and it has the high advantage of minimizing the effect of neutrons scattering, which produces neutron and γ background, due to the focusing in the cone.

3.1.4 Neutron beam from reactor

A nuclear reactor is a natural way of producing neutron beams of very high intensity. On this respect no other method can compete with reactors. However the energy spectrum is broad because it is the result of the spectrum characteristic of fission and of the subsequent moderation process. For example The Institut Laue Langevin (ILL at Grenoble) delivers a high neutron flux which is mainly thermal

with an epithermal component depending on the location. With such beams only integral measurements can be performed because the neutron energy cannot be obtained by time of flight, being the production continuous. However a chopper can be used to get a rough time of flight.

3.1.5 Photo-fission

Photo-fission based neutron source is another widely developed method in the world. It uses a linear accelerator to accelerate electrons up to tens of MeV impinging a heavy fissile target, like natural uranium. Electrons are slowed down inside the target and produce photons by Bremsstrahlung when they collide with the electrons of the target. The generated photons possess high enough energy to electromagnetically excite the target nuclei which ultimately fissions or decays by evaporation. In both cases, neutrons are emitted in all directions and a well defined beam can be obtained by setting a collimating system. The energy spectrum is broad but the possibilty to pulse the electron beam allows to determine the neutron energy by the measurement of its time of flight.

The nELBE facility at Helmholtz-Zentrum-Dresden-Rossendorf has a high-intensity electron beam which allows producing a neutron beam with an energy spectrum in the range 0.2 to 7 MeV and a flux close to 10^6 $(s.cm^2.E - decade)^{-1}$. Besides nELBE, the Institute for Reference Materials and Measurements (IRMM) at Geel Belgium and the Oak Ridge Electron Linear Accelerator Pulsed Neutron Source (ORELA) are based on this method.

3.1.6 Spallation

Spallation consists of high energy proton-induced reactions (more than hundreds of MeV) on a heavy target (Pb, Hg). Each collision ejects quickly some energetic particles (n, p, d, μ, γ, π...) and leaves the residual target nucleus at high excitation energy. The latter releases this energy by evaporating many particles, mostly neutrons due to the Coulomb barrier experienced by the charged particles in the heavy nucleus. This evaporation is the main source of neutrons in spallation. The emitted fast particles propagate inside the target and induce other spallation reactions. Therefore a high energy incident proton (1 GeV and above) induces

chain reactions on the target (ex: a lead target) until all energetic particles stopped in the target, it may recover about around 25 neutrons per 1 GeV incident protons. This numbers scales according to the incident energy.

The neutron energy spectrum by this spallation contains several components: evaporated neutrons peaked at 1 MeV (the main component), higher-energy neutrons extending up to the proton incident energy, due to the particles ejected in the first step of the reaction and low energy tails due to the moderation if a light material has been installed close to the target.

One of the assets of spallation-based facility is their ability to cover the largest possible energy range and to measure the time of flight.

LANSCE at Los Alamos, based on a 800 MeV proton LINAC, is one of the major facilities. The n_TOF facility at CERN where we performed our experiment is also based on spallation reactions.

3.2 The n_TOF facility

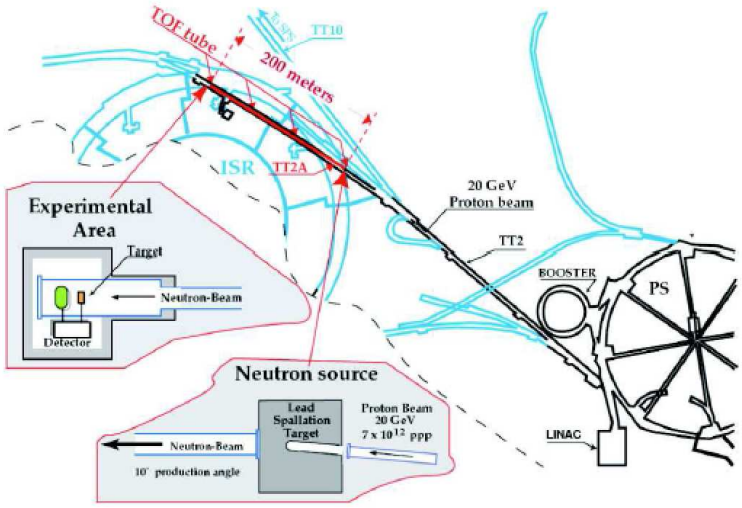

FIGURE 3.1: Sketch of the n_TOF facility at CERN with expanded views of the spallation target area and the experimental area

As already mentioned the neutrons are generated by spallation reactions in a massive target. The specificity of the n_TOF facility is that the energy of the protons is very high (20 GeV instead of the order of 1 GeV for other facilities)

and this allows to produce very intense neutron bunches well seperated in time. This is a very interesting feature for minimizing the background when studying reactions with radioactive targets.

3.2.1 The proton beam

The neutron time-of-flight facility (n_TOF) has been built at CERN, Geneva. The main objectives of the facility were the study of neutron-induced radiative capture and fission reactions. Applications include astrophysics, nuclear production energy and more importantly nuclear waste treatment for actinides and minor actinides [16].

At n_TOF, neutrons are produced by spallation reactions induced by the 20 GeV protons accelerated by he CERN Proton Synchrotron (PS). The beam is directed onto a thick lead target where a huge number of neutrons is generated by spallation reactions on the lead nuclei. Those which go at 10° from the proton beam direction are transported 185 m further where they induce the reactions under study, as sketched in figure 3.1

The released neutrons cover a very broad energy spectrum, from thermal energy to several GeV. As the protons bunches have 7 ns r.m.s, this gives a well defined time for the production of neutrons and the measurement of their time of flight over the 185 m path allows an accurate determination of their kinetic energy.

Each proton bunch contains $7\,10^{12}$ protons for pulses dedicated to n_TOF, or half this value in parasitic mode. This mode is favored for some experiments where the high instantaneous counting rate is an issue. The intensity of each proton bunch is probed with a Beam Current Transformer (BCT) which is an electromagnetic loop sensing the beam current. The BCT delivers a fast signal which gives a time reference of the bunch and whose amplitude is proportional to the number of protons.

The proton bunches are separated in time by at least 1.2 s, when a bunch is spilled all neutrons in the previous one have already arrived long before, so that no wrap around background correction is needed.

3.2.2 The spallation target

The spallation target consists of a cylindrical lead block 60 cm in diameter and 40 cm in length, surrounded and cooled by a 1 cm thick water flow. The water also acts as an energy moderator for the neutrons produced in the spallation target, while an additional 4 cm-thick moderator volume was installed and can be filled with either water or borated water. The latter absorbs most thermal neutrons in $^{10}B(n,\alpha)$ reactions and thus minimizes the 2.2 MeV γ rays produced in the neutron radioactive capture of ^{1}H. The neutron moderation in the water has to be taken into account for neutron energy calculation. The neutron spectrum has been simulated with Fluka [17] (fully integrated particle physics Monte Carlo simulation up to very high energy), Geant4 [18] (toolkit for the simulation of the passage of particles through matter in the whole energy range), and MCNPX [19] (a general-purpose Monte Carlo radiation transport code for modeling the interaction of radiation with everything).

3.2.3 The n_TOF tube

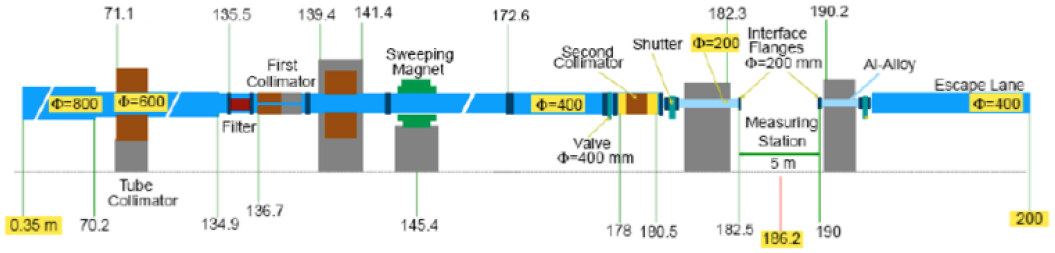

FIGURE 3.2: The 200 m neutron line

The neutrons emitted from the spallation target travel in a pipe kept under vacuum (10^{-2} mbar) to avoid the scattering by N and O in air. The neutrons fly towards the experimental area situated 185 m downstream from the target through two collimators. The second one close to the experimental area defines the beam spot in this area. In the case of fission where large targets are typically used the aperture is 8 cm in diameter, whereas for capture measurements the diameter is reduced to 1.9 cm. The main purpose of the first collimator located 135 m downstream from the spallation target is to reduce the number of neutrons reaching the second one to reduce the γ background.

In addition to neutrons many charged particles are produced in the spallation process : p, μ, π, etc.... They are not desirable because they can trigger reactions on the sample, increasing the background in neutron-induced ones. Therefore they should be discarded and this is done by the sweeping magnet which divert most of those charged particle from the pipe axis.

Several shielding walls have been installed in order to intercept particles traveling out of the neutron pipe. In particular a 3 m concrete wall has been placed right before the experimental area to minimize the neutron and γ background generated in the second collimator. A 6 m iron wall has been placed after the sweeping magnet to absorb most of the μ^- which can generate a neutron background following muon capture in the walls of the experimental area.

Absorbing filters can be inserted in the line to measure the background in the resonance region. They are made of thick materials having strong resonances: all neutrons having an energy corresponding to the resonance are absorbed so that those which are still seen at this energy come from a background or from neutrons outside the expected time-energy dependence.

At the end, neutrons travel across the experimental area and reach the beam dump in the neutron escape line where they are stopped into a block made of borated parafin. Again a thick concrete wall between the experimental area and the escape line prevents the back scattered neutrons to reach the experimental area.

The transversal size of the experimental area is rather small compared to halls in other facilities where the walls, floor and ceiling are several meters apart to reduce the effect of back scattered neutrons. Nevertheless at n_TOF the background level is very low thanks to the very efficient collimating and shielding system.

3.2.4 The neutron flux

In the Phase I configuration the spallation target was cooled by pure light water and a slab of 5 cm water was installed at the exit. The resulting flux is shown in figure 3.3, as simulated with FLUKA [17] for the reactions with highly energetic particles and MCNPX [19] at lower energies. The figure also shows the comparison with the measurements with the PTB ionisation chamber based of fission of ^{235}U

and the radiative capture measurement on gold foils with C_6D_6 in the first resonances. The flux is in fact a fluence normalized to a bunch of protons, dedicated to n_TOF.

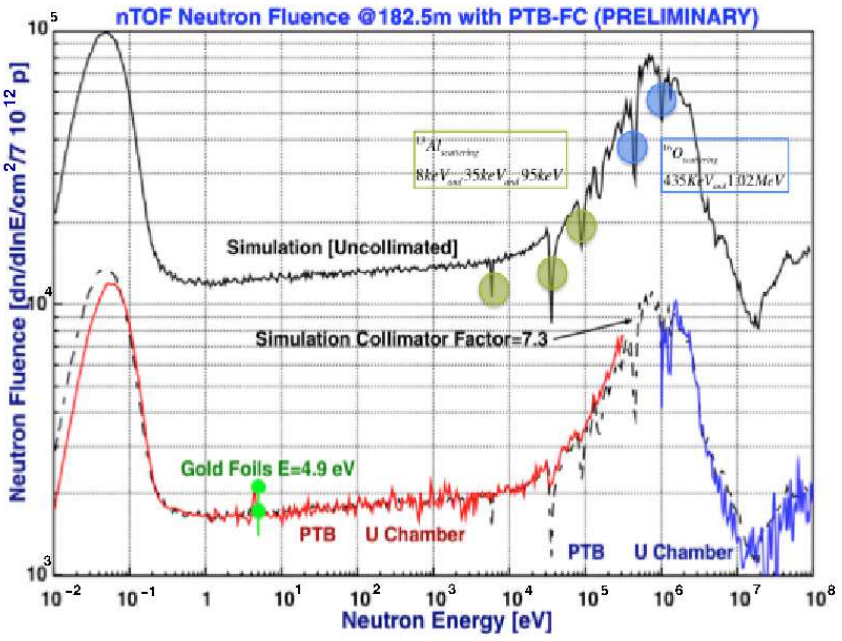

FIGURE 3.3: Phase I n_TOF neutron fluence simulated and compared to measurements behind a 1.1 cm collimator.

The bump around 1 MeV comes from the evaporation of the highly excited spallation residues. It is the main contribution to the neutron production and it is slightly moderated by collisions in the massive lead block. Below 100 keV the plateau comes from the quasi-isolethargic moderation in the water slab, and the moderation process completes when the thermal energy (25 meV) at 293K is reached. This thermal point is an accumulation because it is the end point of moderation, therefore it shows up as a high bump between 10 and 100 meV. Above 10 MeV the neutrons are produced by energetic reactions.

The dips in the energy spectrum are due to resonant absorption of ^{16}O contained in the moderating water, and of ^{27}Al in the thick entrance window of the neutron pipe.

Figure 3.4 shows the flux measured with the fission of ^{235}U and the PPACs up to 1 GeV. The fission cross section used was the evaluation from JENDL-HE. The measurements agrees with the simulation, taking into account that the factor 2 lower than the uncollimated simulated flux comes from the cutting effect of the first collimator.

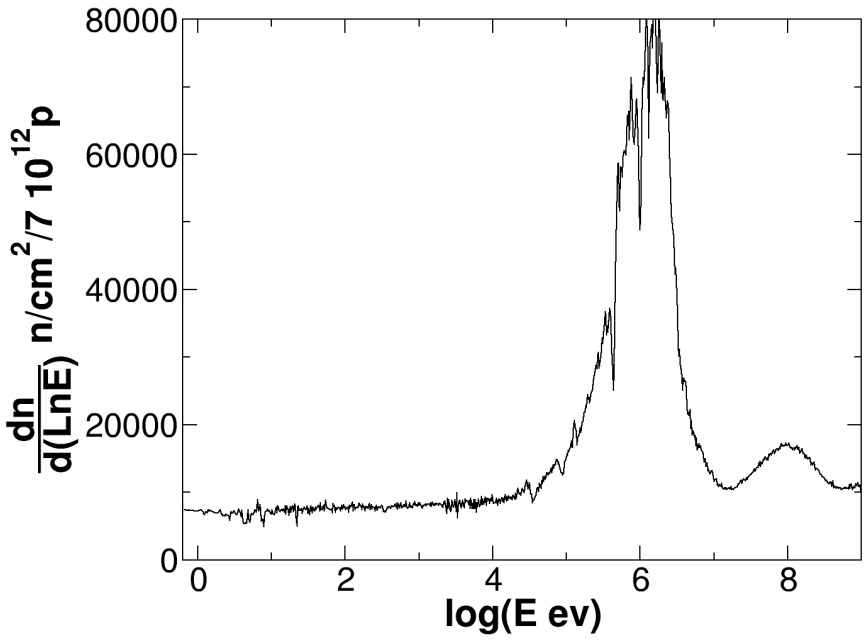

FIGURE 3.4: Phase I n_TOF neutron fluence measured with ^{235}U and PPACs . The last collimator was 8 cm in diameter.

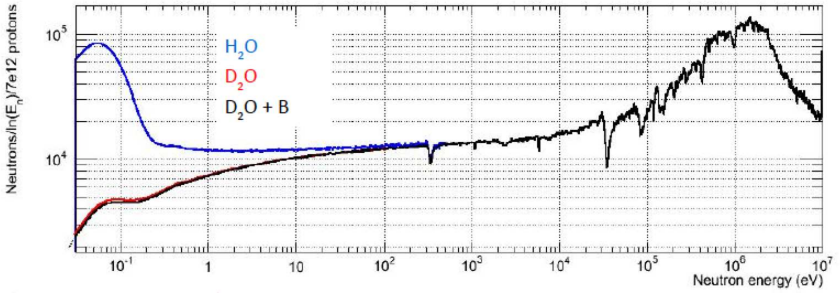

FIGURE 3.5: n_TOF beam flux in Phase II, the thermal and epithermal moderated components are absorbed in the borated water.

Later, in the phase II configuration a borated water has been used. ^{10}B absorbs low energy neutrons as seen in figure 3.5. The advantage of this setting is that the radiative capture of slow neutrons by the protons of water (with emission of a γ of 2.2 MeV) is significantly reduced because the neutrons first react with ^{10}B. The 2.2 MeV γ are very harmful for capture measurements because they travel in the neutron pipe, are scattered by the capture target and induce in the γ detectors a large background in the MeV region.

3.3 PPAC experimental set-up

Fission fragment angular distributions (FFAD) have been measured with different kind of detectors. Obviously all of them have to offer a localization capability to obtain the fission direction by localizing the 2 fission fragments, or only one if the target size is small enough.

Makrofol detector is one of the typical track detectors, frequently used for FFAD measurements due to the advantages of low cost, good reproducibility and very good spatial resolution. It is made of plastic foils of composition $C_6H_{14}O_3$ and density around 1.2 g/cm^3. When penetrating the foil the fission fragment induces a latent track which can be revealed by chemical attack. The FFAD and also the fission cross section are obtained by visually counting the tracks under a microscope.

The two main limitations of track detectors is that they are analyzed off-line without any timestamp so that they allow only in fact integral measurements, suitable for mono-energetic beams. In addition the visual counting limits the numbers of tracks that can be accumulated and therefore the statistics is always accordingly limited.

FFAD can be obtained with other detectors such as fission chambers mounted in Bragg mode. The fissioning layer is deposited on the cathode. For each fission reaction the fragment directed toward the cathode is lost whereas the other leaves the layer and travels in the gas-filled ionization gap where it is stopped. The cosine of the angle is deduced from the ratio of the amplitude of the signals collected on the cathode and on the anode which is shielded by a Frisch grid [1].

3.3.1 Basic principle of the fission tracking

In our experimental set up we used Parallel Plate Avalanche Counters (PPAC) designed and built at IPN Orsay (France) for fission cross section measurements [20]. Before going into the details of the set up, the basic principles behind them is explained.

The principle of the angle measurement is sketched in figure 3.6 where 2 PPACs detect the 2 fission fragments. The PPACs are position sensitive in two dimensions

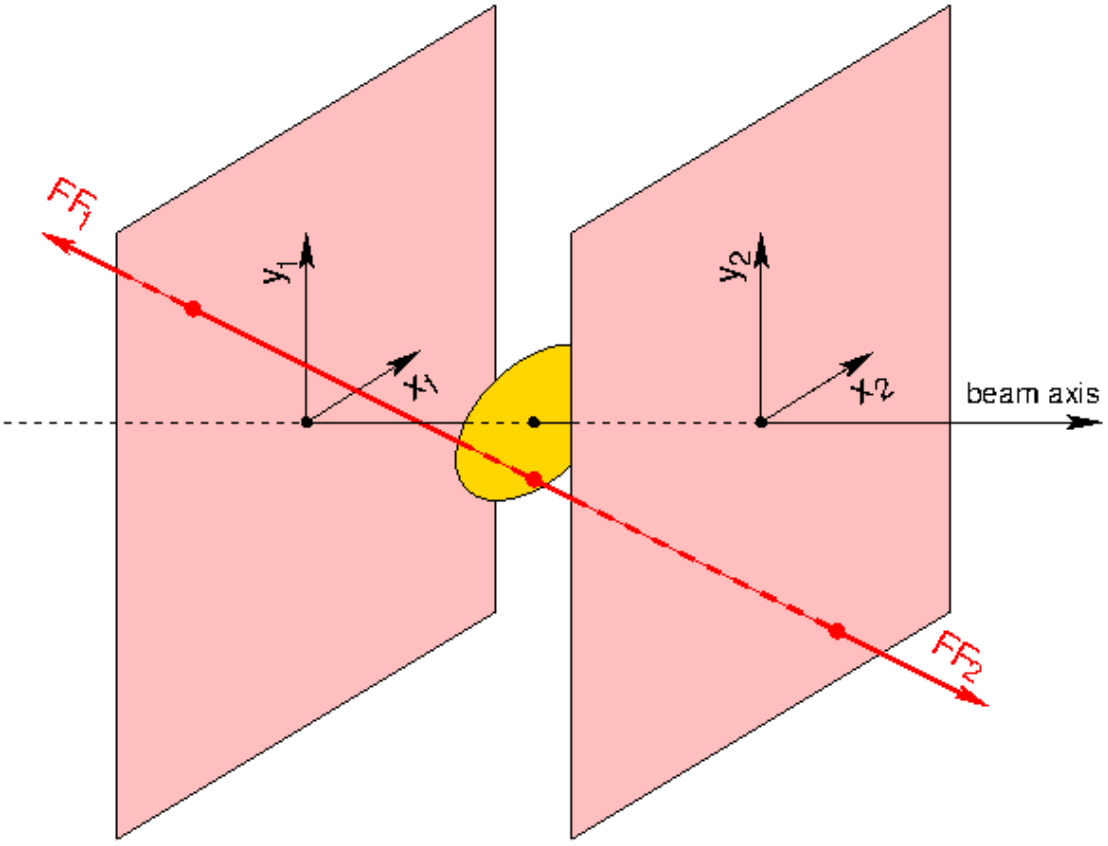

FIGURE 3.6: Principle of measurement of the fission angle with 2 PPACs

so that they are able to localize the crossing point of a fission fragment in X and Y. The main ideas leading to this schemes are the following:

- The detection system should be compact so that an array of targets/detectors can be accommodated in a small volume. This leads to a short distance between targets and detectors, requested also for covering a large solid angle.
- The target size is large (8 cm in diameter) to fully benefit from the large neutron beam spot size and collect large statistics.
- The two above constraints require that the two fragments have to be detected because the emission point is unknown over a large area.
- The previous constraint requests very thin backings so that the fission fragment emitted in this direction could cross it and reach the PPAC.

When the two fission fragments reach the PPACs one obtains the 2 positions (X_1,Y_1) and (X_2,Y_2). Then a back to back emission is assumed so that the fission

direction is given by the straight line crossing the two localized impact points. However, there are two effects spoiling the back to back hypothesis:

- During the fission process some particles, mainly neutrons, may be emitted and the momentum conservation implies a misalignment of the fragment directions. This effect is very small and it is always neglected.
- The back to back emission holds in the frame of the fissioning nucleus, but this frame is not at rest in the laboratory due to the momentum brought by the incoming neutron and fully or partially deposited in the fissioning nucleus. We performed GEANT4 simulations of this effect and it turns out that it can be also neglected [4]. This is due to the saturation of the deposited linear moment when the incoming energy increases and pre-equilibrium reactions set on.

In conclusion the localization of the two fragments allows to define the fission direction and as a consequence the emission point on the target is also determined as the crossing point of the fission trajectory in the target plane.

3.3.2 Parallel Plate Avalanche Counters

A PPAC consists of 3 electrodes, 1 central anode surrounded by 2 cathodes with a spacing distance of 3.2 mm. Each electrode is made of a thin mylar foil of 1.7 μm made conductive by deposition of aluminium coating under vacuum. The foil is glued on an epoxy frame which ensures the parallel spacing, the signal and voltage connections, as well as holding the pre-amplifiers. The gaps are filled with a low pressure gas which is ionized when a fission fragment goes through and produces a track of primary ion pairs. The electrons and positive ions drift towards the anode and the cathode, respectively. During this drift, electrons can collide with neutral gas molecules, generating more ion pairs. The electrons liberated by this secondary ionization process are also accelerated by the electric field and can collide again with other neutral gas molecules, creating a swarm of electrons directed towards the anode. The low gas pressure combined with the high electric field (540 V over 3.2 mm) create the conditions of a proportional regime (Townsend avalanche).

The frames are made of an epoxy resin, coated with a thin copper layer for shielding against electromagnetic noise and gold-plated to prevent its oxidation. The overal

dimensions of the frames are 30×30 cm^2 and the active area, where the fission fragments have only to cross the mylar foils and the gas is a square of 20×20 cm^2.

For the anode the mylar foil is coated on each side with an aluminium layer of 30 nm (8 μg/cm^2) to make it conductive on both sides for the two gaps. The cathodes are coated only on the side which is facing the gap with a 60 nm aluminium layer. Whereas the aluminium layer on the anode is uniform, on the cathodes it is divided into strips with a 2 mm pitch to allow a localization of the impact of the fission fragment. This is obtained by depositing the aluminium under vacuum with a mask made of wires of 0.1 mm in diameter every 2 mm.

A drop of aluminium is heated and melted by an electron beam. The evaporated atoms travel along straight trajectories under vacuum and deposit on the mylar foil. As the aluminium deposition deforms the foil this operation cannot be performed after the foil has been glued and stretched on the electrode frame because the foil becomes slack and cannot remain parallel to other electrodes when the PPAC is assembled. Therefore for the aluminium deposition the mylar is stretched on an special frame and transfered after the deposition onto an intermediate frame which allows a final stretching of the foil without modification of the pitch of the strips. Finally it is glued on the electrode frame.

FIGURE 3.7: Stripped cathode of PPAC

When the electrons drift toward the anode and create an avalanche cascade in the anode plane, at the same time these negative charges induce a positive charge in the cathode, with the position centred on the avalanche position. The velocity of the free electrons is very fast, its collection times is around several ns. Each strip acquires part of the induced charge, and provides accurate information about the fission fragment position of the avalanche. The localization of the hit strip is

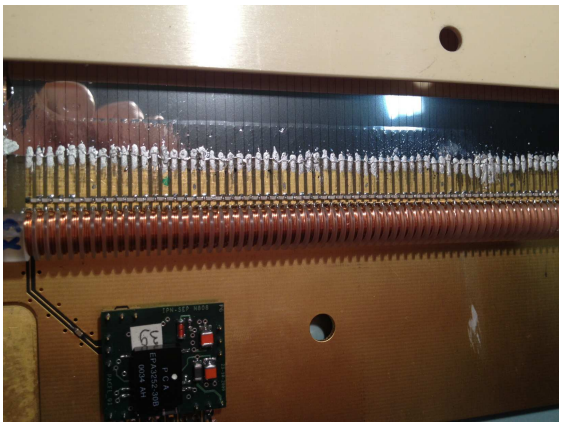

FIGURE 3.8: Expanded view of the cathode frame showing the delay line, the capacitors between strips, the connections with silver pastry, the charge preamplifier.

achieved by using a delay line, each strip being connected to an intermediate point of this delay line. The time difference of the signals reaching the ends of the line is used to determine the position.

When assembled in the PPAC the cathode planes are crossed so that the strips of one cathode are orthogonal to those of the other. This arrangement makes possible the X and Y localization, provided the fission fragment crossed the 2 detecting gaps.

The delay line has also been designed and built at IPN Orsay. It is a plastic rod of 7 mm diameter supporting coils of length 1.4 mm every 2 mm. Each coil is made of 6 turns of 0.3 mm copper wire. The epoxy cathode frames supports the delay line and additional capacitors: 6.8 pF between adjacent strips, and for each strip 10 pF to ground. With this arrangement the characteristic impedance is about 300 Ω and the propagation velocity along the line is 3.2 ns/strip. All aluminium strips on the cathode are connected to the delay line with a silver loaded dough and both sides of the line are connected to a charge pre-amplifier matched in impedance, as illustrated in fig.3.7. Figure 3.7 is a picture of a cathode frame equiped with its stripped mylar electrode and its delay line visible on the left side. Figure 3.8 is an expanded view of the cathode showing the delay line plugged into the frame, the silver connexions between the electrode strips and the copper pads, the 6.8 pF capacitors between the strips and the charge pre-amplifier card plugged on the electrode frame.

The C_3F_8 gas pressure inside the chamber is stabilized at 4 mbar with an external regulator which injects a steady flow of fresh gas within the detecting gaps

maintained at around 60 SCCM/gap.

3.3.3 Advantage of using PPAC for FFAD

When neutrons of high energy reach the targets and the detectors they can not only induce fission reactions, but also other types of reactions on light elements, such as the aluminium of target backings, the oxygen and carbon of the mylar electrode foils. This produces recoiling nuclei (spallation residual nuclei) which deliver signals similar to fission fragments although of lower amplitude. The main characteristic of the PPAC set up is the coincidence method which requires the presence of two fragments coincident in time. This request rejects most of the reactions competing with fission. In addition the α particles coming from the radioactive targets are also mostly rejected for the same reason. Only the random coincidences remain at a very low level. This discrimination method relies on the very accurate timing properties of PPAC with 9 ns FWHM for the anode signal giving a time resolution close to 0.3 ns.

The PPAC electrodes are made of very thin foils so that the fission fragments could cross them. This is very useful in case of neutron induced reactions where the neutron beam has to traverse all detectors: the neutron scattering is reduced to the lowest level and the related background too.

This thin material is also an asset respect to another crucial aspect, the so-called γ-flash. It is the bunch of energetic particles which is produced when the protons hits the spallation target. Those particles are essentially γ travelling in the neutron pipe at the light speed. When they reach any material they eject electrons and other particles by electromagnetic reactions. Those charge particles are seen by the detectors. This is a general phenomenon occuring in all detectors, however the consequences depend on the detectors type or set-up. In many of them (C_6D_6 and BaF_2 scintillators close to the target, in-beam ionization chambers, etc...) the sizeable amount of material inserted in the beam produces a huge γ-flash signal blinding the detector for a long time. This puts a maximal energy of neutron observable by the detector which can be of the order of a 50 MeV or even about MeV's for some of them. In the case of PPAC the amount of material is so tiny and the time response so fast (a few ns) that the detector has recovered a normal status 20 ns after the γ-flash and it becomes possible to look at reactions induced by neutrons of energy about 1 GeV.

In addition, unlike scintillators or semiconductor detectors, PPAC are not damaged by radiation and high energy particles counting rates, which also makes them useful for in-beam applications of neutron and proton-induced reactions.

Besides the advantages of PPAC performances, they are relatively easy and inexpensive to build with large sensitive areas. This makes them more convenient and appropriate for our work at the n_TOF facility, where they are exposed to high-intensity neutron flux with a γ background characteristic of spallation neutron sources.

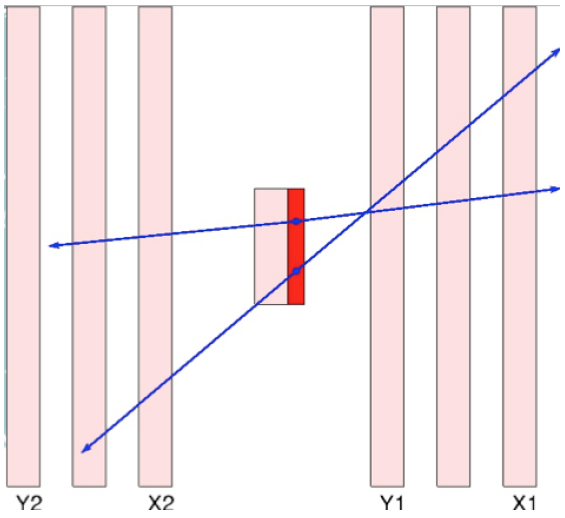

FIGURE 3.9: Fission fragment lost due to the the stopping of the fission fragment at large angle

The main drawback of the set up based on the coincidence method is the limited detection efficiency. In ionization chambers where the fissioning deposit is inside the detecting gaps and where a single fragment is detected, the fragment has only to escape from the layer made of fissile nuclei. This can be realized even for grazing trajectories. Therefore the detection efficiency is about 95%. It's so close to 1 that even a significant error in the simulation to estimate the lost fraction has a small impact on the overall efficiency. On the contary in the case of the PPAC set up the target is out of the detectors, and the coincidence method requires that one fragment has to cross the target backing. This is illustrated in figure 3.9 where the emitting layer is painted in red whereas the dead materials are pink (aluminium target backing and mylar electrodes). To be fully detected the two fission fragments have to reach the second gap. This is possible when the trajectory is almost orthogonal to the detectors. But when the angle increases the energy loss also increases (the thickness goes as $1/\sin\theta'$) and one of the fragments is stopped

before reaching the second gap, as illustrated on the left of figure 3.9. This results in the limited detection angle which is of the order of 45-60° depending on the backing thickness.

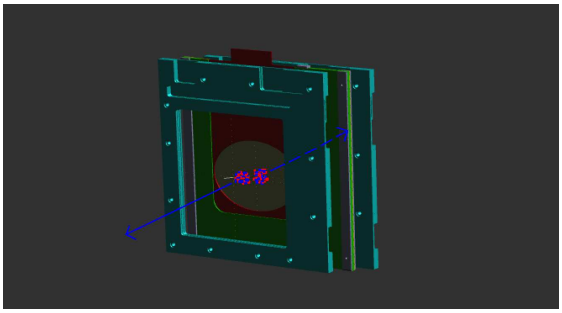

FIGURE 3.10: View of a 2 PPAC+target ensemble tilted by 45° against the neutron beam direction.

Therefore in configuration where the PPAC and targets are orthogonal to the neutron beam a significant fraction of the FFAD is unreachable because it lies beyond this limit. To solve this problem we tilted the detectors and the target by 45° allowing to cover all the emitting angles. Figure 3.10 shows a drawing of this configuration with the 2 PPACs surrounding the metallic target holder supporting the epoxy frame on which the target is glued. The elliptic hole in the frame allows to leave a free route to the circular beam spot, when tilted at 45 °.

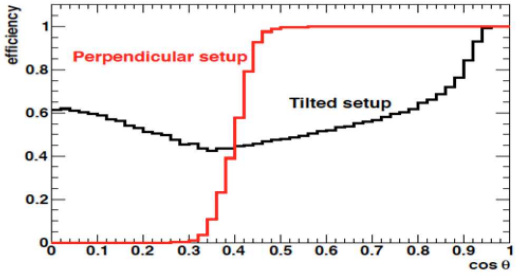

FIGURE 3.11: Simulation of detection efficiency for the 2 geometrical configurations: orthogonal to the beam and tilted by 45° [4]

Figure 3.11 shows a simulation of the detection efficiency, depending on the cosine of the fission angle against the neutron beam, for the 2 geometrical configurations. The simulation is done for the ^{235}U target, taking the fission isotopic yield given by ENDF/B-VII at thermal energy and using the Viola systematics for the kinetic energies. The simulation is performed in Geant4 using its implementation of energy loss. The fission event is recognized as detected if the fission fragments on each side reach the 2 detecting gaps. The figure exhibits the limiting angle ($\cos\theta \approx 0.4$) in orthogonal configuration. In the tilted configuration all angles are covered, and

this is compensated by the reduction of the efficiency at each angle due to the cut in the angle ϕ around the beam again due to the stopping of the fragments in the dead layers. The global efficiency (integral of the curve) is the same as expected.

3.3.4 PPAC ensemble

As described so far a minimal measuring system is made of a target surrounded by 2 PPACs, as sketched in figure 3.10 representing a basic cell. However the simultaneous measurement of several targets is highly desirable to optimize the use of the neutron beam. The first natural idea to go in this direction would be to multiply the number of such cells. We implemented a much more optimized configuration by using a stack of 10 detectors interleaved with 9 targets. As a fission fragment may cross 2 targets and detectors an ambiguity shows up on the emitting target in this situation. This can be easily solved thanks to the property of fast timing of the PPACs: as we will show later the comparison of coincidence times between detectors delivers the information on the fission source.

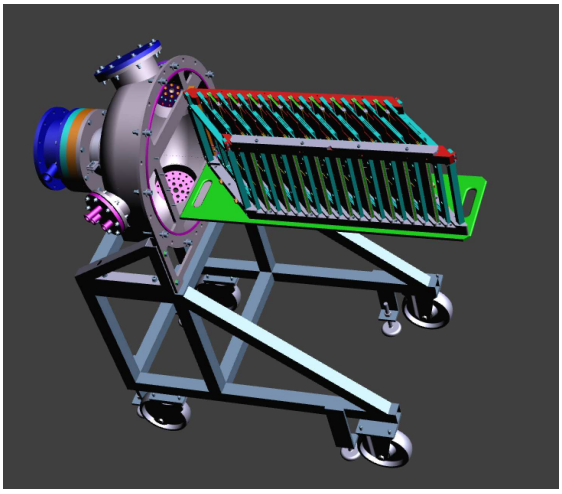

FIGURE 3.12: Ensemble of 10 detectors and 9 targets tilted by 45° against the neutron beam. The holding craddle is fastened on the closing dome mounted on a chariot for transportation.

The 10 detectors and 9 targets are supported on an aluminium craddle as drawn in figure 3.12 and shown really in picture 3.13. The craddle is also used as a gas flow distributor to the PPAC and as a support for the cables and connectors. The spacing between adjacent detectors is 5 cm along their normal, at 45° against the beam. Figure 3.14 illustrates the look of the chamber when it is closed with the stainless steel cylinder. The tightness of the chamber against the atmosphere or

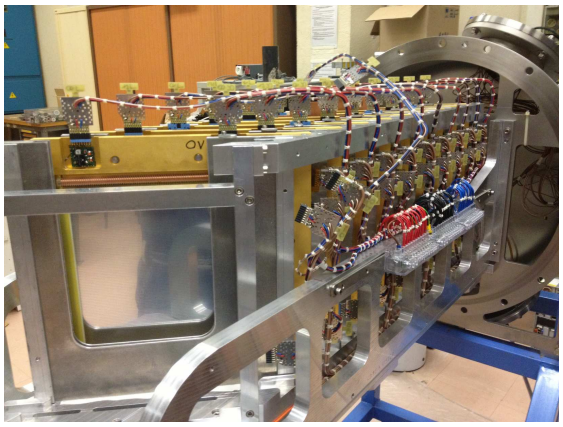

FIGURE 3.13: Real view of the detectors and targets on the craddle holding also the cables and connectors.

the connected vacuum pipe is insured by 125 μm capton sheets mounted in the entrance and the exit flanges. The neutron beam enters by the chamber dome, goes through all detectors and targets, and escapes by the flat bottom of the cylinder. Even though neutrons travel across several detectors and targets, the neutron flux loss due to the neutron scattering remains very low (less than 1% even at the top of intense resonances, due to the tiny amount of material.

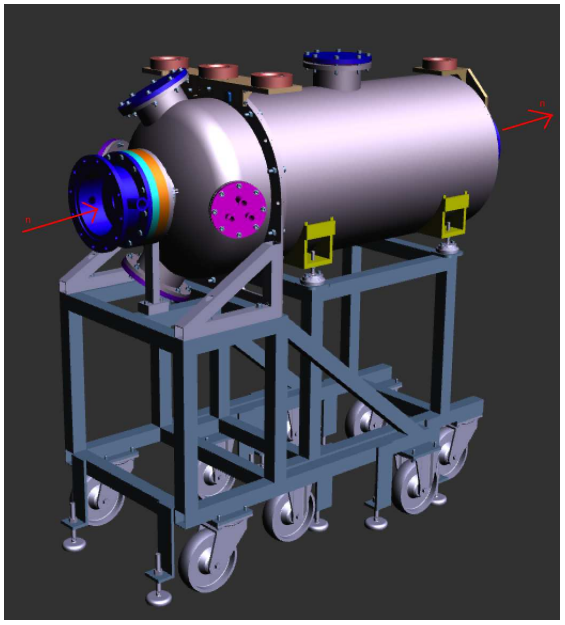

FIGURE 3.14: PPAC chamber when it is closed

3.3.5 Description of targets

The targets have been made by the radio-chemistry group at IPN Orsay. A total of nine targets were used in each experiment with the PPAC chamber. Three experiments have been done in 2010, 2011 and 2012 respectively. In the first and second experiments six ^{232}Th targets, one ^{237}Np, one ^{235}U and one ^{238}U targets were installed. In the third experiment three ^{234}U targets, two ^{235}U, three ^{238}U and one ^{237}Np were used. ^{235}U was used as a reference for cross section and FFAD and ^{238}U was also used as a reference cross section. In this work we only consider the measurements done in 2010 and 2011.

The targets are made of a thin radioactive layer (between 0.2 and 0.3 mg/cm2) [21] deposited as a 80 mm diameter disk over an aluminium foil. The thickness of the aluminium foil is 0.75 μm for the ^{232}Th targets and 2.5 μm for ^{235}U, ^{238}U and ^{237}Np targets. The aluminium backing has been glued on a 1.6 mm thick epoxy frame.

The fissioning materials came from several places: ^{232}Th and ^{237}Np from IPN Orsay, ^{235}U from CSNSM Orsay, ^{234}U target from Geel. The deposited layer is always in oxided form and hydrated to different levels.

The targets were measured by α-counting with a silicon detector in a well defined geometrical configuration at IPN. The α spectroscopy was used to assess the amount of contaminants as ^{241}Am in ^{237}Np targets, daughters in the ^{232}Th chain for ^{232}Th targets. The ^{238}U sample was of high purity due to its magnetic separation. The isotopic composition of the ^{235}U sample has been carefully measured by magnetic analysis. In number of atoms: 6.28% of ^{238}U, 0.74% of ^{234}U and 0.27% of ^{236}U were found.

3.4 Other experiments at n_TOF

As the principle motivations of the n_TOF facility are related to nuclear physics, nuclear astrophysics and nuclear technology, neutron-based fission and radiative capture are the main studied channels. Several detectors have been developed for these works.

3.4.1 Fission ionization chamber

Fission ionization chamber (FIC) permits to measure fission cross section [22]. The fabrication of targets of this type of chamber are easier than for PPAC because the backing may be thick and rigid as only one fission fragment is detected. We have also used this type of detector to monitor the neutron beam with ^{235}U and ^{238}U targets.

3.4.2 Micromegas detector

Micro-megas detector is a double-stage parallel plate chamber [23], consisting of a conversion gap and an amplification gap, separated by a micromesh. Charged particles drift through the conversion gap, then transfer energy to the cathode micromesh and are multiplied in the small gap (avalanche). The multiplied charges are collected by the anode micro-strips. By using an additional induction plane of strips a X and Y localisation can be achieved. Recently this detector has been used for absolute flux measurement with ^{10}B(n,α) which cross section is very well-known at low energies, and also for mapping the neutron beam extension.

3.4.3 γ detectors

3.4.3.1 TAC

The Total Absorption alorimeter (TAC) [24] is a 4π segmented array made of 42 BaF_2 crystals of two different shapes [24] (pentagonal and hexagonal) specially built for detecting the γ-ray cascades emitted in neutron capture reactions.

The BaF_2 crystals, encapsulated in ^{10}B-loaded carbon fibre, form a spherical shell of 15 cm thickness with an inner diameter of 20 cm. A 5 cm thick spherical shell made of $C_{12}H_{20}O_2^6Li_2$ is placed in the inner hole of the TAC for moderating and partially absorbing neutrons that are scattered from the sample. The combination of this moderator with the ^{10}B-loaded carbon fiber capsules results in a neutron sensitivity lower than 1% in the neutron energy range of interest.

The characteristics of the TAC provide the means for performing high quality neutron capture measurements of small mass and/or radioactive samples. For

instance, the high efficiency of the TAC and the high intensity of the n_TOF neutron flux allow reducing the background caused by the intrinsic activity in the case of radioactive samples. Furthermore, the high total absorption efficiency, segmentation and energy resolution of the detector allow discriminating between different reactions according to their γ-ray multiplicities.

3.4.3.2 C_6D_6

C_6D_6 scintillators consist of deuterated benzene coupled to a photo-multiplier [25]. The casing is made of aluminium and beryllium to minimize the neutron and γ scattering. Its main asset is its very low neutron sensitivity. As its energy resolution is very poor it's not suited for any γ spectroscopy and the weighting function method is applied to make the detection sensitive to the capture rate independently of the details of the γ cascade. This is the way such detectors are used to measure capture cross sections.

Chapter 4

Data analysis

4.1 Steps of the analysis

Every time a proton bunch is delivered to the n_TOF spallation target the Data AcQuisition system (DAQ) acquires the 50 channels of the PPACs, 5 channels per PPAC: 1 anode, 4 delay lines (top, bottom, right, left), during a few ms.

Figure 4.1 shows an example of the starting sequence for 2 recorded anode frames. Peaks are clearly visible, they correspond most of the time to fission fragments. The first peak in the sequence is the γ-flash which will be discussed later.

Some peaks coincide exactly in time in the 2 sequences corresponding to fission fragments emitted by the target located between the detectors (^{235}U in this case).

The first task of the analysis is to scan the frames, find all peaks in the signal and list them with their time and amplitude. This process is done individually on each channel, without looking at the correlation between channels. At the end one gets for each channel a file containing the list of peaks. This file is called a DST and it is a reduction of the initial file called RAW. This reduction process needs some parameters which can be modified and the reduction can be replayed to obtain new DST files. However this process is time consuming, thereby limiting the number of such replays.

The second step consists of re-building the proton event by collecting all the lists of peaks pertaining to the same proton bunch and all peaks are stored into a buffer which is filled at each new proton bunch.

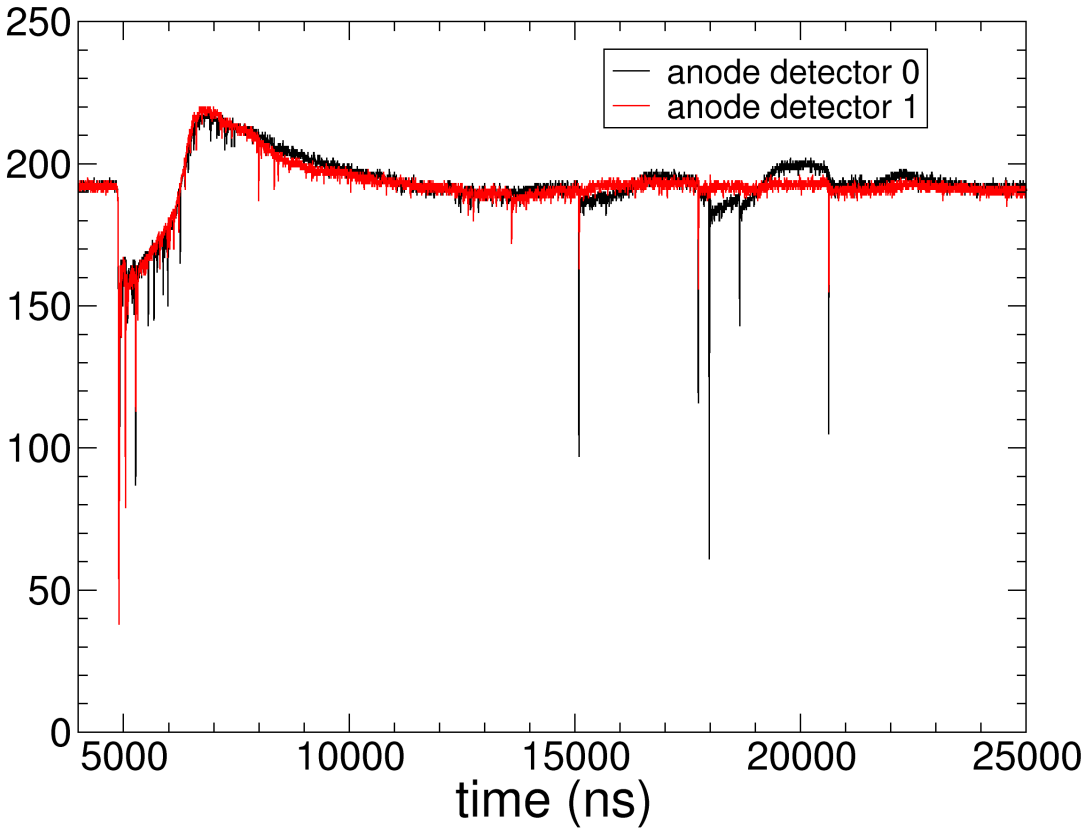

FIGURE 4.1: Expanded view of the beginning of a frame recorded on anodes 0 and 1 surrounding the ^{235}U target. Each frame is a series of amplitude measurements every 2 ns

At the next step each buffer is treated to find the fission events, recognozed as coincidences between anode peaks, find the position of each fission fragment and re-build the fission trajectory. All fission events are tagged according to their emitting targets and stored into ROOT TTRees.

The amount of RAW data recorded by the DAQ is about 8 TB/week. After the peak recognition step stored in the DST's, the amount is scaled down by a factor 750 depending on the radioactivity level of the targets. After full reconstruction of the fission events the amount is further scaled down by a factor of 30, so that it is of the order of 0.4 GB per week of beam time.

4.2 Peak recognition

This section describes the process applied to RAW files to obtain the DST's as mentioned in the previous section as the first task.

A simple glance at figure 4.1 is enough to understand that the peaks in the frames cannot be inventoried by applying a threshold to the signal.This is due to the strong oscillations of the baseline, specially close to the γ-flash.

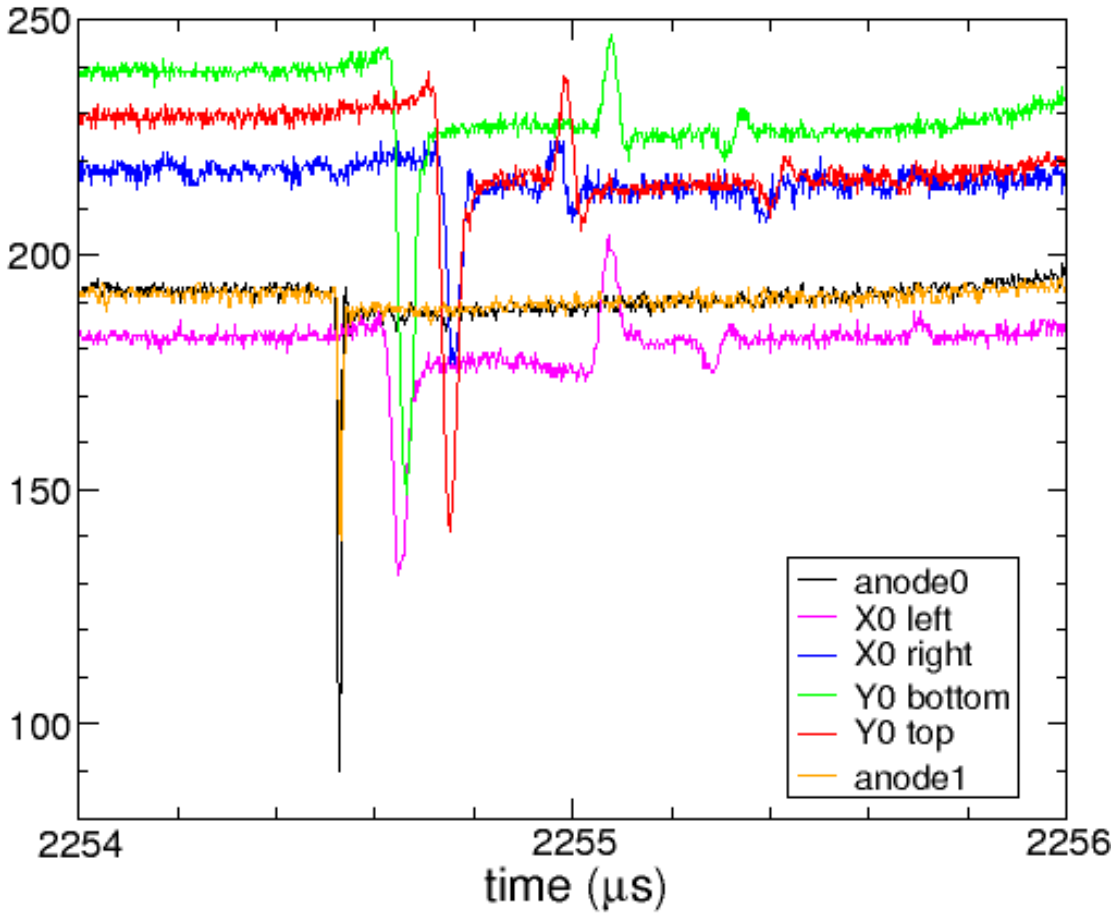

FIGURE 4.2: Expanded view around a fission event of the 5 frames recorded on detector 0 and the anode of detector 1, surrounding the ^{235}U target. The anode peaks coincide in time showing a coincidence of the fission fragments. The X0 and Y0 peaks are delayed due to the propagation in the delay line. The after-pulses in X0 and Y0 frames are reflections in the delay line due to a mismatch of the impedance of the delay line and the pre-amplifier.

A natural idea is to apply a derivative to the signal so as to remove the low frequency variations of the baseline and leave intact the sharp peaks produced by fission fragments. However a look at figure 4.2 shows that each signal is subjected

to a very high frequency noise which is of low amplitude but which will be enhanced by a pure derivative.

The solution is to filter the frames with a low-pass filter which reduces the noise and to apply a derivative afterward. If $s(t)$ is the frame and $f(t)$ is the time response of the filter (its Fourier transform $F(\omega)$ is a low-pass filter) one performs their convolution product and apply a derivative:

$$s_1(t) = (s(t) \otimes f(t))' \tag{4.1}$$

The properties of the convolution product lead to:

$$s_1(t) = s(t) \otimes f'(t) \tag{4.2}$$

The best choice for the filter $f(t)$ is the one which enhances the Fourier components of the peaks and reduces the others. This is approximately achieved by taking $f(t)$ as the peak shape. The relevant parameter is not the details of the shape but its time width which sets the frequency cut. We adopted the following filter:

$$f(t) = \begin{cases} \rho \left[1 + \cos\left(\pi \dfrac{t}{w}\right)\right] & \text{if } -w < t < w \\ 0 & \text{if } t \leq -w \text{ or } t \geq w \end{cases} \tag{4.3}$$

where ρ is a normalization factor and w is the FWHM of the peak. According to equation 4.2 the frame should be convoluted with the function:

$$f'(t) = \begin{cases} -\rho \sin\left(\pi \dfrac{t}{w}\right) & \text{if } -w < t < w \\ 0 & \text{if } t \leq -w \text{ or } t \geq w \end{cases} \tag{4.4}$$

and the result is the derivative of the frame after its passing through a low-pass filter. This function is pre-computed and the discrete convolution product over the basis of length $2w$ is computed for each frame. As shown in figure 4.2 the width is different for anodes and cathodes due to the high frequency cut of the delay line. The FWHM of the peaks are 9 ns for the anodes and 36 ns for the cathodes. Those values have been applied to the respective w values.

Figure 4.3 illustrates the convolution process for an anode signal and for two signals read from a delay line. Each negative peak in the original frame is converted into a bipolar shape starting with a negative part followed by a positive one, with a

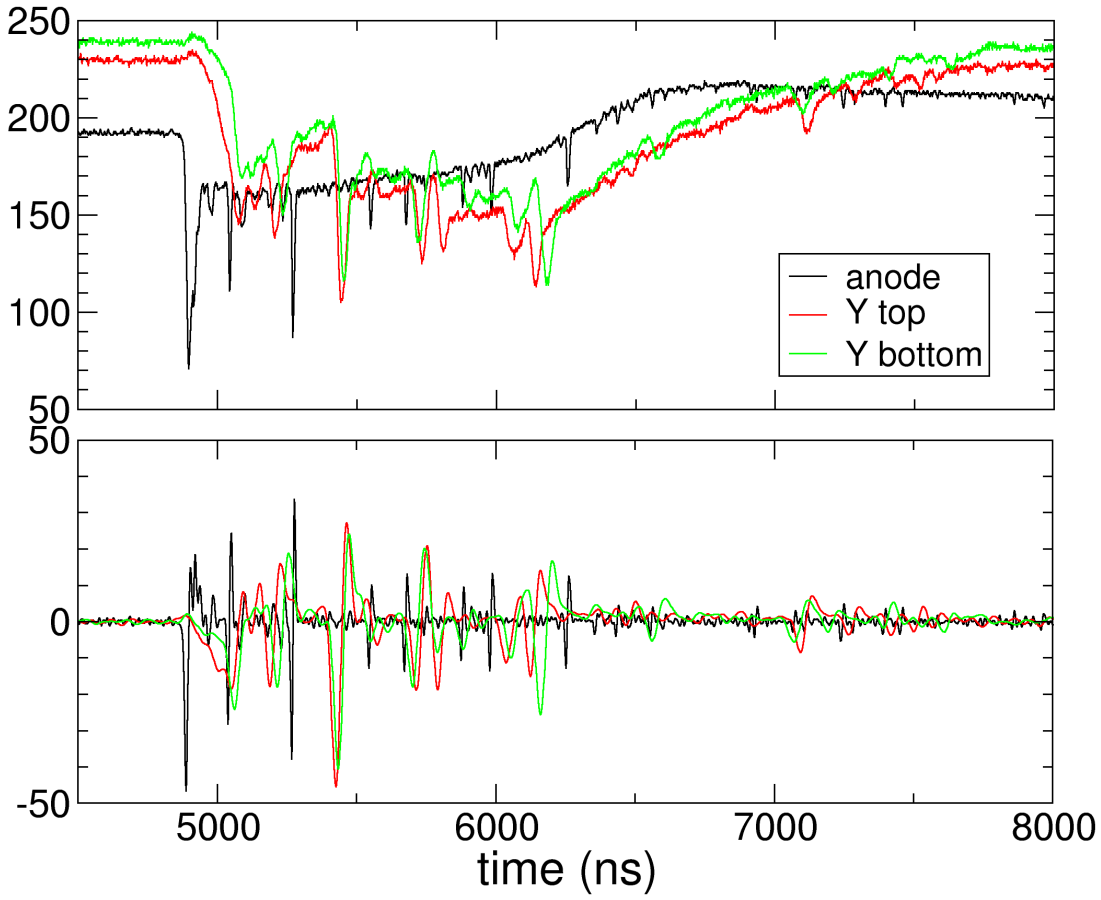

FIGURE 4.3: Upper diagram: original frames after the γ-flash for detector 0, anode and two Y delay line channels. Lower part: same signals after the convolution with function (4.4)

0-crossing in between. The important point is that the waving of the base line completely vanished through the derivative and that the noise remains at the same level compared to the peaks.

The recognition of the peaks is performed on the convoluted frames by searching the bipolar shapes. A negative and a positive thresholds are set slightly above the noise, and a pattern is searched for a first crossing down of the negative threshold, its crossing back, the crossing up of the positive threshold, and its crossing back. Once such a pattern is found and the negative and positive parts are similar in amplitude the peak is validated, its time stamp is given by the 0-crossing of the bipolar shape and its amplitude by the minimum-maximum vertical distance.

Although the sampling time is 2 ns (500 MHz FADC's) the time accuracy of peaks is much better due to the interpolation of the 0-crossing, it is of the order of 0.5 ns.

4.3 The γ-flash

A magnet located in the neutron line deflects the charged particles, but not the γ rays and relativistic muons which are produced in the target and reach the experimental area. The origin of this γ-flash is not fully clear, but some information is given by signals delivered by the PPACs. Figure 4.3 shows that the γ-flash starts with a sharp peak slightly wider ($\approx$ 15 ns) than fission signals with a comparable height, followed by a large bump lasting about 1.5 μs. Contrary to fission signals the sharp peak doesn't show up in the delay line frames. This proves that the number of electrons in the gas of PPACS is comparable to the case of fission fragments but they are not deposited in a given position (contrary to fission fragments) but spread over the detector area, so that at the end of the delay line they are serialized in time and don't produce a peak.

When a material is inserted in the neutron line (flange or window) the amplitude of the γ-flash increases, showing that it comes from the conversion of incoming particles. As most of the charged particles are deflected out the sharp peak, visible on the anode signals, probably comes from neutral particles converted into charged particles in the vicinity of the experimental area. But the neutral particles are hardly massive (neutrons for example) because they would be produced with a broad velocity spectrum and instead of a sharp peak one would get a step with a long tail. The sharp peak is likely coming from the flash of γ's produced when the proton bunch hits the spallation target, this is consistent with its time width. The photons propagate in the neutron pipe at speed of light, and emit electrons by Compton scattering when they pass through materials as aluminized mylar foils, target backings, etc... and the electrons are detected by the PPACs.

Most of the detectors (ionization chambers, C_6D_6) are blind for several μs due to this γ-flash. The PPAC is ready after 20 ns thanks to the very thin materials inserted in the beam drastically limiting the Compton scattering of photons. The sharp signal on the anodes can be used as a time reference: it corresponds to photons travelling with speed of light, immediately after the protons entered the spallation target.

If t_{gf} is the time stamp in the frame of the γ-flash and L_{geom} is the geometrical flight path (L_{geom} $\approx$185 m), the time stamp for the spilling of the protons in the

spallation target is:

$$t_0 = t_{gf} - \frac{L_{geom}}{c} \tag{4.5}$$

where c is the speed of light. This t_0 is the start time for the measurement of the time of flight which is computed as the difference of any fission time and t_0. With $L_{geom} \approx 185$ m one gets for the photons contained in the γ-flash a time of flight of 617 ns.

4.4 Time-energy correlation

The measurement of the time of flight is the basis of the determination of the energy of the incoming neutron. This section describes how it is practically performed.

We denote T_{OF} as the true time of a neutron travelling from the spallation target (water surface) to the experimental area. Again L_{geom} is the length of this flight path, about 185 m. The velocity is:

$$\beta = \frac{L_{geom}}{c\,T_{OF}} \tag{4.6}$$

The kinetic energy is derived with the relativistic formula with the usual notation $\gamma = 1/\sqrt{1-\beta^2}$:

$$E_n = (\gamma - 1)m_n c^2 = \frac{\gamma^2 - 1}{\gamma + 1} m_n c^2 = \frac{\beta^2 \gamma^2}{\gamma + 1} m_n c^2 \tag{4.7}$$

where the last form is very useful because it is not subject to rounding errors for low energy neutrons.

When the protons are spilled in the spallation target the neutrons are immediately released through spallation reactions and they start to propagate in the massive lead block where they moderate. They can be moderated further in the water before entering the neutron line as illustrated in figure 4.4.

The measured time of flight T_{mes} is the difference between the detecting time and the t_0 defined by equation 4.5. It is the sum of the moderation t_{mod} and the true time of flight T_{OF}:

$$T_{OF} = T_{mes} - t_{mod} \tag{4.8}$$

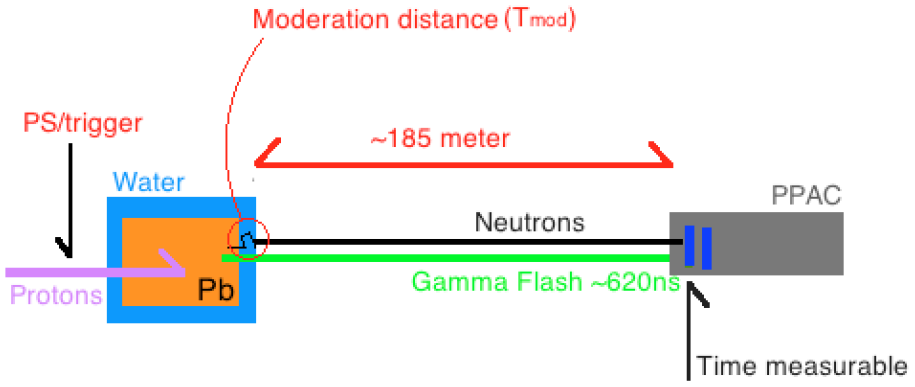

FIGURE 4.4: Time sequence from proton spilling to fission detection

After substitution of this relation into 4.6 one gets:

$$\beta = \frac{L_{geom}}{c\,T_{mes}}\frac{T_{mes}}{T_{OF}} = \frac{L_{geom}}{c\,T_{mes}}\left(1+\frac{t_{mod}}{T_{OF}}\right) = \frac{L_{geom}+\lambda}{c\,T_{mes}} \tag{4.9}$$

with λ naming the moderation distance defined as:

$$\lambda = v\,t_{mod} = \beta\,c\,t_{mod} \tag{4.10}$$

where v is the neutron velocity.

As the moderation time, the moderation distance is a fluctuating quantity which cannot be known on an event basis. Although the moderation time is spread over a very broad spectrum (from ns to several μs) the moderation distance lies always in the same range, a few cm in our case, reflecting the dimensions of the moderating material.

The moderation distance is a stochastic quantity which has a probability density depending on the neutron energy. This probability density has been simulated using FLUKA including the transmission through the collimators defining the neutron beam. It has an asymmetric bell shape with a peak corresponding to the most probable distance and a tail. For the calculation of β by relation 4.9 we used the most probable value λ_m of the simulated moderation distance. Its dependence with the neutron energy is plotted in figure 4.5 together with the mean value and the dispersion. Above 10 keV the shift between these 2 values indicate the strong skewness of the distribution.

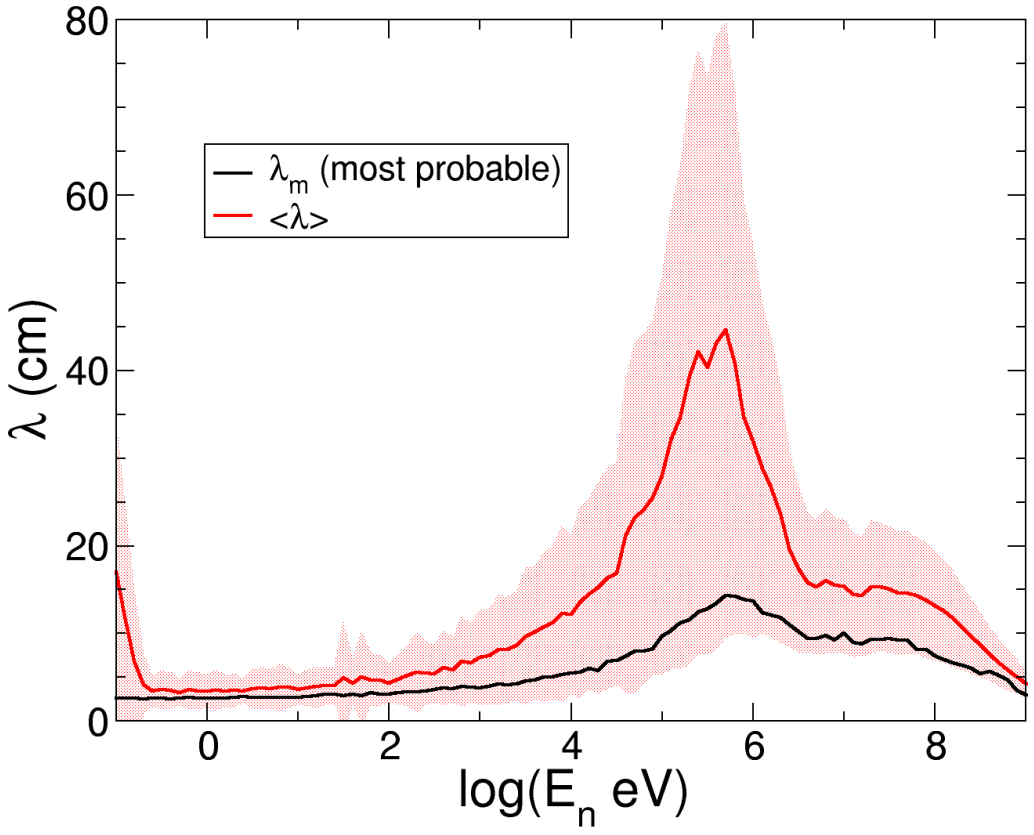

FIGURE 4.5: Most probable and average moderation distance versus the neutron energy. The hatched area indicates the spread of the distribution: $< \lambda > \pm\sigma$.

As a matter of fact the length of the flight path L_{geom} is not known with accuracy and we used the low energy resonances of ^{235}U to determine it with precision. In a first step a guess value is used for L_{geom}, close to 185 m, and the fission cross section of ^{235}U is plotted with this value and compared with the evaluated ENDF/B-VII.0 cross section (figure 4.6, upper part). Then L_{geom} is tuned to get a good matching as shown in the lower part of figure 4.6.

4.5 Energy Resolution

The energy resolution of incoming neutrons is directly related to the velocity resolution through the flight path and time of flight. From the relation:

$$\frac{d\gamma}{\gamma - 1} = \gamma(\gamma + 1)\frac{d\beta}{\beta} \tag{4.11}$$

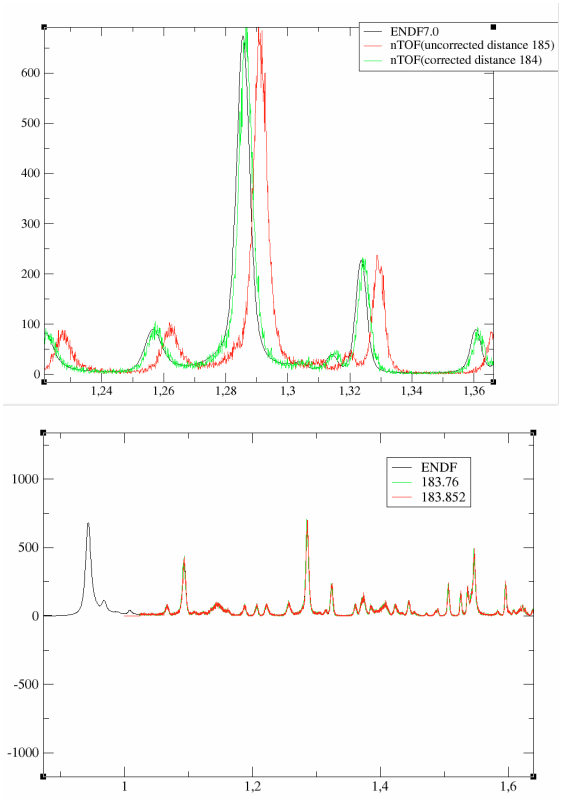

FIGURE 4.6: Comparison of resonant fission cross section of ^{235}U with ENDF/B-VII.0. Upper diagram: a first gess of L_{geom} has been used. Lower diagram: L_{geom} has been tuned to match the ENDF/B-VII.0 cross section.

one gets for the energy resolution:

$$\frac{\Delta E}{E} = \gamma(\gamma+1)\sqrt{\left(\frac{\Delta L}{L}\right)^2 + \left(\frac{\Delta T}{T}\right)^2} \tag{4.12}$$

where Δ is for the standard-deviation. In case of non-relativistic neutrons, as in the resonance region, we get the simplification: $\gamma(\gamma+1) = 2$. In the above formula ΔL is due to the fluctuation on the moderation distance:

$$\frac{\Delta L}{L} = \frac{\Delta \lambda}{L_{geom}} \tag{4.13}$$

and the fluctuation ΔT is that associated with the proton bunch width: ΔT=9 ns, because the PPAC time pick off is much shorter, of the order of 0.3 ns.

Obviously the longer the flight path, the better the resolution. In the resonance region the time contribution is negligible and the length dispersion dominates the resolution which is about 0.01%. At high energy, above 10 MeV, the timing resolution dominates and the energy resolution is about 1.4% at 100 MeV.

4.6 Counting rate

The instantaneous counting rate can be an issue at high energy due the contraction in time although PPAC have a very fast response. In addition above tens of MeV other reactions than fission take place on light elements of the backings and electrodes. Although they are in principle rejected by the coincidence method they may generate a high counting rate of single fragments which may coincide in time randomly. Therefore it's worth estimating the instantaneous counting rate.

The reaction rate is:

$$N_r = n_t \, \sigma(E) \, \Phi \tag{4.14}$$

where $\sigma(E)$ is the reaction cross section, n_t is the number of target atoms in the beam spot, and Φ is the neutron flux (neutrons/cm^2/second). This is the definition of the cross section.

The mean time between 2 reactions is therefore :

$$\Delta T = \frac{1}{N_r} = \frac{1}{n_t \, \sigma(E) \, \Phi} \tag{4.15}$$

Now we should relate the instantaneous flux Φ with the more well known lethargic flux : $\phi(E) = dN/d\log E$ expressed in neutron/cm^2/decade/burst.

We consider a kinetic energy interval $[E,E+dE]$ for 1 burst.

By using equation (4.11) one gets for relation between the time and energy increments (relativistic formula):

$$\frac{d\log E}{\log(e)} = \frac{dE}{E} = \frac{d\gamma}{\gamma - 1} = \gamma(1+\gamma)\,\frac{d\beta}{\beta} \tag{4.16}$$

$$= \gamma(1+\gamma)\,\frac{dt}{t} \tag{4.17}$$

$$= \frac{c}{L}\,\beta\gamma(1+\gamma)\,dt \tag{4.18}$$

$$\tag{4.19}$$

with L for the path length. Substituting with:

$$\beta = \frac{\sqrt{\gamma^2 - 1}}{\gamma} \tag{4.20}$$

we get:

$$\frac{d\log E}{\log(e)} = \frac{c}{L}\sqrt{\gamma^2-1}(1+\gamma)\,dt \tag{4.21}$$

$$= \frac{c}{L}\sqrt{(\gamma-1)(1+\gamma)^3}\,dt \tag{4.22}$$

$$= \frac{c}{L}\sqrt{\frac{E}{m_nc^2}\left(2+\frac{E}{m_nc^2}\right)^3}\,dt \tag{4.23}$$

$$\tag{4.24}$$

This gives for the instantaneous flux:

$$\Phi = \frac{dN}{dt} = \frac{dN}{d\log E}\frac{d\log E}{dt} \tag{4.25}$$

$$= \log(e)\,\frac{c}{L}\,\phi(E)\sqrt{\frac{E}{m_nc^2}\left(2+\frac{E}{m_nc^2}\right)^3} \tag{4.26}$$

$$\tag{4.27}$$

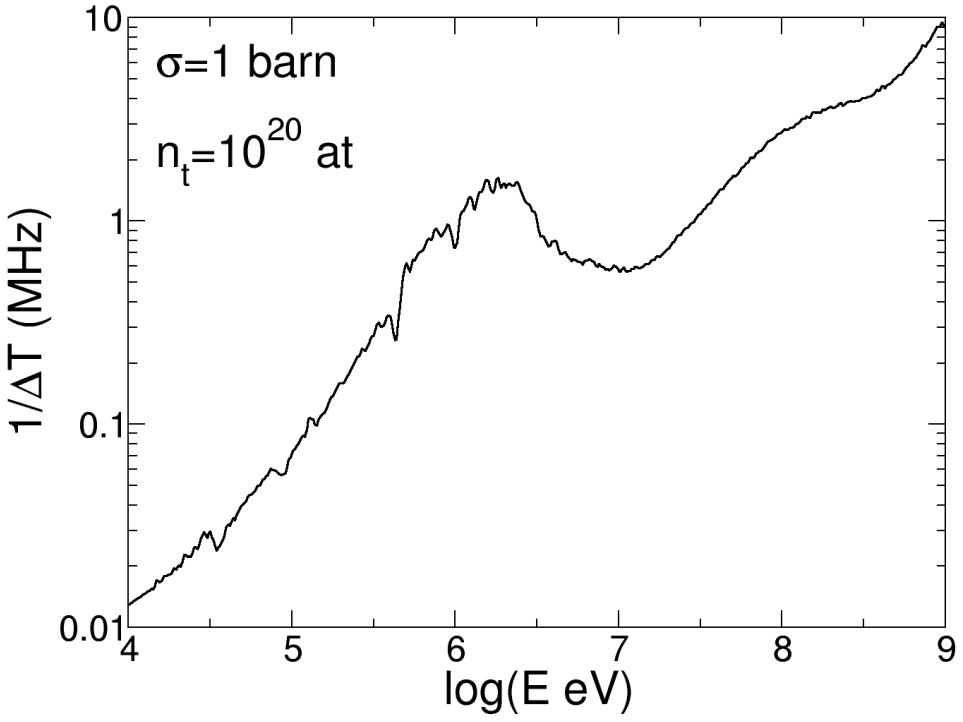

FIGURE 4.7: Reaction rate as a function of the neutron energy for a cross section of 1 barn and a number of target atoms of 10^{20}.

After replacement of this expresion into relation 4.15 one gets the average time between reactions:

$$\Delta T = \frac{1}{\log(e)\,\frac{c}{L}\,n_t\,\sigma(E)\,\phi(E)\sqrt{\frac{E}{m_n c^2}\left(2+\frac{E}{m_n c^2}\right)^3}} \tag{4.28}$$

We see that in the epithermal region, where the cross section goes as $1/v$ and where $\phi(E)$ is approximately constant, the average time is constant and so is the counting rate. But at high energy, in particular above hundreds MeV, the counting rate increases steeply. This is illustrated in figure 4.7 which shows the reaction rate for a constant cross section of 1 barn and 10^{20} target atoms, when using the neutron flux shown in chapter 3. Our actinide targets have $0.4\,10^{20}$ atoms with a fission cross section of 2 barn at high energy and a detection efficiency of 0.6 so that the counting rate is half the plotted one.

It's interesting to estimate the contribution of reactions on light elements of backings (Al) and electrodes (C, O). At high energy one can assume that the cross section is geometrical and one gets for the backing of 1 target (^{235}U, ^{238}U, ^{237}Np) and for the electrodes of 1 PPAC:

Z	σ (barn)	n_t (10^{20}atoms)	$\sigma \times n_t$
^{235}U	2.0	0.4	0.8
Al	0.47	6.	3.
O	0.33	4.5	1.5
C	0.28	11	3.0

We see that at high energy the contribution to the reaction rate on the light elements of dead layers can be much higher that fission of the actinides. Fortunately the detection efficiency for those parasitic reactions is much lower due to the light nuclei which are produced and the coincidence method helps reject most of them, but we will see that they are still present in the data.

4.7 Fission event recognition by coincidences

From a buffer containing for every proton bunch the list of all peaks of all signals (anode, top, bottom, right, left) of the 10 detectors, the reconstruction of the fission events needs the following steps performed in order:

- Find the coincidences between adjacent detectors. This is done by using only the very sharp anode signals. From this inventory of coincident detectors we determine which target the fission came from.
- Find the localization signals associated to each selected anode peak of the coincidence sequence.
- Determine the X and Y localizations for all detectors of the coincidence sequence by the delay between the delay line peaks and the related anode peak.
- Reconstruct the angles of the fission trajectory and find the emitting point on the target by the crossing of the trajectory with the target plane.

We look now at the details of each of these operations.

4.7.1 Anode signal coincidences

The recognition of a fission trajectory is based on the fact that every time a fission fragment crosses a detecting gap of a PPAC, between anode and cathode, it is seen as a peak in the anode signal, and also in the two delay line signals associated to this gap. In other words the detection efficiency of the PPAC is always 1 provided the fission fragment crosses the gap. Therefore the real PPAC efficiency is only limited by the fact that some fission fragments do not reach the gap because they have been stopped in the dead layers as backings and mylar electrodes. This happens when the thickness of crossed materials is high as it is the case for trajectories strongly tilted against the orthogonal to detectors.

Figures 4.1 and 4.2 show examples of coincident signals on the anodes of adjacent detectors. This coincidence is very accurate in time but one has to take into account the possibility for a fragment for crossing several detectors.

If only two adjacent detectors are coincident the emitting target is obviously the one between the two detectors. This happens in most of the cases ($\approx 2/3$ of the fission events. But as already noticed some fission fragments may cross two detectors, in this case 3 detectors appear to be coincident and there is an ambiguity on the emitting target. This is the price we paid for minimizing all material thicknesses and overall for the detector spare resulting from their possibility to

look at two targets simultaneously, one on each side. But we show now how the accurate timing property of PPACs solves cleanly this problem.

4.7.2 Identification of the emitting target

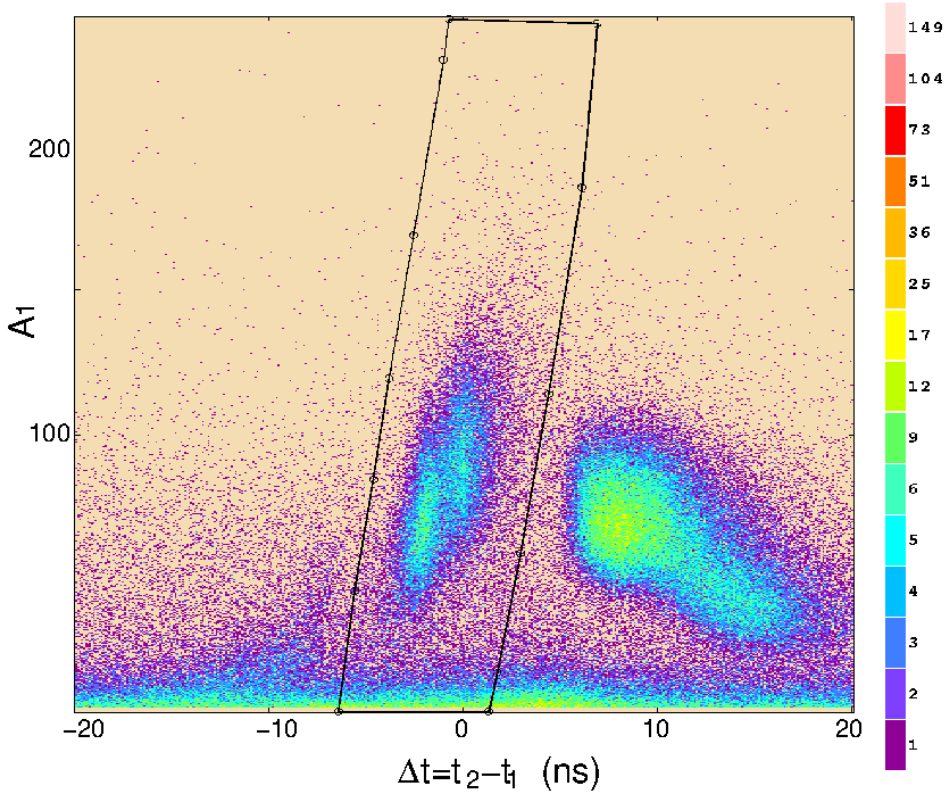

FIGURE 4.8: Correlation between amplitude on detector 1 with the time difference between detectors 2 and 1. The ^{238}U is between detectors 1 and 2, the ^{235}U target is upstream and a ^{232}Th is downstream.

The basic idea relies on the fact that when a fission comes from the target between two detectors, the fission fragments reach each detector almost at the same time because they have to travel the same distance between target and detector which is 2.5 cm along the perpendicular. This synchronization is not perfect because the velocity of the 2 fission fragments is not the same due to the asymmetry of mass division, and the length may be more than 2.5 cm due to the angle of the trajectory (it can be up to 7 cm). Nevertheless the coincidence holds approximately. Now when a fission fragment crosses one detector and reaches the next one, the time for the latter is delayed by the traveling time between the two detectors, distant by 5 cm. Therefore looking at the time differences between adjacent detectors should allow to disentangle the emitting target.

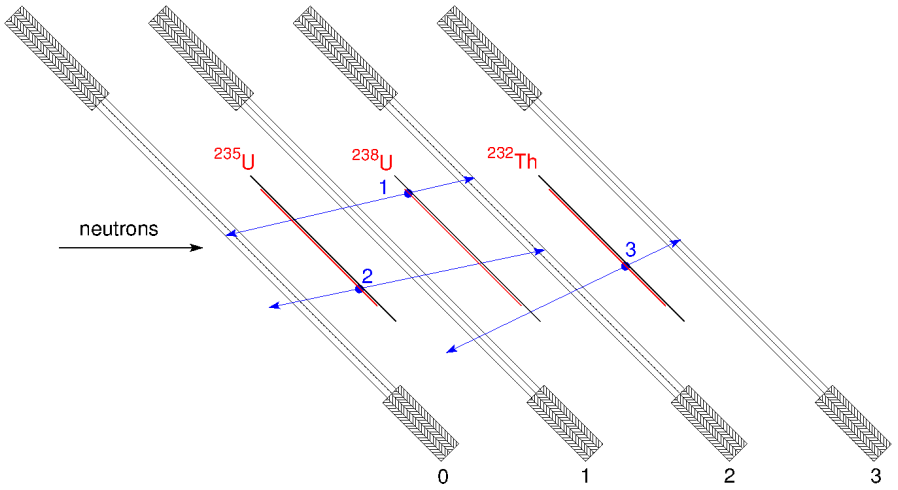

FIGURE 4.9: Different possibilities in case several detectors are coinicident. The blue point indicates the emission point on the target and the blue arrowed lines the trajectories of fission fragments. The secheme is a top view of detectors and targets at a given geometrical scale, the target layers are in red and their backings in black.

Starting from an anode peak of one detector (detector 1 for example) a time window of 20 ns is opened to search for coincidences in the anode of adjacent detectors. This window is large enough to contain the signals from the complementary fragments crossing a first and a second detector. When a sequence of coincident detectors is found, if the number is greater than 2 the emitting target has to be identified.

Let's take the case of the detectors 1 and 2 surrounding the ^{238}U target and let's consider the case where detectors 1 and 2 are coincident and that they coincide with another adjacent detector (0 or 3). Figure 4.8 shows the 2D-plot of amplitude of anode 1 versus the difference in time between detectors 2 and 1.

The central spot at $\Delta t \approx 0$ corresponds to fission fragments emitted by the ^{238}U target, as indicated by trajectory 1 in figure 4.9. Two bumps show up in this spot because of the asymmetric fission. The left hand bump is for the case where detector 1 is hit by the heavy fragment and detector 2 by the lighter one. The right hand bump is for the reverse case. The heavier fragments releases less energy in the gas than the lighter although it doesn'stop inside the gas, due to the fact that for energy loss the incident energy is lower than the Bragg peak.

The strong bump at about 10 ns is due to fragments coming from the ^{235}U target as indicated by trajectory 2 in figure 4.9. The longer delay of 10 ns is due to the travelling time to detector 2 after slowing down in target 1 and detector 1. Here

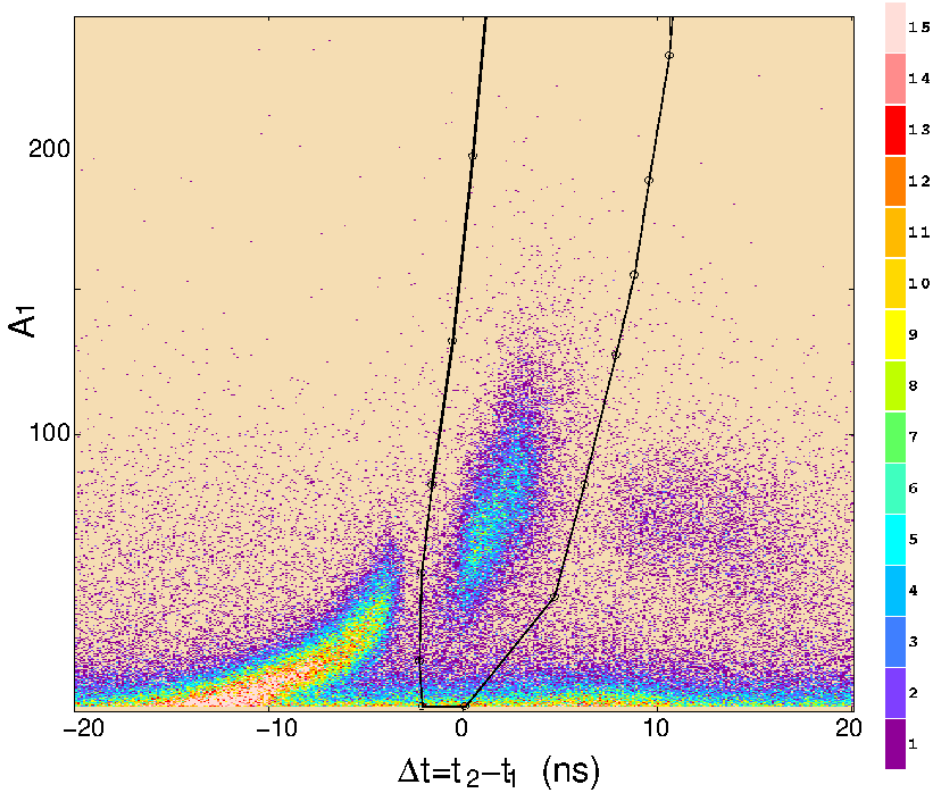

FIGURE 4.10: Same as figure 4.8 but for detectors surrounding a ^{232}Th, with the ^{237}Np target downstream.

2 bumps are visible too, due to the asymmetric fission of ^{235}U. The left hand bump is the faster with the higher amplitude and corresponds to the lighter fragment crossing detectors 1 and 2. The other case where the heavier fragment goes toward detectors 1 and 2 is less populated because it's more probable for this fragment to be stopped in the dead layers at large angles.

The events coming from target 2 (^{232}Th), as sketched by trajectory 3 in figure 4.9, are visible on the other side of the central spot in figure 4.8 at about -10 ns. They are much less populated due to the low fission cross section of ^{232}Th. The effect can be better seen in figure 4.10 for 2 detectors surrounding a ^{232}Th with a ^{237}Np downstream producing the tails on the left starting at -4 ns. The amplitude is low because the fragment had to pass through an additional target and detector to reach detector 1.

In all cases the events coming from the target between 2 detectors can be clearly selected by a contour as illustrated in figures 4.8 and 4.10, and in case of a series of coincident detectors, the target is seeked by looping over the couples of detectors and searching the inclusion in the related contour. In the case of only 2 detectors

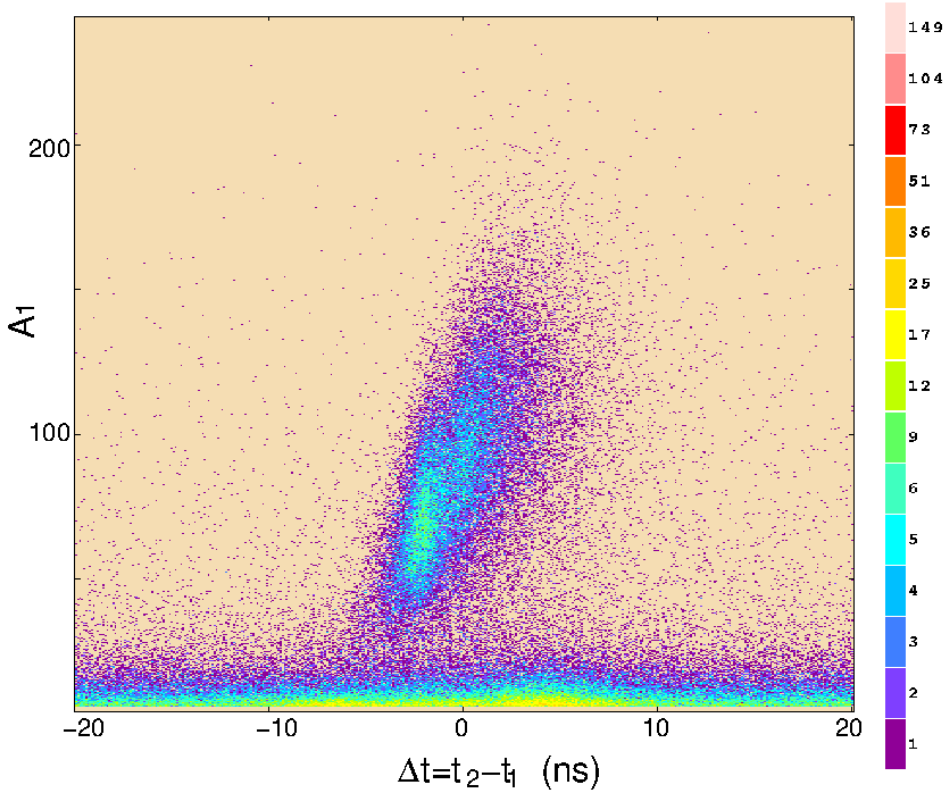

FIGURE 4.11: Same as figure 4.8 but for the case of only detectors 1 and 2 (around ^{238}U target) in coincidence.

found in coincidence the situation is simpler and the emitting target is the one between the 2 detectors. It can be checked that this is consistent with the timings seen in figures 4.8 and 4.10. Figure 4.11 shows the time correlation of detectors 1 and 2 around the ^{238}U when they are not in coincidence with other detectors. The central spot is again clearly visible but it is more spread in time and amplitude compared to the multiple coincidence case. This is due to the fact that coincidences restricted to 2 detectors allow to look at trajectories more tilted against the perpendicular to the detectors, which are stopped in dead layers before reaching additional detectors. Those trajectories have longer paths for the fragments and the time dispersion increases.

It can be seen in figure 4.11 that no track is visible coming from the neighboring target ^{235}U, validating the assumption that all fissions come from the ^{238}U. Nevertheless a a wider contour can be applied in this case too to reduce the contribution of random coincidences.

At this point the emitting target has been identified and we keep track of the information available on the 2 detectors (named 1 and 2) surrounding the target:

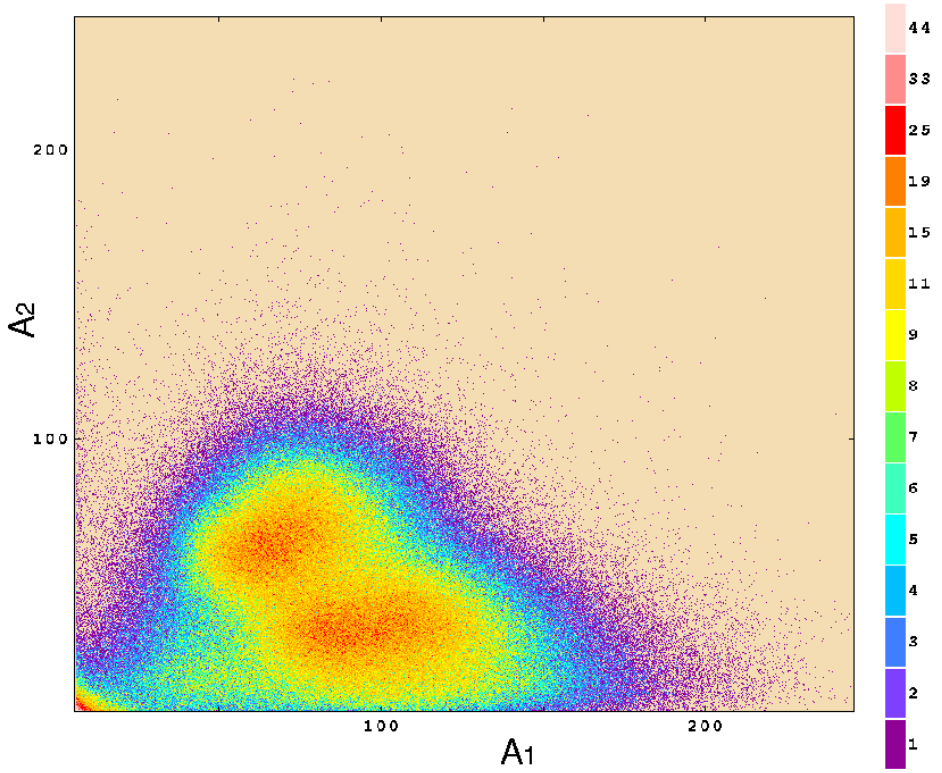

FIGURE 4.12: Correlation between anode amplitudes in detectors around the ^{237}Np target.

timings, localization signals.

4.7.3 Low amplitude background

So far we didn't mention the low amplitude background visible in figures 4.8, 4.10, 4.11. We discuss it now.

By using the information of the 2 detectors around the emitting target one can plot the correlation between the 2 anode amplitudes. It is shown in figure 4.12 for the ^{237}Np target. The 2 bumps of the asymmetric fission are clearly visible. The spread in amplitude is not only due to the mass division spectrum but also to the fission angle: for grazing angles both amplitudes drop due to the slowing down in the electrodes and the target backing. The amplitude A_2 is lower than A_1 in average because the fragment has to cross the target backing to reach detector 2.

The low A_1 events are seen in the corner, they clearly correspond to low amplitudes in both detectors. From this picture it turns out that the sum of both amplitudes is better discriminating true fission events from this background.

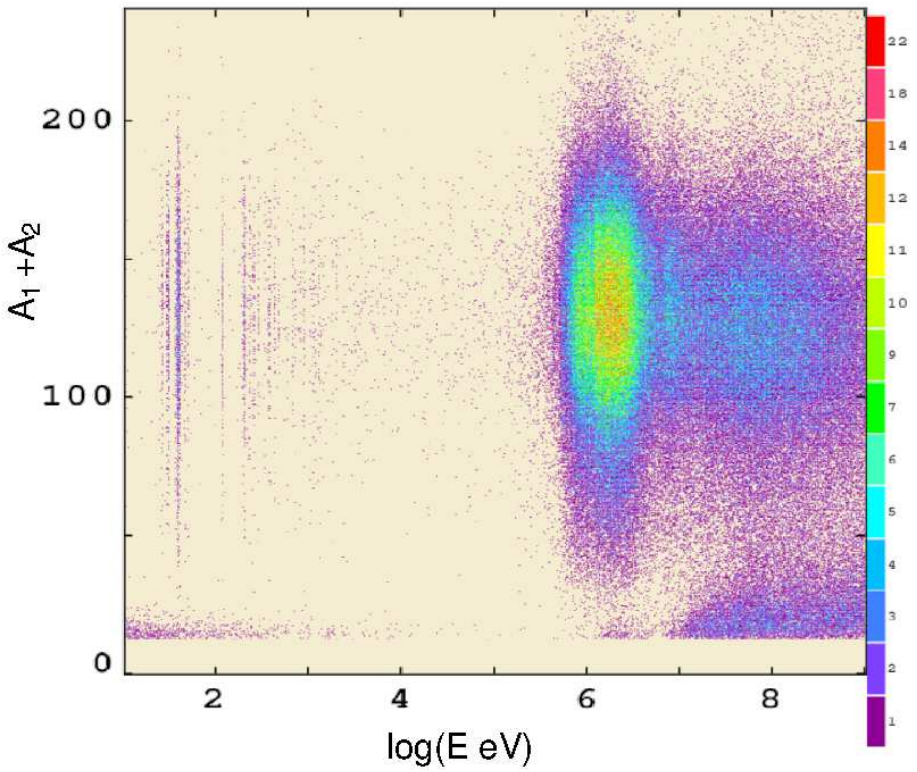

FIGURE 4.13: Distribution of the sum of anode amplitudes in detectors around the ^{237}Np target, as a function of the neutron energy.

Figure 4.13 represents the distribution of the sum of anode amplitudes versus the neutron energy for the ^{237}Np target. The below-threshold fission resonances are visible from the lowest energy of 10 eV up to 1 keV. The low amplitude background is mainly present at high energy, specially above 10 MeV. A small contribution at low energy is also present and comes from the α-radioactivity as suggested by the fact it's not present for the other targets.

The origin of the high energy background can be inferred from its characteristics. Above 10 MeV reactions on low Z elements of dead layers (C, O of mylar, Al of backings and electrode coating) set on. They produce several light particles and recoiling light spallation residuals. Most of them have been rejected by the requirement of the coincidence. But the counting rate due to these spallation reactions is very high, as already mentioned in the "Counting rate" section, and it produces random coincidences between them as demonstrated by the continuous time spectrum seen in figures 4.8, 4.10, 4.11. The application of a short coincidence time of the order of 10 ns allows to discard most of those parasitic events but a fraction of them still remains in the data and it can be removed by applying a threshold to the sum of the anode amplitudes.

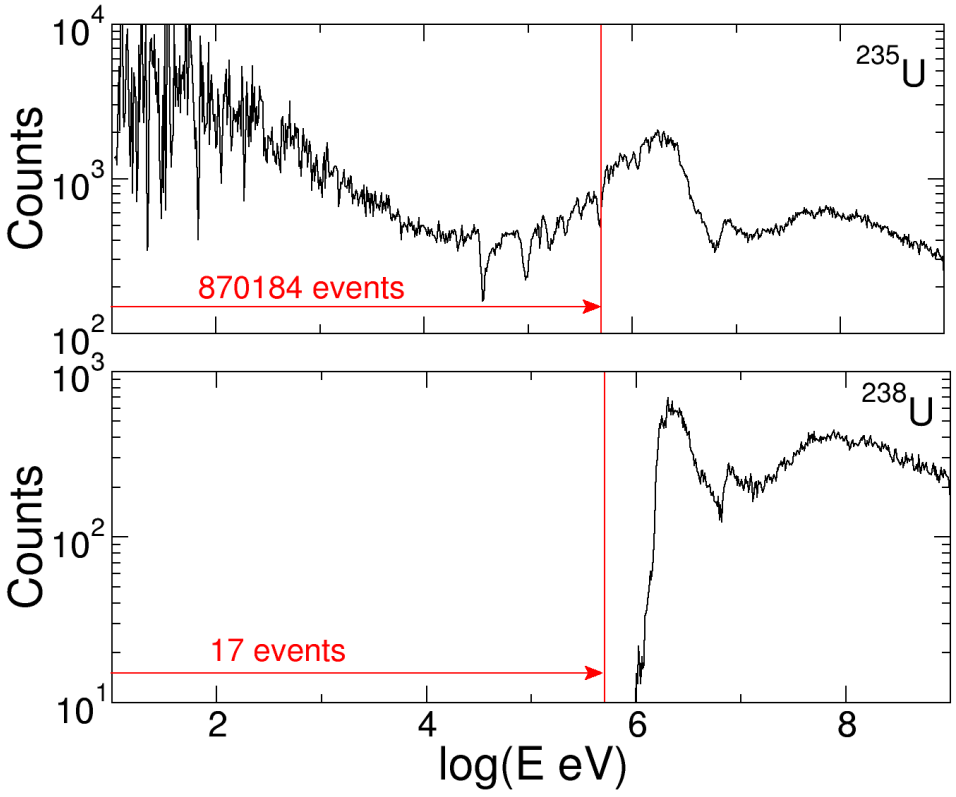

FIGURE 4.14: Energy spectrum of counts for the ^{235}U target and its ^{238}U neighbor. The red vertical lines are located at 0.5 MeV and indicate the limit of integration of counts indicated in red too.

4.7.4 Efficiency of the target identification

In our setup a fissile target ^{235}U is neighboring a less fissile ^{238}U. It provides a simple means to test how accurate is the target tagging of the fission events. Below 0.5 MeV the ^{238}U target doesn't fission and the counts seen below this limit are likely coming from fissions of the neighboring ^{235}U. For both targets the number of counts is plotted versus the energy in figure 4.14. The 17 counts recorded for the ^{238}U below 0.5 MeV are a contamination of the 870184 counts recorded in ^{235}U in the same energy range. It means that the discrimination level for target assignment is better than $5\,10^4$.

4.8 Reconstruction of fission trajectory

The previous section showed how the fissions are recognized with the coincidence method and disentangled from other possible reaction channels thanks to the excellent time resolution of PPACs. In this section, we are going to discuss how the

fission fragments are localized in each detector so that the fission trajectory can be reconstructed.

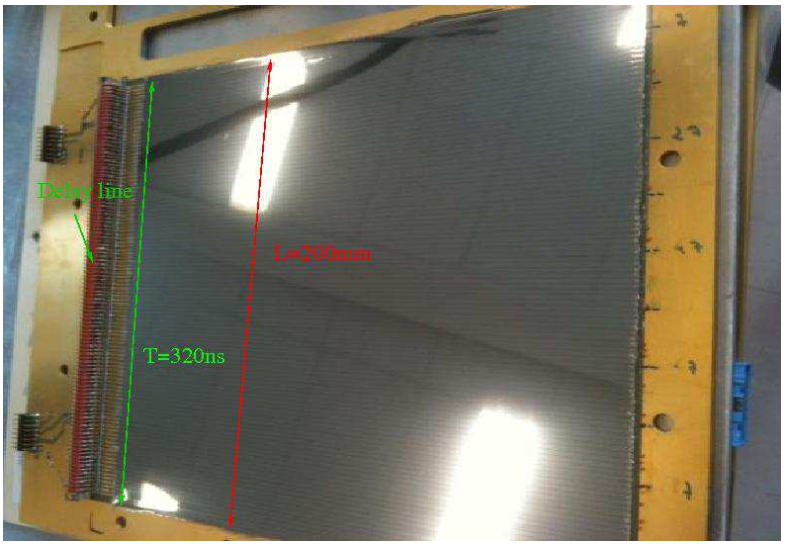

FIGURE 4.15: Picture of a cathode showing the strips, 20 cm long and 2 mm wide, connected to the delay line having a 320 ns propagation time over the 20 cm active area.

4.8.1 Principles of the localization method

As mentioned in chapter 3, each PPAC detector has two segmented cathodes with strips oriented in perpendicular directions. The strips are connected to a delay line where the signal is propagated and read at both ends by a preamplifier. The total length of the active area is 20 cm covered with 100 strips and the total propagation time is 320 ns (see fig. 4.15). The localization on the cathode is obtained from the propagation time on each side of the delay line. This determines the position perpendicular to the strips. For the other direction the cathode located on the other side of the anode is used.

Fig. 4.16 shows an example of the 5 recorded frames corresponding to a detector. The black curve represents the anode channel and the others are those collected at the ends of the delay lines: the green one is for the signal left (SL) the red one is the signal right (SR), blue for the signal top (ST) and yellow ror the signal bottom (SB).

The first strong peak in the anode signal is the γ-flash and the second strong one is a fission in coincidence with an anode peak of an adjacent detector. The

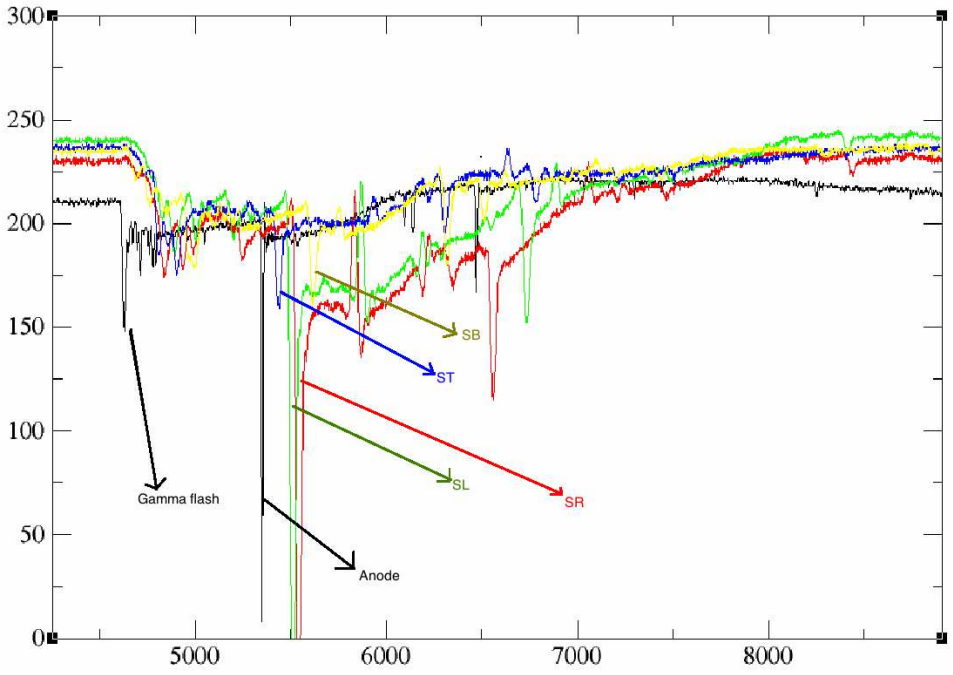

FIGURE 4.16: Signals from the 5 channels of a detector, anode (black), left SL (green), right SR (red), top ST (blue), bottom SB (yellow). The strong peak around 5400 ns in the anode signal is fission a fragment and the corresponding delay line peaks follow around 5500 ns. The time on the horizontal axis starts whith the triggering of the DAQ.

delays between the delay line peaks showing up around 5500 ns and the anode peak are due to the propagation time in the delay lines. Other peaks in SR and SL are visible around 6600 ns, related to another fission event in the anode signal at 6500 ns. The bipolar peaks appearing in SL and SR at 5800 ns and 6200 ns are reflections of the signal due to a mismatch between the impedances of the delay line and the pre-amplifiers.

It can be noticed that the peaks in signals of the same delay line (SL and SR for example) are of almost equal amplitude. This is due to the fact that they originate from the same signal (induced current on a strip) and that the attenuation of the delay line is low. But signals from different delay lines may be very different in amplitude even for the same fission fragment because they come from different detecting gaps where the energy release differs due to slowing down of the fragment through the anode foil. In particular the signals from one delay line may be absent if the fragment is stopped in this foil. The anode peak corresponds to the sum of

the charges released in both gaps.

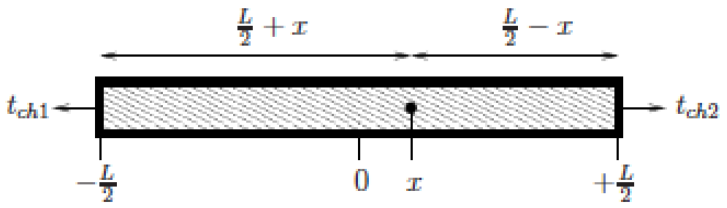

FIGURE 4.17: Signal propagation along a delay line of length L from a point x referred to the center.

We define the propagation times as:

$$t_X = t_{SX} - t_{anode} \tag{4.29}$$

where X is one of the 4 cathode symbols (L, R, T or B). These delays are determined by the length the signal propagates as sketched in figure 4.17. The relations determining the peaking times in the localization signals and the positions are:

$$\begin{aligned} t_{SL} &= t_{anode} + \delta t + \frac{1}{v}(\frac{L}{2} + x) \\ t_{SR} &= t_{amode} + \delta t + \frac{1}{v}(\frac{L}{2} - x) \\ x &= \frac{v}{2}(t_{SL} - t_{SR}) \\ y &= \frac{v}{2}(t_{SB} - t_{ST}) \end{aligned} \tag{4.30}$$

where v is the propagation velocity ($\sim$ 2 mm/3.20 ns), L is the total length of the delay line over the active area, and δt is an additional delay taking into account of the fact that the delay line is slightly longer than the active area (symmetrically) and that electronics are slower for localization signals because charge sensitive pre-amplifiers are used instead of fast current pre-amplifier on the anode, and because of the limiting bandwidth of the delay line.

The interesting feature is that according to the last 2 equations the position can be extracted by using only the cathode signals without including the anode signal and this is illustrated in figure 4.18 which shows how the delay between the ends of the delay line bears the position information. In addition this brings a simplification for the calibration: if all cables have the same length (it is the case) the center of the spectrum is exactly the center of the detector.

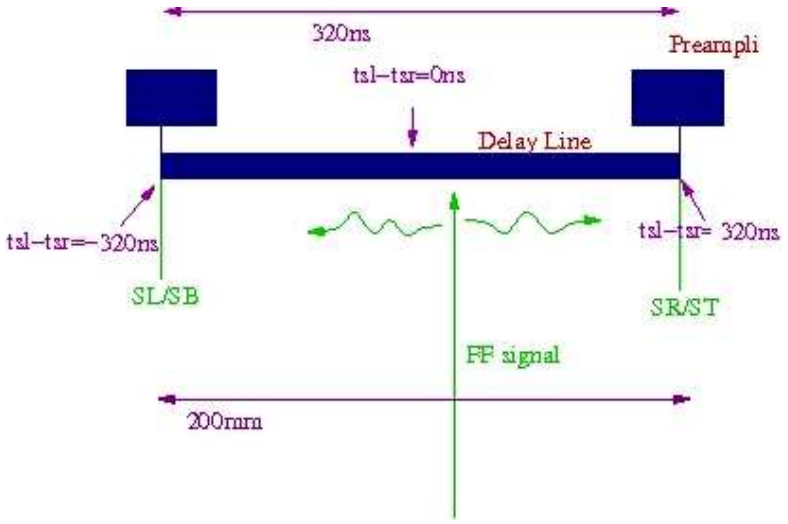

FIGURE 4.18: Scheme of the delay between SL and SR signals according the injection horizontal position in the delay line.

The delay between cathode and anode peaks is however absolutely needed to perform the right correspondance between localization signals and anode signals which define the fission event through the coincidence. This is the object of the next subsection.

4.8.2 Correspondance between cathode and anode signals

By looking at the frames of figures 4.3 and 4.16 one can see that the density of peaks may be high and due to the propagation delay it is not obvious to associate the peaks on each side of a delay line and to associate them with the correct anode signal. We can define two criteria which help perform those associations safely: the test of the sum of delays and the comparison of amplitudes.

4.8.2.1 Sum of delays on a delay line

From equations 4.30 and 4.29 one can write the following relations between the delays from the anode:

$$\begin{aligned} t_L + t_R &= (t_{SL} - t_{anode}) + (t_{SR} - t_{anode}) = 2\delta t + \frac{L}{v} \\ t_B + t_T &= (t_{SB} - t_{anode}) + (t_{ST} - t_{anode}) = 2\delta t + \frac{L}{v} \end{aligned} \tag{4.31}$$

which shows that the sum of delays is independent of the position and it is related to the total propagation time in the delay line. These relations should hold for any event in any detector.

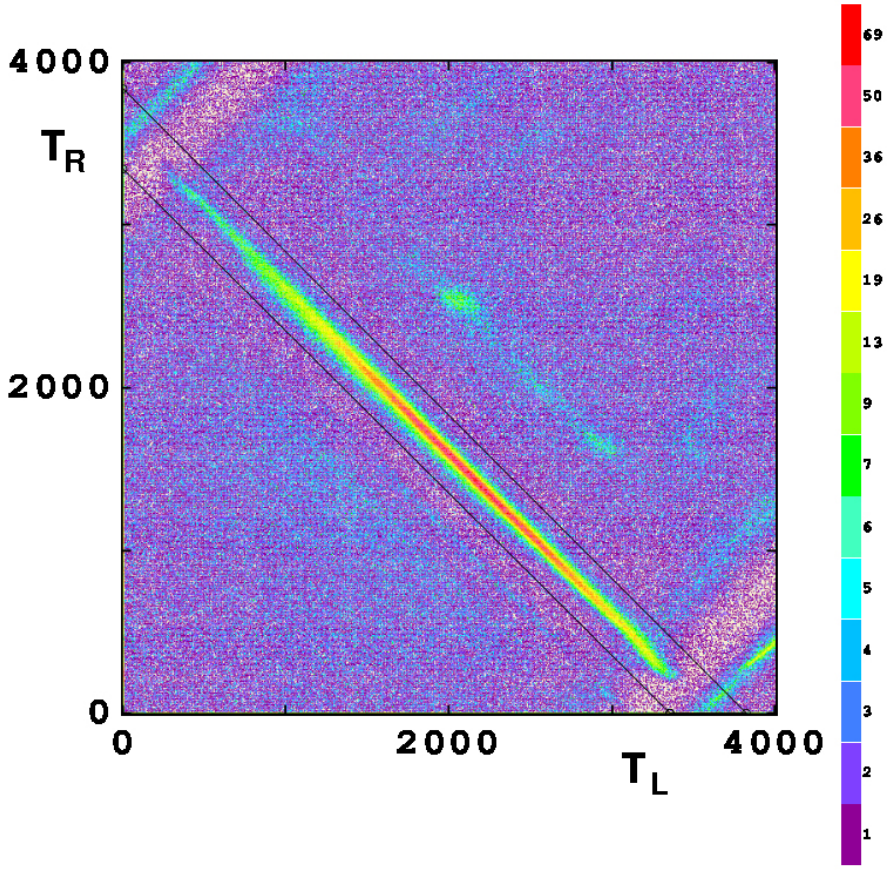

FIGURE 4.19: Plot of all combinations of delays (T_L,T_R) respect to the anode peak for many anode peaks of detector 0 without coincidence requirement. The time units are 0.1 ns.

We can check how this constraint acts really on the data by applying the following algorithm. Each time an anode signal is found by scanning the anode frame, we open a window on the SL frame (left) starting at the anode peak time and lasting 400 ns which is more than the total propagation time in the delay line. We record all the peaks found inside this window. We do the same on the SR frame (right). For all the combinations made of one peak in SL and one peak in SR we plot the (T_L,T_R) couple in a bidimensional plot as shown in figure 4.19 for the first detector close to the ^{235}U target.

A strongly populated diagonal shows up corresponding to relations 4.31. Those correlated points lie above a flat background with some structures due to after pulses and signals peaks coming from reflections in the delay line. The background

is due to the high counting rate at high neutron energy: for high energy, anode peak many localization signals are present in the 400 ns windows even if they are note related to this anode event.

The correlation provides an obvious way of selecting the correct signal peaks associated with an anode peak: the delays of the localization peaks should correlate to lie in the diagonal. This selection criterion is illustrated by the contour drawn in figure 4.19. The same selection applies to the vertical delay line and for all detectors.

Athough this selection discards most of the wrong associations between localization peaks of a delay line, at high energy the density of peaks is so high that sometimes an ambiguity remains: more than one combination may lie inside the limits defining the diagonal and the correct one has to be selected. In this case we look at the amplitudes of localization peaks.

4.8.2.2 Amplitudes of localization peaks

As already mentioned the amplitudes of peaks on each side of the delay line should be the same if they come from the same event, because they originate from the same signal injected on the delay line, and because the attenuation of the delay line is low. This provides a means to determine if one peak in the SL signal can be associated to a peak in the SR one for example.

Figure 4.20 shows the distribution of the ratio of the amplitudes of peaks in the right and left sides, for events lying in the diagonal shown in figure 4.19. Clearly the ratio is close to 1 most of the time, and it accumulates along a line with a low slope revealing the attenuation of the delay line when the propagation distance increases. The line waves toward the ends due to edge effects in the delay line.

In addition to this accumulation the ratio can extend to much lower or higher values producing a kind of background. This background is not present at low energies (below 1 MeV) and it shows up strongly at high energy. It is due to the pile up of peaks at high counting rate which deforms the peaks and changes their apparent amplitude. Therefore the condition on the amplitudes should not be too strict at the risk of loosing true events.

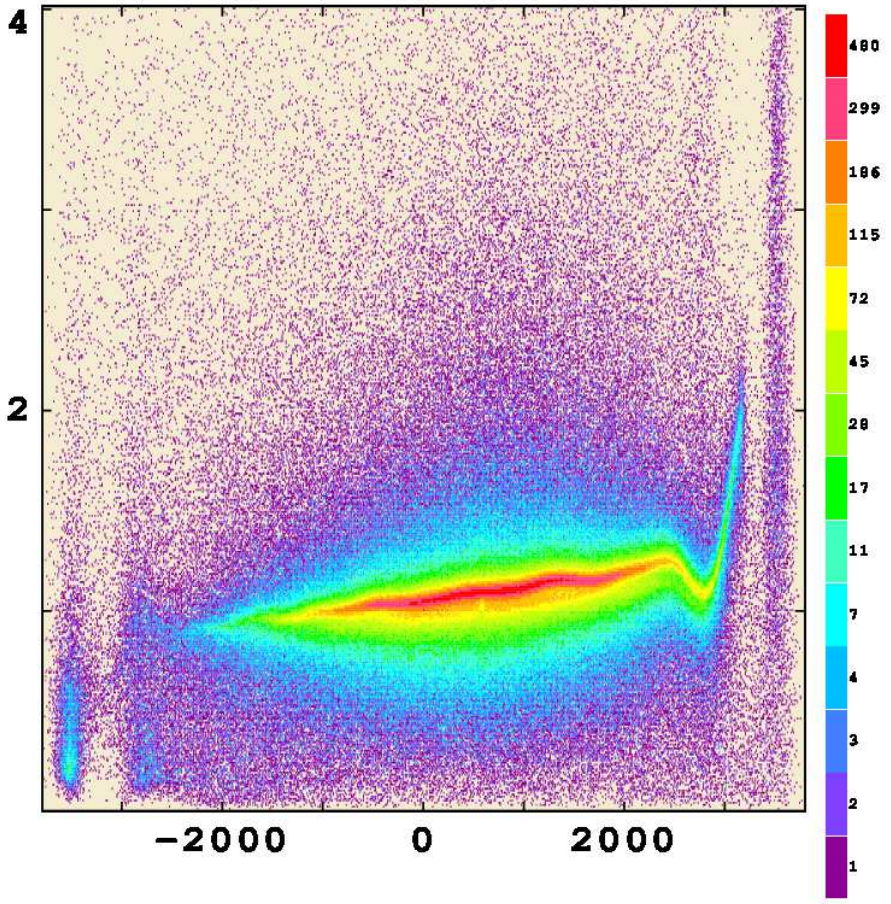

FIGURE 4.20: Distribution of amplitude ratio between peaks in SR and SL for events lying inside the diagonal contoured in figure 4.19. The horizontal axis is the difference time, in units of 0.1 ns, between SL and SR peaks, related to the position.

4.8.2.3 Criteria for association of localization peaks

From the above considerations we adopted the following algorithm to associate the peaks from the delay line signals to a fission peak on the anode. The description applies to the SL and SR signals (horizontal delay line) but it is the same for the SB and ST signals.

- For each anode peak we open a window on the SL frame (left) starting at the anode peak time and lasting 400 ns. We record all the peaks found inside this window. We do the same on the SR frame (right).
- For all the combinations made of one peak in SL and one peak in SR we retain those which fall inside the contour around the diagonal, as illustrated in figure 4.19 and we discard the others.

- If no combination is retained no position information is present and the event is discarded. If one combination is registered it is the right combination. If more than one combination is possible we select a single one with the following step.

- For each combination we compute its distance to the diagonal line in the (T_L,T_R) plane. We also compute its distance to the accumulation line in the ($T_{SL} - T_{SR}$,A_R/A_L) plane as shown in figure 4.20. We compute a global deviation distance by weighing the 2 distances according to the dispersions in each plane. The combination having the smallest deviation is retained as the right one.

- Once a single combination of peaks in SL and SR is found the difference $T_{SL} - T_{SR}$ is kept for the position information of the event showing up in the anode signal.

4.8.3 Calibration

The purpose of the calibration is to obtain the absolute coordinates in mm from the time differences $T_{SL} - T_{SR}$ and $T_{SB} - T_{ST}$.

The center of the detector is obtained when those differences are equal 0, that's to say when the peaks in SL and SR, or in SB and ST, coincide in time. This is a consequence of the homogeneity of electronics: all the delay line preamplifiers are identical and the cables lengths too. The FADC's are clocked at a frequency accurate to 10^{-6} and in addition the 2 signals of a delay line are plugged to the same FADC module. As a result the dispersion of the center cannot exceed 2 ns, corresponding to a center dispersion of at most 0.5 mm, negligible respect to other geometrical errors.

Therefore the only parameter in the calibration is the propagation velocity according to equations 4.30. We measured this velocity before the experiment by injecting a fast signal from an electronic pulser at different points of the delay line and measuring the delay between the signals at the ends of the delay line. We did it for all detectors and we found that the inverse of the velocity is in average 3.20 ns/pitch (pitch of 2 mm) with a dispersion lower than 1% over all detectors, and we adopted this value with an uncertainty of 1 mm on the calibration. The uncertainty associated to each localization event is larger due to the resolution

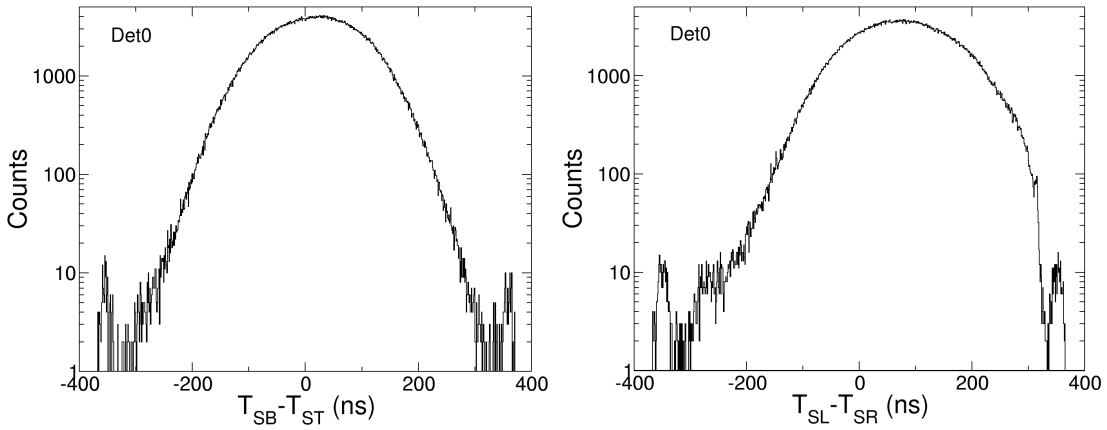

FIGURE 4.21: Spectra of time differences $T_{SB} - T_{ST}$ (left) and $T_{SL} - T_{SR}$ (right) representing the Y and X localization in detector 0 of figure 4.9.

and it is of the order of 2 mm. According to those values one expects the spectra in $T_{SL} - T_{SR}$ and $T_{SB} - T_{ST}$ extend at maximum to ± 320 ns.

Figure 4.21 shows their spectra for detector 0 of figure 4.9. We see that the vertical distribution is symmetrical as expected. It is slightly upward shifted which is well understood because the ^{235}U target is shifted up by 3 mm in agreement with the observed spectrum shift.

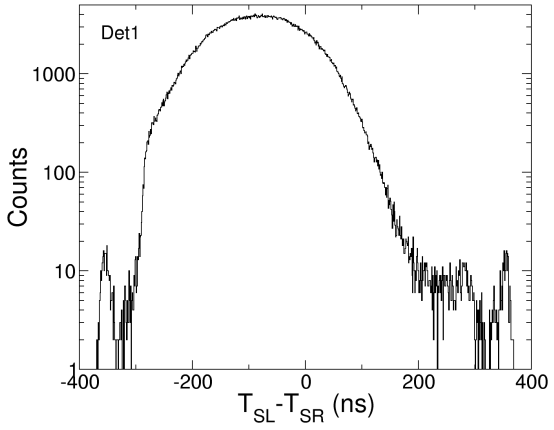

FIGURE 4.22: Spectrum of time difference $T_{SL} - T_{SR}$ (horizontal localization) on detector 1 for fission coming from the ^{235}U target.

The horizontal spectrum is similar but it is shifted to the right. This is expected because the position is referred to the center of the detector whereas the counts reflect the target position with respect to the detector center. As can be seen from figure 4.9 the ^{235}U appears shifted on the right by its distance (2.5 cm) to the detector. Its fingerprint on detector 1 on the other side should be shifted to the left by the same offset and it is checked in figure 4.22.

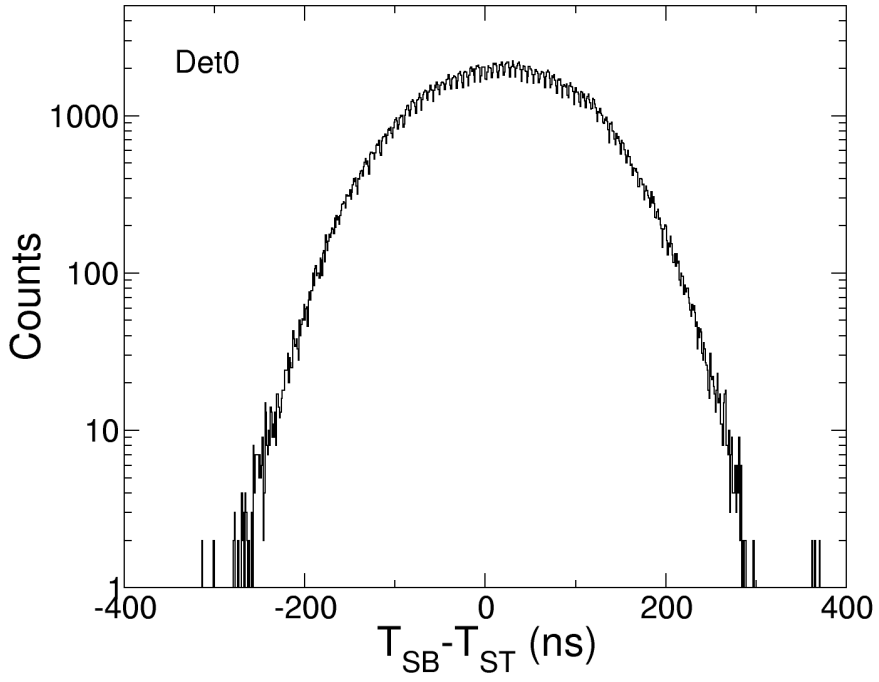

FIGURE 4.23: Spectrum of vertical position on detector 0 similar to the left part of figure 4.21 but cutting out the low amplitude peaks.

In all cases the spectrum drops steeply at ±320 ns in accordance with the measured propagation velocity. However some events are present beyond those limits. They show up only for energies above 10 MeV and they have very small amplitudes. They correspond to fake localization peaks of small amplitude which were accepted by the above described filters and they are rejected as they lie outside the expected range. Such random events might be also present inside the normal range but their fraction is very low thanks to the efficient filtering procedure.

An interesting feature of the time difference spectra is that they can be self-calibrated. This is illustrated with figure 4.23 which shows the the $T_{SB} - T_{ST}$ spectrum of detector 0 when a threshold has been applied to the amplitudes of the peaks. The overall shape is similar to that without threshold but it exhibits a regular structure which is an image of the strips: 2 neighboring dips are 2 mm apart. By counting 54 strips between -161.5 ns and 189.1 ns one can derive the inverse of the propagation velocity: (189.1+161.5)/54/2=3.24 ns/strip in accordance with the adopted value of 3.20 ns within 1%.

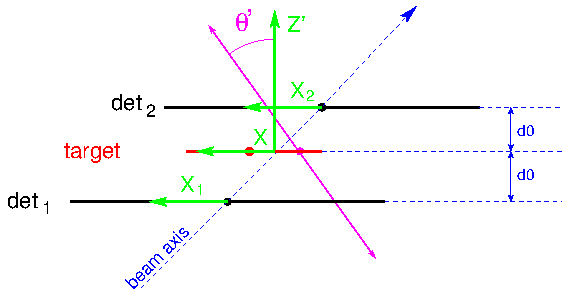

FIGURE 4.24: Top view of the 2 PPACs surrounding the emitting target. The X coordinate is defined in each plane by the green arrows the 0 is the geometric center of the detectors and the target. The Y axis points out upward from the plane and is common to the 2 detectors and the target.

4.9 Trajectory reconstruction

The fission trajectory is recontructed from the X and Y positions obtained on each detector surrounding the emitting target. It may happen that one position is missing and the event is discarded. This case happens when one fission fragment is stopped in the anode foil of one detector and this is always for trajectories strongly tilted against the perpendicular to the detectors because the fragments have to cross a large amount of material. Therefore the missing position information reduces the reconstruction efficiency at large angles, and it is the object of the next chapter to handle this problem. In this section we explain how the trajectory is reconstructed when all the position informations are available.

We first define the reference frames as shown in figure 4.24 which is a topview of the pair of detectors surrounding the emitting target. The X axes in the 3 planes are horizontal, parallel to each other and the origin is always the geometrical center of the detector or the target. The detectors are always centered on the beam axis. It is not necessarily the case for the targets due to the delicate operation of mounting them in their frames. Therefore the target center is not necessarily located at the absissa 0 in the target plane. The Y axis is vertical pointing upward and it is common for all detectors and targets. Again the PPACs are always centered in vertical position whereas the targets may be shifted for the same reason.

We define the Z' axis perpendicular to the detector and target planes oriented at 45° from the beam direction. We define the polar angle θ' of the trajectory against this axis and ϕ' the azimuthal angle around the axis. θ' and ϕ' are not the physical angles of interest, which are referred to the beam axis but they are very important

for reasons we will detail later. Let say for the moment that the physical angles can be deduced easily from θ' and ϕ'.

The objective of the reconstruction is to obtain from X_1, Y_1, X_2, Y_2 the angles θ' and ϕ' of the trajectory and the coordinates X, Y of the emission point. The X_i and Y_i are directly obtained as the localizations in the detectors.

We denote the coordinate system relative to the detectors as $(\overrightarrow{X'}, \overrightarrow{Y'}, \overrightarrow{Z'})$ with the origin located at the geometrical center of the target, with $\overrightarrow{X'}$ horizontal and parallel to X_1 and X_2, $\overrightarrow{Y'}$ vertical pointing up, and $\overrightarrow{Z'}$ perpendicular to the detectors oriented in the forward direction.

The system is not fully symmetric because for each detector the X electrode is upstream and the Y one is downstream, therefore the gap thickness e is included in the formulas, in addition to the detector-target distance d. The coordinates of the hitting points are :

$$P_{1X}\left|\begin{array}{l} X'_1 = X_1 + d + e \\ ? \\ Z'_{1X} = -(d+e) \end{array}\right. \qquad P_{1Y}\left|\begin{array}{l} ? \\ Y'_1 = Y_1 + d - e \\ Z'_{1Y} = -(d-e) \end{array}\right. \tag{4.32}$$

$$P_{2X}\left|\begin{array}{l} X'_2 = X_2 - (d-e) \\ ? \\ Z'_{2X} = d - e \end{array}\right. \qquad P_{2Y}\left|\begin{array}{l} ? \\ Y'_2 = Y_2 - (d+e) \\ Z'_{2Y} = d + e \end{array}\right. \tag{4.33}$$

If we define:

$$\begin{aligned} X' &= X'_2 - X'_1 = X_2 - X_1 - 2d \\ Y' &= Y'_2 - Y'_1 = Y_2 - Y_1 \\ Z' &= Z'_2 - Z'_1 = 2d \end{aligned} \tag{4.34}$$

the cosine of the fission angle $\cos\theta'$ relative to the $\overrightarrow{Z'}$ direction is:

$$\cos\theta' = \frac{Z'}{\sqrt{X'^2 + Y'^2 + Z'^2}} \tag{4.35}$$

This angle is essential as it determines the detector efficiency that we are going to discuss in the next chapter, and for the azimuthal angle around the perpendicular to detectors and targets: $\tan\phi' = \frac{\overrightarrow{Y'}}{\overrightarrow{X'}}$

The coordinates of the emitting point in the target is the crossing on the target of the straight line passing by the hitting points:

$$\begin{array}{ll} X = \frac{X_2'(d+e)+X_1'(d-e)}{2d} & = \frac{1}{2}(X_2+X_1)+\frac{e}{2d}(X_2-X_1) \\ Y = \frac{Y_2'(d-e)+Y_1'(d+e)}{2d} & = \frac{1}{2}(Y_1+Y_2)+\frac{e}{2d}(Y_1-Y_2) \end{array} \tag{4.36}$$

From the $\cos\theta'$ and ϕ' angles, the physical angles $\cos\theta$ and ϕ related to the beam axis can be obtained from a rotational transformation:

$$\begin{aligned} \cos\theta &= \frac{1}{\sqrt{2}}(-\sin\theta'\cos\phi'+\cos\theta') \\ \phi &= \arctan\left(\sqrt{2}\frac{\sin\theta'\sin\phi'}{\sin\theta'\cos\phi'+\cos\theta'}\right) \end{aligned} \tag{4.37}$$

and the reciprocal:

$$\begin{aligned} \cos\theta' &= \frac{1}{\sqrt{2}}(\sin\theta\cos\phi+\cos\theta) \\ \phi' &= \arctan\left(\sqrt{2}\frac{\sin\theta\sin\phi}{\sin\theta\cos\phi-\cos\theta}\right) \end{aligned} \tag{4.38}$$

The quality of the trajectory reconstruction can be checked by looking at the distribution of emitting points on the target. For example figure 4.25 shows the distribution of hitting points on the two detectors surrounding the ^{235}U target. On each detector a circular spot shows up, which is an image of the circular

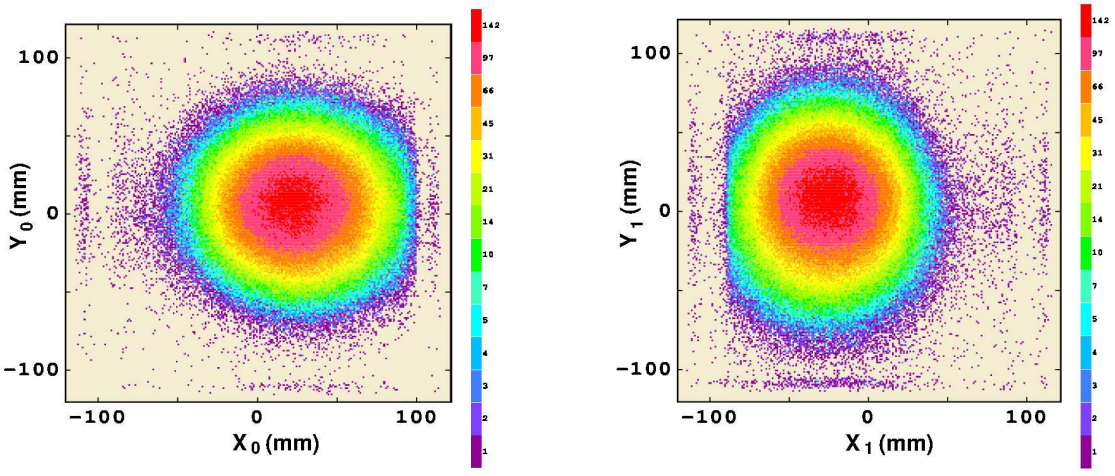

FIGURE 4.25: Distribution of hitting points on the detectors surrounding the ^{235}U target, the upstream detector is on the left side and the downstream one on the right side. The X axis is horizontal and oriented to the left hand side when travelling along the beam.

neighboring target. The image is however blurry due to the 2.5 cm distance between detector and target. In addition it is shifted due to the alignment of detectors and targets along the beam axis and the 45° tilting angle, as can be checked from figure 4.24. Due to the limited active area the distribution is slightly cut on one side and we will see in the next chapter how this effect is taken into account in the efficiency.

The distribution of emitting points in the target is obtained from equations 4.36, and it is plotted in figure 4.26 for ^{235}U and ^{232}Th. The distribution is again circular

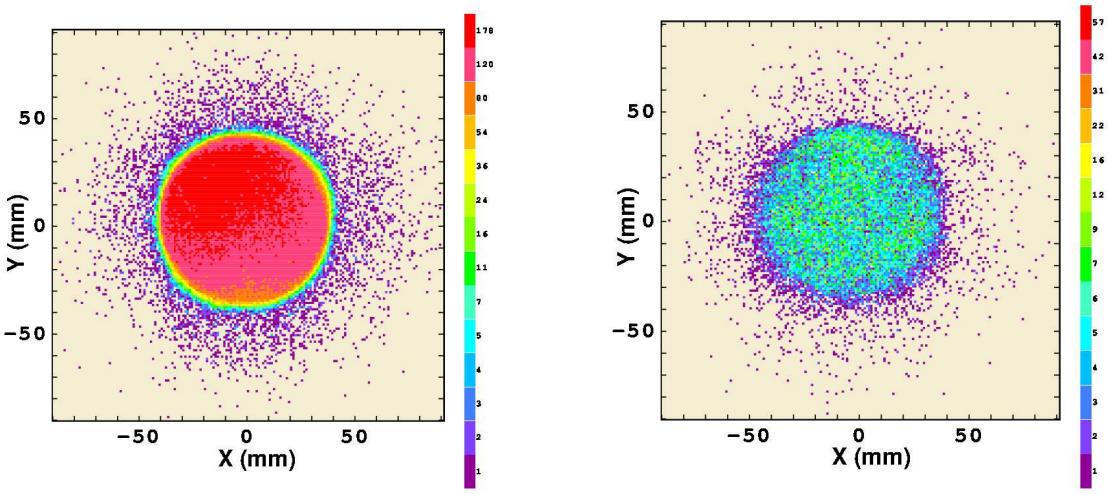

FIGURE 4.26: Distribution of emitting points on the ^{235}U target (left) and one of the ^{232}Th targets (right).

but it is now sharp-edged at the border of the circular actinide layer. The diameter of the disk is 8.0 cm as expected from the manufacturing of the targets.

In figure 4.26 we see that some counts lie beyond the limits of the fissioning layer (radius greater than 40 mm). They are due to erroneous localizations when the instantaneous counting rate is high, mainly above 20 MeV and to a lesser extent around 1 MeV

At the end every fission event is stored in a Tree with ROOT [26] that can be plotted with histogram for physics analysis. Each tree stores the following information:

- target number
- neutron energy
- X_1

- Y_1
- X_2
- Y_2
- X
- Y
- $\cos\theta'$
- ϕ'
- $\cos\theta$
- ϕ

Some additional parameters are also stored like the signal amplitudes, the coincidence time, for possible further checks.

Chapter 5

Angular distributions

We showed in the previous chapter how for each fission event the geometric parameters of the trajectory, in particular its angles ($\cos\theta$,ϕ) or ($\cos\theta'$,ϕ'), are obtained from the signals delivered by the detector. To get the angular distribution a step further is needed because the detection efficiency is lower than 1 and it depends on the angles.

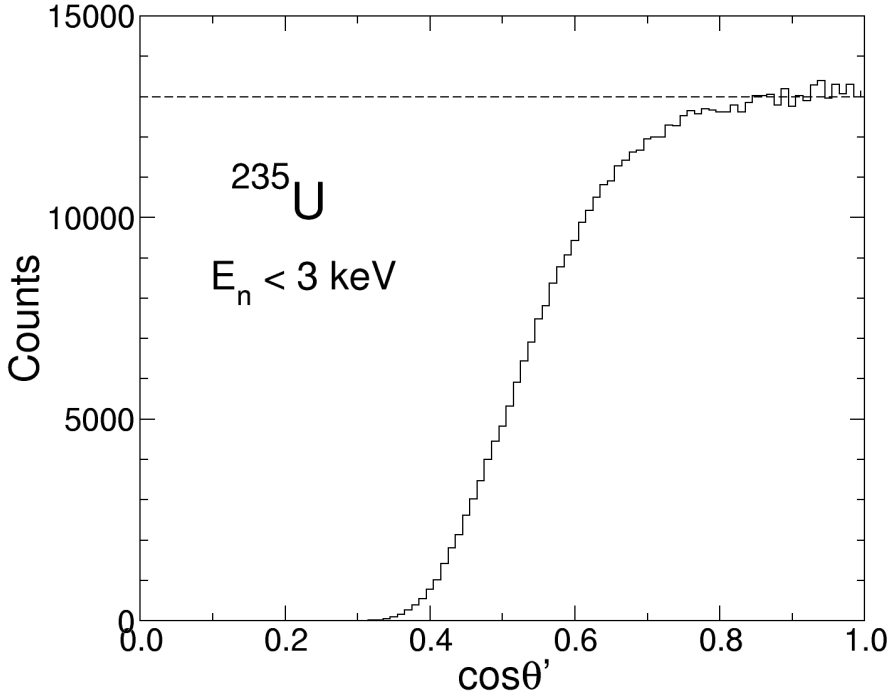

FIGURE 5.1: Distribution of $\cos\theta'$ for ^{235}U and $E_n < 3$ keV. As the emission is isotropic a full efficiency would lead to a constant number of counts as depicted by the horizontal dashed line.

This is illustrated by figure 5.1 which shows the $\cos\theta'$ spectrum obtained with the ^{235}U target for neutrons of energy lower than 3 keV. In this case only s-waves contribute significantly to the fission cross section, and even if a small contribution of p-waves is present its angular distribution is washed out by the unpolarized target ($I_0 = 7/2$) and neutron ($s = 1/2$). Therefore the fission emission is isotropic and a constant number of counts is expected versus $\cos\theta'$ in case of full efficiency. The spectrum clearly exhibits a drop at low $\cos\theta'$ showing that the efficiency drops at large angles. This is well understood by the stopping of fission fragments which have to travel across thicker distances in matter at large angles.

Therefore a procedure has to be found to get the efficiency and to correct for it.

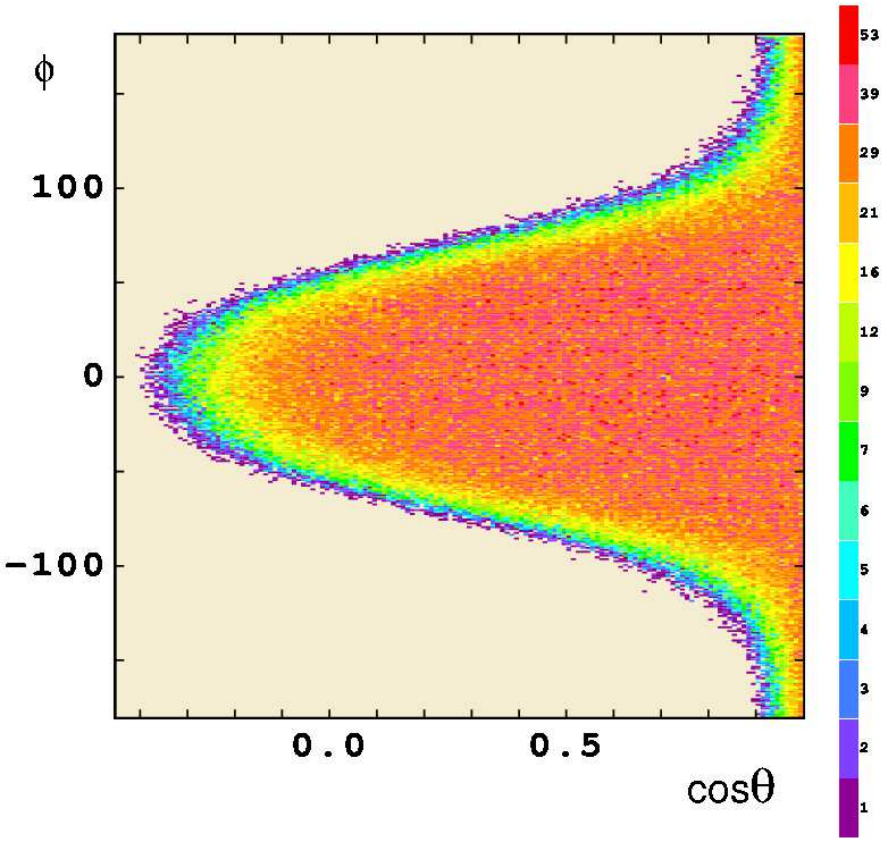

FIGURE 5.2: Distribution in angles ($\cos\theta$,ϕ) of isotropic events emitted by the ^{235}U target for neutron energies $E_n < 3$ keV.

We see in figure 5.1 that the efficiency is highly dependent on $\cos\theta'$ respect to the perpendicular to detectors and targets. One can look at its effect in the ($\cos\theta$,ϕ) plane which is more linked with physics of fission. This is displayed in figure 5.2 again for events emitted by ^{235}U for energies below 3 keV where the emission is isotropic. A constant full efficiency ($\epsilon = 1$) would populate uniformly the plane which is not the case.

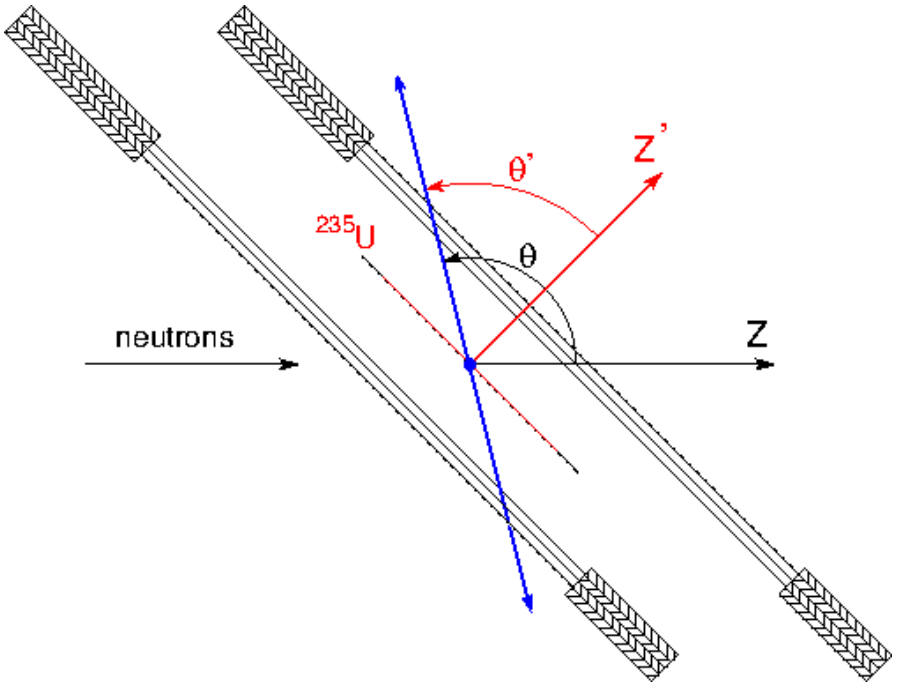

FIGURE 5.3: Example of case where the fragment detected in the forward detector has a backward direction respect to the beam axis.

One can notice that negative $\cos\theta$ are present. This is due to the way the fission direction is defined. We choosed the direction of the fragment crossing the forward detector as the fission direction. This assures that $\cos\theta'$ is always positive. But if the fission trajectory is at $\cos\theta' > 45°$ this fragment may go backward although it is detected in the downstream detector, as depicted in figure 5.3. In this case we should have selected the other fragment as bearing the fission direction. This is easily done by taking $|\cos\theta|$ instead of $\cos\theta$, as the angular distributions are symmetrical around $\cos\theta$=0. For the final results we will add the data recorded at $\cos\theta$ negative with the data at the corresponding positive value. But in some pictures we will leave the representation with negative $\cos\theta$ for sake of clarity.

Coming back to figure 5.2 we see that at $\phi = 0$ the $\cos\theta$ distribution is flat reflecting the fact that the efficiency remains equal to 1 for $\theta' < 45°$. The horizontal projection gives the $\cos\theta$ spectrum displayed in figure 5.4. As the emission is isotropic it is representative of the $\cos\theta$ dependence of the efficiency, which is very strong.

Obviously the construction of the angular distributions requires a safe determination of this dependence. One could imagine to merely use the spectrum shown in figure 5.4 as it is proportional to this efficiency. But it is only applicable to ^{235}U at low energy, it may differ at high energy according to the mass division

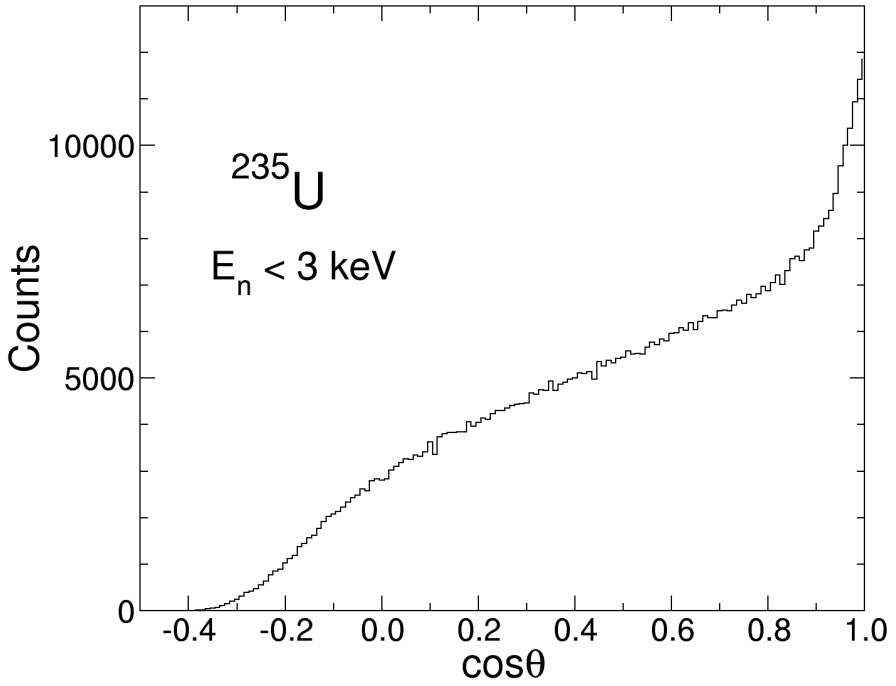

FIGURE 5.4: $\cos\theta$ spectrum for ^{235}U and $E_n < 3$ keV, proportional to the detection efficiency

evolution, and over all it depends on the target mainly because of the different backing thicknesses.

Two methods are possible and have been used. The first one relies on simulations of the efficency by simulating the penetration of fission fragments in the matter layers. Those simulations provide an estimate of the ratio of efficiency between targets and this ratio is used as a correcting factor for the experimental efficiency based on the ^{235}U isotropic emission at low energy. This method has been developed by Diego Tarrío [4] and has been used successfully for some cases, but it suffers from some flaws. In particular it doesn't take into account some parameters different between detectors (thresholds for examples), and it assumes that the physical structure of the emitting actinide layer (flat or with some roughness) is the same for all targets.

We developed another method we name "self-calibrated method" because it entirely relies on the data and doesn't need any simulation. Before going into its description we explain in the next section the main details of the simulation method.

5.1 Efficiency based on simulations

This method has been developed by Tarrío [4] in the framework of his thesis in analysing the data in parallel with us.

The main principle of Diego's method is the use of the low energy isotropic emission in ^{235}U (displayed in figure 5.4) as a reference efficiency for this target. Then simulations are developed to calculate this efficiency and check that it is close to the measured one. The same simulations are run for other targets having a different backing thickness. The ratio of the simulated efficiencies for the 2 targets is used as a correcting factor applied to the ^{235}U efficiency to get the efficiency of the other target. This is a kind of perturbation method assuming that the difference between targets is small and it is well described by simulations.

$$\epsilon_{targetX}(\cos\theta) = \epsilon_{235U}(\cos\theta) \times \frac{\epsilon_{targetX/simul}(\cos\theta)}{\epsilon_{235U/simul}(\cos\theta)} \tag{5.1}$$

$W_{235U}(\cos\theta)$ is the ^{235}U $\cos\theta$ spectrum measured at low energy and taken as the reference efficiency.
$\epsilon_{235U/simul}(\cos\theta)$ is the simulated ^{235}U efficiency.
$\epsilon_{targetX/simul}(\cos\theta)$ is the simulated target X efficiency with a different backing thickness.

Let's recall that the backing thickness is 2.5 μm of Al for ^{235}U, ^{238}U, ^{237}Np and 0.7 μm for ^{232}Th.

The simulations have been performed under Geant4 [18]. The principle of the process is to create the fission fragments sources from the target randomly in $\cos\theta$ and ϕ, and take into account those fragment characteristics (charges, mass, kinetic energy, mass distribution, etc). The target is placed between both adjacent PPAC detectors $20cm \times 20cm$ and tilted by 45°. The fragment distributions were extracted from the ENDF/B-VII.1 library [27]. The fragment scatterings, slowing down or stopping in the materials were taken into account. The number of fragments reaching the detecting gaps are recorded and the efficiency is obtained from their scoring. The result is shown in figure 5.5, compared to the measured spectrum where the negative $\cos\theta$ are added to the positive ones.

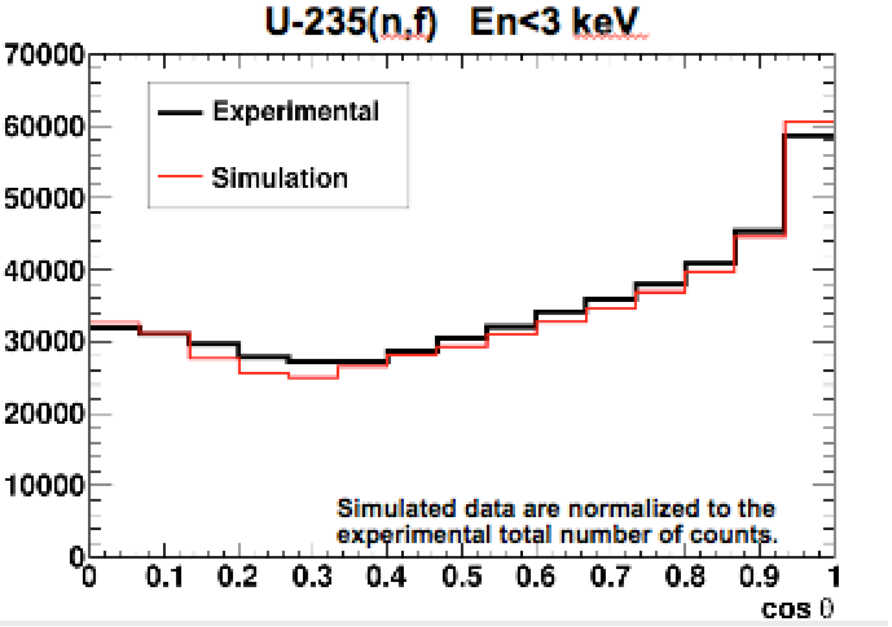

FIGURE 5.5: Detection efficiency for ^{235}U and $E_n < 3$ keV (isotropic) versus angle between fission fragment and the beam direction. Comparison between experiment and simulation [4].

The agreement is good and gives an idea of the precision of the simulation. It validates its use for other targets where no efficiency measurement is possible due to the lack of isotropic emission.

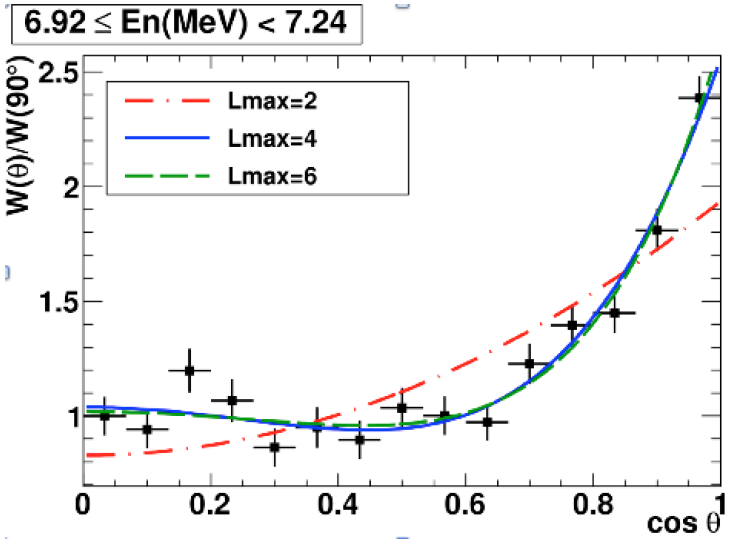

FIGURE 5.6: ^{232}Th angular distribution around 7 MeV

Figure. 5.6 shows a ^{232}Th FFAD around 7 MeV after division of the $\cos\theta$ spectrum by the efficiency obtained by the above procedure. The black points represent the measurement and the other curves are fits with Lengendre polynomials. The

distribution is forward-backward peaked with a high anisotropy at this energy where second chance fission just opened.

5.2 New method: self-determination of efficiency

The detection efficiency is only dependent on the thickness of material to cross before reaching the detecting gap. From the emitting point in the upstream direction the fragment has to go through a part of the actinide oxide, the mylar of the Y cathode foil and the mylar of the anode. The gas pressure is so low that its slowing down contribution can be neglected. In the downstream direction the fragment has to travel in the rest of the actinide layer, the backing, the X cathode foil and the anode foil. All the thicknesses of these materials are constant over the active area. But the real thickness seen by the traveling fragment increases with the angle θ' relative to the perpendicular to detectors. More precisely any sheet of thickness e is seen by the fragment as having the thickness $e/\cos\theta'$. For a given thickness to be crossed the fraction of fission which is seen corresponds to particular mass and charge divisions and this number of acceptable divisions drops when the thickness increases beyond a critical value.

From these considerations it can be stated that the efficiency only depends on $\cos\theta'$ which defines the amount of matter to be crossed. The main idea of the method is that due to the 45° tilting of the detectors and targets the same $\cos\theta$ relative to the beam can be reached by different $\cos\theta'$ values (with different ϕ and ϕ' values). As the angular distribution only depends on $\cos\theta$ all the above combinations contribute according to their efficiency and give a means of calibration of this efficiency versus $\cos\theta'$.

5.2.1 Principles of the method

Let's first look at the case where the detectors and targets are orthogonal to the beam, as in the 2003 set up. In this case the axes Oz and Oz' coincide and the angles θ and θ' are equal. Any variation in the counting rate with $\cos\theta$ is a combined effect of angular distribution and efficiency without any possibility of disentanglement.

In the tilted geometry several $\cos\theta'$ can lead to the same $\cos\theta$ and the variation of counts reflects only the variation of the efficiency with $\cos\theta'$. When $\cos\theta'$=1 the efficiency is 1 and step by step a calibration of the efficiency with $\cos\theta'$ can be obtained. In other words the tilting not only allows to span the entire range of the angular distribution, it has the virtue of decoupling the variations due to the physics of fission (angular distribution) and the detection efficiency, because each depends on a different angle.

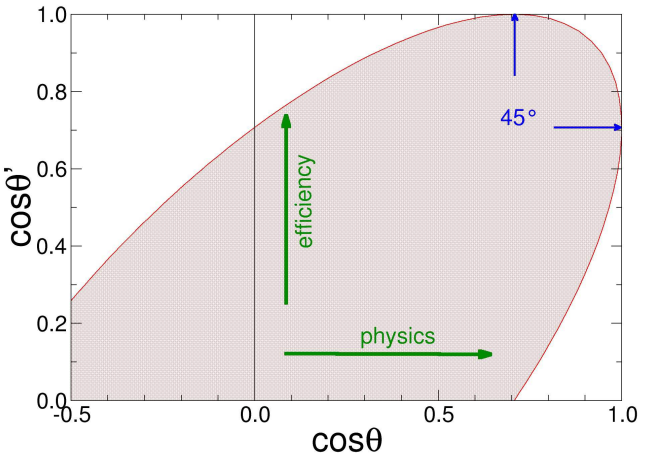

FIGURE 5.7: Geometrical area accessible in the ($\cos\theta$,$\cos\theta'$) plane

Any fission direction can be defined by the couples ($\cos\theta'$,ϕ') or ($\cos\theta$,ϕ). It may alternatively be defined in a hybrid way, and the interesting couple is ($\cos\theta$,$\cos\theta'$) from which ϕ and ϕ' can be deduced from the relations 4.37 and 4.38 given in the previous chapter, that we paste below for convenience:

$$\begin{aligned} \cos\theta &= \frac{1}{\sqrt{2}}(-\sin\theta'\cos\phi' + \cos\theta') \\ \phi &= \arctan\left(\sqrt{2}\frac{\sin\theta'\sin\phi'}{\sin\theta'\cos\phi' + \cos\theta'}\right) \end{aligned} \tag{5.2}$$

and the reciprocal:

$$\begin{aligned} \cos\theta' &= \frac{1}{\sqrt{2}}(\sin\theta\cos\phi + \cos\theta) \\ \phi' &= \arctan\left(\sqrt{2}\frac{\sin\theta\sin\phi}{\sin\theta\cos\phi - \cos\theta}\right) \end{aligned} \tag{5.3}$$

From the latter equation it can be seen that for a given $\cos\theta$ the range of possible $\cos\theta'$ is covered by varying ϕ between $-\pi$ and π. Introducing $\cos\phi = \pm 1$ in 5.3

gives the limits of the $\cos\theta'$ range:

$$\cos\theta' = \frac{1}{\sqrt{2}}(\pm\sin\theta + \cos\theta) \tag{5.4}$$

which becomes:

$$\cos^2\theta + \cos^2\theta' - \sqrt{2}\,\cos\theta\,\cos\theta' - \frac{1}{2} = 0 \tag{5.5}$$

This is an ellipse tilted at 45° in the ($\cos\theta$,$\cos\theta'$) plane as shown in figure 5.7. The hatched zone indicates the area acceptable from the geometry viewpoint.

The interesting features in this representation are the followings:

- Any horizontal slice of height $\Delta\cos\theta'$ corresponds to a constant solid angle $\Delta\Omega = 4\pi\Delta\cos\theta'$ because it is associated with a range $\phi' \in [-\pi, \pi]$ and symmetrical values of ϕ' are counted.
- For the same reason any vertical slice of width $\Delta\cos\theta$ corresponds to a constant solid angle of $\Delta\Omega = 4\pi\Delta\cos\theta$
- Along a horizontal slice the efficiency is constant and the spectrum of counts in $\cos\theta$, for a given solid angle, is the true angular distribution.
- Along a vertical band $\cos\theta$ is constant and the spectrum of counts in $\cos\theta'$ reflects the variation of the efficiency.

Those statements can be translated into the following equations. The number of fissions detected in any direction is:

$$\begin{aligned} dN &= W(\cos\theta)\,\epsilon(\cos\theta')\,d\Omega \\ &= W(\cos\theta)\,\epsilon(\cos\theta')\,d(\cos\theta)\,d\phi \\ &= W(\cos\theta)\,\epsilon(\cos\theta')\,d(\cos\theta')\,d\phi' \end{aligned} \tag{5.6}$$

$W(\cos\theta)$ is the angular distribution, the physical quantity we are interested in.
$\epsilon(\cos\theta')$ is the detection efficiency depending only on $\cos\theta'$.
$d\Omega$ is the differential of solid angle.

In a plot with the representation of figure 5.7 the counts are scored in cells (dcosθ,dcosθ') of constant width and height having different solid angles. For each cell we get:

$$dN = W(\cos\theta)\,\epsilon(\cos\theta')\,\frac{d\Omega}{d(\cos\theta)\,d(\cos\theta')}d(\cos\theta)\,d(\cos\theta') \tag{5.7}$$

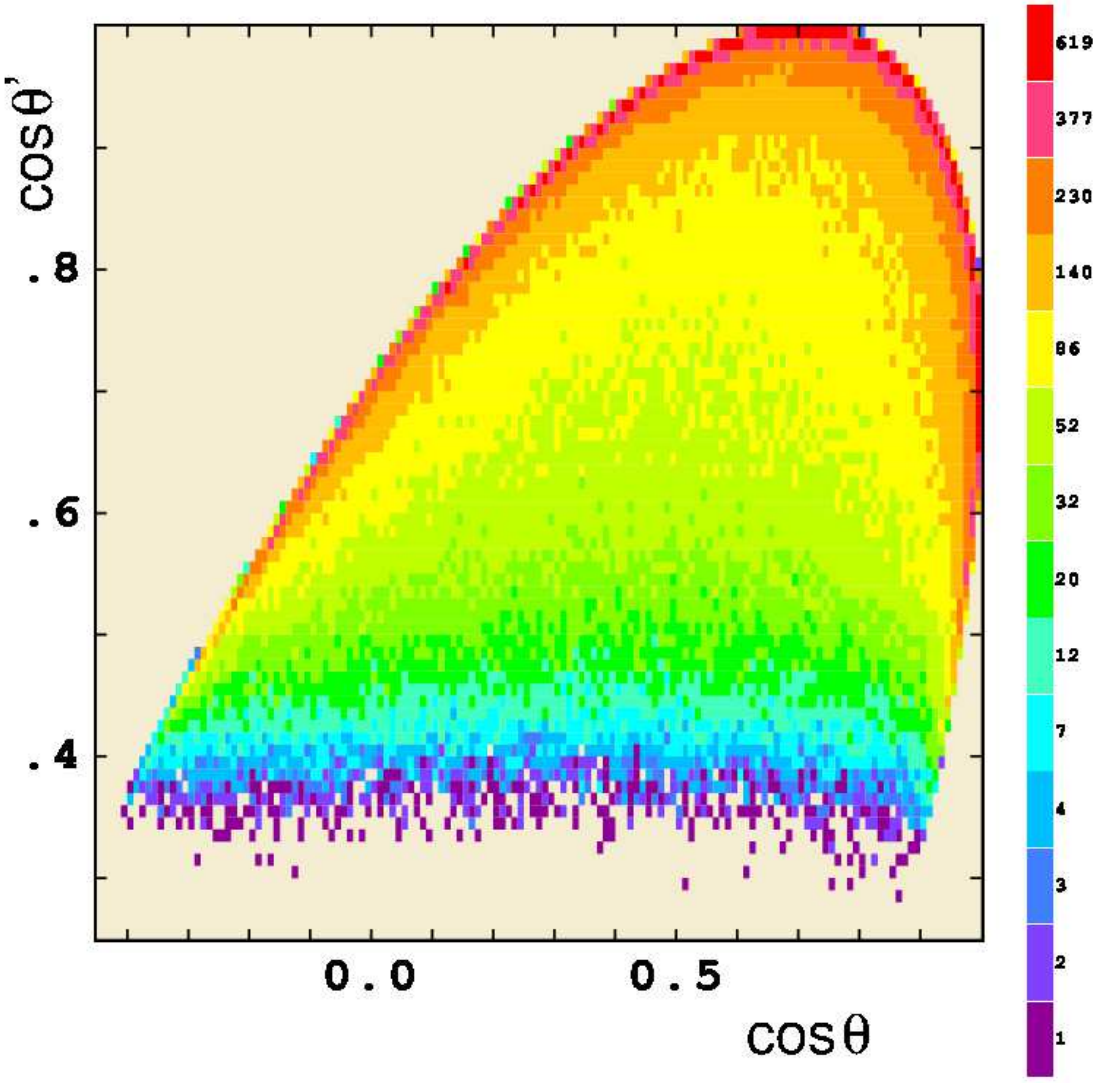

FIGURE 5.8: Distribution of counts in the ($\cos\theta$,$\cos\theta'$) plane for the ^{235}U target and $E_n < 100$ keV.

Figure 5.8 shows the distribution of counts in the plane ($\cos\theta$,$\cos\theta'$) for the ^{235}U target and $E_n < 100$ keV where fission is isotropic. One can recognize easily the elliptic shape sketched in figure 5.7. We notice that the counts accumulate close to the elliptic contour. As we will see below this is due to the large solid angle for the peripheral cells.

We are mostly interested in the product $W(\cos\theta)\,\epsilon(\cos\theta')$ which is obtained by dividing the counts in each cell by its solid angle size proportional to $\frac{d\Omega}{d(\cos\theta)\,d(\cos\theta')}$.

For each cell this factor is obtained by numerical integration using a Gauss-Legendre method. Several points are taken in $\cos\theta'$ and for each of them the limits in ϕ' are computed for the horizontal limits in $\cos\theta$ by using 5.2. This gives for each $\cos\theta'$ an interval $\Delta\phi'$ which is integrated over $\cos\theta'$. Figure 5.9 represents

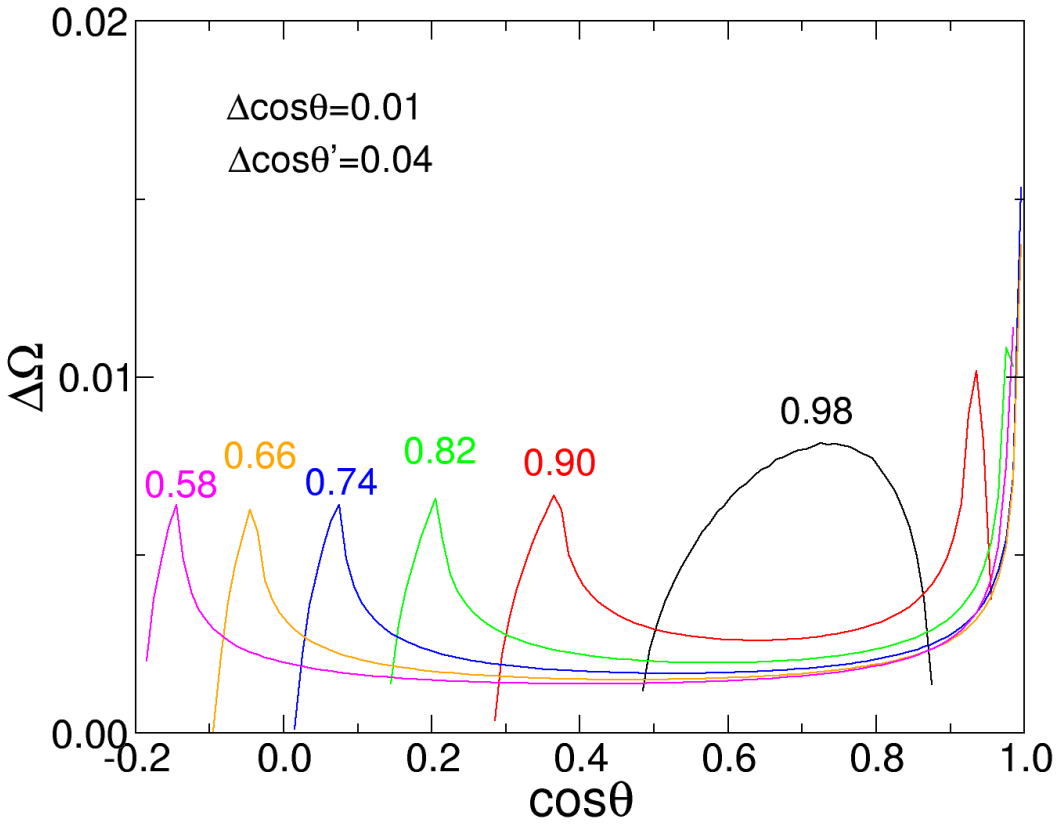

FIGURE 5.9: Solid angle of ($\cos\theta$,$\cos\theta'$) cells for cells of width $\Delta\cos\theta = 0.01$ and height $\Delta\cos\theta' = 0.04$. The numbers over the curves label the central value of $\cos\theta'$ of the horizontal band.

how the solid angle varies with the cell position inside several horizontal bands. We see that the solid angle increases quickly close to the lower and upper limits in $\cos\theta$, that's to say close to the elliptic contour in the ($\cos\theta$,$\cos\theta'$) contour. This is the reason of the accumulation of counts along this elliptic line in figure 5.8.

Figure 5.10 illustrates, again in the case of ^{235}U at energies below 100 keV where the emission is isotropic, the main features of the method. On the left is plotted the number of counts divided by the solid angle, named normalized counts N', representing the product $W(\cos\theta)\,\epsilon(\cos\theta')$. A horizontal slice has a constant efficiency and its projection onto the $\cos\theta$ axis, shown in the right part, is the angular distribution which is flat in this case as expected.

Looking back at figure 5.10 one can imagine that just by taking the $\cos\theta$ projection of a horizontal band we would get the desired angular distribution, as illustrated on the right part of the figure.

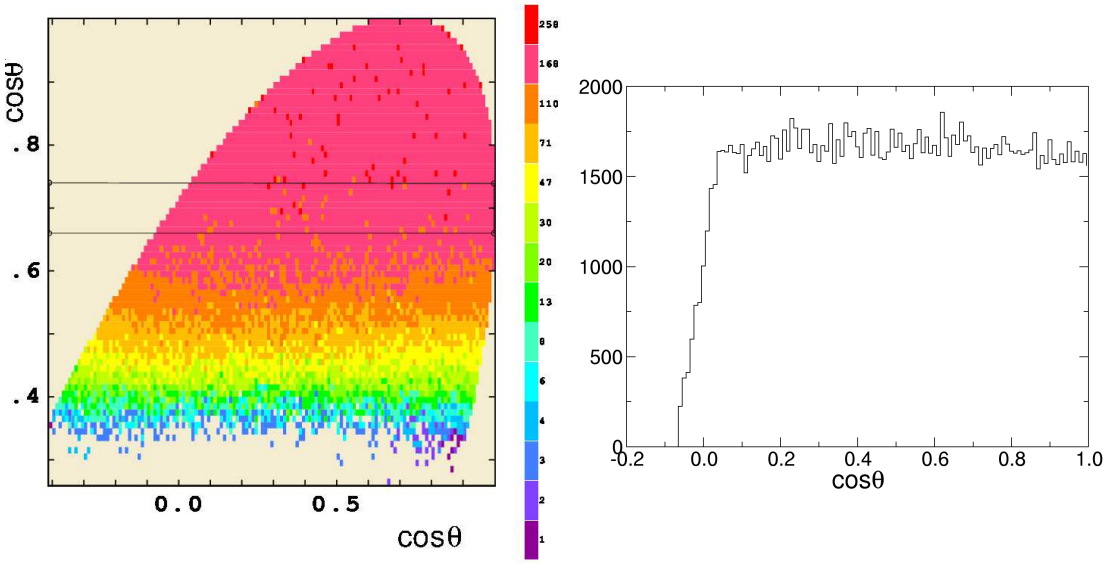

FIGURE 5.10: Left: distribution of counts divided by the solid angle for the ^{235}U target and $E_n < 100$ keV. Right: projection on $\cos\theta$ of the band of constant efficiency (constant $\cos\theta'$), drawn on the left size.

This is true but the main drawback of this procedure is that only a fraction of the recorded data are used (those located inside the band). It's not a problem for ^{235}U at low energy because the cross section is high and the number of counts too, as seen in figure 5.8. However for other isotopes having a lower fission cross section or if the energy intervals are narrow the number of counts are low and all of them should be used. Therefore the efficiciency on the full range of $\cos\theta'$ has to be determined.

Two horizontal slices of same height correspond to the same solid angle($\Delta\Omega = 4\pi\Delta\cos\theta'$). Therefore the ratio of their normalized counts is exactly the ratio of the efficiencies for these two slices. The uppermost slice is that with an upper bound $\cos\theta'$=1. For this slice the efficiency is 1 because all trajectories are almost orthogonal to the material layers and the effective thickness is minimal. This slice can be used as an efficiency reference and the number of normalized counts of slice n divided by the normalized counts in the upper slice is the efficiency ϵ_n of slice n.

Now when the $\cos\theta'$ dependence of the efficiency is known over a broad energy range, we can see how the angular distribution can be re-constructed for any energy interval where those efficiencies are applicable. By partitioning the ($\cos\theta$,$\cos\theta'$) plane into horizontal slices of same height, one can get as described above the efficiency ϵ_i of each slice. Once this set of efficiencies has been obtained it can be applied to extract the angular distribution for any energy interval where this set

is applicable, as detailed below. We divide the ($\cos\theta$,$\cos\theta'$) into a matrix of cells, with lines corresponding to the horizontal slices, and columns corresponding to the points of the angular distribution, as illustrated in figure 5.11.

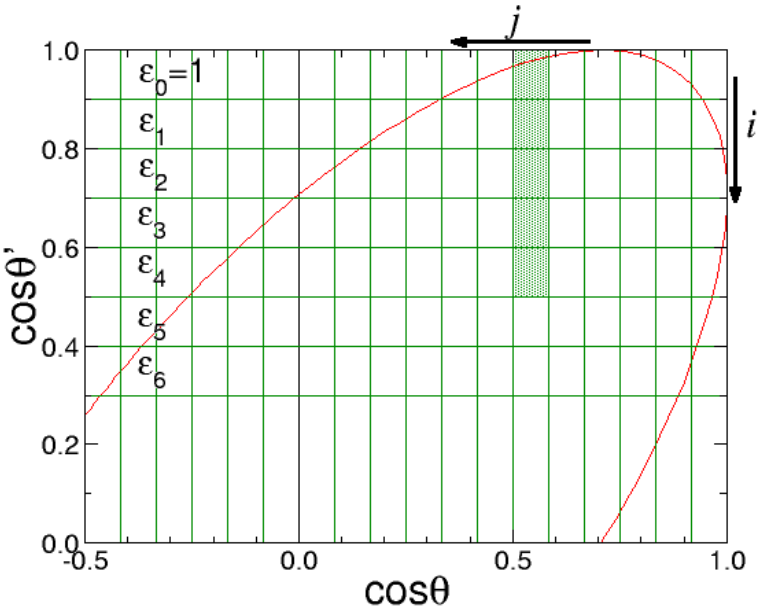

FIGURE 5.11: Partitioning of the ($\cos\theta$,$\cos\theta'$) plane into a matrix of cells. Along horizontal lines the cells have the same efficiency. The columns correspond to the $\cos\theta'$ values where the angular distribution has to be obtained. The lines are numbered with i, starting from the top, and the columns are numbered with j starting from the right.

If N_{ij} is the number of counts in the cell in line i and column j (for the considered energy interval), $\Delta\Omega_{ij}$ the solid angle of this cell and ϵ_i the efficiency of the cells of this line, one can obtain the angular distribution by summing up over the columns:

$$W(\cos\theta_j) = K\frac{\sum\limits_i N_{ij}}{\sum\limits_i \epsilon_i\,\Delta\Omega_{ij}} \tag{5.8}$$

where K is a global normalisation factor fixing the normalisation of the $W(\cos\theta)$ function.

This way of estimating the angular distribution minimizes the impact of the statistical fluctuations of the N_{ij}

We will give the details of the procedure extended to targets where no isotropic emission is available to extract the efficiencies, but we first have to introduce another efficiency reduction due to the cutting effect of the edges of the detector active area.

5.2.2 Correction for geometrical cut

So far we assumed that the only phenomenon limiting the efficiency is the stopping of fragments at large angles. Another effect contributes to reducing the efficiency in some regions of $(\cos\theta',\phi')$: the geometrical cut due to the limited size of the active area of detectors. This is already visible in figures 4.25, 4.21 and 4.22.

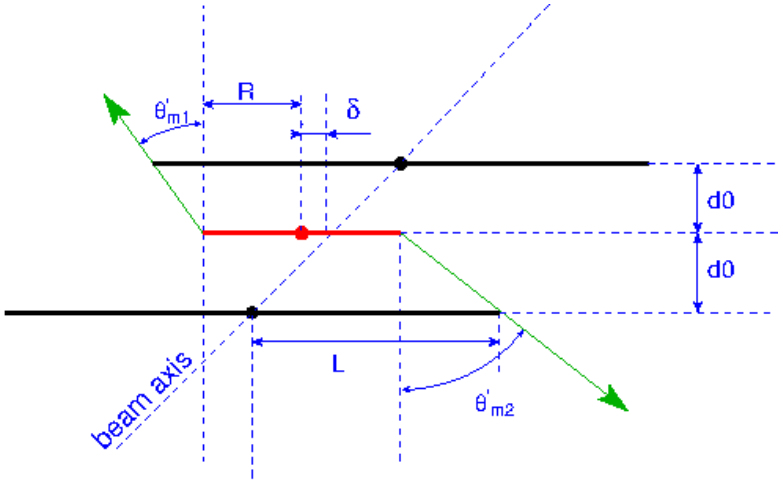

FIGURE 5.12: Top view of 2 detectors and target showing that at smal $\cos\theta'$ trajectories emitted from the edge of the target may fall outside the active area. δ is the horizontal shift of the target, R its radius, L the half length of the active area and d_0 the separation distance.

This happens for emission points at the edge of the target in the horizontal plane and for emission angles θ' relative to the perpendicular to the detectors which exceeds a threshold. This situation is depicted in figure 5.12 where the green arrows represent fission directions which are at the limit where this effect starts to show up.

The figure is a top view of a pair of detectors represented by the black thick horizontal lines, and the red thick line represents the target. The filled circles indicate the centers of PPACs (black) on the beam axis and the center of the target (red) which may be shifted by δ. L if the half length of the rectangular active area (= 10 cm), R is the radius of the circular target (=4 cm), d_0 is the target-detector distance (=2.5 cm). θ'_{m1} and θ'_{m2} are the minimal angles for which the fission trajectories may miss the active detecting area.

The efficiency associated with this geometrical limitation can be interpreted as a reduction of the visible target area for some angles $(\cos\theta',\phi')$ and it can be computed analytically.

Any trajectory is defined by its solid angle ($\cos\theta'$,ϕ'). For a given solid angle the geometrical cut is equivalent to limiting the visible area of the target as sketched on figure 5.13 The colored area is the available target area for a given fission

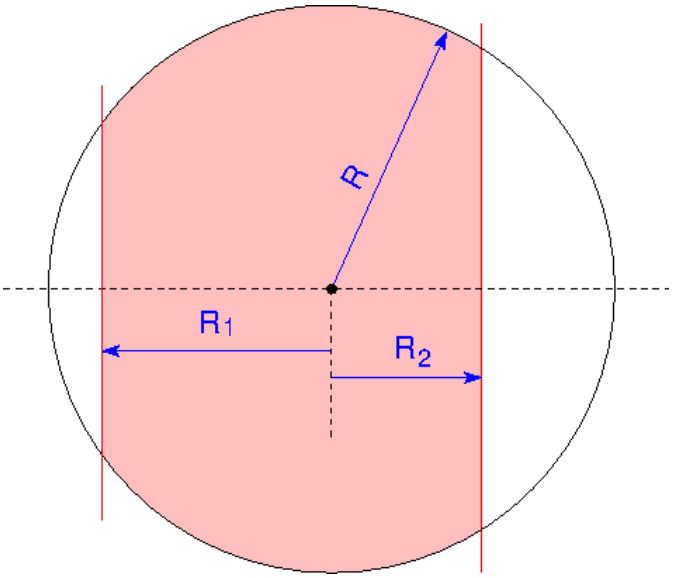

FIGURE 5.13: For a given emission direction ($\cos\theta'$,ϕ') limitation of the possible emission points on the target due to to limited detection area of the detectctors.

direction, the efficiency is the ratio of this area to the total area of the circle. The distances R_1 and R_2 depend on the fission direction and the geometrical quantities L, R, d_0 and δ.

We will first compute the colored area and its fraction to the total area denoted as: $F(x_1, x_2)$ where $x_1 = R_1/R$ and $x_2 = R_2/R$. A simple integration gives :

$$F(x_1, x_2) = \frac{g(x_1) + g(x_2)}{pi} \tag{5.9}$$

and

$$g(x) = \begin{cases} \arcsin(x) + x\sqrt{1-x^2}, & \text{if } x < 1 \\ \pi/2, & \text{if } x \geq 1 \end{cases} \tag{5.10}$$

From figure 5.12 it can be seen that:

$$\tan\theta'_{m1} = \frac{L - d_0 - R - \delta}{d_0} \tag{5.11}$$

$$\tan\theta'_{m2} = \frac{L - d_0 - R + \delta}{d_0} \tag{5.12}$$

and for a given fission direction ($\cos\theta'$,ϕ') we have :

$$x_1 = \frac{L - d_0 - \delta - d_0 \tan\theta' \cos\phi'}{R} \tag{5.13}$$

$$x_2 = \frac{L - d_0 + \delta - d_0 \tan\theta' \cos\phi'}{R} \tag{5.14}$$

The efficiency can be computed by combining the equations 5.14 and 5.10. This correction factor is computed at the same time as the solid angle of each cell in the ($\cos\theta$,$\cos\theta'$) plane, so that the calculation returns the effective solid angle $\Delta\Omega' = \Delta\Omega \times F$ for each cell.

5.2.3 Construction of the angular distributions : the general case

In section 5.2.1 we showed how the $\cos\theta'$ dependence of the efficiency is obtained by taking horizontal slices in the ($\cos\theta$,$\cos\theta'$) plane. However this method relied on the availability of an isotropic emission. In the case of anisotropic emission the ratio of 2 horizontal slices doesn't only depend on the efficiency, but also on the angular distribution because different parts of this distribution are sensed in the 2 slices.

In most of the cases we don't have available isotropic emissions either because we don't have low energy fission available (for ^{232}Th or ^{238}U) or even because we want to estimate the efficiency for energies where fission is anisotropic. Therefore we have to extend the method although we retain the same spirit. The method is based on the fact that from one horizontal slice to another one the same angular distribution is seen although in a more restricted or extended angular range. Therefore the comparison of the two bands should deliver the ratio of the efficiencies.

We start with equation 5.6 that we rewrite as:

$$N_{ij} = W(\cos\theta_i)\, \epsilon_i\, \Delta\Omega_{ij}\, F_{ij} \tag{5.15}$$

Where the N_{ij} are the counts recorded in cell (i,j) for a broad energy range where we assume that the efficiency is constant, $\delta\Omega_{ij}$ is the solid angle and F_{ij} is the cutting factor (≤ 1) of the active area of detectors. Now the angular distribution

$W(\cos\theta)$ is no more constant. As counts cover a broad energy range the angular distribution is rather smooth and can be well approximated by a polynomial in $\cos\theta$ with even terms up to order 4 (we did an a posteriori check), so that we can set:

$$W(\cos\theta) = \alpha_0(1 + \alpha_2 \cos\theta + \alpha_4 \cos^2\theta) \tag{5.16}$$

We have to define the coefficients α_0, α_2, α_4 and the efficiencies ϵ_i to reproduce as closely as possible the numbers of counts N_{ij} in the cells. This is achieved by a fit, which from equations 5.15 and 5.16, is a minimisation of the quantity:

$$\chi^2 = \sum_{i,j} \frac{\left[\alpha_0(1 + \alpha_2 \cos\theta_j + \alpha_4 \cos^2\theta_j)\, \epsilon_i\, \Delta\Omega_{ij}\, F_{ij} - N_{ij}\right]^2}{N_{ij}} \tag{5.17}$$

with $\epsilon_0 = 1$.

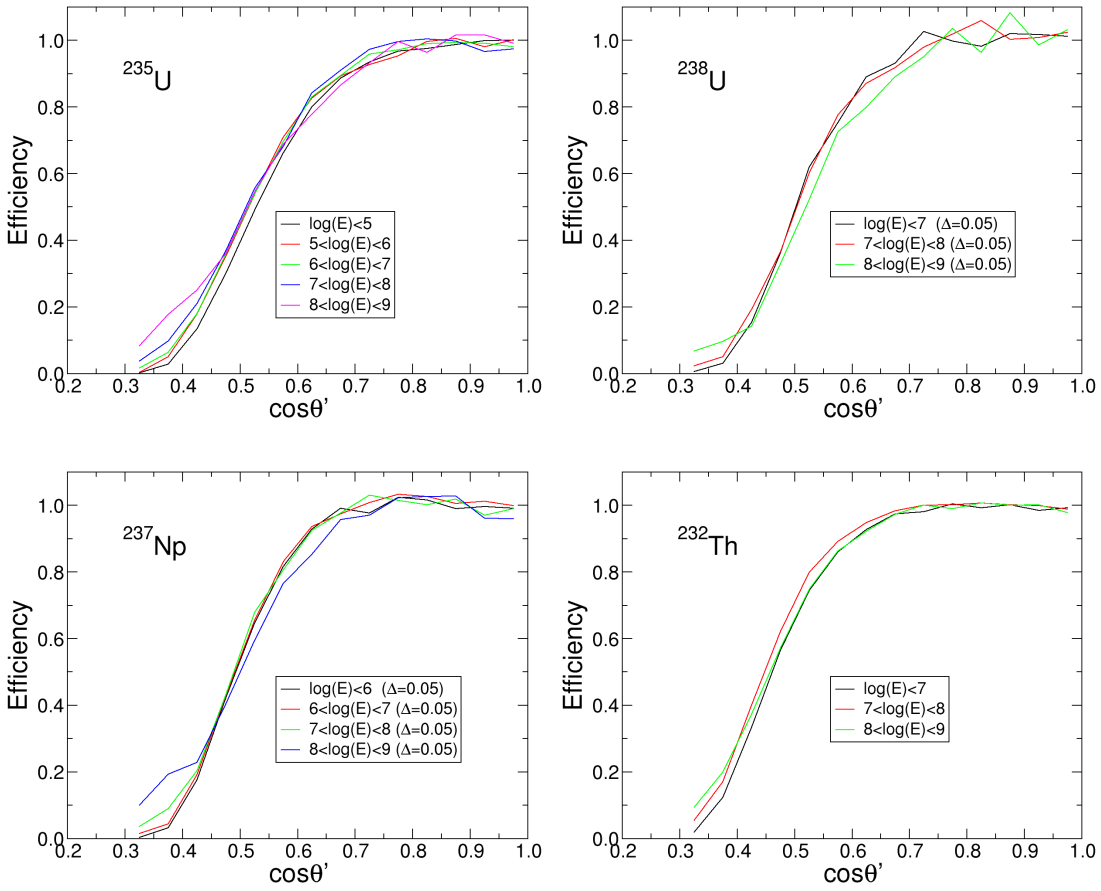

FIGURE 5.14: Detection efficiency as a function of $\cos\theta'$ for ^{235}U (top-left), ^{238}U (top-right), ^{237}Np (bottom-left), ^{232}Th (bottom-right) for different energy intervals. Horizontal slices of height $\Delta\cos\theta' = 0.05$ have been used, and the labels refer to energy intervals defined with their limits in log (E eV).

The results for the 4 samples are shown in figure 5.14. In the case of ^{232}Th the 6 targets have been summed up to get significant statistics. We observe that the angular dependence is not very sensitive to the energy. except perhaps above 100 MeV but it could be due to a mis-recognition of the localization signals at high counting rate. In all further treatments we will discard events having $\cos\theta' < 0.5$ therefore the energy dependence of the efficiency will remain small. We see that ^{235}U and ^{238}U are very similar which is expected: same backing and same chemistry to make the target. The ^{237}Np seems to have a better efficiency although the backing is the same and the amount of actinide atoms is the same too. This could be due to an oxide layer of better quality or a fission mass distribution more favorable because less asymmetric. The ^{232}Th targets have the best behavior with a long plateau at full efficiency due to their thin backing (0.7 μm).

Those efficiencies are used for reconstruction of the angular distribution. Instead of using the directly extracted values we use fits to smooth the statistical fluctuations. For this purpose we used a Fermi-like functional of the type:

$$\epsilon(\cos\theta') = \frac{1}{[1+\exp\left(a_1 1 - a_2\ \cos\theta'\right)]^{a_0}} \tag{5.18}$$

with the 3 parameters a_0, a_1, a_2 to be fitted. This functional form is able to reproduce accurately all the distributions displayed in figure 5.14 even the front and the low efficiency tail at all energies, as illustrated in figure 5.15.

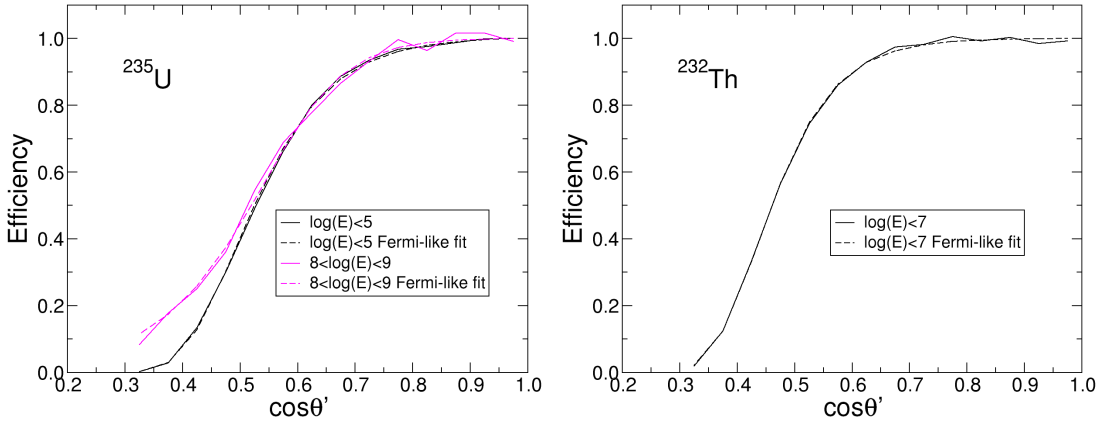

FIGURE 5.15: Comparison of the efficiency with its fit with a fermi-like functional according to 5.18 for ^{235}U (left part) and ^{232}Th (right part).

In the case of ^{235}U at low energy ($E_n < 100\ keV$) the fit of the sum 5.17 provides the values $\alpha_2 = 0.075$ and $\alpha_4 = -0.089$ for ($W(\cos\theta)$ showing that the angular distribution is almost flat, as expected because it is isotropic in this energy range.

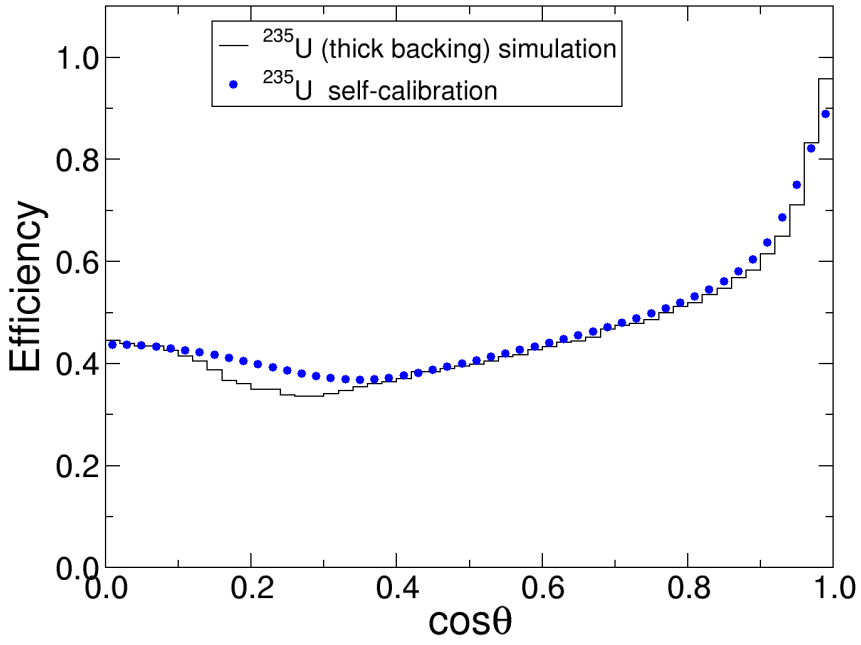

FIGURE 5.16: Comparison of the efficiency obtained from the self-calibration method and the efficiency resulting from a Geant4 simulation.

Figure 5.16 compares the $\cos\theta$ dependence of the efficiency for ^{235}U resulting from the Geant4 simulation described in section 5.1 with that from the self calibration method using relation 5.18. The agreement is good except close to forward angles and in the region around $\cos\theta$=0.2.

Once the efficiency has been determined, it is used to extract the angular distribution for any energy interval, by following the same procedure as that leading to equation 5.8 in section 5.2.1. We again use the map of counts in the ($\cos\theta$,$\cos\theta'$) plane which is partitioned in cells according to figure 5.11.

For a selected column j a first sum is performed over the counts contained in all cells above a threshold $\cos\theta'$=0.5:

$$S_{1j} = \sum_{i\,,\cos\theta'>0.5} N_{ij} \tag{5.19}$$

A second summation is performed on the same cells but with the product of solid angle, cutting factor and efficiency:

$$S_{2j} = \sum_{i\,,\cos\theta'>0.5} \Delta\Omega_{ij} \times F_{ij} \times \epsilon_i \tag{5.20}$$

As already mentioned, for ϵ_i we don't take the value given by the minimisation of 5.17 but that given by the Fermi-like function 5.18 fitted on the efficiencies delivered by the minimisation of 5.17.

The point corresponding to this column in the angular distribution is:

$$W(\cos\theta_j) = K\frac{S_{1j}}{S_{2j}} \tag{5.21}$$

where again K is a global normalizing factor depending on the definition of $W(\cos\theta)$ because W may represent different quantities each other proportional. For example W can be normalized so as to represent the differential fission cross section: $W = d\sigma_f/d\Omega$. Alternatively it can be normalized so that its integral is equal to 1 (W is a probability in this case) or the total solid angle (4π). We selected another option: we normalize W so that $W(0) = 1$ ($W = 1$ at 90°), which is convenient to obtain the anisotropy A: $A = W(1)$, and K is defined to follow this requirement.

It can be demonstrated that this procedure described by equations 5.19 to 5.21 is the one which minimizes the statistical fluctuations and all events considered as safe because they are above the threshold $\cos\theta'$=0.5 contribute to the final value with a weight related to its statistical uncertainty.

The statistical uncertainty on each point is computed as:

$$\sigma_{W_j} = K\frac{\sqrt{\sum_{i\,,\cos\theta'>0.5} N_{ij}}}{S_{2j}} \tag{5.22}$$

It assumes that the statistical uncertainty on the efficiency is negligible compared to that on the sum S_{1j}. This is justified because the efficiency is obtained on broad energy ranges involving large countings and in addition it is further smoothed through the fit 5.18.

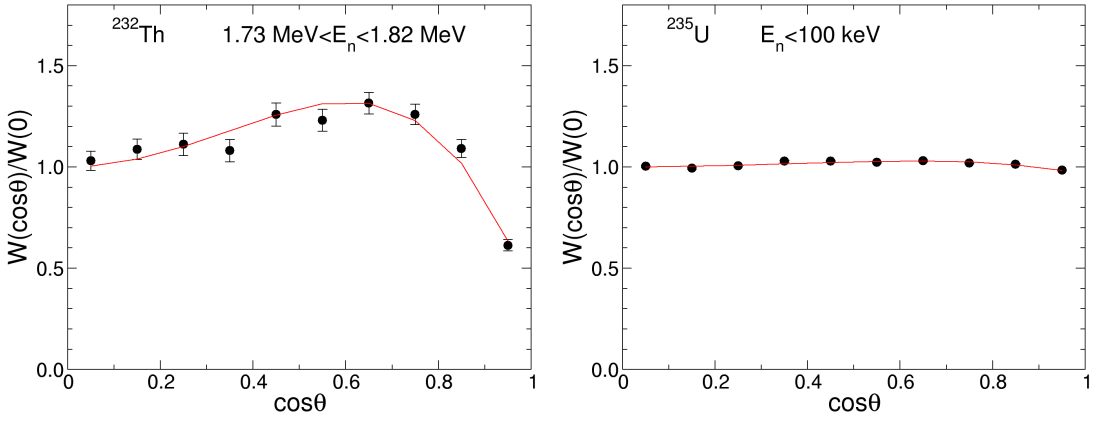

FIGURE 5.17: Left: angular distribution for ^{232}Th for a narrow energy interval about the 1.6 MeV resonance where fission is sideward peaked. Right: same for ^{235}U at low energy where the emission is isotropic, represented with the same scale. The points represent the data with the statistical error bars whereas the red curve is the Legendre polynomial fit with P_2 and P_4.

Figure 5.17 illustrates the result of this procedure for 2 selected cases: ^{232}Th in an energy range close to 1.6 MeV where the emission is sideward favored, and ^{235}U at low energy where it is isotropic.

A more extensive landscape of the angular distributions is given in appendix B.

The resulting angular distributions can be parametrized by a sum of Legendre polynomials $P_L(\cos\theta)$:

$$W(\theta) = \sum_{Leven}^{Lmax} A_L P_L(cos\theta) \tag{5.23}$$

or equivalently with polynomials of $\cos^{2n}\theta$, with $A_0 = 1$.

The anisotropy parameter is a global means of representing by how much the angular distribution departs from an isotropic one. It is defined as:

$$A = \frac{W(0°)}{W(90°)} \tag{5.24}$$

When the emission is isotropic A is equal to 1. But the distribution may be anisotropic even if A is close to 1, however is is always anisotropic if A is above or under 1.

A is taken from the polynomial fit of the angular distribution. Its statistical uncertainty is derived from the error covariance matrix on the 2 parameters adjusted

by the fit (on P_2 and P_4), and this matrix derives in its turn from the statistical uncertainty on the data points.

Chapter 6

Results and discussions

6.1 Reminder

We will use in this chapter the same notation conventions as discussed in chapter. 2.
$\overrightarrow{l}$: Orbital angular momentum.
$\overrightarrow{S}$: Sum of target and projectile spin.
$\overrightarrow{J}$: Angular momentum: $\overrightarrow{J} = \overrightarrow{l} + \overrightarrow{S}$
$\overrightarrow{M}$: Projection of $\overrightarrow{J}$ and $\overrightarrow{S}$ on the neutron beam direction.
$\overrightarrow{K}$: Projection of $\overrightarrow{J}$ on the fissioning symmetric axis.

- The angular distribution $W(J, K, M) \approx |d^J_{K,M}|^2$
- If $K \ll J \longrightarrow$: angular distribution is forward-backward peaked.
  $K \approx J \longrightarrow$: angular distribution is sideward peaked.
- If many $\overrightarrow{K}$ or many $\overrightarrow{M}$ between 0 and $\overrightarrow{J}$: angular distribution is isotropic.
- When a number of nuclear states are present at energy U:
  $W^J_{M,U}(\theta) \approx \sum_{K=-J}^{K=J} |d^J_{M,K}|^2 \exp(-K^2/2K_0^2(U))$
  U is the nucleus thermal energy: $U = E^* - B_f = a_f T^2$.
  K_0: $\overrightarrow{K}$ distribution standard deviation.
  if K_0^2 is high: angular distribution is isotropic.
  if K_0^2 is low: angular distribution is forward-backward peaked.

- if $\overrightarrow{l} = 0 \longrightarrow \overrightarrow{M} = \overrightarrow{M_s}$: angular distribution is isotropic due to the summation over M_s (de-orientation).

- $W_{neutron}(\theta) \gg W_{proton}(\theta)$?

$$B_f \propto \frac{1}{Z^2/A} \longrightarrow U \propto Z^2/A \tag{6.1}$$

where the symbol $\propto$ means "*varies in the same direction as*",

$$P_f \approx \exp(-[B_f(Z^2/A) - B_n]/T) \tag{6.2}$$

where B_f and B_n are the fission barrier and the neutron binding energy.
$K_0 \propto Z^2/A \longrightarrow W(0^o)/W(90^o) \propto \frac{1}{Z^2/A}$
and for the anistropies: $n +^A X > p +^A X$

6.2 Fission fragment angular distributions in ^{232}Th

6.2.1 Experimental results

Figure 6.1 (upper graph) presents the n_TOF ^{232}Th anisotropy measurement ($W(0°)/W(90°)$) obtained as described in the previous chapter. The results from this work are plotted in black. The high energy data plotted in purple were obtained using the method from Tarrío [4]. We also plotted previous existing data [28–38], extracted from the EXFOR library [39]. The complete angular distribution data for different energy bins are presented in Appendix B. Thanks to a fair statistics, we can keep a detailed binning across the whole energy range. Only around 1 MeV we have larger error bars: this is due to the lack of statistics below the fission threshold around 800 keV.

This work provides the first continuous coverage from the fission threshold up to hundreds of MeV. With the exception of the measurement of Hankel in the 10-20 MeV region, our data are in overall good agreement with previous measurements up to 20 MeV, including the well-explored 14 MeV region. Moving on toward the spallation region, from 20 MeV to hundreds of MeV, our data start to differ slightly from the results of Tarrío analysis. We have no clear explanation for this; however, the two sets of result remain compatible within their error bars. The discrepancies are more significant with the results obtained at Uppsala by Ryzhov [5], which

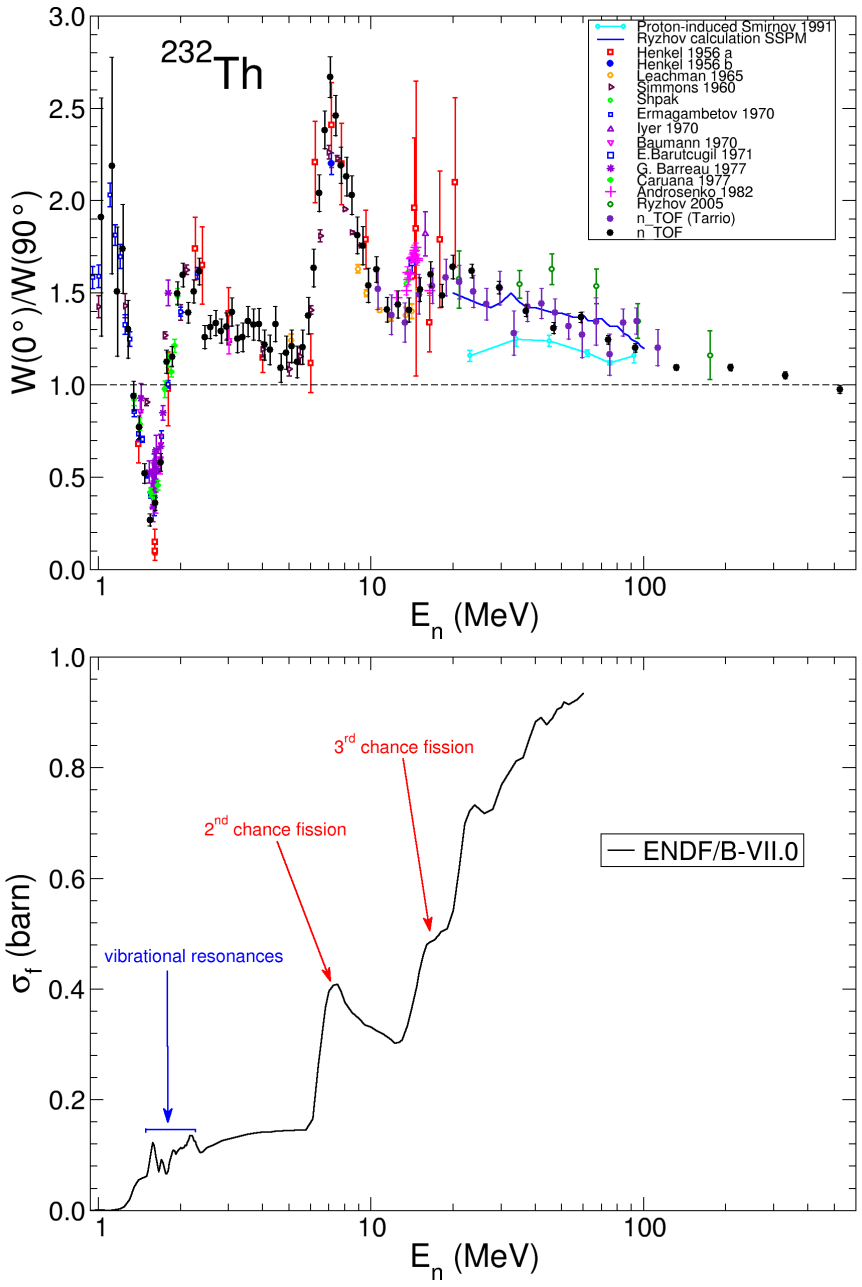

FIGURE 6.1: Upper part: ^{232}Th anisotropy, the n_TOF data are the black points and previous measurements. The lower part represents the ^{232}Th fission cross section and the successive fission chance openings.

were up to now the only ones existing for ^{232}Th FFAD in the high energy range. We will address the questions of this discrepancy and the comparison between neutron-induced and proton-induced fission below.

6.2.2 Anisotropy, fission chances and vibrational resonances

The comparison of the anisotropy with the cross section clearly illustrates the strong correlation between the value of the anisotropy and the opening of a fission chance. Each multiple-chance fission (Fig. 6.1:lower graph) corresponds to the emission of neutrons before the excited nucleus undergoes fission. For example, the second chance fission corresponds to the emission of one neutron, third chance fission, two neutrons, and so on. Each emitted neutron costs excitation energy, hence the nuclei temperature T is decreased by each emission, and K_0 becomes narrow. This explains why the anisotropy suddenly increases at the opening of each fission chance. This phenomenon is particularly visible for the second chance and at the threshold.

On the other hand, the anisotropy exhibits a sudden dip around 1.6 MeV. This small energy range corresponds to the vibrational resonances of the ^{232}Th fission cross section. They are related to the nuclear state transition from the first well of potential to the second, as previously discussed. This effect is also visible in the ^{232}Th fission cross section (figure 6.1, lower graph). In this region, only one or two high K-states are populated with $K \approx J$ and the FFAD tends to peak sideward.

6.2.3 FFAD in the spallation region : influence of pre-equilibrium and statistical neutrons

A first obvious comment is that the anisotropy remains significantly larger than 1 over a broad energy range up to 100 MeV. As discussed in chapter 2, this is an expected behavior, especially for an even-even nucleus. Although K_0 rises with the temperature it remains low compared to J due to the contribution of l which gets larger when the energy increases, hence the FFAD is forward-backward peaked.

As already pointed out, our results exhibit a moderate, but constant difference with the measurement by Ryzhov et al. However, Ryzhov also made a significant theoretical effort by calculating ^{232}Th and ^{238}U angular distributions with SSPSM, a standard saddle-point statistical model combined with pre-equilibrium and Hauser-Feshbach calculations of partial fission cross sections. Being a statistical model, it is well-suited to situations in which the density of transition states is large, i.e. moderate or large excitation energies. Conversely, it is not expected to

describe correctly the behavior of compound nucleus with excitation energy just above a fission barrier or in the vibrational resonances region.

An important ingredient of this calculation is the accounting for the pre-equilibrium emission of nucleons. Each emitted neutron carry away a significant amount of energy and tends to "wash out" the final anisotropy due to its random emission direction. The estimation of the role of the pre-equilibrium stage remains difficult as the emitted particles can be responsible for significant changes of J,M, and U.

The calculation of the angular distribution for a fissioning nucleus of given quantum numbers J, M, Z, A and excitation energy at the saddle point U is given by:

$$W^J_{M,\,U}(\theta, Z, A) \sim \frac{2J+1}{2} \sum_{K=-J}^{K=J} \left|d^J_{M,K}(\theta)\right|^2 \exp\left(K^2/2K_0^2(U, Z, A)\right) \tag{6.3}$$

The final angular distribution is obtained by summation over the individual $W^J_{M,\,U}$ fissioning contributors, weighted by their probability to be formed and to end up with fission. In this procedure the statistical emission of neutrons prior to fission is properly taken into account. For the formation of the fissioning nuclei, in addition to the compound nucleus formation the preequilibrium channels (n,n'), (n,$2n$), (n,p) and (n,np) are explicitely included.

As it can be seen in figure 6.2, the pre-equilibrium neutron emission (n, n') does not play an important role at low energy, but in the tens MeV region and beyond, it becomes decisive. Note that this figure displays the results of a calculation on ^{238}U.

The anisotropy have been calculated using the simplified expression:

$$\frac{W(0^o)}{W(90^o)} - 1 = \frac{< J^2 >}{4K_0^2} \tag{6.4}$$

with K_0^2 given by 2.23.

Following the pre-equilibrium phase, an evaporation stage may also take place before the fission occurs. In this case, a variable number of neutrons are emitted (protons may also be emitted in the case of a very energetic collision), each carrying away 7-8 MeV. An important difference with respect to pre-equilibrium neutrons is that they mostly carry $0.5\hbar$, resulting in a very limited change of J and M. The

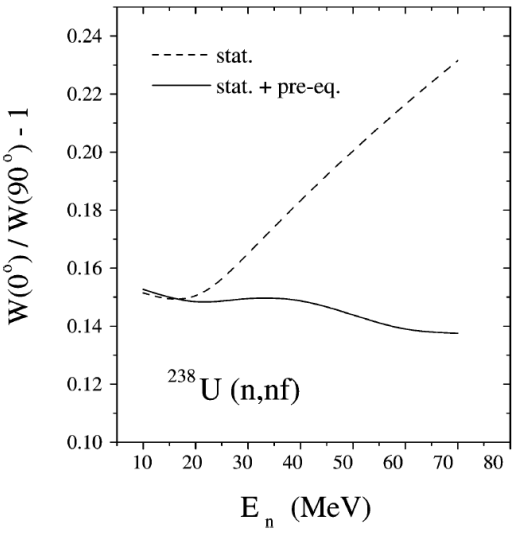

FIGURE 6.2: ^{238}U anisotropy calculations with and without the inclusion of a pre-equilibrium model [5].

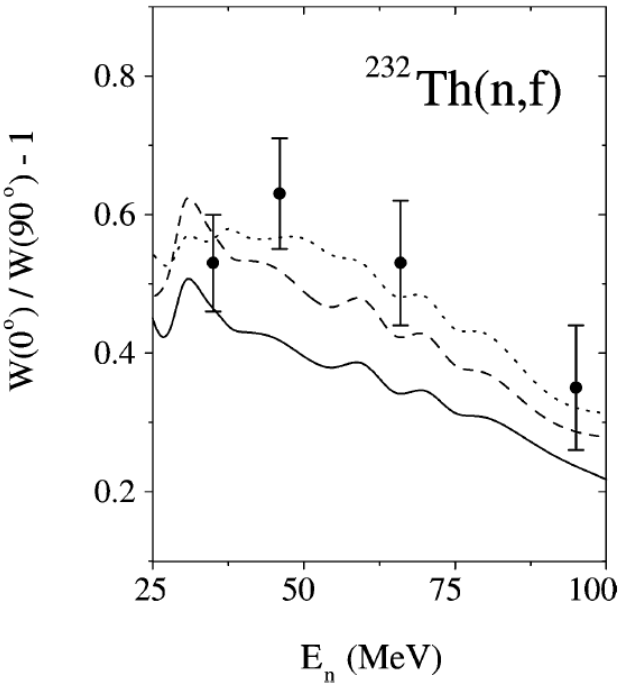

FIGURE 6.3: Comparison of ^{232}Th FFAD (points) and SSPSM model (solid line) and within the effect of 30% reduction of K_0^2 (dashed line), from [5].

resulting cooling of the prefragment leads to a decrease of K_0^2, hence increasing the forward anisotropy.

As can be seen in figure 6.3, which compares Ryzhov's measurement on ^{232}Th and the SSPSM calculation (continuous line), accounting for both the pre-equilibrium

and equilibrium phases does not lead to a satisfactory reproduction of the experimental results. A possible way to reach a better agreement consists of reducing arbitrarily K_0 in the case of neutron-deficient isotopes. Around 30% reduction tested by Ryzhov leads in the right direction (dashed line in figure 6.3), but still the calculation underestimates the anisotropy.

It is however worth pointing out that, as our data are significantly below Ryzhov's, this theoretical calculation is reasonably consistent with our data, within its systematic error. This is illustrated by fig 6.4.

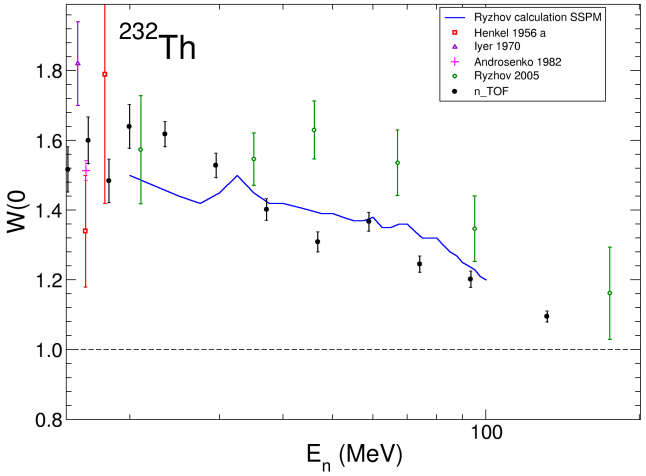

FIGURE 6.4: Comparison between n_TOF data, Ryzhov data and Ryzhov SSPSM calculation (without reduction of K_0^2).

6.2.4 Comparison with proton-induced ^{232}Th fission

Proton-induced fission is another way to compare FFAD at high energies. Tutin [1] compared neutron- and proton-induced FFAD in order to evaluate the reliability of the Ryzhov data. At high energy (GeV region), the incoming nucleon can't be stopped and captured in the target, after having deposited some of its energy in the nucleus it escapes quickly. This phenomenon explains the saturation of the linear momentum transfer. After this quick step the excited nucleus undergoes fission. In other words, the fission should be independent of the incident nucleon. Nevertheless, the lower limit of the energy range where this process is dominant is not well known. Fig.6.5 shows the difference between Ryzhov neutron data and Smirnov proton data [6], which are well representative of the trend of proton measurements from [40–42]. The proton anisotropy is always lower than neutron-related one below 100 MeV, as already noticed by Tutin [1]. Such a difference leads

to consider that the fissioning nuclei in the case of proton- and neutron-induced fission are still different and the incoming nucleon has a large probability to be captured even in the intermediate energy domain, although some preequilibrium emission is present.

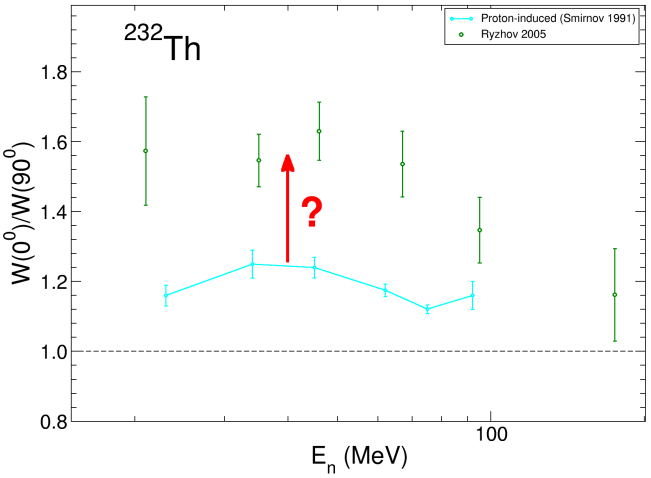

FIGURE 6.5: Comparison between neutron-induced anisotropy from [5] and proton-induced anisotropy [6].

Previously, Eismont [7] had proposed a similar comparison in the intermediate energy range (tens of MeV) for actinide and subactinide nuclei. Indeed, Eismont pointed out that in this energy regime the fission ansisotropy depends mainly on the fissility parameter Z^2/A of the compound system, regardless of the type of incoming nucleon (proton or neutron).

This notion can be understood according to the formulas given at the beginning of this chapter. If the fissility of the fissioning nucleus increases its fission barrier decreases. As a consequence the available thermal energy U at the saddle point increases, and the temperature too (equation 2.21). Due to the temperature dependence of K_0^2 given by 2.23, K_0^2 increases and the anisotropy fades out. If one assumes that the incoming nucleon is captured by the target to form a compound nucleus the fissility of the system $p+^X$A is higher than that of $n+^X$A therefore one expects a higher anisotropy in the latter case.

The fissility systematics of the anisotropy from different projectile-target combinations is displayed in figure 6.6 taken from [7], showing the expected fissility dependence. The differences showing up for projectiles of different masses can be explained by an incoming angular momentum which rises with the projectile mass.

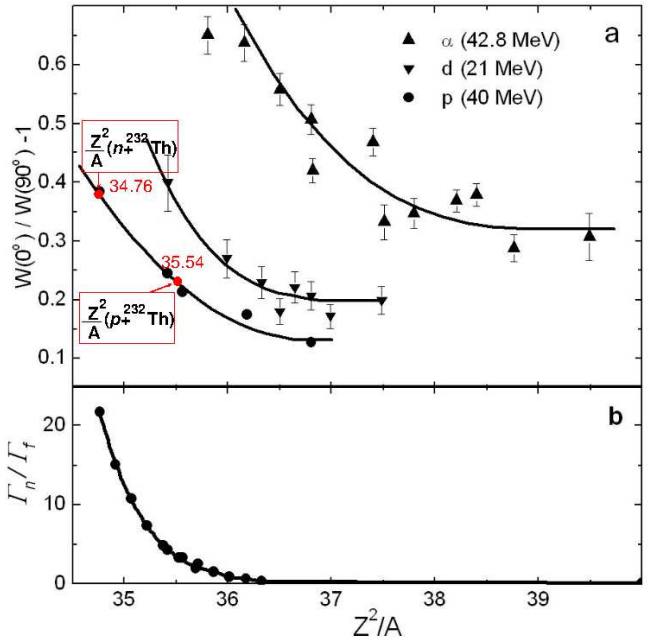

FIGURE 6.6: The dependence of anisotropy coefficient for fission induced by p, d and α-particles with different targets. The curves are fits of the experimental data, from Eismont et al. [7].

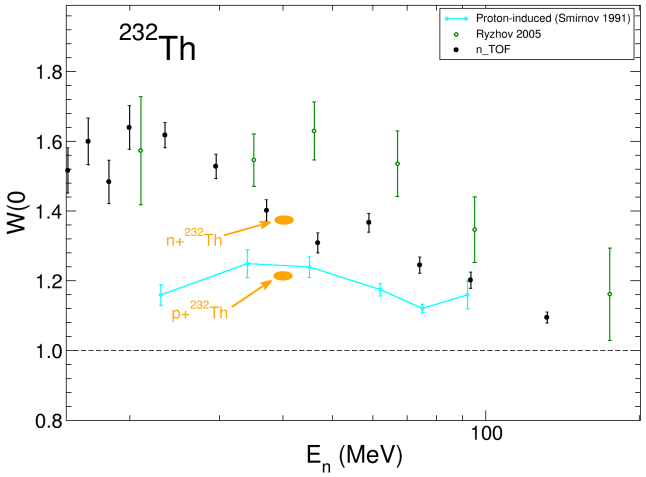

FIGURE 6.7: ^{232}Th anisotropy with Ryzhov data, n_TOF data and proton-induced data from Smirnov [6].

From the above statements, it has been proposed that the anisotropy of actinides in neutron-induced fission could be directly compared to results of proton-induced reactions, providing a correction accounting for the different values of the Z^2/A of the compound nucleus is applied. In particular for a given target, the anisotropy of neutron-induced fission is expected to be systematically higher than for proton-induced fission.

In the case of ^{232}Th reactions, the fissility parameter is 35.54 for proton-induced

reaction and 34.76 for neutrons. Using figure 6.6 for nucleons at 40 MeV one can evaluate the impact of this change of the fissibility parameter on the anisotropy. The two red points on the figure correspond to p+Th and n+Th fissility parameters. As a conclusion the systematics gives the respective anisotropies: 1.21 and 1.37.

Now we can carry those predicted values at 40 MeV in the plot of the measured anisotropies. This is done in figure 6.7. We see that they match the proton data as expected because the systematics is partially built on those data. They match also the n_TOF neutron data whereas the Ryzhov data lie at much higher values. The deviation between Ryzhov and the proton data is almost 0.4, twice the expected value. The difference between this work and proton data is 0.2, in very good agreement with the prediction of the systematics.

This bears a strong implication on the reaction mechanism: this agreement is based on the fact the fissioning nuclei are different in proton- and neutron-induced fission. It means that at 40 MeV most of the time the incoming nucleon is captured by the target so that its nature is retained by the compound nucleus. This doesn't rule out any preequilibrium processe but this says that these processes should be small or at least very similar in both cases. Such an outcome is consistent with the fact that the linear momentum transfer in nuclon-induced reactions starts to depart from the full deposit only at about 30-40 MeV.

Beyond 100 MeV the difference between protons and neutrons vanishes progressively. Indeed, with higher energies, the hypothesis of projectile stopping is less and less valid and the pre-fragments resulting from this fast reaction, including preequilibrium emission, are the same for incoming proton and neutron. Hence the anisotropy factor is less and less dependent on the fissibility parameter of the target+particle system. In addition the anistropy converges to 1 (isotropy) because of the increase of K_0^2 through the temperature whereas J stays constant due to to the leveling off with energy of the transferred angular momentum.

6.3 FFAD of other actinides

Although with much less statistics, we have also obtained FFAD for other actinides: ^{238}U, ^{235}U and ^{237}Np. In spite of the poor statistics, we can still observe some interesting behavior in these data.

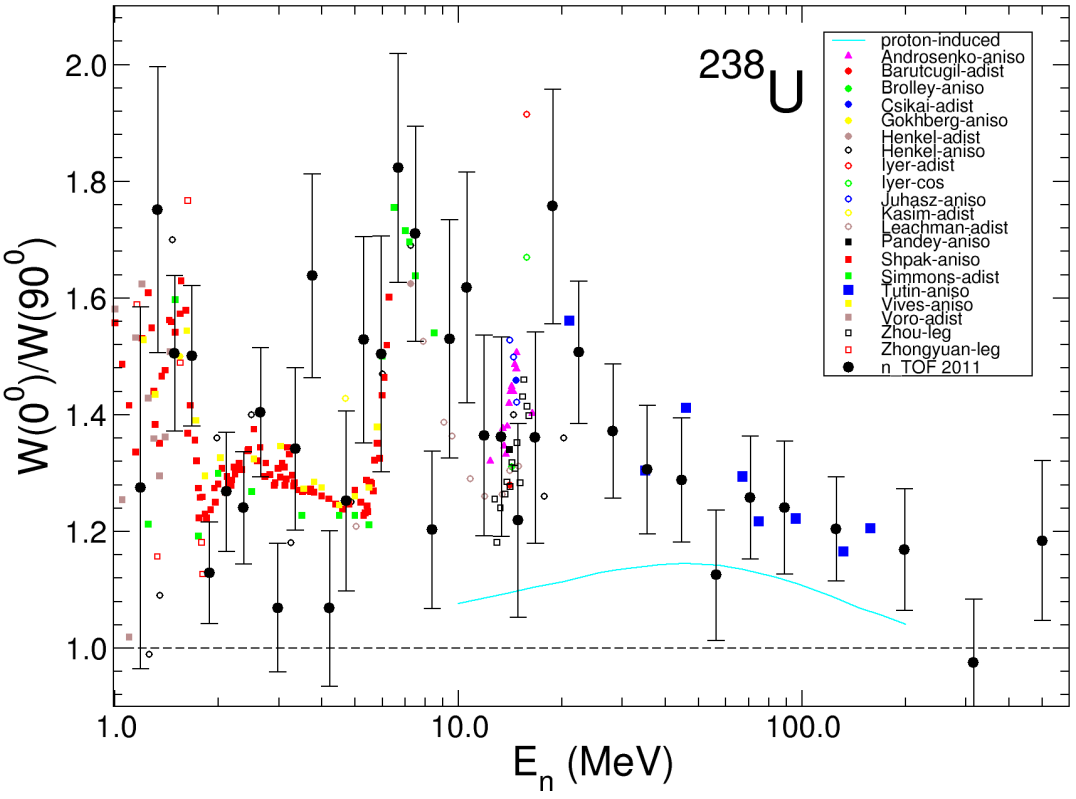

FIGURE 6.8: ^{238}U anisotropy with the old measurements, n_TOF data and proton induced data

Data for ^{238}U are presented in figure 6.8. They are in good agreement with previous measurements [1, 5, 32–35, 37, 43–55]. On this figure, one can clearly identify the large anisotropy due to the second and third chance fission. For this nucleus the agreement is also good with the Ryzhov data, except for a point near 50 MeV, but it may be due to the statistical error.

It is worth pointing out that Ryzhov also calculated ^{238}U FFAD with the SSPSM code. The calculation predicts a smoothly decreasing anisotropy in the high energy range, in good agreement with the measurements, as shown in fig. 6.9. Just as in the case of ^{232}Th, our data and Ryzhov's and the proton-induced anistropy converge in the high energy range, confirming the vanishing of the fissility dependence above 100 MeV.

Results for ^{235}U are presented in figure 6.10, along with previous measurements [32, 33, 33, 35, 37, 49, 56–60]. FFAD from ^{235}U are completely isotropic below 1 MeV, as shown in appendix B. Above this energy, as l increases, the forward-backward direction is favored, so the anisotropy increases as illustrated in fig. 6.10. Nevertheless, the intrinsic spin of ^{235}U is large (7/2), so there are many M contributing

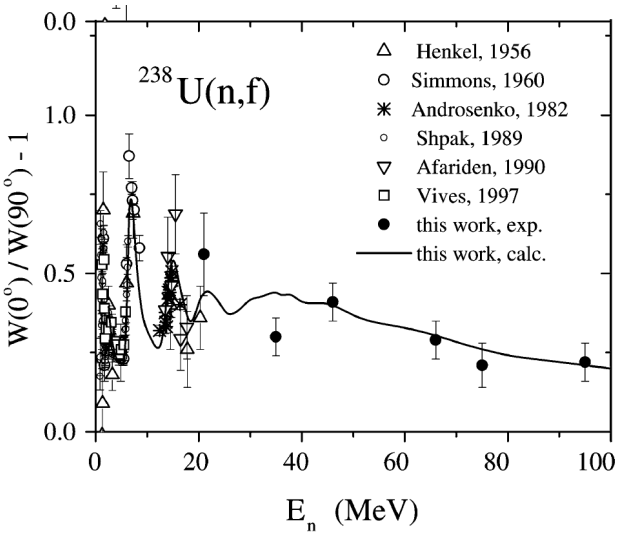

FIGURE 6.9: ^{238}U anisotropy calculated with SSPSM by Ryzhov.

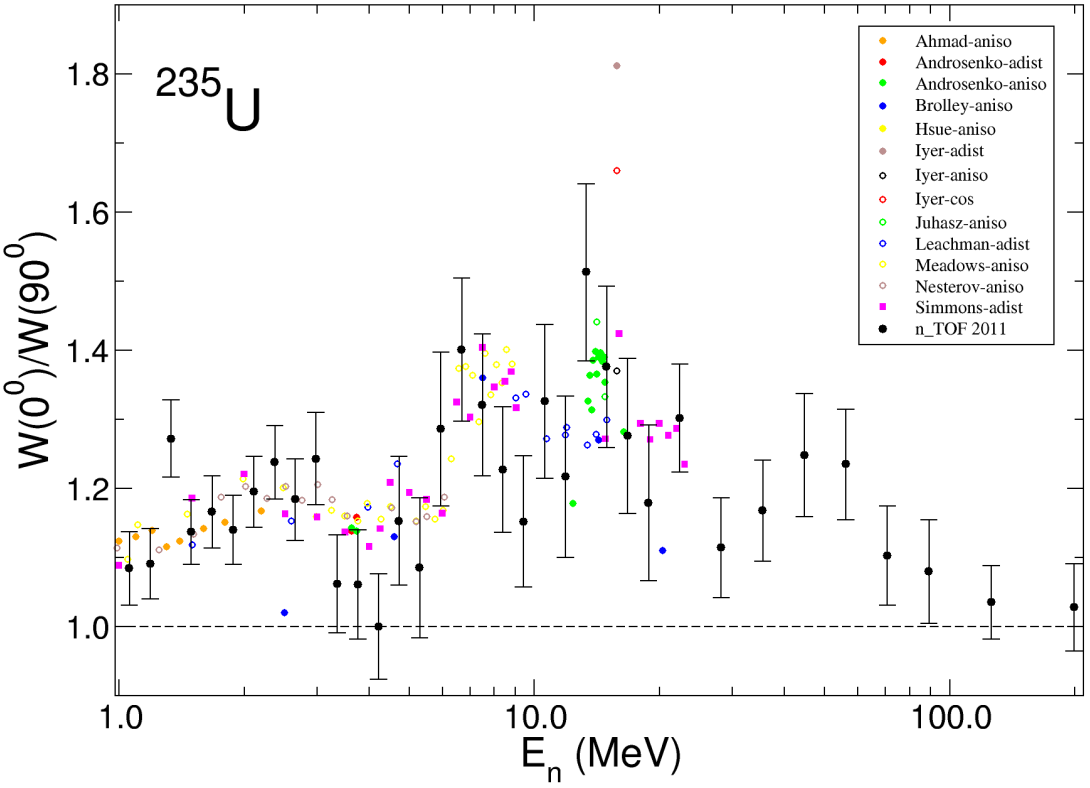

FIGURE 6.10: ^{235}U anisotropy with the old measurements

by the spin (unpolarized target). Hence the anisotropy is much more lower than in the case of an even-even nucleus.

The same remark applies to the ^{237}Np data [32, 33, 35–37, 47, 61] shown in fig. 6.11. It is not easy to to draw conclusions from the data as the error bars are particularly large. Still the signature of the second and third chance fission are

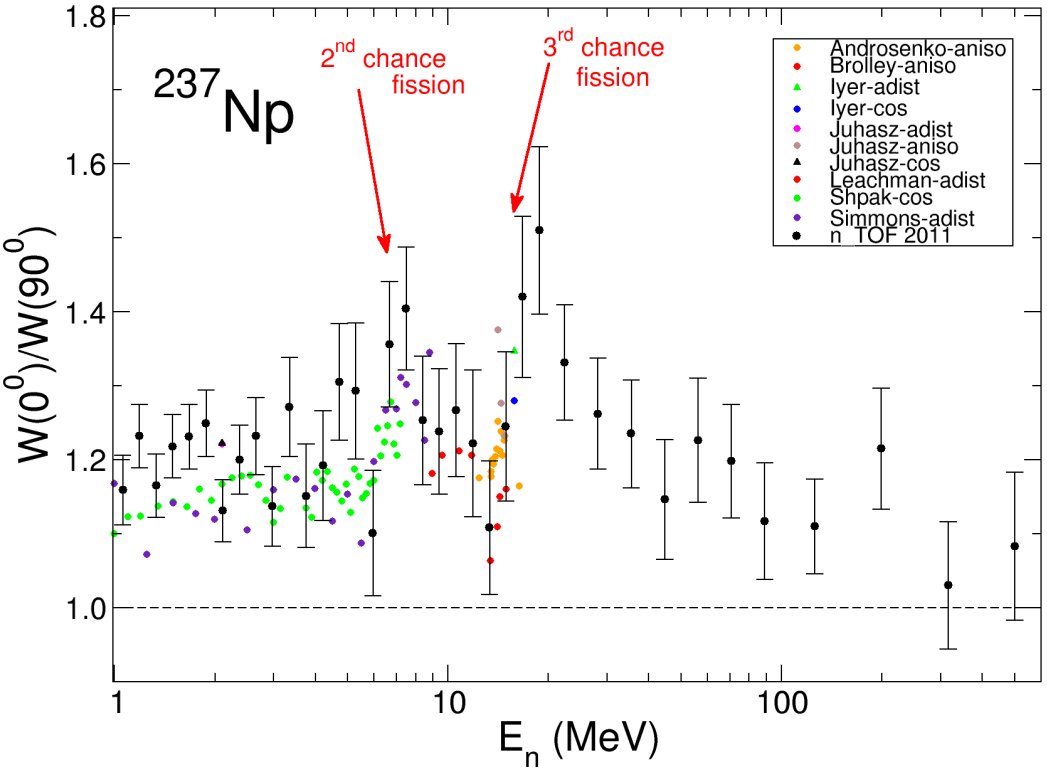

FIGURE 6.11: ^{237}Np anisotropy compared to the existing data

clearly visible in figure. 6.11. A remarkable result is that the anisotropies for the second and third chance fission have very similar values. A more general remark is related to the even or odd mass targets. For the even-even targets, the anisotropy at the second opening chance fission is always higher than at the third opening chance corresponding anisotropy. For the odd-mass targets, both anisotropies, in second and third opening chances, are very similar. This is the first time that this phenomenon has been observed and opens interesting perspectives for the study of the ^{237}Np structure. However this has to be confirmed as the statistical error bars are large.

Chapter 7

Criticality experiment

Fission cross sections have been measured in the recent past in the n_TOF collaboration, with ionization chambers and also by the coincidence method with PPACs, by using the fission of ^{235}U as a reference cross section. In the latter case for several isotopes as ^{238}U, ^{233}U, ^{234}U a good agreement with older measurements was obtained. However in the case of ^{237}Np a significant mismatch showed up and we attempted to find a means to test or validate the fission cross section of this isotope.

One possible way to do it is to use a critical experiment involving a large amount of ^{237}Np so that the criticality depends on its fission cross section. The other possibility is to analyze experiments where a ^{237}Np sample is subjected to a known or well simulated neutron flux. The measured fission rate is directly linked to the fission cross section.

It is the purpose of this chapter to describe such integral experiments involving ^{237}Np samples and to analyze their results when different cross section sets are used as input in the simulation of the experiments.

7.1 Status of ^{237}Np fission cross section

^{237}Np is a highly studied isotope in the field of nuclear data mainly because it is abundantly produced in nuclear power plants and for its long half-life of 2.1 My. Its production quantities depends on many parameters: neutron spectrum, type

of fuels, burn-up, etc...

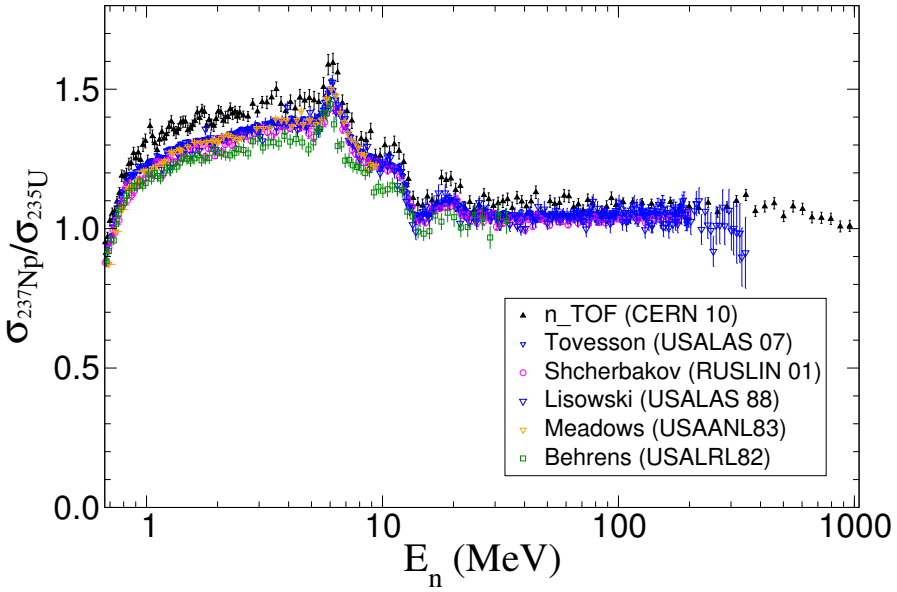

FIGURE 7.1: Comparison of different ^{237}Np fission cross sections measured relative to ^{235}U.

Several experiments based on the time-of-flight technique were dedicated to the measurement of ^{237}Np cross section. Several mono-energetic measurements also exist, specially close to 14 MeV, but we list below those which cover a larger neutron energy range. Meadows [62] measured ^{237}Np (n,f) from 1 to 10 MeV in Argonne Fast Neutron Generator (FNG) laboratory. Later, Lisowski [63] measured the cross section in Los Alamos Meson Physics Facility (LAMPF) covering a broad neutron energy range from 1 to 400 MeV. Then Shcherbakov [64] performed another measurement at the Gneiss neutron source in Gatchina. More recently, Tovesson measured this cross section at Los Alamos Neutron Science Center, covering both subthreshold [65] and above threshold fission from 100 keV to 200 MeV [66]. A comparison of the results from the above-mentioned experiments is displayed in Fig. 7.1 as a ratio to the fission cross section of ^{235}U. Within the experimental uncertainties, all these data are consistent with each other, except the Behrens measurement [67].

^{237}Np fission cross section has recently been measured by Paradela with PPACs at the n_TOF facility at CERN [68]. In fact, Paradela ^{237}Np measurement showed, contrary to the previous data, a significant discrepancy on his ^{237}Np(n,f) cross section when compared to some older data sets.
The n_TOF data exhibit values higher by about 5-7% above 1 MeV (Fig. 7.1)

against data sets which are consistent within the estimated uncertainty, and the mismatch is well beyond the uncertainty on the evaluated cross section, about 3-4%.

7.1.1 Remarks on the experimental status

The majority of ^{237}Np fission cross section measurements are based on ionization chambers whereas the n_TOF experiment is based on the coincidence method with PPACs.

In the range of a few MeV ionization chambers are very well suited because the fission process dominates and the only source of background is the α radioactivity. In the case of ^{237}Np it's moderate and can be removed by amplitude discrimination. The main advantage of such detectors is their high efficiency close to 96% so that the efficiency correction is highly reliable.

As already explained in previous chapters the PPAC setup has a high capability of selecting fission reactions, but on the other hand the efficiency is close to 50% so that a careful correction should be applied, depending on the backing thickness. The ^{237}Np experiment used the previous set-up (we called it Phase I), slightly different from the set-up for FFAD (Phase II) measurements. The PPAC detectors in both set-up are the same and have been already described in the previous chapters, put the detectors and targets' position are different. The Phase I PPAC stacked perpendicularly to the neutron beam direction and differ from the Phase II chamber where PPACs were titled by 45° against the beam direction. Beside this geometrical modification, the gas circulation system and electronics are the same.

The n_TOF Phase-I PPAC set-up, contains four ^{237}Np targets, three made with a CEA sample and one with material provided by Geel. Both contain a tiny contaminant of ^{241}Am but at a different level.

Targets have been well characterized in chemical composition by RBS, in total amount by α-counting, in homogeneity by α-scanning and the aluminium backing thickness has been probed by the energy loss of the α's emitted by the radioactive layer.

This seemingly singular behavior of the n_TOF measurement might shed some doubt on its validity. However two arguments indicate that it's not really the case:

- In the n_TOF measurement 4 ^{237}Np targets were in place with 2 different origin and levels of purity. The 4 targets deliver the same fission cross section within 2%.
- One should be aware that several of the previous results are not independent because they have been re-normalized to older ones at some energy as the number of atoms in the targets was unknown (we recall that in the PPAC case the targets are fully characterized). For example in Tovesson's measurement the cross section has been normalized to the ENDF/B-VI.8 nuclear data at 14.8 MeV. This evaluated data file is based on Lisowski's measurement which was normalized to Meadows' data over the 1 to 10 MeV energy range. Therefore the consistency of several experimental data sets, and of the derived evaluated libraries, is in the first place a consequence of these normalizations. And it is worth noting that most of the existing results around 14 MeV, obtained in mono-energetic beam experiments, are not consistent with the ENDF/B-VI.8 value [69].

The above findings show that the status of the ^{237}Np fission cross section is unclear and dedicated integral experiments would help lift the veil. We start with a critical experiment with a ^{237}Np ball involving neutrons with a mean energy around 1 MeV well suited to probe the observed discrepancy between the fission cross sections.

7.2 The critical ^{237}Np benchmark

The principle of the experiment is to assemble a sufficient quantity of fissile material so that criticality is reached. The exact geometrical configuration where this point is attained depends on the cross sections. A comparaison of the real situation with a simulation involving the supposedly known cross sections gives information on the accuracy of those cross sections.

The experiment has been performed at Los Alamos and it is fully described in all detail [70]. It consisted of a spherical-like assembly made of a ^{237}Np sphere surrounded by a spherical shell of Highly Enriched Uranium (HEU) in which the

neutron multiplication factor k_{eff} is measured with an accuracy of 0.36%. Actually k_{eff} is an integral quantity depending on many neutron reaction parameters; however many of them are accurately known, and its sensitivity to the ^{237}Np fission cross section is large enough (150pcm/%) to get a relevant test.
Thus the fission cross section check is based on the comparison of k_{eff} calculated by simulation by using the MCNP code which permits to have a very precise k_{eff} and the experimental one that will be shown in next section. Even if the criticality experiment cannot be considered as a definitive test, due to its integral nature, it is a good indicator of the reliability of the ^{237}Np(n,f) cross section.

7.2.1 MCNP code

MCNP (Monte Carlo N Particles) is a particle probabilistic transport code, for neutrons, electrons and photons. It has been developed at LANL (Los Alamos National Laboratory) [71]. For all isotopes, the neutron energy extends from 10^{-11} MeV to 20 MeV in the code library. All tri-dimensional configurations can be implemented to simulate realistic geometries. MCNP is a static transport code, it means that no evolution of the materials by nuclear reactions during the transport process is taken into account. In addition the interactions between the transported particles are neglected.
MCNP permits to calculate the reaction rate and flux at every position and also the global multiplication coefficient k_{eff}. We firstly build the input file and provide the input information (geometry, energy, cross sections and neutron number) and a file ("xsdir") which contains the evaluated cross section data in all needed materials. With the given neutron generations and cycles, MCNP transports the neutrons and follows them with calculation of different tallies requested by the user until the end of all the cycles.
A code MURE which has been developed by IPN Orsay and LPSC Grenoble [72] can solve the problem of inventory evolution. We did not use MURE for this evolution capability but only because it offers a user-friendly way to describe the geometry which is then translated to the final MCNP geometry description.

7.2.1.1 Principle of the Monte Carlo simulation

The particles followed by the simulation are supposed to be representative of the real particles, but as their number is much lower they limit the statistical uncertainty of the method.

The simulation starts with a given number of initial neutrons which are followed individually until their disappearance through nuclear reactions. The neutrons produced in those reactions, called second generation neutrons, are followed in turn until they disappear too. The neutrons of the third generation are then followed and so on. The calculation stops when all neutrons died or when the maximal number of cycles has been reached. One cycle corresponds to all the neutrons being followed until their disappearance in each generation.

In the case of a critical medium this algorithm has to be modified because the number of neutrons increases exponentially with the cycle number and the execution time grows accordingly, so that the number of cycles remains limited. This is a drawback because a large number of cycles is needed to probe all the locations of the critical medium. This problem is solved by following the same number of neutrons at each cycle. If the number of neutrons produced at the end of a generation exceeds that fixed number, some neutrons are dropped randomly. Conversely if it's lower some neutrons are cloned randomly. The scaling factors are recorded as they allow to calculate k_{eff}. This mode is called Kcode, by contrast with the normal mode called Ksource, and it is well suited for critical systems. We used the Kcode mode to compute the critical assembly with ^{237}Np. Several inactive cycles are used at the beginning, without recording any quantity, in order that neutrons be produced proportianally to the eigenmodes: the neutrons have to explore the full multiplicating medium to be representative of the real system. After those starting inactive cycles the cycles become active and the physical quantities are scored with the tallies.

When a neutron is followed inside a medium several tests are done in order:

- If the neutron interact with the material.
- Which material the particle interact with.
- With what type of reaction.

- What are the secondary emitted particles.

At a given energy, the particle mean free path $\lambda(E)$ is calculated as:

$$\lambda(E) = \frac{1}{\sum^{tot}(E)} \tag{7.1}$$

where $\sum^{tot}(E)$ is particle-material macroscopic total cross section expressed by:

$$\sum^{tot}(E) = \sum_{nucleusi} N_i \sigma_i^{tot}(E) \tag{7.2}$$

N_i is the density (number of atoms i per cm^3). The interaction distance $l(E)$ is taken as:

$$l(E) = -\lambda(E) ln(1-p)$$

$p \in [0;1[$is an uniform random number. When a collision takes place the type of reaction occuring is obtained by random drawing over the cross sections of the different processes (fission, scattering, capture, (n,2n), etc...).

7.2.1.2 Geometry

The MCNP geometry is defined with three main parts: surface, material and cell.

- Different surfaces are available: infinite planar surface, cylinder surface, sphere surface or cone surface...

- We can define all compositions which data cross section exist in libraries. (JEFF, ENDF, JENDL, etc...)

- At the end, we define each cell as a volume delimited by surfaces and containing materials.

7.2.1.3 MCNP tally

A tally is an indication given to the code to score a physical quantity inside a cell, over a surface or globally: neutron flux, reaction rate, number of neutrons crossing

a surface, effective cross section, etc... All quantities are normalized to 1 neutron source.

Flux

When following individual neutrons the flux in a given volume V is scored from the length travelled by the neutrons in the volume. If $L(E)$ is this travelled length for a neutron of energy E, its contribution to the flux at energy E is:

$$\Phi(E) = \frac{L(E)}{V} \tag{7.3}$$

This contribution is expressed as neutron/cm^2 as there is no time coordinate in MCNP.

When summing over all the simulated neutrons the flux is normalized to the number of initial source neutrons N_S. While k is the number of the neutrons travelling at energy E_k, the total flux in the volume is:

$$\Phi_C(E_k) = \frac{1}{N_S} \frac{\sum_k L(E_k)}{V} \tag{7.4}$$

The flux is expressed in neutron/cm^2/source neutron.

Reaction Rate

Reaction rates could be in principle estimated from the simulated interactions but it's not a good method because if the cross section is low the number of simulated interaction going to the corresponding channel is low and the estimation is spoiled by a large statistic uncertainty. A much better method consists of computing the reaction probabiliy along the neutron trajectory and sum up all the contributions. The probability for a neutron to trigger the reaction type i on a nucleus of type j when travelling the length L in the cell of volume V is:

$$< P_i^j >= L\, \sigma_i^j\, N_j \tag{7.5}$$

Therefore the reaction rate normalized to 1 neutron source and 1 target atom reduces to:

$$< \sigma\Phi >_c^{i,j} = \frac{1}{N_S} \frac{\sum_k \sigma_i^j(E_k) l(E_k)}{V} \tag{7.6}$$

Mean cross section

The mean cross section is also always used for cross section validation and it is

defined as the average of the reaction rate over the energy, and it can be considered as an effective cross section independent of the energy. By definition:

$$< \sigma >_i^j = \frac{\int < \sigma\Phi >_c^{i,j} \, dE}{\int \Phi_c \, dE} \tag{7.7}$$

7.2.2 The composite critical experiment

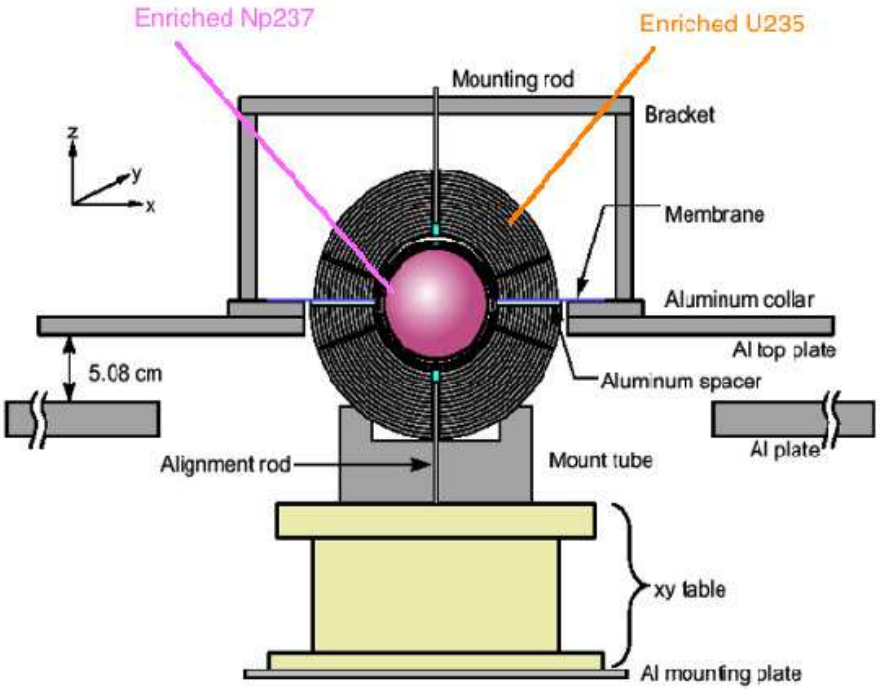

FIGURE 7.2: Overall scheme of the composite (^{237}Np and HEU) assembly in compact configuration.

A critical experiment with a composite assembly associating neptunium and HEU has been conducted at Los Alamos with the aim of better defining the critical mass of ^{237}Np [73]. This experiment is based on a ^{237}Np sphere surrounded by nested hemispherical shells of HEU, as sketched in Fig. 7.2, so as to reach criticality in compact configuration of the system. The neptunium sphere was 8.29 cm in diameter and weighed 6070.4 g. To reduce the radiation exposure to the experimenters, the ^{237}Np sphere was cladded with a thick layer of tungsten and two layers of nickel and it weighed 8026.9 g. To accurately determine the HEU mass to reach criticality at the beginning they were added layer by layer and the approach to criticality was controled by measuring the number of neutrons coming out of the assembly with four BF_3 detectors. Those neutrons were the result of the multiplication of neutrons emitted by an internal source (spontaneous fission

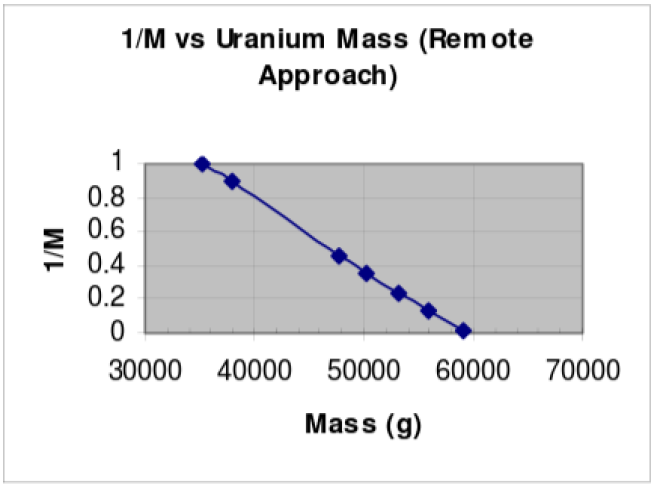

FIGURE 7.3: Determination of the critical mass by extrapolation of the inverse of number of detected neutrons.

of ^{240}Pu impurity in neptunium). If k_{eff} is the average multiplication factor at every generation the number M of detected neutrons is:

$$M = \epsilon(1 + k_{eff} + k_{eff}^2 + k_{eff}^3 + ...) = \frac{\epsilon}{1 - k_{eff}} \implies \frac{1}{M} = \frac{1 - k_{eff}}{\epsilon} \tag{7.8}$$

where ϵ is the efficiency of neutron detectors. From the above equation it's easy to see that $1/M$ crosses the 0-axis ($M = \infty$) at criticality. This indicates the way to approach criticality: after each added layer of HEU the neutron number is measured and $1/M$ is plotted against the total added mass as illustrated in figure 7.3. The mass for criticality is obtained by extrapolating the line to the horizontal axis and it amounts to 62.555 kg of HEU [73].

^{237}Np is less fissile than ^{235}U due to its threshold, so that only fast neutrons of energy higher than 0.6 MeV can trigger fission. Furthermore ^{235}U contributes to 85% of the fissile mass. Yet 13% of the fission occur in the neptunium because the neutron flux is higher in the central part. Therefore the k_{eff} is significantly sensitive to the ^{237}Np cross sections, especially to the fission one since fission is the dominant process for multiplying neutrons.

Finally, when all components are in contact, criticality was determined to be k_{eff}=1.0026$\pm$0.0034, that is 360 pcm uncertainty (1 pcm=0.001%). The different contributions to this uncertainty [70, 74] are listed in figure 7.4.

Source of Uncertainty	Parameter Variation in Calculation	Calculated Effect (Δk_{eff}) of Variation	Standard Uncertainty of Parameter	Standard Uncertainty in Δk_{eff}
Material Mass				
^{237}Np Mass	0.2 g	± 0.0011	0.2	± 0.0011
Tungsten Shield Mass	0.2 g	± 0.0008	0.2	± 0.0008
Nickel Inner Cladding Mass	0.2 g	± 0.0009	0.2	± 0.0009
Nickel Outer Cladding Mass	0.2 g	± 0.0008	0.2	± 0.0008
HEU Hemisphere Mass	0.537%	± 0.0032	0.107	± 0.0006
Enrichment in ^{235}U Shell	0.015 wt.%	± 0.0010	0.015	± 0.0010
^{237}Np Content	0.5%	± 0.0013	0.5	± 0.0013
Uranium Content	0.0011 wt.%	± 0.0011	0.0011/2	± 0.0005
Plutonium Content	0.001 wt.%	± 0.0006	0.001/2	± 0.0003
Geometry Dimensions				
^{237}Np sphere	0.00274 in.	± 0.0011	0.00274	± 0.0011
Tungsten Shield	0.002 in.	± 0.0007	0.002/√3	± 0.0004
Nickel Inner Cladding	0.002 in.	± 0.0005	0.002/√3	± 0.0003
Nickel Outer Cladding	0.002 in.	± 0.0006	0.002/√3	± 0.0004
HEU Hemisphere	0.002 in.	± 0.0008	0.002	± 0.0008
SS Membrane	0.001 in.	± 0.0012	0.001/√3	± 0.0007
Aluminum Spacer	0.002 in.	± 0.0009	0.002/√3	± 0.0005
Material Composition				
Impurity in Al Support	Included	0.0006	1/√3	± 0.0004
Impurity in SS membrane	Included	0.0009	1/√3	± 0.0005
Impurity in Tungsten shield	Included	0.0007	1/√3	± 0.0004
Additional Calculations				
Support Structure	Included	- 0.0092		± 0.0092
Room Return	Included	<0.001		± 0.001
Reactivity Measurement		<0.0001		± 0.0001
Total Uncertainty	Quadratically Combined Total: ± 0.0034			

FIGURE 7.4: Summary of uncertainties for the ^{237}Np critical experiment.

7.2.3 The critical neptunium benchmark

To promote this experiment as a benchmark much easier to simulate in the ICSBEP Handbook [70, 75], applied some simplifications to the geometry by homogenizing some parts with the actual small gaps and by approximating the outer structural materials. As the benchmark is very close to the real experiment, the variation of k_{eff} which is expected from the simplifications can be quantified by simulation [74, 75] and the criticality that would be found if they would be really applied would be k_{eff}=1.0019 ± 0.0036. This is the reference benchmark value that should be found by simulations based on correct cross sections when using the simplified geometry and composition. This benchmark geometry is represented in Fig. 7.5 and we used it in all the simulations.

We computed the benchmark with MCNP5 (Monte Carlo code for neutron transport) [71] driven by MURE (MCNP Utility for Reactor Evolution) [72]. The default cross sections were those from the evaluated library ENDF/B-VII.0 [76].

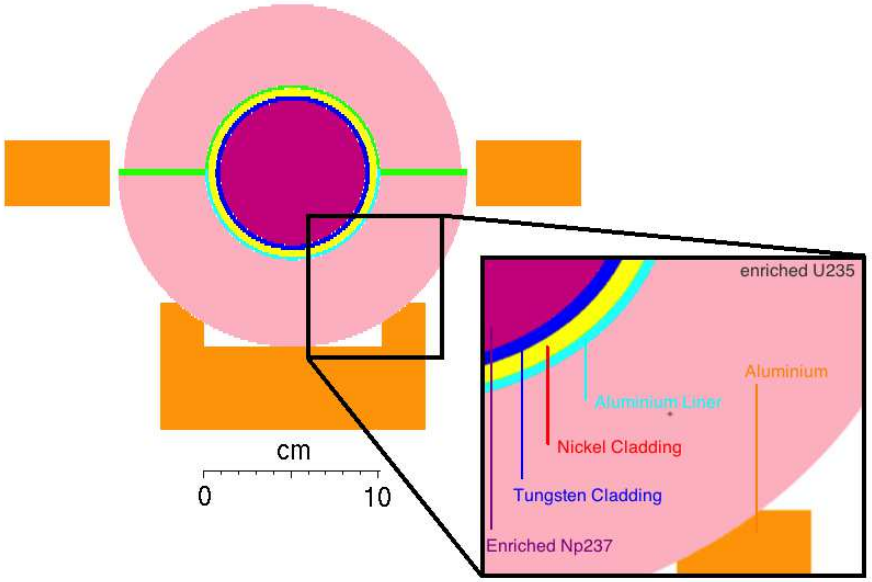

FIGURE 7.5: Neptunium's benchmark geometry. The right-hand side rectangle is an expanded view of a part of the spherical-like assembly.

We used 5750000 active neutrons distributed over 1200 generations of 5000 neutrons and the 50 first generations were discarded, so that the starting generation was representative of the average distribution.

In such conditions the computed criticality is k_{eff}=0.99418 ± 0.00006, very close to the value computed by the Los Alamos group [77] (k_{eff}=0.995 ± 0.00006). The deviation from the benchmark value is -770 pcm, more than twice the experimental uncertainty. This arouses suspicions about the ^{237}Np cross sections.

It is worth pointing out that the ^{237}Np fission cross section in ENDF/B-VII.0 is essentially based on Tovesson's measurement. As the n_TOF cross section is higher by about 6% above 1 MeV it could help to increase the k_{eff} and bring it closer to the benchmark value. To check this hypothesis we replaced the ENDF/B-VII.0 ^{237}Np fission cross section by the tabulated n_TOF data. All the other cross sections were left unchanged, therefore the total reaction cross section was scaled to accommodate the variation of the fission cross section.

After this substitution we obtained k_{eff}=1.00435±0.00006. Although this slightly exceeds the benchmark value, the deviation is significantly reduced to 250 pcm, 0.7 times the experimental uncertainty. As k_{eff} is sensitive to other parameters, this finding cannot be taken as definitely conclusive on the better fission cross section set. it indicates that the hypothesis of a ^{237}Np fission cross section higher than expected before should be considered seriously.

7.2.4 Role of inelastic cross section of ^{235}U

The disagreement between the experimental criticality and its simulated value when using the ENDF/B-VII.0 library, even more so when using ENDF/B-VI.8, has already been noticed [74, 76, 77]. The authors ascribed this effect to a possible deficiency of the inelastic cross section in ^{235}U. This hypothesis was also formulated following the under-prediction of fission rate ratios ^{237}Np/^{235}U at the center of several critical experiments [76].

We first study how this cross section affects the k_{eff} in the benchmark configuration, and then we examine how the variation required to match the experimental value compares with measurements of the inelastic cross section.

7.2.4.1 Impact of the ^{235}U inelastic cross section

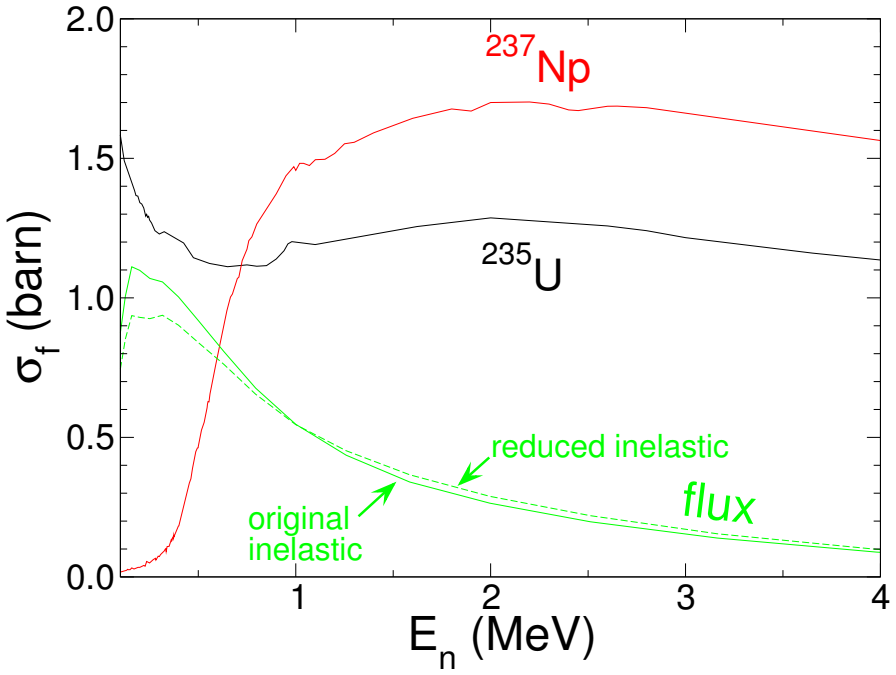

FIGURE 7.6: Effect of a distortion of the inelastic cross section on the neutron flux and fission cross sections of ^{237}Np and ^{235}U.

The (n,n') reaction is treated as a set of individual cross sections, one for each excited level in the target nucleus. These levels are populated at the expense of the incident neutron energy. Changes in the set of inelastic cross sections alter the neutron spectrum. For example, if the cross section for the highest levels is decreased while it is increased for the lowest ones, outgoing neutrons are expected

to have a higher average energy : the neutron spectrum is harder (it is shifted to the higher energies). This is illustrated in Fig. 7.6 where the bell-shaped curves represent the energy spectrum of the neutron flux in the ^{237}Np sphere. The dashed curve, labeled *reduced inelastic*, results from a modification of the inelastic cross sections as described above. As expected, the flux is shifted toward higher energies. The ^{237}Np and ^{235}U fission cross sections are also displayed in order to emphasize the different sensitivity of these nuclei to the change of the neutron spectrum. The fission cross section of ^{235}U is overall flat, so its fission rate is weakly sensitive to shift in the flux. Conversely, ^{237}Np has a fission threshold, hence a harder neutron flux increases the fission rate (dashed curve).

In order to evaluate if modifications of the ^{235}U inelastic cross sections may reconcile the criticality predicted by the simulation with the ^{237}Np benchmark value, we have performed calculations using various sets of ^{235}U inelastic cross sections. All other cross-sections were left untouched (as in ENDF/B-VII.0, so the total cross section was affected by the variation of the inelastic cross section.

As already noted, the inelastic channel (n,n') involves many cross sections. In MCNP, forty levels are described (MT=51 to 90, starting with the first excited level) ; they sit on top of the continuum (MT=91) where the energy of the outgoing neutron is smoothly distributed. It is worth noting that in MT=91, a large number of excited levels are included, mainly located at high excitation energy, and those missed by the recording of the discrete levels as well. Therefore we adopted a random procedure to vary these cross sections. First, we draw randomly the number of affected levels, which are then selected randomly too, and finally for each of these levels the cross section is multiplied by a random factor ranging from 0 to 2.

All the sets generated in this way are not acceptable because the inelastic cross section of ^{235}U also affects its critical mass which is well known. In other words the modification of the inelastic cross section should not change the computed criticality of a HEU sphere. We checked this feature by running a MCNP calculation with each of the proposed cross section sets over the GODIVA benchmark (HEU-MET-FAST-001) describing a bare HEU sphere reaching criticality [78]. If the resulting k_{eff} deviated by more than 50 pcm from the unperturbed calculation (k_{eff}=1.0000) the cross section set was rejected and another was generated randomly. Among 8000 sets generated, only 551 were validated using the GODIVA benchmark, and were then used for the computation of the ^{237}Np benchmark.

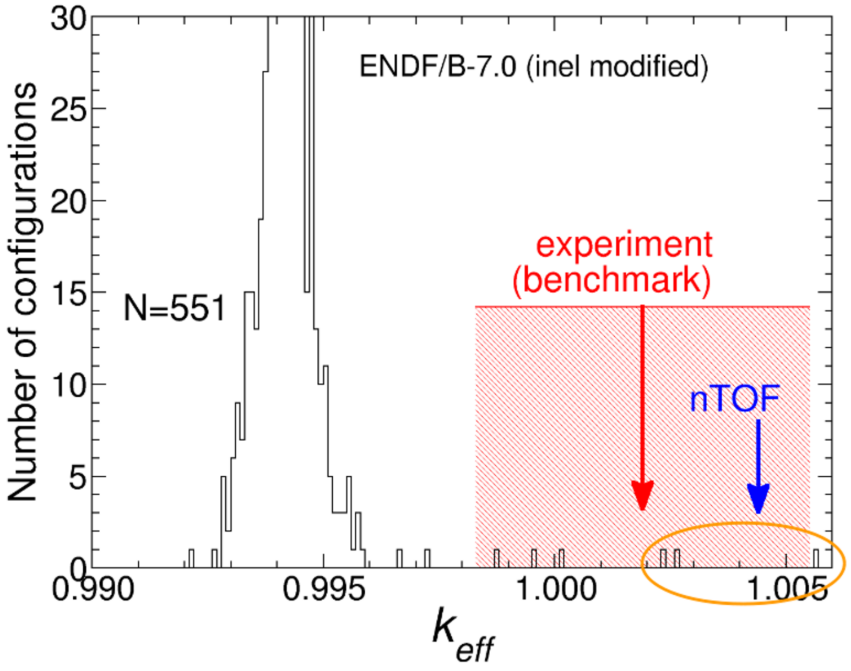

FIGURE 7.7: Spectrum of k_{eff} for the ^{237}Np benchmark computed with acceptable random variations of the inelastic cross section of ^{235}U. The red arrow indicates the benchmark value and the red hatched area the associated uncertainty.

Fig. 7.7 displays the k_{eff} obtained in these 551 computations. As expected it peaks at the unperturbed value for the ^{237}Np benchmark and spreads rather narrowly around its average. Nevertheless, a few values reach the experimental range. This means that some specific modifications of the inelastic cross section comply with the conservation of the ^{235}U critical mass and have a good agreement with the measured criticality for the ^{237}Np benchmark.

However, the examination of these particular sets reveals that they are always generated by highly depressing the continuum contribution (MT=91). As already noted, the continuum part contains a large number of continuous excited levels, mainly located at high excitation energy, and is a significant part of the inelastic cross section. Therefore the required shift of the energy spectrum can only be obtained by reducing strongly its contribution in favor of lower lying levels. This is illustrated in Fig. 7.8, similar to Fig. 7.7, but where the histograms show the k_{eff} distributions associated to a reduction of the continuum part by 0, 10, 25 and 40%. The statistics drop steeply when the level of reduction is enhanced because it becomes more difficult to find cross section configurations conserving the criticality of ^{235}U.

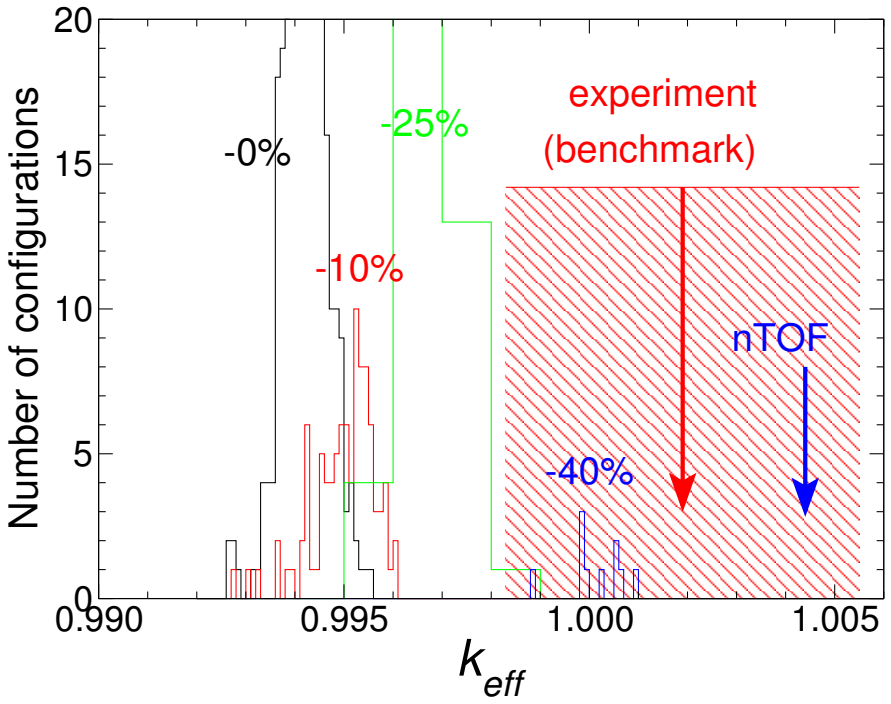

FIGURE 7.8: Same as Fig. 7.7 but the histograms are associated to different levels of reduction of the continuum part of the inelastic cross section. The reduction factor is indicated by labels on the histograms.

As expected, the more depressed the continuum fraction, the larger the increase in k_{eff}. However a reduction of at least 40% is needed to reach values compatible with the experimental benchmark. This is a large reduction : therefore, in the following, we intend to check the consistency of such an outcome with existing measurements.

7.2.4.2 Comparison to previous inelastic measurements

Knitter used a Van de Graaff accelerator to produce mono-energetic neutron beams of 1.5, 1.9 and 2.3 MeV [8] in order to measure the inelastic scattering cross section of ^{235}U. The kinetic energy loss of neutrons was integrated over 200 keV-wide bands from 0.4 MeV to the incident energy minus 0.5 MeV. The results are displayed in table. 7.1 in the Exp columns.

For MCNP5 with ENDF/B-VII.0 we retrieved the energy spectrum of the inelastically scattered neutrons by considering an infinite slab of ^{235}U of 1 cm thickness and 10 g/cm^3 density hit by neutrons with a kinetic energy of 1.5, 1.9 or 2.3 MeV. All cross sections have been disabled except MT=51 to 91, representative of the inelastic channels. Therefore the total cross section (MT=1) contained only these

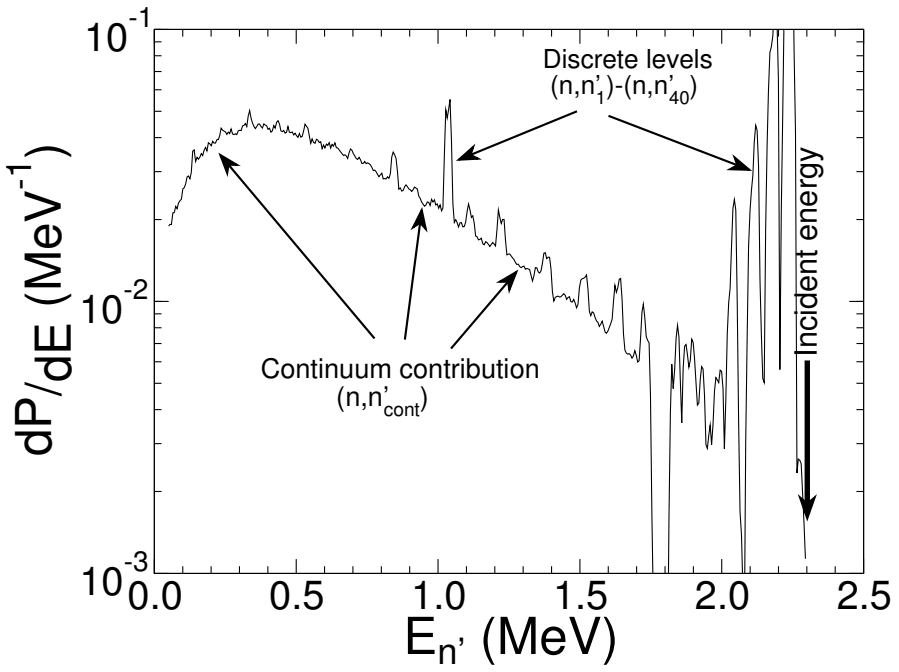

FIGURE 7.9: Energy spectrum of the outgoing inelastic scattered neutron as simulated for ^{235}U using ENDF/B-VII.0 inelastic cross sections (MT=51 to 91), for an incident energy of 2.3 MeV (reaction probability).

inelastic cross sections. The scattered neutrons were counted on each side of the slab using a F1 tally which scores the number of neutrons crossing a surface.

Fig. 7.9 shows the inelastic scattering energy spectrum for an incident neutron of 2.3 MeV. The peaks, widened by the recoil kinematics, are produced by populating discrete excited levels of the remaining ^{235}U (MT=51 to 90), whereas the smooth spectrum represents the continuous part (MT=91) ending at an energy corresponding to the minimum excitation energy of ≈0.5 MeV.

The spectra were then integrated over bands of 200 keV to allow a direct comparison with Knitter's data. The numbers are reported in table 7.1 in the column labeled ENDF/B-VII.0. Fig. 7.10 shows the comparison for the 2.3 MeV incident energy. The ENDF/B-VII.0 evaluation is close to Knitter's measurement, although a systematic overestimation shows up beyond 0.8 MeV. Measurements from Batchelor [79], interpolated between 2 and 3 MeV incident energy and integrated over bands of 200 keV for direct comparison, are also plotted. The agreement with ENDF/B-VII.0 is generally even better than in the case of Knitter's data, although a significant discrepancy appears between 0.6 and 1 MeV.

We plotted also in Fig. 7.10 the spectrum generated by a cross section configuration with 40% reduction of the continuum contribution. We checked that the

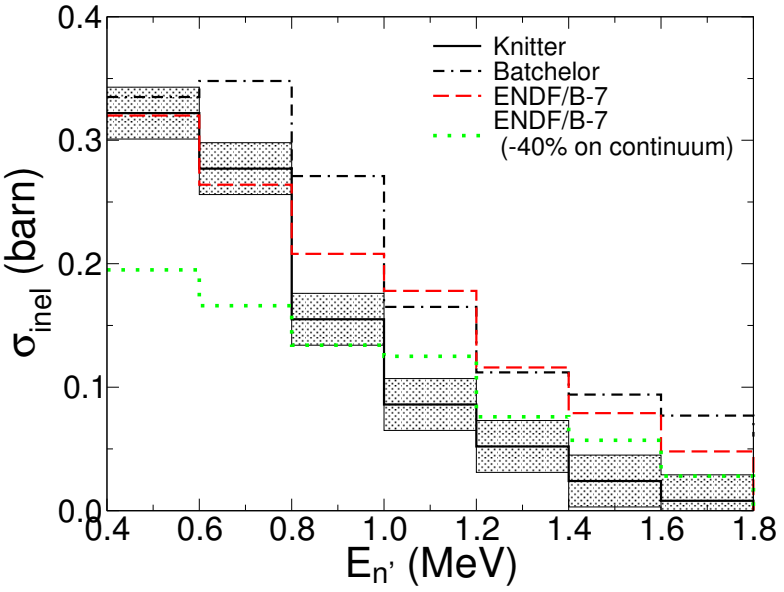

FIGURE 7.10: Comparison of inelastic neutron scattering cross sections of ^{235}U (barn) for energy bands of 200 keV for the outgoing neutron and for an incoming energy of 2.3 MeV. Solid line: Knitter's values with the error bars represented by the hatched rectangles. Dashed line: ENDF/B-VII.0. Dotted-dashed line: measurements from Batchelor. Dotted line: cross section modified with a 40% reduction of the continuum contribution.

pattern doesn't vary significantly among the configurations randomly generated. As expected, the low energy part of the spectrum is depleted and compensated by a strengthening of the part leading to low lying states, hence to high scattered neutrons energy : this will lead to the desired increase of k_{eff} in the ^{237}Np benchmark as some of the low energy neutrons are put beyond the fission threshold. Although such a cross section set seems to be in better agreement with Knitter's measurement above 0.8 MeV, it fails strongly below this energy.

To sort things out, one must stress that one of the main difficulties of such measurements is the subtraction of fission neutrons from the neutron spectra as shown in figure 7.11 for Knitter's experiment. The lower the energy of the scattered neutrons, the lower the fission contribution : in other terms, we consider the low-energy part results more reliable than the high energy part, an assumption which is corroborated by the consistency of the two measurements, which gets better as one looks at lower scattered neutrons energy. The -40% configuration is strongly discrepant with experimental data in the more reliable region, while it gets closer to Knitter, but further from Batchelor, in the more disputable region.

From this study of the impact of the inelastic cross section we conclude that to reconcile the measurement of the k_{eff} of the ^{237}Np benchmark with simulation only

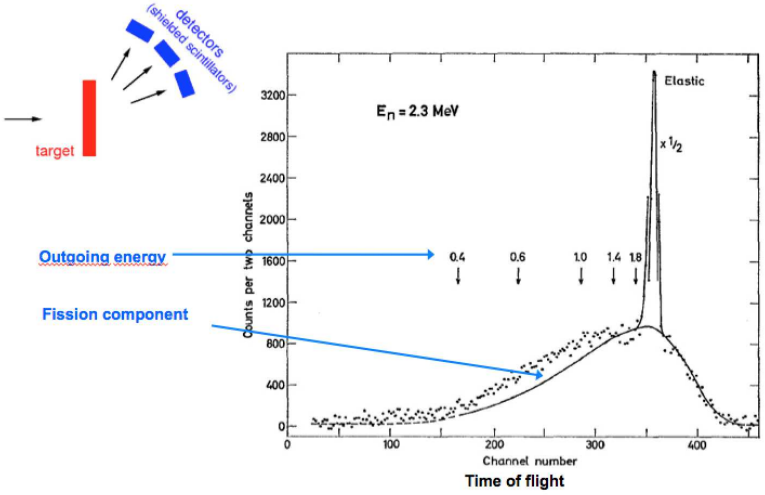

FIGURE 7.11: Knitter experiment: measurement of the outgoing neutrons and subtraction of the fission contribution to get the scattering component.[8]

by modifying the inelastic cross section of ^{235}U, one has to reduce the continuum part by about 40% and this is hardly consistent with measurements.

7.2.5 Influence of ^{237}Np neutron multiplication factor $\overline{\nu}$

A criticality experiment is in fact an integral measurement and k_{eff} is sensitive to other parameters, beside cross sections. The average number of emitted neutrons per fission $\overline{\nu}$ is also an important parameter for the criticality and a little variation of $\overline{\nu}$ could highly affect k_{eff}. As the ^{235}U $\overline{\nu}$ is well constrained by HEU critical experiments we only apply variations to the ^{237}Np $\overline{\nu}$.

The simulation shows that a 3% increase on ^{237}Np $\overline{\nu}$ (prompt+delayed) produces a k_{eff} shift of 766pcm. Although only 13% of fissions occur in the neptunium sphere their contribution in k_{eff} is higher than the ^{235}U fission due to the lower escape probability of the emitted neutrons. Therefore an increase of about 3% of $\overline{\nu}$ is needed to make k_{eff} reach the experimental value. Fig. 7.12 shows the $\overline{\nu}$ energy dependence for several experimental sets normalized to the ENDF/B-VII.0 values. For sake of clarity the error bars are not reported in the figure but they lie mostly between 0.5 and 1.5%. Although $\overline{\nu}_{tot}$ is the relevant parameter in critical experiments we plotted in Fig. 7.12 the ratios of $\overline{\nu}_{prompt}$ as the contribution of delayed neutrons is negligible in those ratios. Most of the experimental values are lower than the evaluated ones, except Veeser's data set around 7 MeV, which is well above the mean energy of neutrons in the critical device. No experimental value

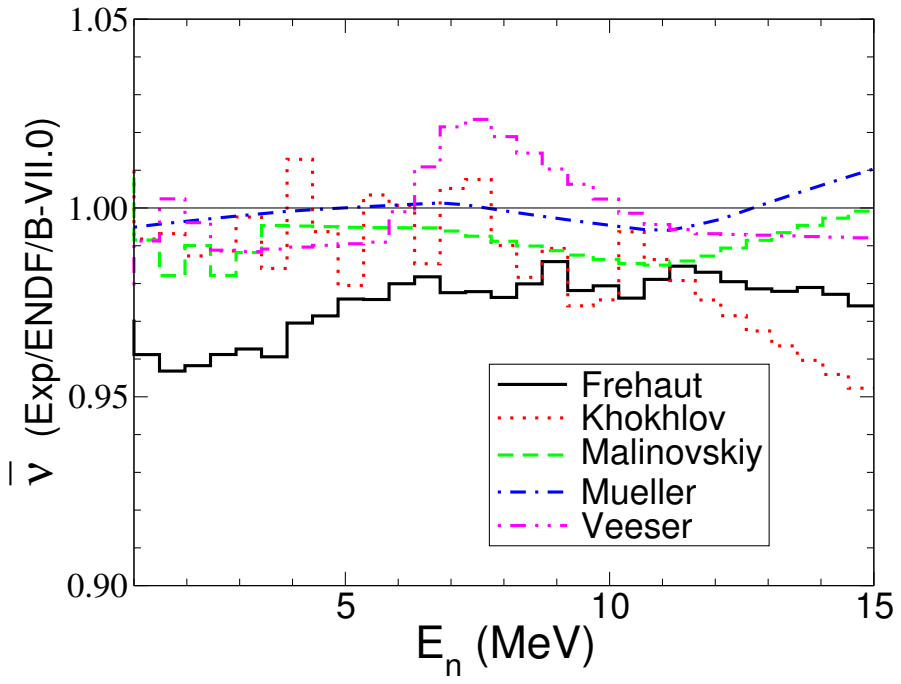

FIGURE 7.12: For fission of ^{237}Np ratio of measured prompt $\overline{\nu}$ to its value given in ENDF/B-VII.0.

reaches the target value 1.03. This comparison doesn't support the plausibility of an underestimation of the total $\overline{\nu}$ that would explain the mismatch between the simulated and the measured criticality.

7.3 Fission rate experiments

Fission rate measurements consist of recording the number of fission, with fission track detectors or inside an ionization chamber, when a sample is subject to a neutron field of known spectrum. The rate is directly related to the fission cross section as it is the folding product over energy of the cross section by the energy spectrum. One can define the averaged cross section as:

$$< \sigma >= \frac{\int W(E)\sigma(E)\,dE}{\int W(E)\,dE} \tag{7.9}$$

where $W(E)$ is the neutron energy spectrum. And the fission rate ratio, or spectral index, as the ratios of averaged cross sections:

$$R_f = \frac{< \sigma >_{Np237}}{< \sigma >_{U235}} \tag{7.10}$$

ENDF/B-VII.0 and ENDF/B-VII.1 [27] libraries have been tested with different fission rate experiments [80]. Unfortunately for several of them the description of the experimental details and the method used to calibrate the fission rate is missing. Therefore we discuss only two of the test cases presented in [80], and we add two other examples, with a ^{252}Cf neutron source, where the experimental details are available.

7.3.1 GODIVA

The first situation we consider is the case of fission rates measured at the center of a GODIVA assembly. It is an enriched ^{235}U sphere [78] and the ratio of fission rates is obtained with ^{237}Np and ^{235}U samples by dividing the former rate by the latter. Table 7.2 (first line) shows the comparison between this measured ratio, its simulated value when using the ENDF/B-VII.0 library, and the computed value when the n_TOF ^{237}Np fission cross section is used. The ENDF/B-VII.0 underestimates the result by 2.4% whereas the n_TOF data is higher by 3.5%.

7.3.2 COSMO

The MASURCA reactor is an experimental nuclear assembly that can be configured as critical or subcritical by loading a different number of fuel tubes. The core is based on uranium/plutonium MOX fuel. Several configurations have been explored for different investigations. We looked only at the COSMO benchmark which is the first and well defined critical configuration of MASURCA (180cm $\times$ 180cm $\times$ 164.2cm) well described in a NEA report [9]. The COSMO configuration is made of 3 parts, which compositions are homogenized: MOX core, reflector and shielding, shown in fig.7.13. The fission rates of ^{237}Np and ^{235}U have been measured at several points with an ionizing chamber inside the core but we refer here to the central measurement where the flux has a maximum.

Again table 7.2 shows the experimental ratio ^{237}Np/^{235}U and the results of the computations with equations.7.9 and 7.10. From this comparison it turns out that the n_TOF cross section is too high by 5% whereas the ENDF/B-VII.0 is very close to the experimental value.

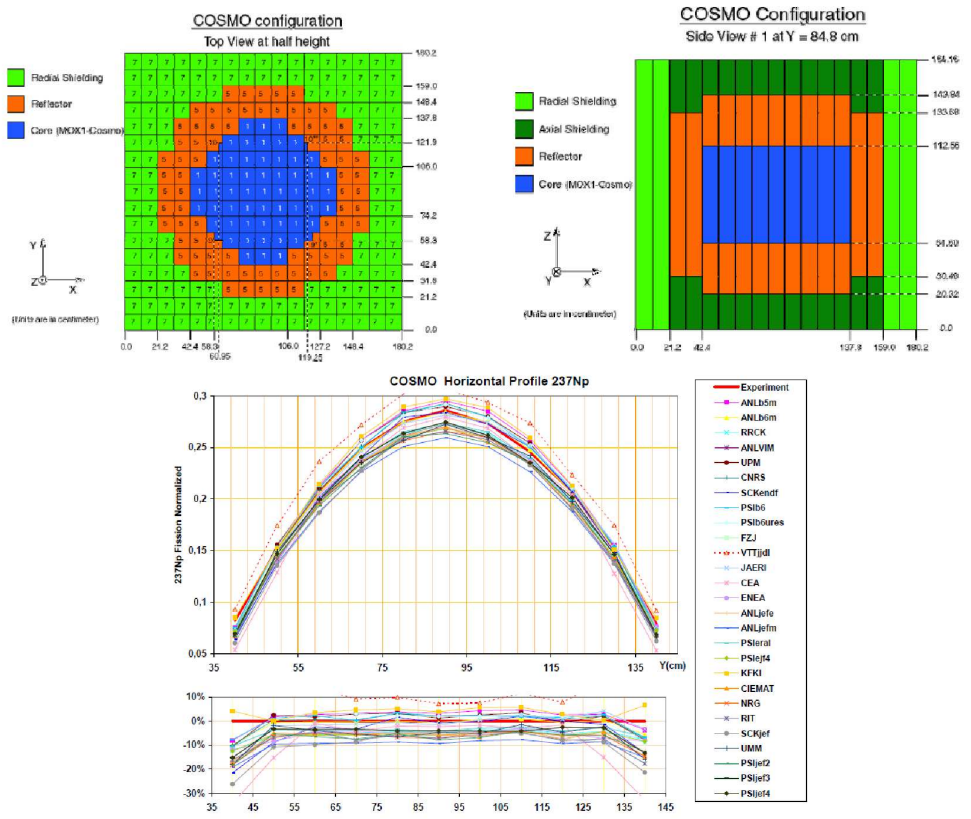

FIGURE 7.13: The upper schemes show the COSMO reactor core geometry which composition is homogenised. The lower part shows the experimental fission ratio ^{237}Np/^{235}U the latter being measured at the center. The experimental ratio at the center is R_f=0.285[9].

7.3.3 ^{252}Cf experiment

The last situation we will discuss is the case of a neutron field generated by the spontaneous fission of a ^{252}Cf source. The fission rates from ^{237}Np and ^{235}U deposits in ionization chambers are recorded when they are placed at different distances from a stainless steel spherical shell containing a ^{252}Cf source, as described in the FUND-NIST-CF-MULT-FISS-001 benchmark [10] and depicted in figure 7.14 The manufacturing of ionization chambers and the fissile deposits is described in [81] and their absolute calibration has been obtained by α-spectroscopy and α-counting. The spherical shell can be filled with water but we just consider the dry case when the sphere is empty. In such conditions the neutrons are only slightly scattered and moderated by the shell and other mechanical pieces as holders and cases, as emphasized in [10]. Instead of carrying a full simulation of the experiment we just performed a simple calculation of the fission averaged fission

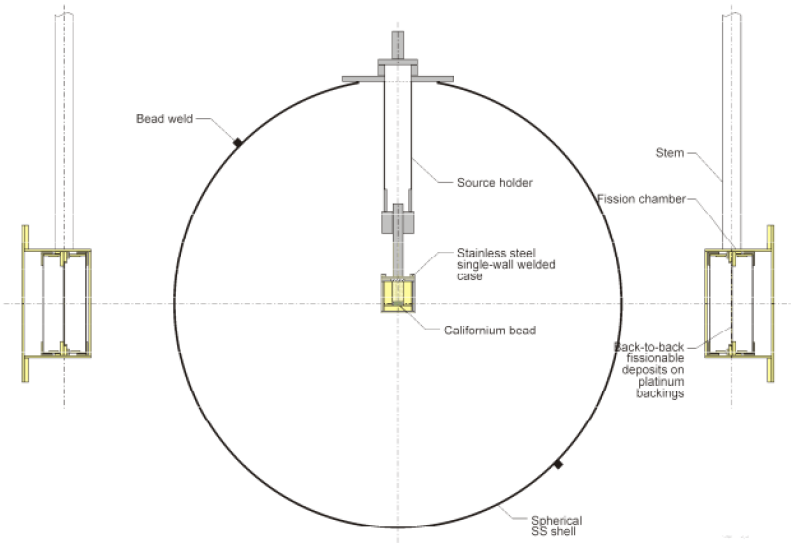

Figure 2. A Typical Experimental Arrangement.

FIGURE 7.14: Neutrons from a ^{252}Cf source inside a spherical stainless steel vessel and two ionization chambers beside containing ^{235}U and ^{237}Np [10].

cross section by assuming a pure Watt spectrum:

$$W(a,b,E') = Ce^{-aE'}\sinh(\sqrt{bE'}) \tag{7.11}$$

where $C = \sqrt{\pi\frac{b}{4a}}e^{\frac{b}{4a}}$. In the case of spontaneous fission of ^{252}Cf we take $a = 0.84746$ MeV^{-1} and $b = 1.03419$ MeV^{-1} [82], which is also the parametrization adopted in ENDF/B-VII.

.

We applied a correction for the tiny moderation of the neutrons. This correction has been estimated from the difference of the unperturbated and moderated fluxes as computed in [10] and shown in figure 7.15. The correction amounts to 1.2%.

7.3.4 Comparison

The comparison between the measured averaged fission cross section of ^{237}Np and the simulation using the ENDF/B-VII.0 ^{237}Np cross section and the n_TOF data is shown in the third line of table 7.2. The latter gives a value much closer to the

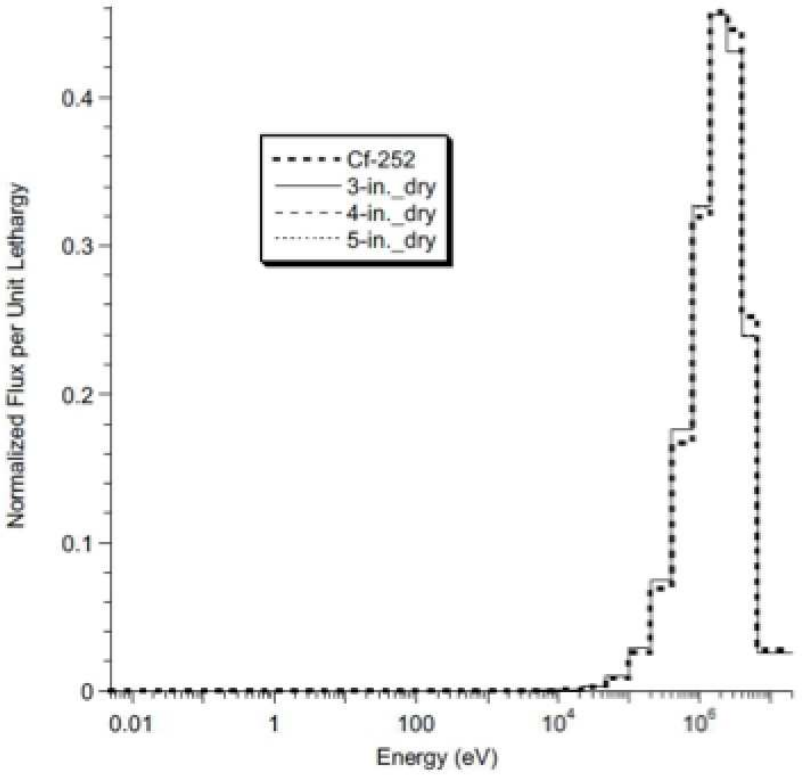

FIGURE 7.15: Difference between original ^{252}Cf neutron spectrum and spectrum at the sample due to the slight moderation [10].

experimental one. It's interesting to note that when using ENDF/B-V the agreement was very good [82] and ENDF/B-VII does worse because the parametrization of Watt's spectrum for ^{252}Cf has been changed between ENDF/B-V and ENDF/B-VI. Nevertheless the combination of the ENDF/B-VII.0 ^{252}Cf neutron energy spectrum with the n_TOF fission cross section of ^{237}Np allows to recover a very good agreement.

Another absolute fission cross section, under the neutron flux generated by a ^{252}Cf source, has been measured by Adamov et al. [83]. The comparison with the simulation displayed on the last line of table 7.2 shows again a good agreement with the n_TOF data.

This comparison of fission rates seems to be puzzling because it leads to contradictory conclusions according to the different experiments. However we would like to stress that some of them are not calibrated in absolute value. As an example, it is the case of the COSMO experiment where the amount of fissile deposit has not been calibrated in absolute value by α-counting, but from fission rates in a

reference neutron flux. Therefore the calibration depends on the fission cross section itself, and the agreement obtained in other neutrons fields like the COSMO measurement merely indicates that the cross section has the right energy dependence but doesn't say anything on its absolute value. In that respect the shown COSMO comparison is not really significant as the cross section data set used for the calibration and the reactor measurement is not the same.

In the GODIVA case we don't have any information on the calibration procedure of the samples which have been used, but in the case of FUND-NIST-CF-MULT-FISS-001 we know that the samples have been absolutely calibrated either by α counting or by weighing. Overall the fission rates experiment are not contradictory with an increase of the fission cross section of ^{237}Np by 4-5%.

7.3.5 ^{237}Np(n,f) cross section conclusion

We used the ^{237}Np critical benchmark to test the validity of the ^{237}Np fission cross section measured at n_TOF, which appeared to be larger than previous measurements. The k_{eff} predicted using the n_TOF cross section, although slightly exceeding the experimental value, is much closer to the benchmark value and falls inside the uncertainty range whereas this was not the case for older ^{237}Np fission cross sections. As some authors invoked a possible deficiency of the (n,n') cross section in ^{235}U to explain the mismatch we investigated this hypothesis. It turns out that the experimental range can be reached only by depressing the continuum contribution of the inelastic cross section by at least 40%. Such a modification is hardly consistent with existing measurements of the ^{235}U inelastic cross section. Beside, we showed that the discrepancy can't be ascribed to the ^{237}Np $\overline{\nu}$. Although other effects and uncertainties can affect the criticality, our prediction of the criticality of the ^{237}Np benchmark may indicate that the ^{237}Np fission cross section is higher than expected from previous measurements. When testing the ^{237}Np fission cross section with fission rate experiments the outcomes are not univoque, but we showed that the calibration procedure of the targets (number of atoms) is of crucial importance and its description is often lacking. In two cases where all the information is available and the targets have been calibrated in absolute value, the n_TOF cross section gives a much better agreement with the measured value. Although this can't be considered as definitely conclusive, it indicates that

a global increase of the ^{237}Np fission cross section by 4-5%, against the data libraries and more peculiarly ENDF/B-VII.0, would reconcile all the comparisons we have shown.

E_n-$E_{n'}$ (MeV)	E_n=1.5 MeV		E_n=1.9 MeV		E_n=2.3 MeV	
	Exp $\sigma_{inel} \pm \Delta\sigma_{inel}$	ENDF/B-VII.0	Exp $\sigma_{inel} \pm \Delta\sigma_{inel}$	ENDF/B-VII.0	Exp $\sigma_{inel} \pm \Delta\sigma_{inel}$	ENDF/B-VII.0
0.5 - 0.7	0.117±0.022	0.154	0.046±0.022	0.087	0.008±0.022	0.048
0.7 - 0.9	0.196±0.022	0.257	0.113±0.022	0.147	0.024±0.022	0.078
0.9 - 1.1	0.334±0.022	0.321	0.213±0.022	0.205	0.052±0.022	0.115
1.1 - 1.3			0.294±0.022	0.290	0.086±0.022	0.178
1.3 - 1.5			0.267±0.022	0.320	0.155±0.022	0.207
1.5 - 1.7					0.277±0.022	0.264
1.7 - 1.9					0.322±0.022	0.319

TABLE 7.1: Comparison between Knitter's inelastic cross section measured for ^{235}U and ENDF/B-VII.0 for energy bands of 200 keV of the outgoing neutron.

Observable	Set-up	Exp.	Calc. (ENDF/B-VII.0)	Calc. (n_TOF)
R_f	GODIVA(HMF001-002)	0.8516 (12)	0.83	0.88
	MASURCA(COSMO)	0.285	0.284	0.299
$< \sigma >_{^{237}Np}$ (barn)	FUND-NIST-CF-MULT-FISS-001	1.420 (25)	1.34	1.41
	Adamov et al.	1.442 (23)	1.364	1.431

TABLE 7.2: Comparison of experimental and simulated fission rates and averaged fission cross section

Chapter 8

Conclusion

This thesis work is made of two parts related to two research topics. The first part is a study of the neutron-induced fission fragment angular distribution of actinides with the n_TOF facility at CERN, using a fast Parallel Plate Avalanche Counters (PPACs) setup. This facility can provide a very high resolution energy from thermal to 1 GeV due to the long flight path of 185 m. This PPAC setup provides a very high time resolution, reduces significantly the background and discriminates light particles and spallation reactions from fission fragments with the coincidence method. PPACs detectors are insensitive to the γ-flash and present an excellent capability to measure the fission fragment angular distribution in a wide energy range from eV up to GeV. The stripped cathodes give an excellent spatial position of the fission fragment hits in the detectors, so that the emission angle of the fission fragments can be measured and the emission point on the target can be lovalized too.

The new aspect of this experiment is the geometrical arrangement of the 9 targets and 10 detectors tilted by 45° with respect to the neutron beam direction. This configuration allows to cover the full angular range with a good efficiency.

We developed a method of self-determination of the efficiency which is based on the decoupling of the angular distribution and the efficiency depending on two different angles: the fission fragment emission depends on the angle relative to the neutron beam direction whereas the efficiency depends on the angle relative to the axis perpendicular to the detector surface. The two angles give and independent information on FFAD and detector efficiency which permits to obtain an absolute FFAD estimation. This procedure can be applied to restricted energy ranges

and to individual targets, without any need of a reference target. This is very important because the surface state of the fissioning layer, its roughness, has a significant impact on the detection efficiency and is not well controled. The self-determination of the efficiency solves this difficulty by extracting the efficiency on a per-target basis. In addition this method opens the perspective of improving the measurements of fission cross sections by an accurate determination of the efficiency. This has not been used in this work, which remained centered on the angular distributions, but cross section checks can be performed, in particular for ^{232}Th and ^{237}Np.

Our ^{232}Th results are well consistent with the previous data up to 20 MeV. We provide accurate results for the anisotropy in the region around second-chance and third-chance fission.

In the intermediate energy range, between 20 and 200 MeV, n_TOF is not consistent with Ryzhov data which were the only existing before our measurement. Ryzhov ^{232}Th data were hardly explained in the framework of the model he developed and artificial parametrizations had to be applied to get the model closer to his data, like the arbitrary K_0^2 reduction. Our n_TOF data are well reproduced by the model without arbitrary modification.

We also compared our measured ^{232}Th anisotropy with that coming from proton-induced fission, in particular with Smirnov data. The two data sets differ significantly in this intermediate energy range. At 40 MeV this difference is well explained within the fissility systematics of fission anisotropy. It can be noticed that Ryzhov's data were falling well outside the fissility systematics. This dependence on the fissility of the compound system implies that at this energy the incoming nucleon is captured most of the time. In the case of ^{238}U, in spite of the low statistics of our measurement, we can see that it is in agreement with Ryzhov's data, contrary to the ^{232}Th case.

We also measured also the angular distributions for ^{235}U and ^{237}Np targets, although with low statistics due to the number of targets and the reduced exposure time. The seemingly high value of the anisotropy at the opening of the third chance fission might be a feature of odd mass nuclei. This would be worth confirmed in future experiments for ^{237}Np. For ^{235}U and ^{238}U the 2012 campaign should already bring answers because the number of targets were respectively 2 and 3 and the

number of protons dedicated to the n_TOF experiment was significantly higher than in 2010 and 2011.

The second part of this work is focused on the use of integral benchmarks to validate the fission cross section of ^{237}Np which was found higher by 6% in n_TOF compared to existing data. This is essentially a simulation study for the propagation of neutrons.

We first simulated a critical assembly containing a significant amount of ^{237}Np and showed that the n_TOF data gives a better agreement with the experimental criticality. We investigated other possible causes of the criticality mismatch between the experiment and the simulation with library cross sections: inelastic cross section, neutron multiplicity. We showed that the modifications required to reduce the criticality mismatch are not consistent with the related measurements.

In a second step we confronted the n_TOF data in situations where the neutron flux and its spectral shape are well known, in particular at the center of a critical assembly (GODIVA) and with a ^{252}Cf source. The conclusion is not univoque because the measurements in such conditions are not all consistent, and the information on the calibration procedure, in particular the quantity of atoms in the targets, is often missing. At least in two cases where this information is available, and corresponding for one of them to a full documented benchmark, a better agreement is obtained with the n_TOF data set.

Overall a global increase of the ^{237}Np fission cross section by 4-5%, against the data libraries and more peculiarly ENDF/B-VII.0, would reconcile all the comparisons we have shown. This study can't lead to a definite conclusion on this respect due to the sensitivity of integral experiments to other not considered parameters. Nevertheless it shows that an increase of the ^{237}Np fission cross section is plausible and should be really checked with experiments where the number of atoms is targets is calibrated in absolute value.

As in our case the targets are well characterized by α-counting an accurate knwoledge of the detection efficiency, as delivered by the self-calibrating method, should allow us an additional check for the ^{237}Np case. this will be done in the near future.

Appendix A

Legendre polynomials

Legendre polynomials is one of the varieties of special functions which are encountered in the solution of many physical problems. For example in the separation of variables of the Schrodinger wave equation:

$$-\frac{\hbar^2}{2\mu}\nabla^2\psi + V(r,s)\psi_i = E\psi \tag{A.1}$$

We are interested in the angular dependence part in spherical polar coordinates, which obey the equation:

$$\left[\frac{1}{\sin\theta}\frac{\partial}{\partial\theta}\left(\sin\theta\frac{\partial Y}{\partial\theta}\right) + \frac{1}{\sin^2\theta}\frac{\partial^2 Y}{\partial\phi^2}\right] = -l(l+1)Y \tag{A.2}$$

The wavefunctions of the Schrodinger equation need to be normalized, so the list of functions below will include the normalization factor:

$$N_{lm} = \left[\frac{(2l+1)(l-m)!}{4\pi(l+m)!}\right]^{1/2} \tag{A.3}$$

Thus this angular equation are the spherical harmonics $Y(\theta,\phi)$, that have the form:

$$Y_l^m(\theta,\phi) = (-1)^m N_{lm} \mathrm{e}^{im\phi} P_l^m(\cos\theta) \tag{A.4}$$

The particular case where there is no dependence on the azimuthal angle ϕ, $m = 0$ and the $P_l^m(\cos\theta)$ are reduced to the $P_l(\cos\theta)$, which are named Legendre polynomials, and they can be obtained from:

$$P_n(\cos\theta) = \frac{1}{2^n n!}\frac{d^n}{d(\cos\theta)^n}\left[(\cos^2\theta - 1)^n\right] \tag{A.5}$$

The $P_l(\cos\theta)$ make a set of orthogonal polynomials:

$$\int_{-1}^{1} P_k P_l \, d(\cos\theta) = \frac{2}{2l+1}\delta_{kl} \tag{A.6}$$

The first few polyomials are shown below:

n	Legendre polynomial
0	1
1	$\cos\theta$
2	$\frac{1}{2}(3\cos^2\theta - 1)$
3	$\frac{1}{2}(5\cos^3\theta - 3\cos\theta)$
4	$\frac{1}{8}(35\cos^4\theta - 30\cos^2\theta + 3)$
5	$\frac{1}{8}(63\cos^5\theta - 70\cos^3\theta + 15\cos\theta)$
6	$\frac{1}{16}(231\cos^6\theta - 315\cos^4\theta + 105\cos^2\theta - 5)$
7	$\frac{1}{16}(429\cos^7\theta - 693\cos^5\theta + 315\cos^3\theta - 35\cos\theta)$

l and m are integers. In A.4 the functions $P_l^m(\cos\theta)$ are the associated Legendre polynomials of order m that can be derived from $P_l(\cos\theta)$:

$$P_l^m(\cos\theta) = (1-\cos^2\theta)^{m/2}\frac{d^m}{d\cos\theta^m}P_l(\cos\theta) = \frac{(1-\cos^2\theta)^{m/2}}{2^l l!}\frac{d^{l+m}}{d\cos\theta^{l+m}}(\cos^2\theta-1)^l \tag{A.7}$$

Appendix B

Angular distributions

This appendix displays the angular distributions obtained over narrow energy intervals. The black dots are for the data with the error bars representing the statistical uncertainty determined as explained in chapter 5. The red curve represents a Legendre polynomial fit including terms with P_2 and P_4. The anisotropies are derived from this fit. For each graph the related energy interval is written, with the value of the reduced χ^2 of the fit and the $\cos\theta$ polynomial resulting from the fit (equation of the red curve).

B.1 ^{232}Th angular distributions

The plots represent the data for the accumulation of the 6 targets and the campaigns performed in 2010 and 2011. In 2010 $1.47\,10^{18}$ protons were sent to n_TOF to produce neutrons, whereas in 2011 only $0.37\,10^{18}$ protons were received.

B.2 ^{235}U angular distributions

The conditions are the same as for ^{232}Th, except that a single target is placed in the set-up (instead of 6).

B.3 ^{238}U angular distributions

A single target is present, as for ^{235}U, but in addition the data are only those taken in 2011 because in 2010 a localization signal was missing for a detector looking at this target. This explains the larger error bars for this target.

B.4 ^{237}Np angular distributions

Same conditions as for ^{238}U: a single target and the data are only those taken in 2011 because in 2010 a localization signal was missing too, leading to large error bars for this target.

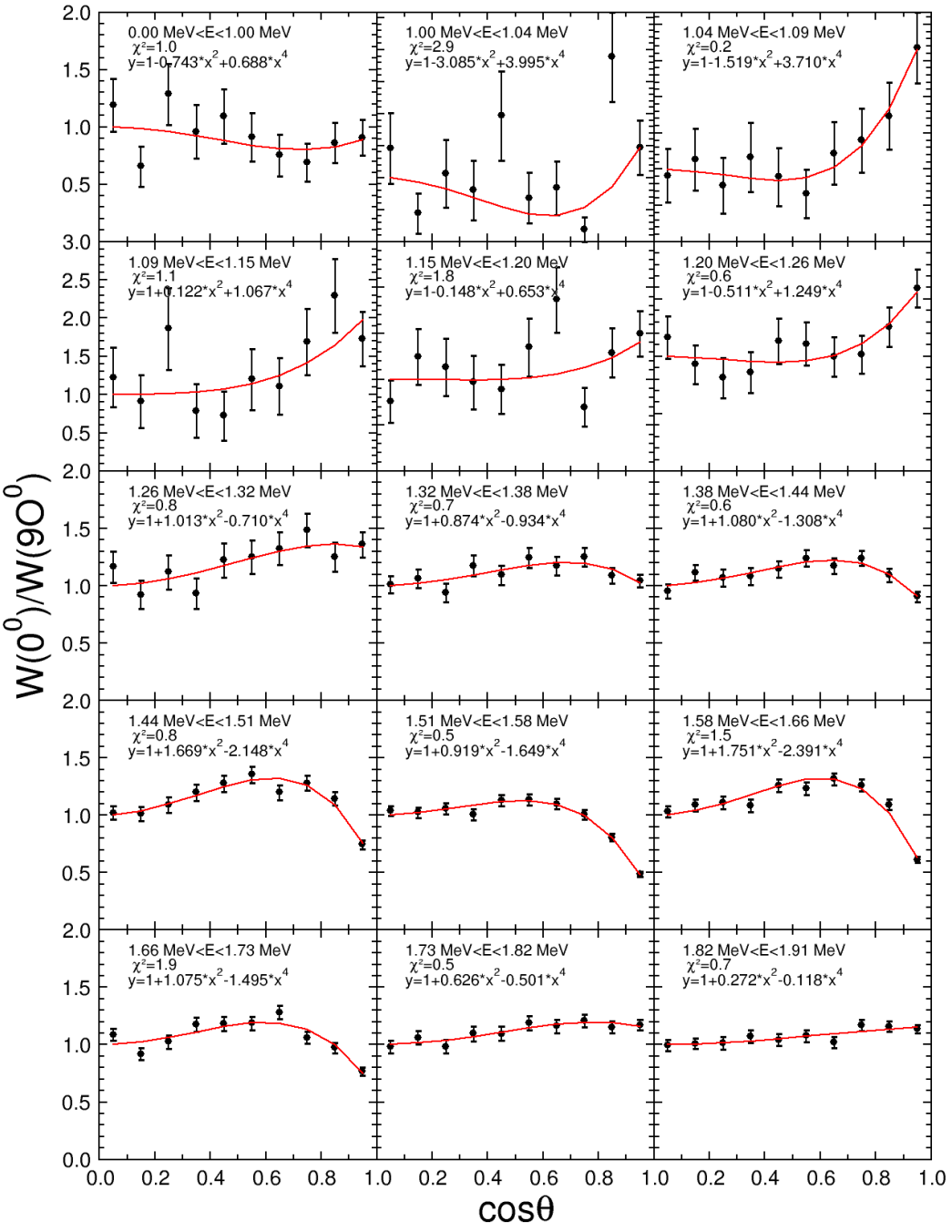

FIGURE B.1: ^{232}Th angular distributions for $E_n < 1.91$ MeV

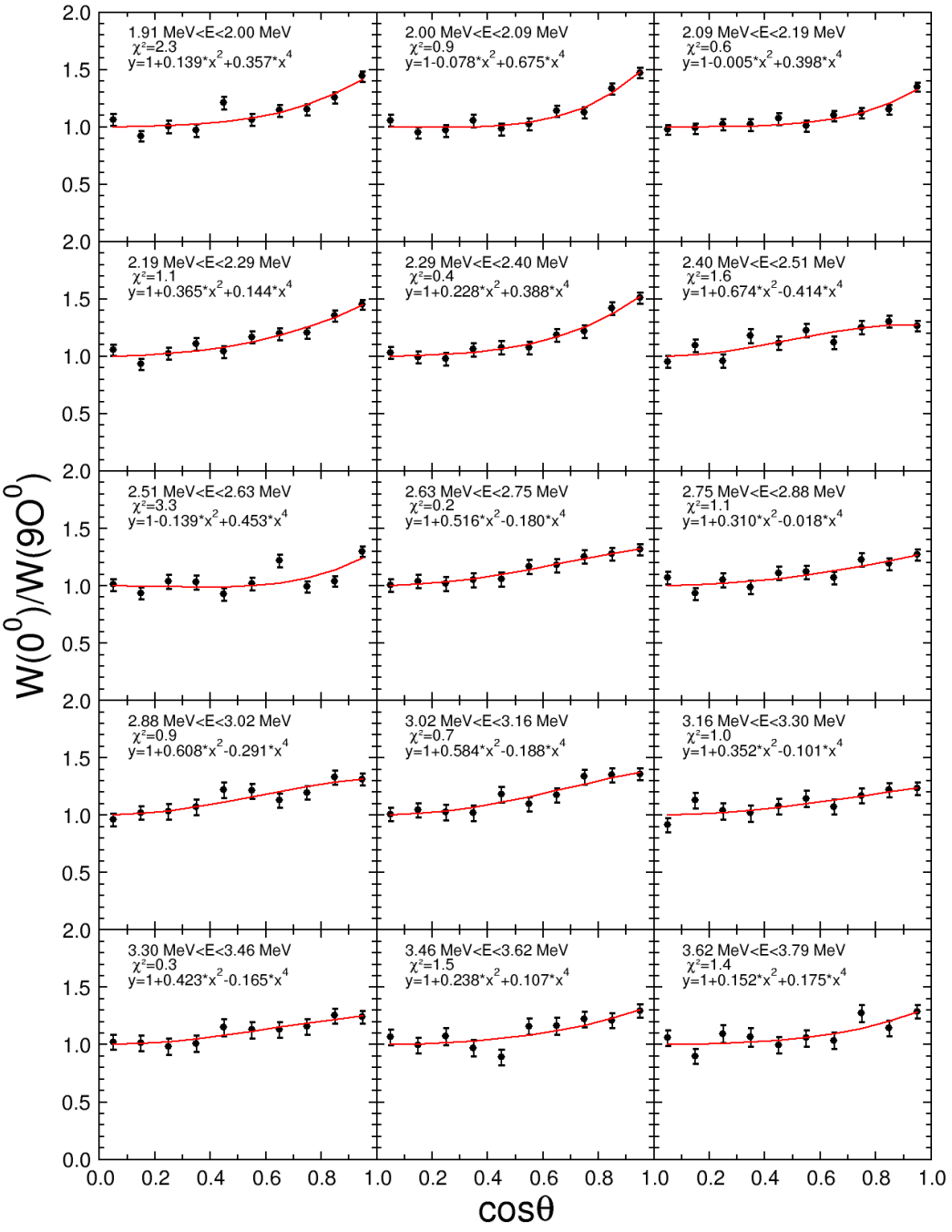

FIGURE B.2: ^{232}Th angular distributions for $1.91 < E_n < 3.79$ MeV

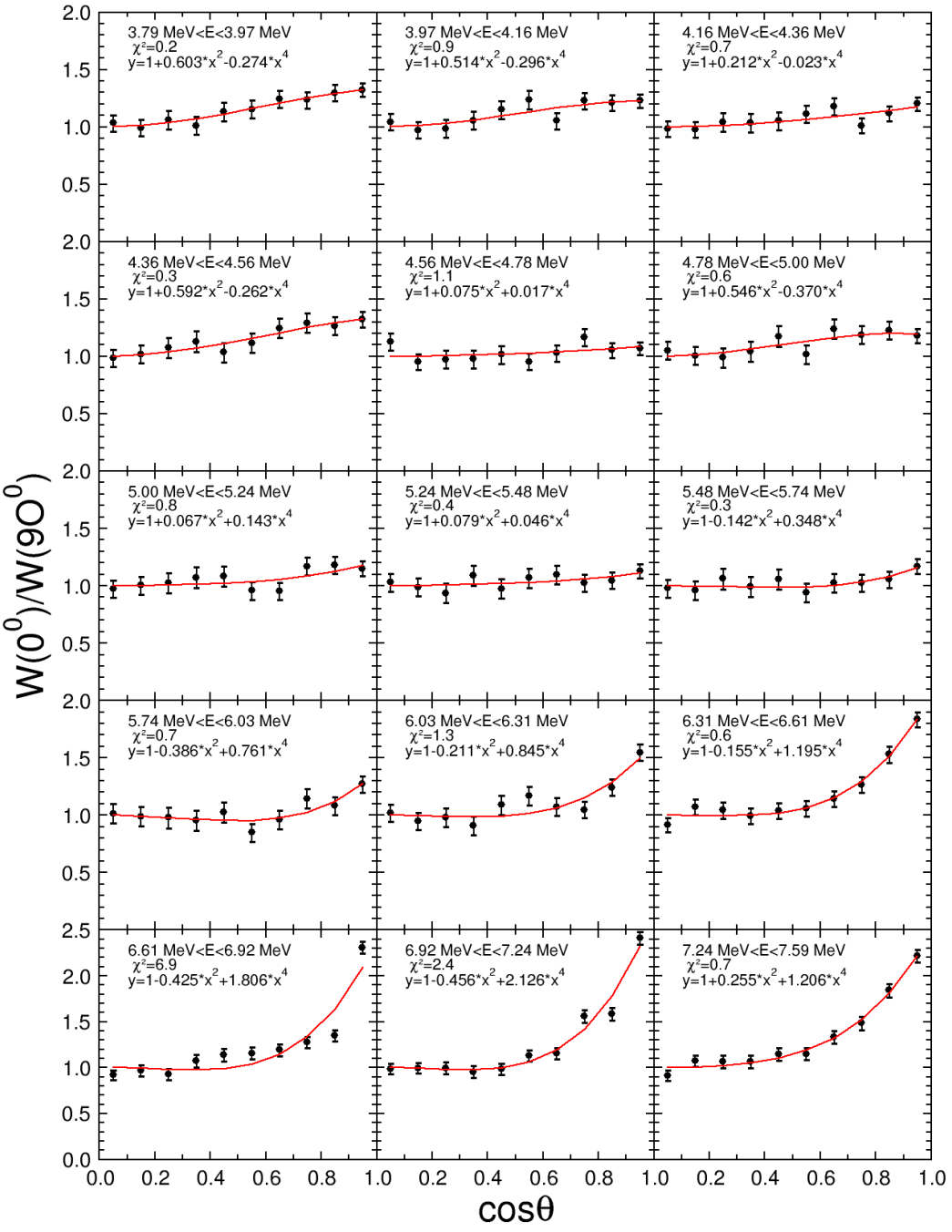

FIGURE B.3: ^{232}Th angular distributions for $3.79 < E_n < 7.59$ MeV

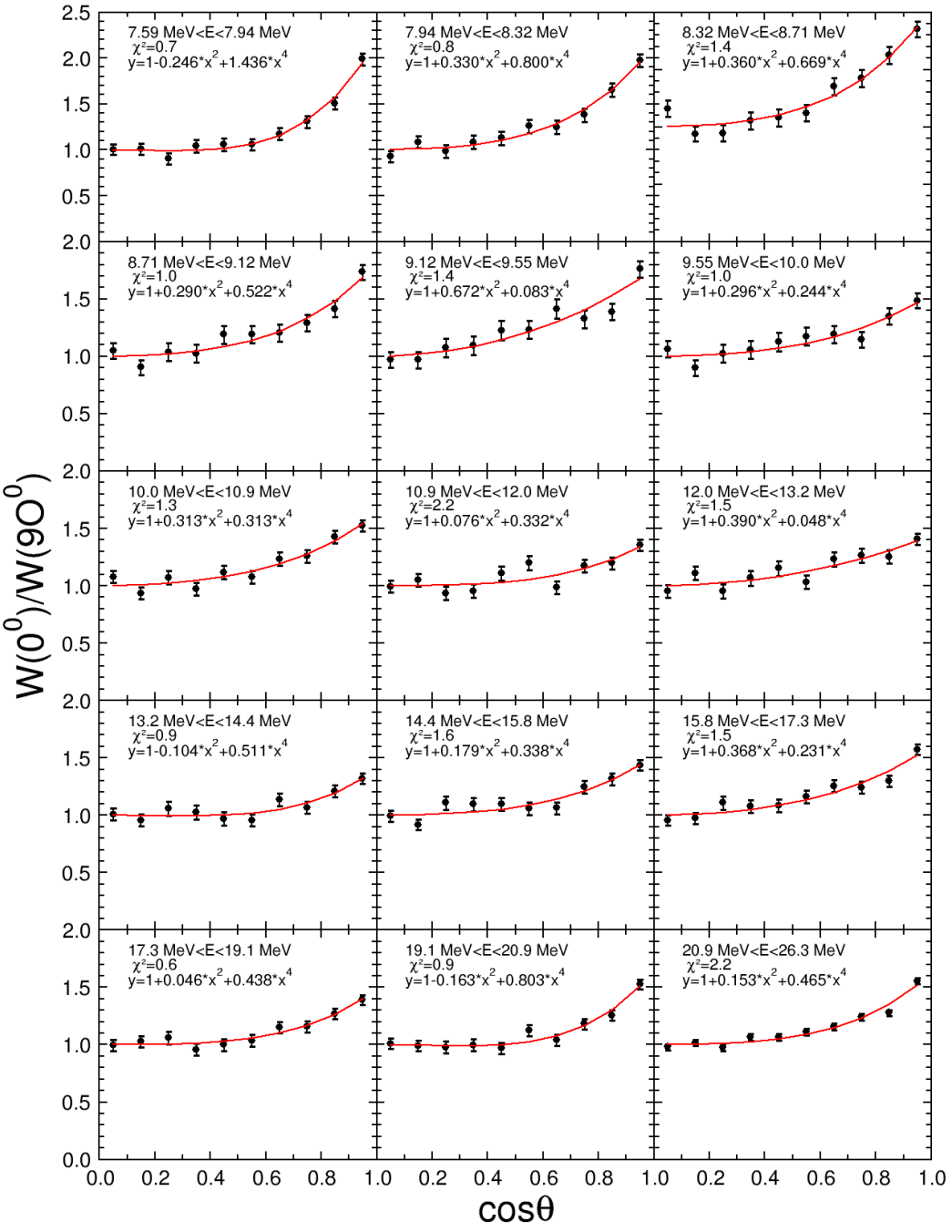

FIGURE B.4: ^{232}Th angular distributions for $7.59 < E_n < 26.3$ MeV

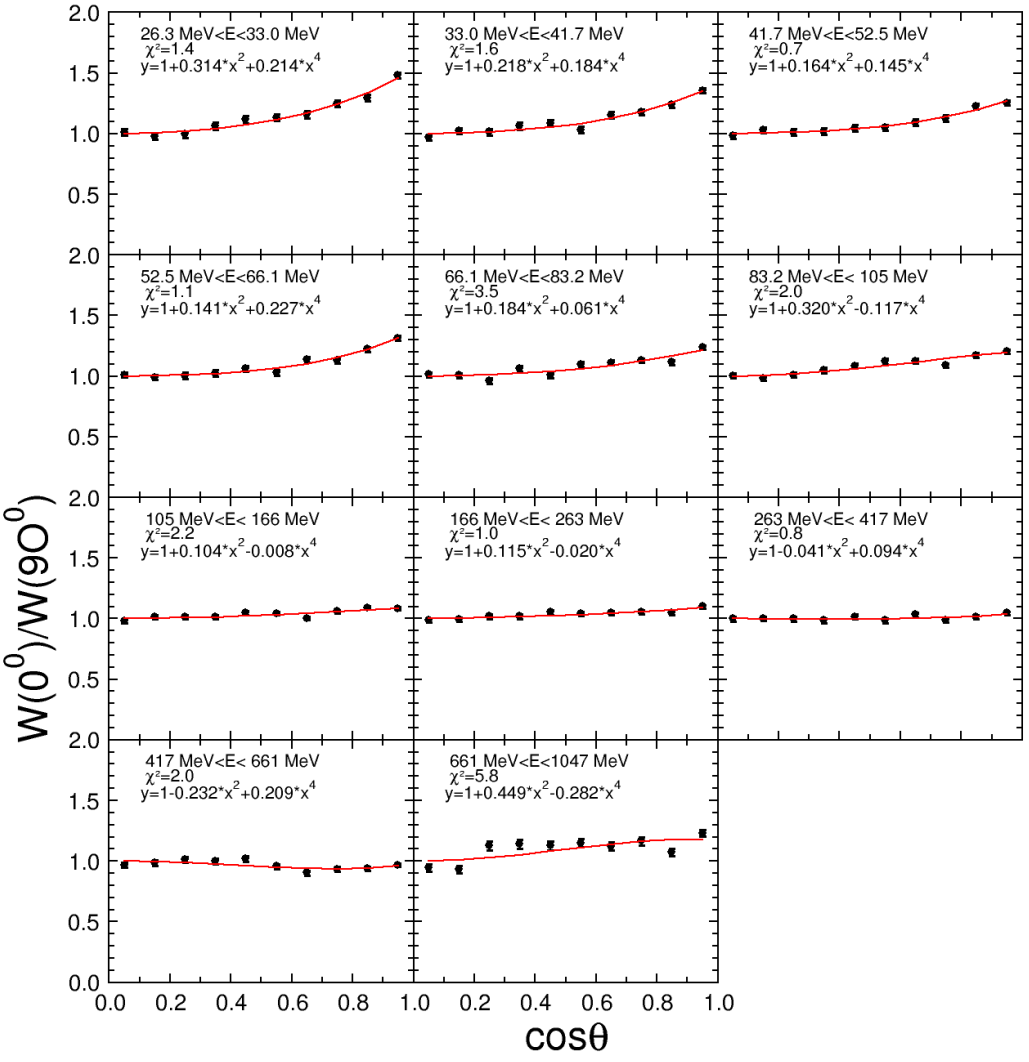

FIGURE B.5: ^{232}Th angular distributions for $26.3 < E_n < 1047$ MeV

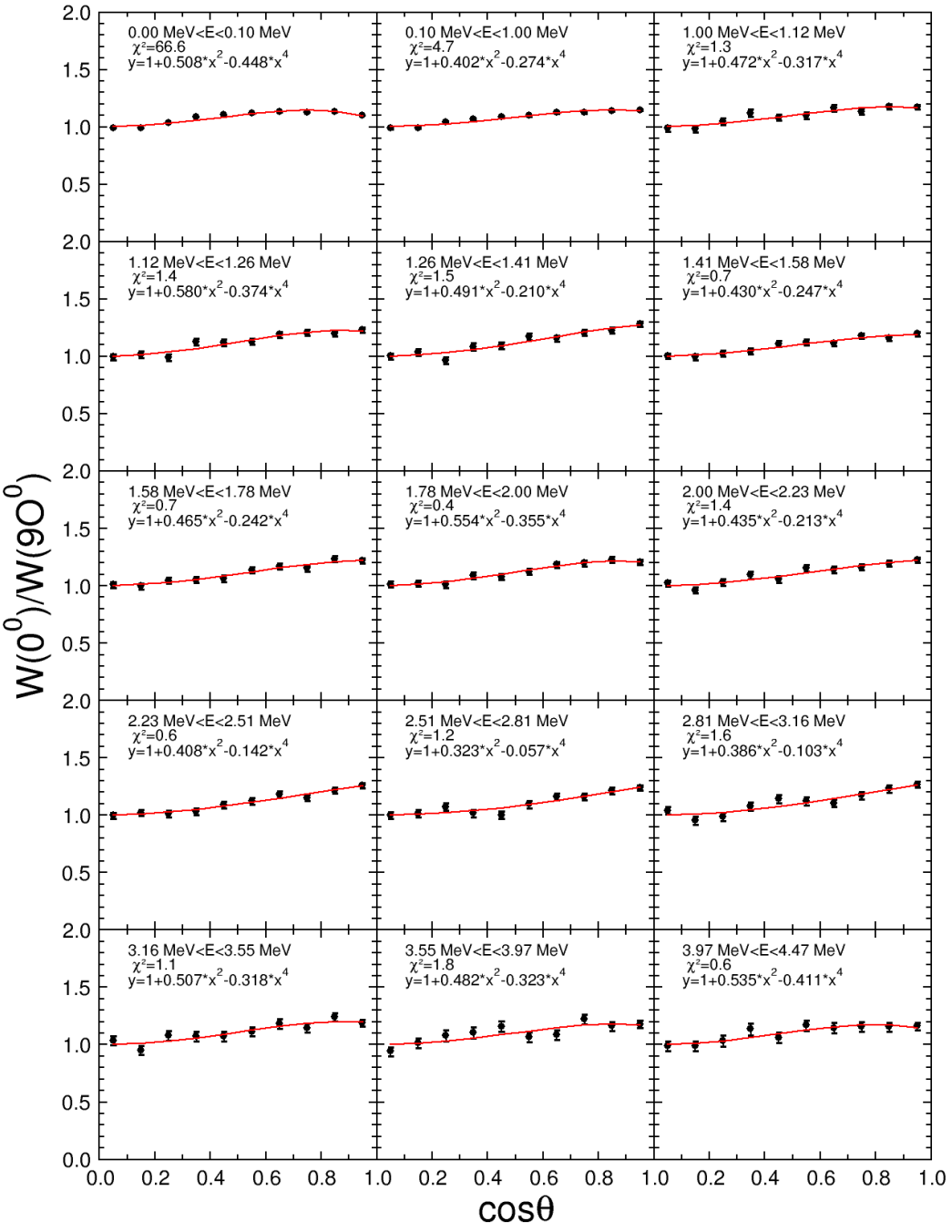

FIGURE B.6: ^{235}U angular distributions for $E_n < 4.47$ MeV

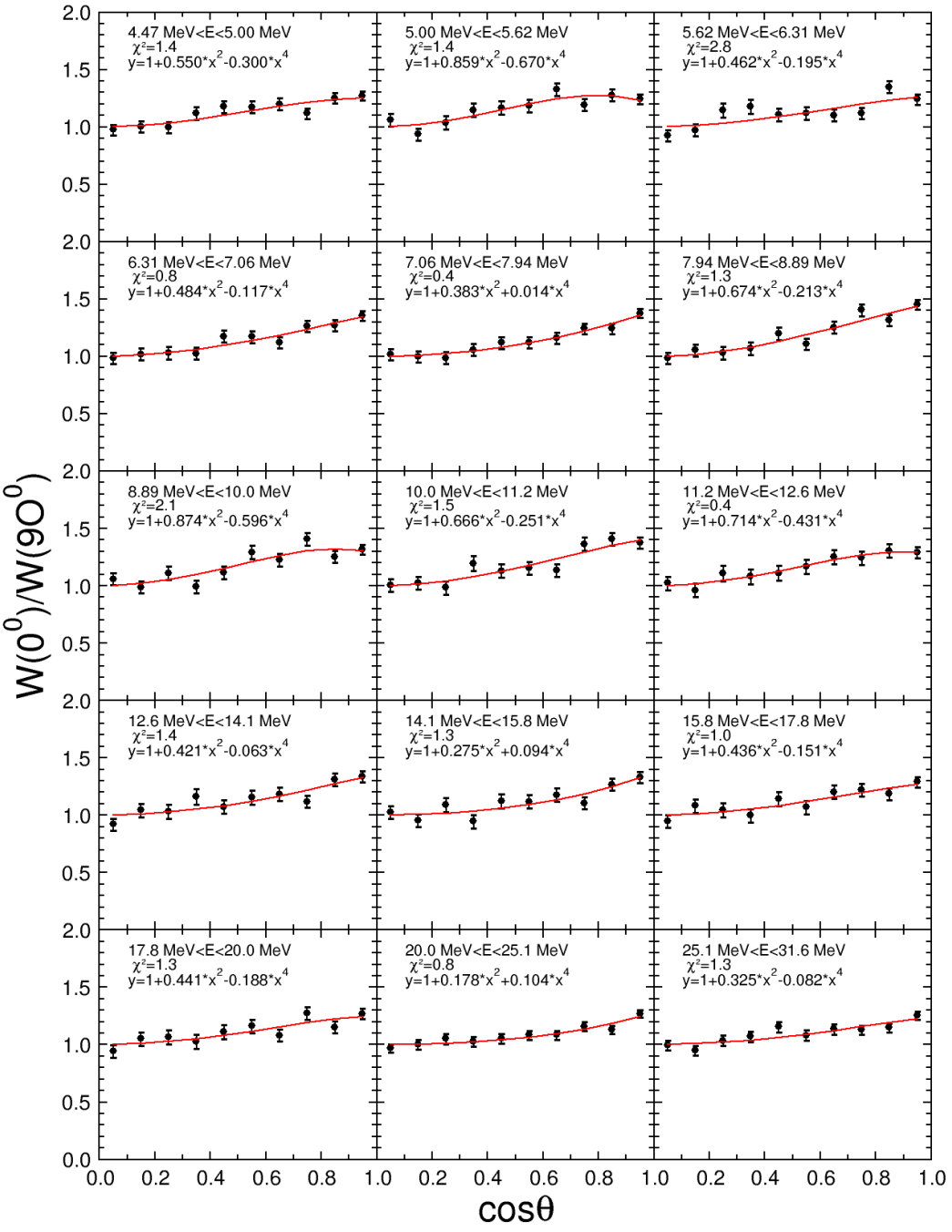

FIGURE B.7: ^{235}U angular distributions for $4.47 < E_n < 31.6$ MeV

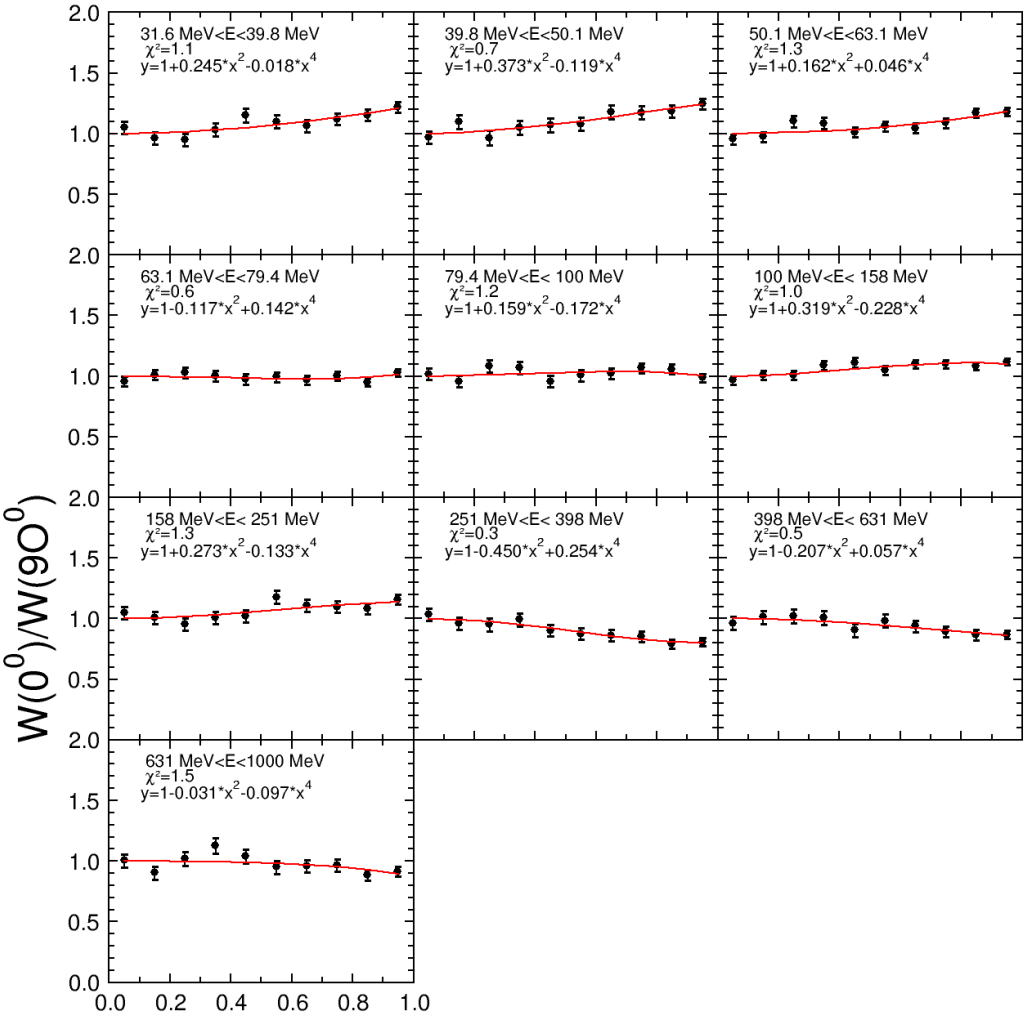

FIGURE B.8: ^{235}U angular distributions for $31.6 < E_n < 1000$ MeV

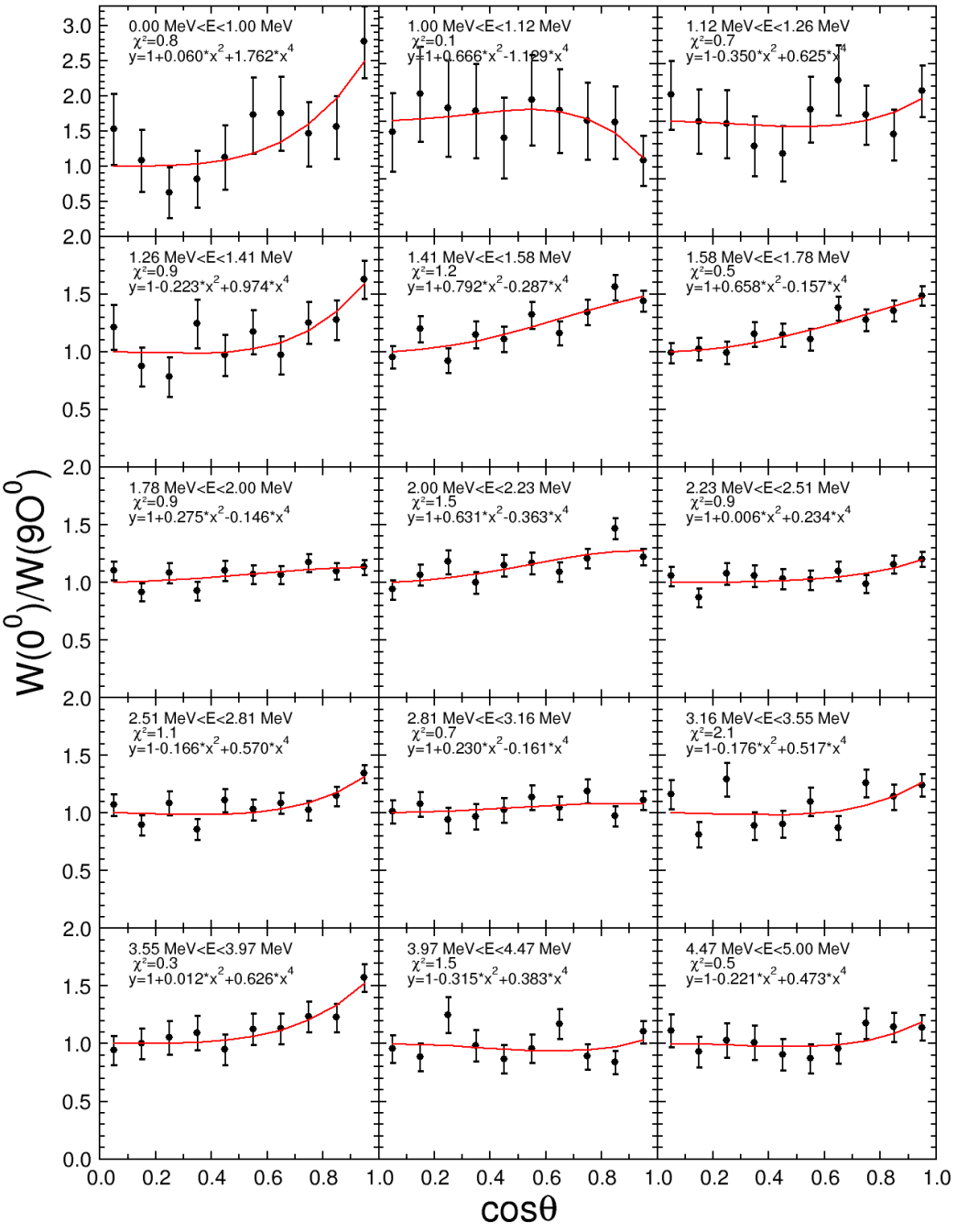

FIGURE B.9: ^{238}U angular distributions for $E_n < 5.00$ MeV

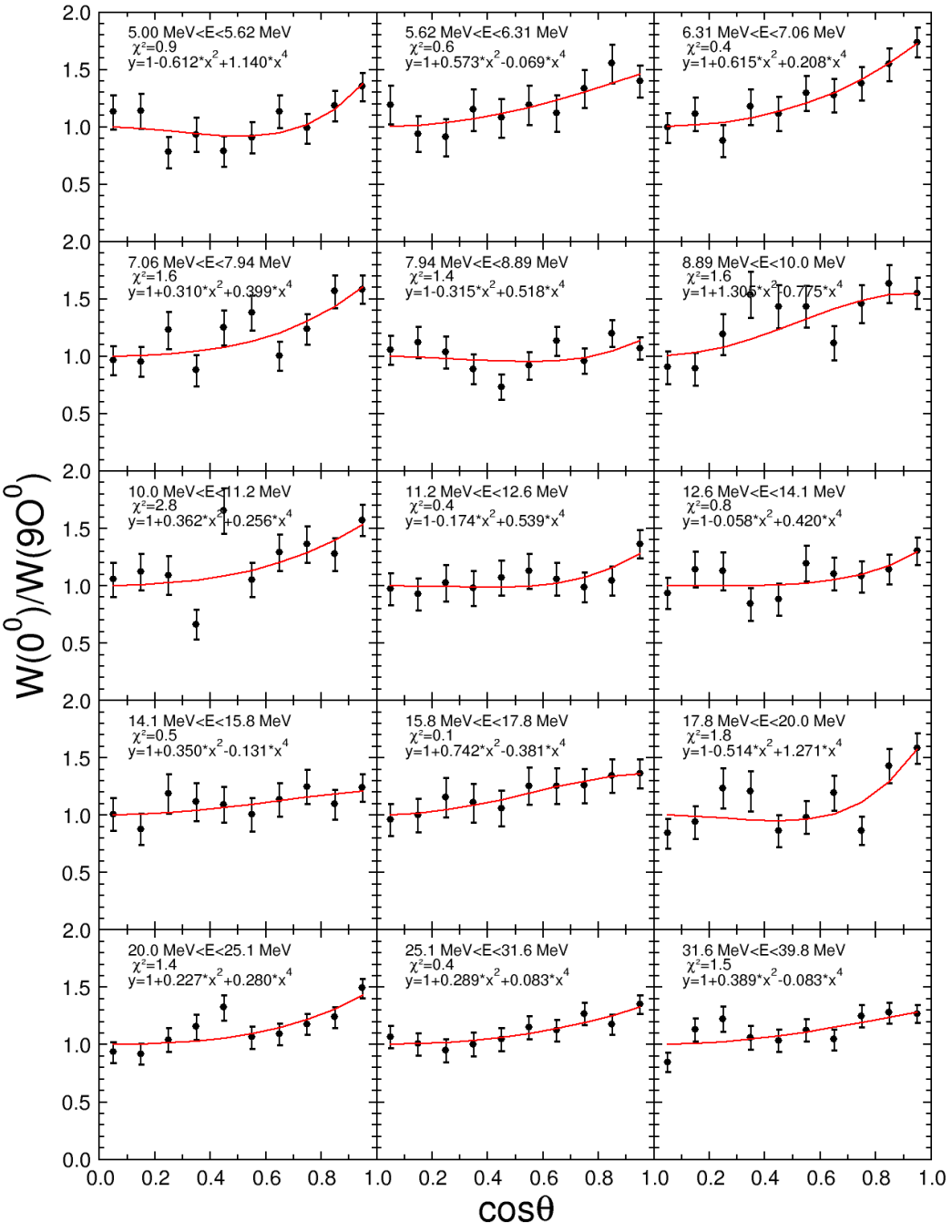

FIGURE B.10: ^{238}U angular distributions for $5.00 < E_n < 39.8$ MeV

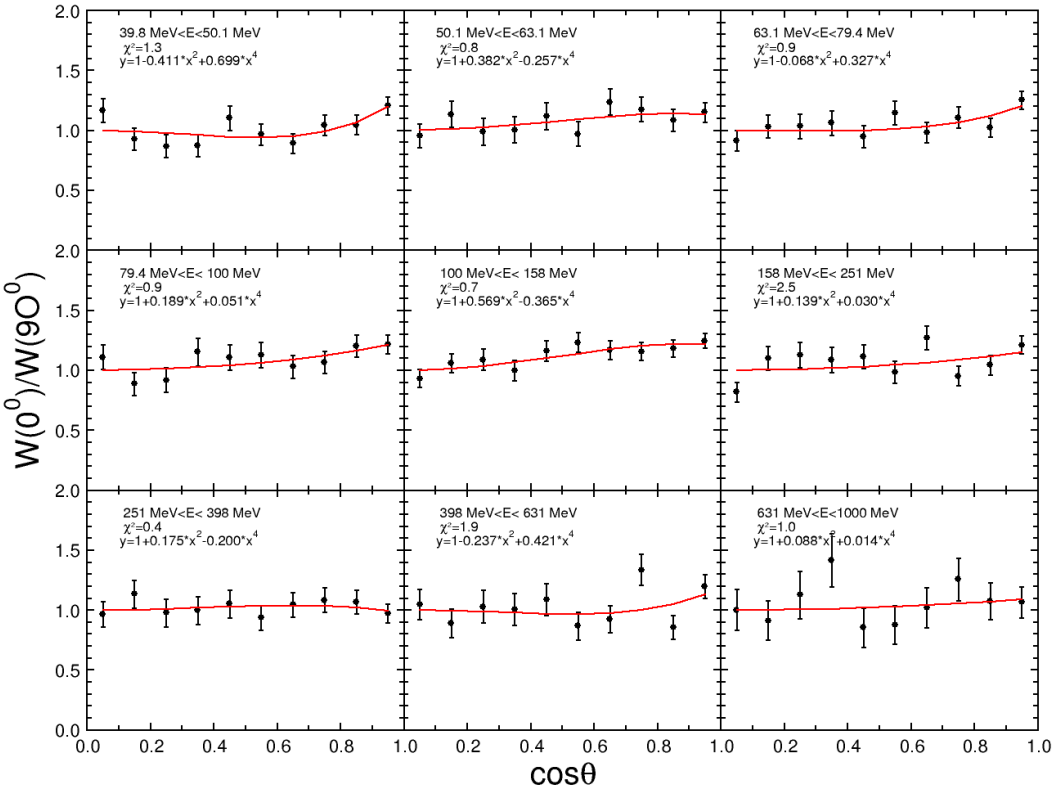

FIGURE B.11: ^{238}U angular distributions for $39.8 < E_n < 1000$ MeV

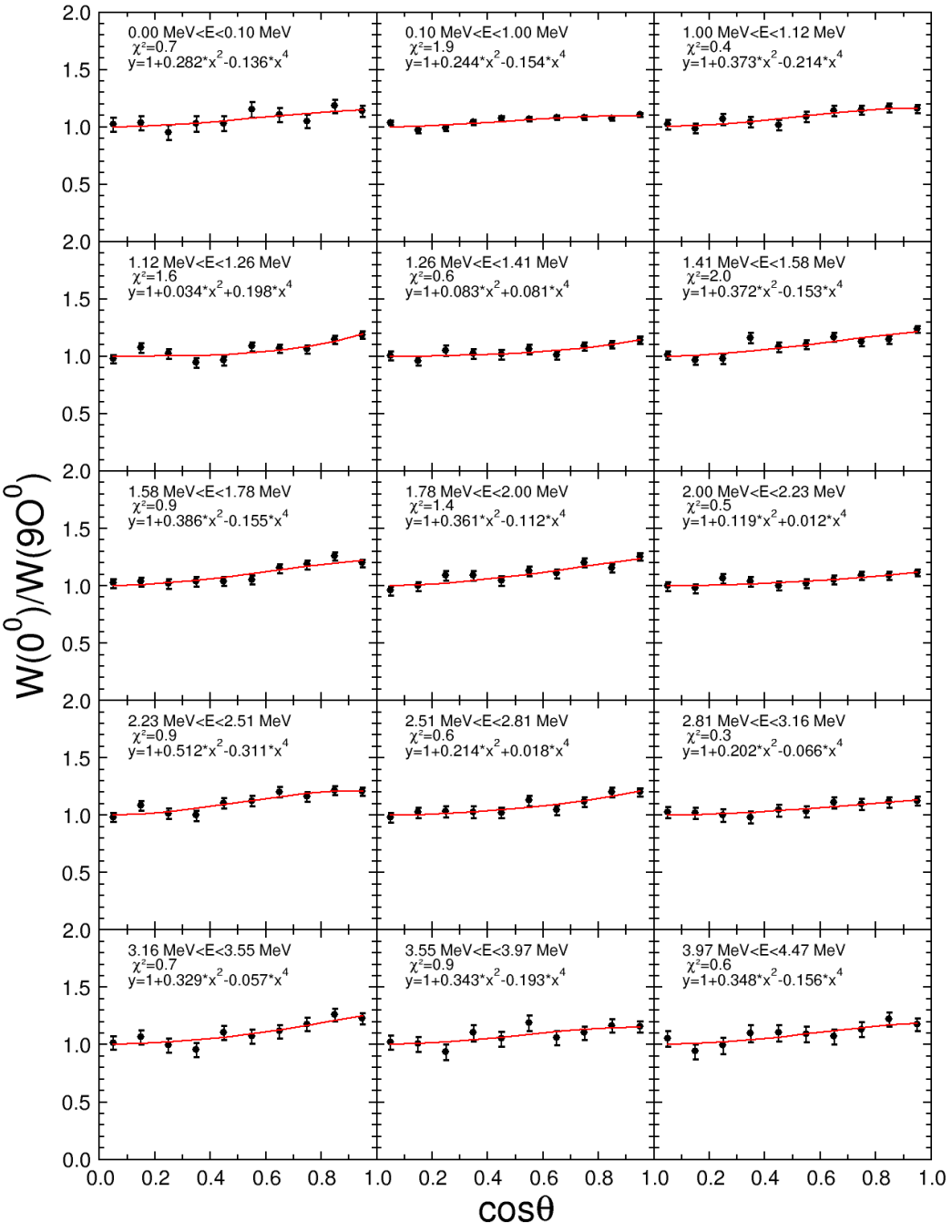

FIGURE B.12: ^{237}Np angular distributions for $E_n < 5.00$ MeV

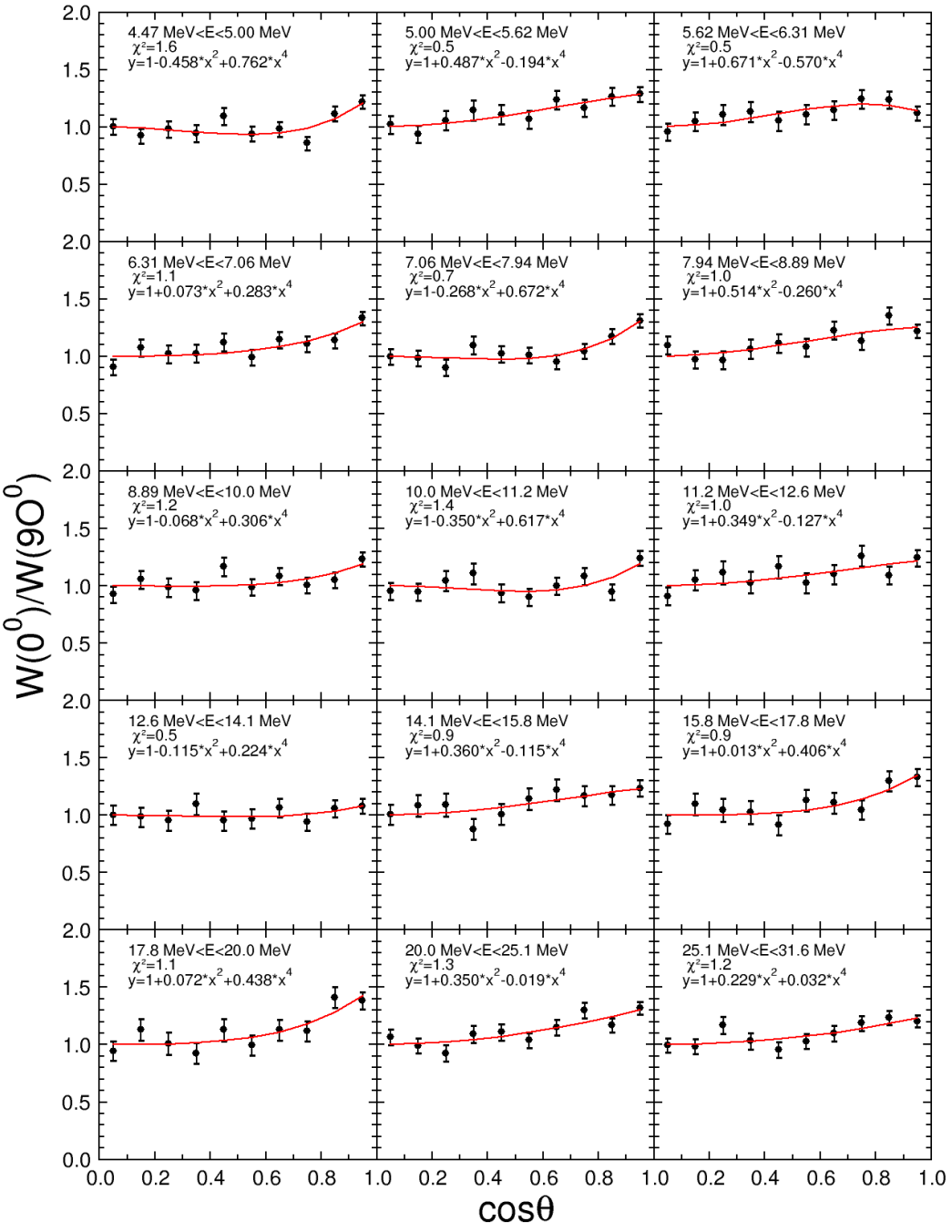

FIGURE B.13: ^{237}Np angular distributions for $5.00 < E_n < 39.8$ MeV

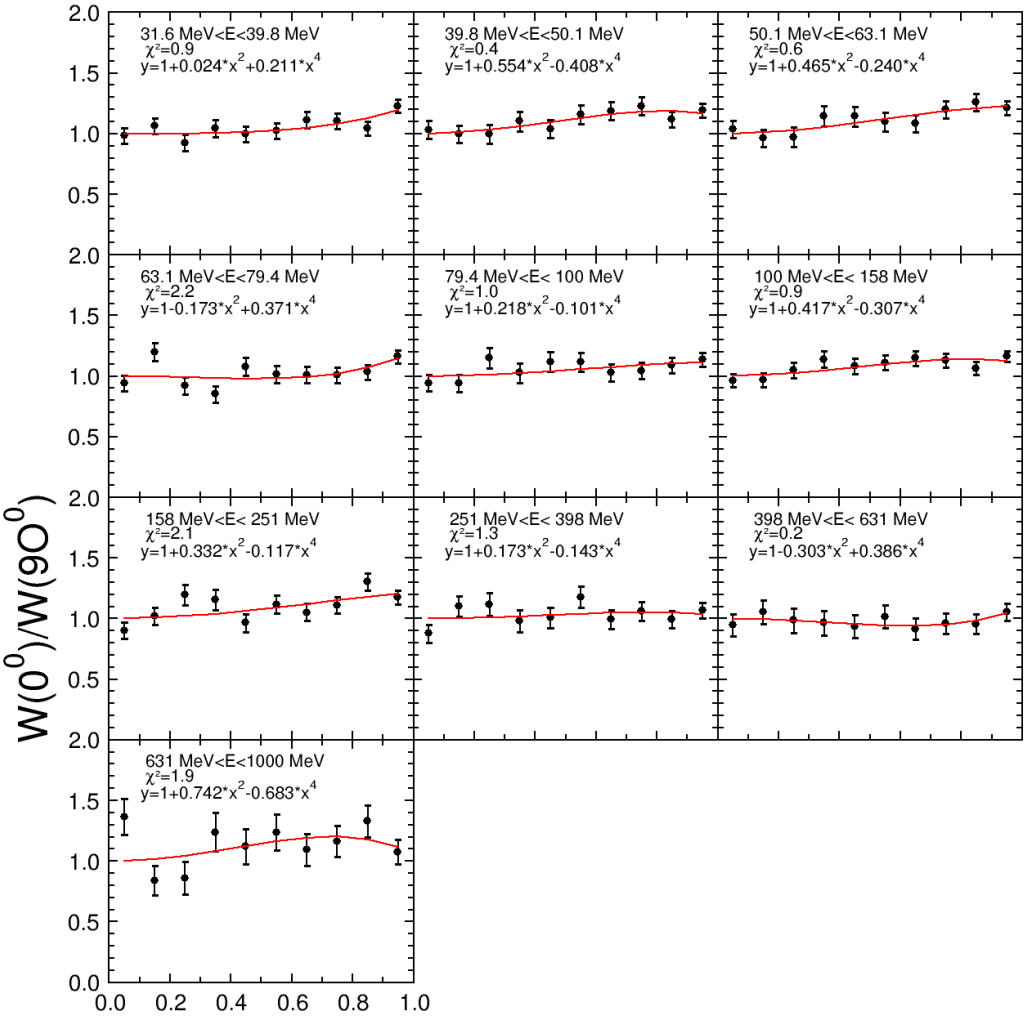

FIGURE B.14: ^{237}Np angular distributions for $39.8 < E_n < 1000$ MeV

Bibliography

[1] G.A. Tutin et al. An ionization chamber with frisch grids for studies of high-energy neutron-induced fission. *Nucl. Instr. Meth.*, A 457:646, 2001.

[2] Robert Vandenbosch and John R. Huizenga. *Nuclear Fission.* Academic Press, New York, 1973.

[3] Guillaume Boutoux. *Sections efficaces neutroniques via la méthode de substitution.* PhD thesis, Université Bordeaux I, 2011.

[4] Diego Tarrío Vilas. *Neutron-induced fission fragment angular distribution at CERN nTOF: The Th-232 case.* PhD thesis, PhD thesis, Universidade de Santiago de Compostela, 2012.

[5] I.V. Ryzhov et al. Influence of multichance fission on fragment angular anisotropy in the ^{232}Th(n,f) and ^{238}U(n,f) reactions at intermediate energies. *Nuclear Physics, Section A*, 760:19, 2005. EXFOR #22898 .

[6] A.N. Smirnov, I.Y. Gorshkov, A.V. Prokofiev, and V.P. Eismont. Total and differential cross sections of 10 to 95 MeV proton-induced fission of actinide nuclei. In 21^{th} *International Symposium on Nuclear Physics, Gaussig, Germany*, page 214, 1991. EXFOR #O0606.013.

[7] V.P. Eismont, N.P. Filatov, A.N. Smirnov, and J. Blomgren. Angular anisotropy of intermediate energy nucleon-induced fission of actinide and sub-actinide nuclei. In *ND2007 International Conference on Nuclear Data for Science and Technology 2007, Nice, France*, page 1077. EDP Sciences, April 22-27 2007. DOI: 10.1051/ndata:07483.

[8] Knitter et al. Investigation of fast neutron interaction with ^{235}U. *Z. Phys.*, 108-123:257, 1972.

[9] MUSE-4. Benchmark on computer simulation of MASURCA critical and subcritical experiments. Technical report, NEA, 2005. NEA/NSC/DOC(2005)23, ISBN 92-64-01086-6.

[10] Kim S.S. and R.W. Schaefer. NIST sphere experiments for ^{235}U, ^{239}Pu, ^{238}U, ^{237}Np fission rates, FUND-NIST-CF-MULT-FISS-01. Technical report, NEA, 2010. International Handbook of Evaluated Criticality Safety Benchmark Experiment, NEA/NSC/DOC/(95)03/IX.

[11] Niels Bohr and John Archibald Weeler. The mechanism of nuclear fission. *Phys. Rev.*, 56:426, 1939.

[12] V.M. Strutinsky. Shell effects in nuclear masses and deformation energies. *Nucl. Phys. A*, 95:420, 1967.

[13] V. Weisskopf. Statistics of nuclear reactions. *Phys. Rev.*, 52:295–303, 1937.

[14] Kronig R. de L. and Rabi I. I. The symmetrical top in the undalotary mechanic. *Phys. Rev.*, 29:262, 1927.

[15] Wigner E. P. *Group Theory and Its Application to the Quantum Mechanics of Atomic Spectra*. Academic Press, New York, 1959.

[16] C. Borcea et al. Results from the commissioning of the n-TOF spallation source at CERN. *Nucl. Instr. Meth. Res. A*, 489:346, 2002.

[17] FLUKA. http://www.fluka.org/fluka.php.

[18] S. Agostinelli et al. GEANT4-a simulation toolkit. *Nucl. Instr. Meth.*, A 506: 250, 2003.

[19] MCNPX, 2003. http://mcnpx.lanl.gov.

[20] C. Stéphan et al. Neutron-induced fission cross section measurements between 1 eV and 250 MeV. *J. Nucl. Sci. and Techn.,Supp.*, 2:276–279, 2002.

[21] Laure Ferrant. *Mesures de sections efficaces de fission induite par neutrons sur des actinides du cycle du thorium à n_ TOF*. PhD thesis, Thèse, Université Paris XI Orsay, 2005.

[22] M. Calviani et al. A fast ionization chamber for fission cross-section measurements at n_tof. *Nuclear Instruments and Methods in Physics Research A*, 594:220, 2008.

[23] S. Andriamonje et al. A new 2D-micromegas detector for neutron beam diagnostic at n_tof. In *ND2010 International Conference on Nuclear Data for Science and Technology 2010, Jeju Island, Republic Of Korea, 26 - 30 Apr 2010*, volume 59, page 1601, 2011.

[24] C. Guerrero et al. The n_TOF total absorption calorimeter for neutron capture measurements at CERN. *Nuclear Instruments and Methods in Physics Research A*, 608:424, 2009.

[25] C. Lederer et al. ^{197}Au(n,γ) cross section in the unresolved resonance region. *Phys. Rev. C*, 83:034608, 2011.

[26] René Brun and Fons Rademakers. ROOT - an object oriented data analysis framework. *Nucl. Instr. Meth.*, A 389:81, 1997.

[27] M.B. Chadwick et al. ENDF/B-VII.1 nuclear data for science and technology: Cross sections, covariances, fission product yields and decay data. *Nucl. Data Sheets*, 112:2887, 2011.

[28] G. Barreau. Contribution to the study of the fast neutron induced fission of the compound nuclei U-235, U-237, U-239 and Th-233. Technical report, CENBG, 1977. CENBG Bordeaux-Gradignan Report, EXFOR #21746 .

[29] F.-M. Baumann, K.Th. Brinkmann, H. Freiesleben, J. Kiesewetter, and H. Sohlbach. Angular distributions of ^{230,232}Th(n,f) and the third-minimum hypothesis. *Nucl. Phys. A*, 502:271, 1989. EXFOR #22141 .

[30] J. Caruana, J.W. Boldeman, and . R.L. Wlash. Fission fragment angular distributions for neutron fission of ^{232}Th and their interpretation with a triple-humped fission barrier. *Nucl. Phys. A*, 285:205, 1977. EXFOR #30455 .

[31] S. B. Ermagambetov and G.N. Smirenkin. Fragment angular distributions and channel analysis of fission of 90-Th-232 by neutrons. *J. Nucl. Phys.*, 11: 646, 1970. EXFOR #40014 .

[32] J.E. Simmons and R.L. Henkel. Angular distribution of fragments in fission induced by MeV neutrons. *Phys. Rev.*, 120:198, 1960. EXFOR #13706 .

[33] K.D. Androsenko, G.G. Korolev, and D.L. Shpak. Angular anisotropy of fission fragments for Th-232, U-233, U-235, U-238, Np-237, Pu-238, Pu-239, for neutron energy 12.4 - 16.4 MeV. *Yad. Konst.*, 2:46, 1982. EXFOR #40825 .

[34] R.L. Henkel and Jr. J.E. Brolley. Angular distribution of fragments from neutron-induced fission of U238 and Th232. *Phys. Rev.*, 103:1292, 1956. EXFOR #13709 .

[35] R.H.Iyer and M.L. sagu. Fragment angular distributions in the 14 MeV neutron induced fission of Th232, U233, U235, U238, Np237, Pu239, Am241. *Nucl. and Solid State Physics Symp., Madurai 1970*, 2:57, 1970. EXFOR #30235 .

[36] S.Juhasz and M. Varnagy. Angular distribution in neutron induced fission of Th-232, natural uranium,Np-237 and Pu-239. Technical report, Zentralinstitut fuer Kernforschung, 1978. EXFOR #30510 .

[37] R.B. Leachman and L. Blumberg. Fragment anisotropies in neutron-, deuteron-, and alpha-particle induced fission. *Phys. Rev.*, 137:B814–825, 1965. EXFOR #13708 .

[38] D.L. Shpak, A.I. Blokhin, J.B. Ostapenko, and G.N. Smirenkin. Angular anisotropy of the fragments from fission of Th-232 and Pu-238 by 13.40-14.80 MeV neutrons. *Yad. Fiz. Issled.*, 13:4, 1972. EXFOR #40111 .

[39] EXFOR. https://www-nds.iaea.org/exfor/exfor.htm.

[40] C.T. Coffin and I. Halpern. Angular distributions in fission induced by alpha particles, deuterons and protons. *Phys. Rev.*, 112:536, 1958.

[41] J.W. Meadows. Angular distributions of fragments from fission of ^{238}U and ^{232}Th by 45-, 80-, and 155-MeV protons. *Phys. Rev.*, 110:1109, 1958.

[42] V.S. Bychenkov et al. *Soviet J. Nucl. Phys*, 17:496, 1973.

[43] J. Csikai and S. Nagy. Investigations on the angular distribution of neutron-induced 238-U fission using solid state track detectors. *Nucl. Sc. and Appl. B*, 9:17, 1976.

[44] D.L. Shpak. Angular anisotropy of fragments from U-238 fission induced by the 0.85 - 6.28 MeV neutrons. *Yad. Fiz.*, 50:922, 1989. EXFOR #41041 .

[45] E. Barutcugil, S. Juhasz, M. Varnagy, S. Nagy, and J. Csikai. Angular distribution of fragments in the fission of uranium and thorium near the (n,2n'f) threshold. *Nucl. Phys. A*, 173:571, 1971. EXFOR #30117 .

[46] P.E. Vorotnikov, S.M. Dubrovina, and G.A. Ostroshchenko. Angular distributions of fragments and fission cross section of U-238 by neutrons near threshold. *Yad. Fiz. Issled. Reports*, 12:22, 1971.

[47] J.E. Brolley and W.C. Dickenson. Angular distribution of fragments from neutron-induced fission. *Phys. Rev.*, 94:640, 1954. EXFOR #13707 .

[48] B.M. Gokhberg et al. Differences of the angular distributions for fission fragments of different masses in nuclear fission. *Yad. Fiz.*, 47:320, 1988. EXFOR #40965 .

[49] S.Juhasz, M. Varnagy, J. Csikai, and S. Ouichaoui. Angular distribution of fragments from fast neutron induced fission of U-235, U-238, Np-237. *Acta Phys. Hung.*, 64:209, 1988. EXFOR #30819 .

[50] C.N. Pandey and S.K. Bose. Angular distributions of fragments in fission of U-238 induced by neutrons in the range 2 to 14 MeV. In *19 Nucl. Phys. Solid State Symp., Ahmedabad, 1976*, volume 2, page 131, 1976. EXFOR #30435 .

[51] M.M. Kasim, A.R. Mallik, and E.U. Molla. Angular distributions of fragments in fission from fast neutron-induced fission of U-238. *Nuclear Science and Applications*, 9:17, 1976. EXFOR #30428 .

[52] F. Vives, F.J. Hambsch, G. Barreau, S. Obertstedt, and H. Bax. Investigation of the fission fragment properties of the reaction U-238(n,f) at incident neutron energies up to 5.8MeV. *Nuclear Physics, Section A*, 662:63, 2000. EXFOR #22402 .

[53] V.G. Vorob'Jova, A.I. Gentosh, B.D. Kuz'Minov, and A.I. Sergachjvov. Angular anisotropy and asymmetry of fragment masses by fission of U-235 and U-238. *Yad. Fiz.*, 10:491, 1969. EXFOR #40240 .

[54] Zhou Shuhua, Guo Shilun, Men Wu, Sun Shengfen, and Hao Xiuhong. Angular distributions of fission fragments at the U-238(n,f) threshold. *Chinese J. of Nucl. Phys.*, 3:39, 1981. EXFOR #30694 .

[55] Ye Zhongyuan, Li Jingwen, Zhou Shuhua, and Hao Xiuhong. The measurement of fragment angular distributions for U-238(n,f) fission reaction near threshold. *Science in China A*, 25:502, 1982. EXFOR #30693 .

[56] S. Ahmad et al. The energy dependence of fission fragment anisotropy in fast-neutron-induced fission of uranium-235. *Nucl. Sci. Eng.*, 71:208, 1979. EXFOR #30520 .

[57] J.E. Brolley, W.C. Dickenson, and R.L. Henkel. Angular dependence of the neutron-induced fission process. *Phys. Rev.*, 99:159, 1955. EXFOR #13711 .

[58] S.T. Hsue, G.F. Knoll, and J. Meadows. Angular distribution of fission fragments from fission of U-235. *Nucl. Sci. Eng.*, 66:24, 1978. EXFOR #10988 .

[59] J.W. Meadows and C. Budtz-Jorgensen. The fission fragment angular distributions and total note=EXFOR #12798 , kinetic energies for 235-U(n,f) from .18 to 8.83 MeV. In *Conference on Nuclear data for Science and technology, Antwerp, 1982*, page 740, 1982.

[60] V.G. Nesterov, G.N. Smirenkin, and D.L. Shpak. Energy dependence of the angular distribution of fragments in the neutron fission of U-233, U-235 and Pu-239. *Yad. Fiz.*, 4:993, 1966. EXFOR #40366 .

[61] D.L. Shpak, B.I. Fursov, and G.N. Smirenkin. Angular anisotropy of fission of Np-237 and Am-241 by neutrons. *Yad. Fiz.*, 12:35, 1970. EXFOR #40277 .

[62] J.W. Meadows. The fission cross section of ^{237}Nprelative to ^{235}U from 0.1 to 9.4 MeV. *Nuclear science and engineering*, 85:271–279, 1983.

[63] Lisowski et al. Neutron induced fission cross section ratios for ^{232}Th, ^{235}U, ^{238}U, ^{237}Np and ^{239}Pu from 1 to 400 MeV. In *Nuclear Data for Science and Technology MITO, Japan*, page 97, 30 May-3 June 1988.

[64] Shcherbakov et al. Neutron induced fission of ^{233}U, ^{238}U, ^{232}Th, ^{239}Pu, ^{237}Np, ^{nat}Pb and ^{209}Bi relative to ^{235}U in the energy range 1-200 MeV. *J. Nucl. Sci. Technol.*, 2:230–233, 2002.

[65] F. Tovesson and T.S. Hill. Subthreshold fission cross section of ^{237}Np. *Nucl. Sci. Eng.*, 159:94–101, 2008.

[66] F. Tovesson and T.S. Hill. Neutron induced fission cross section of ^{237}Np from 100 keV to 200 MeV. *Phys. Rev. C*, 75:034610, 2007.

[67] Behrens J.W. et al. Measurement of the neutron-induced fission cross section of ^{237}Np relative to ^{235}U from 0.02 to 30 MeV. *Nucl. Sci. Eng.*, 85:271, 1983.

[68] C. Paradela et al. Neutron-induced fission cross section of ^{234}U and ^{237}Np measured at the CERN neutron time-of-flight (nTOF) facility. *Phys. Rev. C*, 82:034601, 2010.

[69] C. Paradela et al. ^{237}Np(n,f) cross section: New data and present status. In *ND2010 International Conference on Nuclear Data for Science and Technology 2010, Jeju Island, Republic Of Korea, 26 - 30 Apr 2010*, volume 59, page 1908, 2011.

[70] David Loaiza. Neptunium-237 sphere surrounded by hemispherical shells of highly enriched uranium, SPEC-MET-FAST-008. Technical report, NEA, 1995. International Handbook of Evaluated Criticality Safety Benchmark Experiment,NEA/NSC/DOC/(95)03/VII.

[71] X-5 Monte Carlo Team. Mcnp, overview and theory. Technical report, Los Alamos, 2003. LA-UR-03-1987, https://mcnp.lanl.gov/.

[72] O. Meplan et al. MURE, MCNP Utility for Reactor Evolution, 2009. http://www.nea.fr/tools/abstract/detail/nea-1845.

[73] R. Sanchez et al. Criticality of a ^{237}Np sphere. *Nucl. Sci. Eng.*, 158:1, 2008.

[74] R.D. Mosteller et al. Creation of a simplified benchmark model for the neptunium sphere experiment. Technical report, Los Alamos, 2004. LA-UR-04-0525.

[75] R.D. Mosteller et al. Creation of a simplified benchmark model for the neptunium sphere experiment. In *PHYSOR2004 Chicago Illinois*, pages 25–29, April 25-29 2004.

[76] M.B. Chadwick et al. ENDF/B-VII.0: Next generation evaluated nuclear data library for nuclear science and technology. *Nucl. Data Sheets*, 107:2931, 2006.

[77] B. Mihaila et al. Analysis of Np-237 ENDF for the theoretical interpretation of critical assembly experiments. Technical report, Los Alamos, 2004. LA-UR-04-1959.

[78] LaBauve R.J. et al. Bare, highly enriched uranium sphere (godiva), heu-met-fast-001. Technical report, NEA, 2010. International Handbook of Evaluated Criticality Safety Benchmark Experiment, NEA/NSC/DOC/(95)/03/II.

[79] R. Batchelor and K. Wyld. Neutron scattering by U-235 and Pu-239 for incident neutrons of 2, 3 and 4 MeV, 1969. EXFOR #20036 .

[80] A.C. Kahler et al. ENDF/B-VII.1 neutron cross section data testing with critical assembly benchmarks and reactor experiments. *Nucl. Data Sheets 112*, page 2997, 2011.

[81] Grundle J.A. et al. Measurement of absolute fission rates. *Nucl. Technol.*, 25: 237, 1975.

[82] J.M. Verbeke, C. Hagman, and D. Wright. Simulation of neutron and gamma ray emission from fission and photofission. Technical report, LLNL, May 11 2010. UCRL-AR-228518.

[83] Adamov V.M. et al. Absolute ^{235}U, ^{238}U, ^{237}Np fast neutron fission cross section measurements. In *International Specialists Symposium on Neutron Standards and Applications, Gaithersburg*, page 313, March 28-31 1977.